Development of an Experiment for Ultrahigh-Precision *g-Factor* Measurements in a Penning-Trap Setup

Dissertation zur Erlangung des Grades
Doktor der Naturwissenschaften
am Fachbereich 08: Physik, Mathematik und Informatik
der Johannes Gutenberg-Universität Mainz

Von Joseba Alonso Otamendi
geb. in Madrid (Spanien)
Mainz, 2007

Clause of correct use:

Usage, further investigation or further development, both in a direct or in an indirect manner, of any of the scientific contributions by the author presented in this thesis, are absolutely forbidden to all armies in the world as well as any other armed group and may not serve any military use or any use transgressing human rights or the environment.

Zusammenfassung

Die vorliegende Arbeit befasst sich mit der Entwicklung und dem Aufbau eines Experiments zur hochpräzisen Bestimmung des *g-Faktors* gebundener Elektronen in hochgeladenen Ionen. Der *g-Faktor* eines Teilchens ist eine dimensionslose Konstante, die die Stärke der Wechselwirkung mit einem magnetischen Feld beschreibt. Im Falle eines an ein hochgeladenes Ion gebundenen Elektrons, dient es als einer der genausten Tests der Quantenelektrodynamik gebundener Zustande (BS-QED). Die Messung wird in einem dreifach Penning-Fallen System durchgeführt und basiert auf dem kontinuierlichen Stern-Gerlach-Effekt. Der erste Teil dieser Arbeit gibt den aktuellen Wissensstand über magnetische Momente wieder. Der hier gewählte experimentelle Aufbau wird begründet. Anschließend werden die experimentellen Anforderungen und die verwendeten Messtechniken erläutert. Das Ladungsbrüten der Ionen - einer der wichtigsten Aufgaben dieser Arbeit - ist dargestellt. Seine Realisierung basiert auf einer Feld-Emissions-Spitzen-Anordnung, die die Messung des Wirkungsquerschnitts für Elektronenstoßionisation ermöglicht. Der letzte Teil der Arbeit widmet sich der Entwicklung und dem Aufbau des Penning-Fallen Systems, sowie der Implementierung des Nachweisprozesses. Gegenwärtig ist der Aufbau zur Erzeugung hochgeladener Ionen und der dazugehörigen Messung des *g-Faktors* abgeschlossen, einschließlich des Steuerprogramms für die erste Datennahme. Die Ionenerzeugung und das Ladungsbrüten werden die nächsten Schritte sein.

Summary

This thesis is concerned with the design and construction of an experimental setup aiming to perform ultrahigh-precision *g-factor* measurements on a bound electron in highly-charged ions. The *g-factor* of a particle is a dimensionless constant which determines the strength of its interaction with a magnetic field. In the case of an electron bound to a highly-charged ion, it serves as one of the most stringent tests of bound-state quantum electrodynamics (BS-QED). The measurement is based on a triple-Penning-trap system and the continuous Stern-Gerlach effect. The first part of the thesis is devoted to the current knowledge on magnetic moments and motivates the techniques and experimental setup used during the work described. As a major challenge to overcome, the charge breeding of the ions is dealt with in detail, along with the solution found, based on a field-emission-point array. The tools included allow for the measurement of ionization cross-sections by electron impact. The last part of the thesis is dedicated to the design and operation of the triple-Penning-trap setup and the detection schemes implemented. At present, all the experimental setup for the production of highly-charged ions and the corresponding *g-factor* measurement is completely finalized, including the control system needed for the first measurement stages, so the ion-creation and charge-breeding processes will be the next steps to be taken.

Contents

List of Figures

List of Tables

Chapter 1

Motivation and Introduction

"There are two sorts of curiosity – the momentary and the permanent. The momentary is concerned with the odd appearance on the surface of things. The permanent is attracted by the amazing and consecutive life that flows on beneath the surface of things."

Robert Lynd, Solomon in All His Glory.

It is believed by a large part of the scientific community that we are finally approaching the total understanding of the laws that govern our Universe. This is a bold sentence indeed, and one that might very well be proven wrong, but also one that is not pronounced lightly.

The conceptual idea of a *Final Theory* seems to be well established in our minds; we seem to understand how it should look like, and there is a great variety of literature concerned with it (see, for example, [Wei92]).

During the 20^{th} century our scientific knowledge has grown amazingly. First, Einstein's Special and General Relativity theories changed once and for all our way of understanding space and time. Then, Quantum Mechanics made its appearance in stage, which translated into an even more radical rupture with our classical world. The fusion of both ideas relegated matter from being the central character. Now, the abstract symmetry principles are the protagonists. Upon this basis, a satisfactory theory for electromagnetism, weak and strong nuclear interactions was built: the **Standard Model**. Only gravitation is missing, but there is a lot of effort being made towards the description of a *Grand Unification Theory* where all interactions would be embraced.

It is a common effect that the more one knows about a certain topic, the more difficult it gets to learn further. But the importance of being able to go on never diminishes. That is the reason that high-precision measurements are crucial on our way to a complete description of the laws of physics. This was recently acknowledged by the Nobel-prize committee as they made their decision to give last year's award to T. Hänsch for his "contributions to the development of laser-based precision spectroscopy, including the optical frequency comb technique".

An important limb of the Standard Model is the interaction of electrons with electromagnetic fields: **Quantum Electrodynamics** (or **QED**, for short). Great progress has been done in this field, both theoretically and experimentally, and the main objective of this work is to make a contribution in gaining some more ground.

An impressive goal was achieved in this respect with the experimental measurement [Dyc87] and theoretical calculation [Kin06] of the *g-factor* of the free electron. The accuracy of $4 \cdot 10^{-12}$ with which the *g-factor* determination by R.S. Van Dyck and H.G. Dehmelt resulted, was unprecedented and rewarded Dehmelt with a share of the Nobel-prize in 1989. Their measurement has prevailed for almost 20 years until Dehmelt's former coworker, G. Gabrielse, achieved a six-fold improved relative uncertainty of 0.76 parts-per-*trillion* [Odo06], which led to yet another remarkable result: the determination of the fine-structure constant α with an accuracy of 0.7 parts-per-billion [Gab06].

This thesis is concerned with the development of an experimental setup devoted to the measurement of the *g-factor* of an electron bound to a highly-charged ion. Highly-charged ions in general, and hydrogenlike ions in particular, are a classical subject of quantum physics. The very discovery and further progress of quantum mechanics is intimately connected to the explanation of the main features of the energy levels of the the hydrogen atom. Each step in development of quantum physics led to a better understanding of the bound-state physics. Bohr quantization rules of the old quantum theory were created in order to explain the existence of the stable discrete energy levels. The non-relativistic quantum mechanics of Heisenberg and Schrödinger provided a self-consistent scheme for description of bound states. The relativistic spin-one-half Dirac equation quantitatively described the main experimental features of the hydrogen spectrum. Discovery of the Lamb shift [Lam47], a subtle discrepancy between the predictions of the Dirac equation and the experimental data, triggered development of modern relativistic quantum electrodynamics, and subsequently the Standard Model.

Despite its long and rich history, the theory of atomic bound states is still very much alive today. New importance to the bound state physics was given by the development of quantum chromodynamics, the modern theory of strong interactions. It was realized that all hadrons, once thought to be the elementary building blocks of matter, are themselves atom-like bound states of elementary quarks bound by the color forces. Hence, from a modern point of view, the theory of atomic bound states could be considered as a theoretical laboratory and testing ground for exploration of the subtle properties of the bound-state physics, free from further complications connected with the non-perturbative effects of quantum chromodynamics, which play an especially important role in the case of light hadrons. The quantum electrodynamics and quantum chromodynamics bound-state theories are so intimately intertwined today that one often finds theoretical research where new results are obtained simultaneously, say for positronium and also heavy quarkonium. The other powerful stimulus for further development of the bound-state theory is provided by the spectacular experimental progress in precise measurements of atomic energy levels. It suffices to mention that the relative uncertainty of the frequency measurement of the $1S - 2S$ transition in hydrogen was reduced during the last decade by three orders of magnitude from $3 \cdot 10^{-10}$ [Bos89] to $3.4 \cdot 10^{-13}$ [Ude97]. The relative uncertainty in measurement of the muonium hyperfine splitting was reduced later by a factor of 3 from $3.6 \cdot 10^{-8}$ [Mar82] to $1.2 \cdot 10^{-8}$ [Liu99].

This experimental development was matched in recent years by rapid theoretical progress. The theory of hydrogenic bound states is widely described in the literature. The basics of non-relativistic theory is contained in any textbook on quantum mechanics, and the relativistic Dirac equation and the Lamb shift are discussed in any textbook on quantum electrodynamics and quantum-field theory. A source for the early results is the classic book by Bethe and Salpeter [Bet57]. A coherent discussion of the modern status of the theory is provided by M. Eides *et al.* in [Eid95].

In particular the *g-factor* of the electron bound in a hydrogenlike ion and related properties have attracted also increased interest during the last few years. In that sense, the theoretical results of T. Beier *et al.* [Bei00b], V.A. Yerokhin *et al.* [Yer02] and K. Pachucki *et al.* [Pac05] are of vital importance. On the experimental side, the works of H. Häffner *et al.* [Häf00b] and J. Verdú *et al.* [Ver04a] have given the most precise values for the *g-factors* of the electrons in hydrogenlike carbon and oxygen, respectively. For a recent review on the state-of-the art, see [Wer06].

The work presented in this dissertation is required by a next step in the chain of increasing nuclear charge towards the final goal to measure the *g-factor* of hydrogenlike uranium: calcium. This is due to several reasons:

- $^{40}Ca^{19+}$ is heavy enough to test the bound-state contributions to the theoretical value to a sensitivity of 0.03%, which is a factor of 8 larger than the sensitivity achieved in [Ver04a] (see chapter 2);

- it has a doubly magic nucleus (consisting of 20 neutrons and 20 protons), which results in a better accuracy of the theoretical calculation of the nuclear contribution to the *g-factor*;

- the ionization energy of the 1S shell of the calcium atom is $\sim 5\,\mathrm{keV}$, which means that a 10 keV electron beam suffices to achieve the desired ionization level and it is, thus, possible to create the ions without the need of big facilities, as would be the case for heavier ions;

- with six stable isotopes and being the heaviest (^{48}Ca) 20% heavier than ^{40}Ca, an isotopic effect in the *g-factor* could be studied.

There is also increasing interest in the properties of lithiumlike ions. For a review on the importance of *g-factor* measurements of lithiumlike medium to heavy ions see [Sha02a]. A comparison of the electronic *g-factors* of hydrogenlike and lithiumlike ions of the same nuclear charge Z can provide a test of bound-state QED in the absence of effects coming from atomic core motion and polarization, since these effects are identical (in first order approximation) in both species and therefore cancel in a direct comparison. It is thus possible to separate the effects due to the bound state only and benchmark the according QED predictions separately (see [Bei03]). The importance here comes from the fact that for non-light ions the magnitude of nuclear contributions depends strongly on Z.

The relative uncertainty aimed in a *g-factor* measurement in order to carry out successfully the desired tests is on the level of 10^{-9}. Such high-precision measurements require very demanding environmental conditions. Hence, the experimental setup with which this work has been realized is cooled down to cryogenic temperatures (4.2 K), and the pressure is kept down to an upper limit of 10^{-16} mbar. In a setup matching these conditions, the cleanest solution is to have a completely

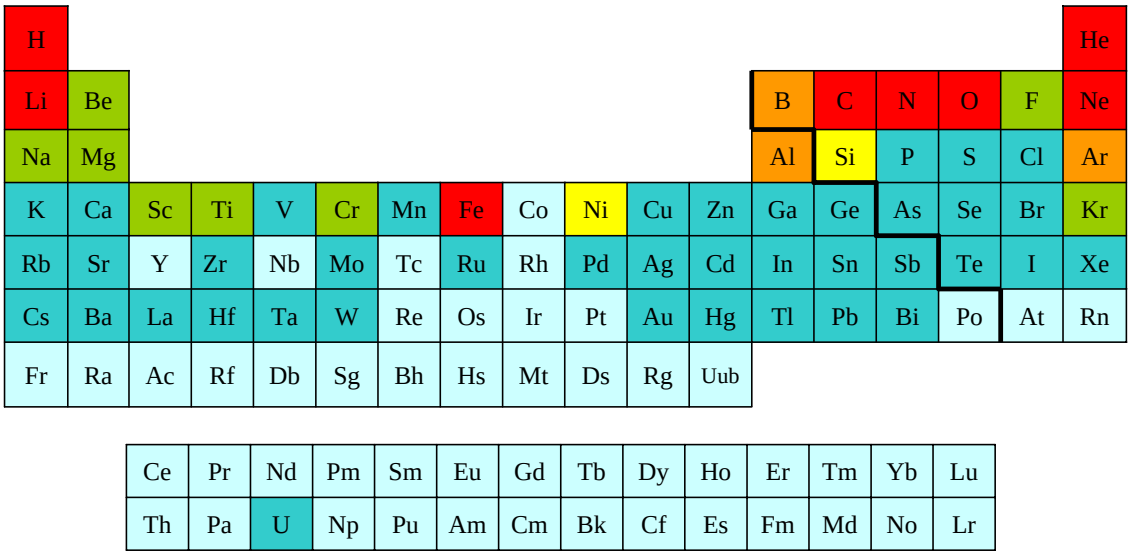

Figure 1.1: Overview of the experimentally measured cross sections of ionization by electron impact. Color code: red is used if the cross sections for all charge states have been measured; orange if the percentage is between 50% and 75%; yellow for 25% to 50%; dark blue for until 25%; and light blue in case none have been measured. Data taken from the databases in [NIFS] and [NIST].

sealed vacuum chamber, so the charge breeding of the ions until the desired state (hydrogen- or lithiumlike) needs to be done *in situ*. To that aim, the setup has been equipped with a miniature electron beam ion source (mini-EBIS) [Alo06].

If one wants to experiment with a single hydrogenlike calcium ion, 19 electrons have to be stripped away. Since voltages of up to 10 kV will have to be set at the heart of the experiment to that aim, it is recommendable to keep the ion creation time as short as possible. Thus, some simulation studies were carried out, for which the cross sections of the electron impact ionization processes need to be known. However, very scarce experimental data is available, and numbers calculated theoretically had to be used. The currently known experimental data is shown in figure 1.1.

Such lack of data is certainly surprising, since ionization by electron impact is the most common ionization process. In addition, electron-impact ionization cross sections are of great relevance in many fields like atomic and molecular physics, plasma physics, astrophysics, mass spectrometry, medical and material research or aeronomy. Its applications also cover a wide range: modelling plasmas for plasma processing of semiconductors, designing mercury-free fluorescent lamps, assessing the efficiency in ion gauges, diagnosing plasmas in magnetic-fusion devices (tokamaks), modelling radiation effects on materials and many more.

With the experiment set up in Mainz, which counts with a mini-EBIS and an FT-ICR detection system (Fourier Transform - Ion Cyclotron Resonance), it is possible to monitor the charge-breeding process on-line. Moreover, the main electron-beam parameters (its energy and current), can be controlled. Thus, this setup allows for the determination of electron-impact ionization cross sections, which will be of utility for the ion-source community among others [Alo06].

In the following, a more detailed insight on the theory of magnetic moments and

the *g-factor* of an electron in a highly-charged ion is given in chapter 2. In chapter 3 the relationship between the *g-factor* and the observables through which it can be experimentally accessed is given, as well as the procedures followed to carry out the measurements and an overview of the setup to perform them with. Chapter 4 deals with the necessity of ion trapping. The details on charge breeding and ion creation are given in chapter 5. As an essential tool which determined the overall design and structure of the experimental setup developed in the scope of this thesis, the double-Penning trap technique in combination with the continuous Stern-Gerlach effect will be introduced in chapter 6. The detection schemes applicable to ion traps and implemented in the setup are presented in section 7. A discussion about the current status of the experiment, along with an outlook on future perspectives, will be given in chapter 8. The experimental procedure to perform a *g-factor* measurement will be detailed in appendix A. Finally, appendix B is dedicated to the development and functionality of the LabView-based code which serves as control system of the experiment.

Chapter 2

Magnetic moments and the *g-factor*

"The pure and simple truth is rarely pure and never simple."

Oscar Wilde.

In this section a theoretical introduction to the *g-factor* will be given, starting from the very beginning for the sake of a clear and complete explanation, with the hope that the sight of the complete evolution of quantum mechanical magnetic moments serves as motivation to continue improving our knowledge on the subject.

2.1 Angular momentum and magnetic moment

Let us start our discussion with the Schrödinger equation generalized for a particle of charge q[1] and mass m in a magnetic field $\mathbf{B}$ (with its corresponding vector potential $\mathbf{A}$) and immersed in an electric potential Φ:

$$\hat{H}\Psi = \frac{1}{2m}(\hat{\mathbf{p}} - q\mathbf{A})^2\Psi + q\Phi\Psi = i\hbar\frac{\partial\Psi}{\partial t}, \tag{2.1}$$

where $\hat{H}$ stands for the Hamiltonian, Ψ for the wave-function and $\hat{\mathbf{p}}$ for the momentum. If we consider the magnetic field to be uniform and static ($\mathbf{B} = (0, 0, B_z)$), and in absence of electric field ($\Phi = 0$) we obtain:

$$\mathbf{A} = \frac{1}{2}\mathbf{r} \times \mathbf{B} = \frac{1}{2}B_z(-y, x, 0), \tag{2.2}$$

with $\mathbf{r}$ being the position vector. From this choice of gauge (known as Coulomb gauge), going back to equation (2.1):

$$\hat{H} = \frac{1}{2m}(\hat{\mathbf{p}} - q\mathbf{A})^2 = \frac{1}{2m}[(\hat{p}_x - qA_x)^2 + (\hat{p}_y - qA_y)^2 + (\hat{p}_z - qA_z)^2], \tag{2.3}$$

which, from the definition of the vector potential $\mathbf{A}$, turns into

$$\hat{H} = \frac{1}{2m}[(\hat{p}_x + \frac{qB_zy}{2})^2 + (\hat{p}_y - \frac{qB_zx}{2})^2 + \hat{p}_z^2]. \tag{2.4}$$

[1]Unless indicated otherwise, the notation in this work will be as follows: scalars will be given in roman style, vectors in bold and operators with a hat.

Taking into account that position and momentum commute ($[\hat{\mathbf{p}}, \mathbf{r}] = 0$),

$$\hat{H} = \frac{\hat{\mathbf{p}}^2}{2m} - \frac{qB_z}{2m}(x\hat{p}_y - y\hat{p}_x) + \frac{q^2B_z^2}{8m}(x^2 + y^2). \tag{2.5}$$

In equation (2.5), the second term is the responsible for paramagnetism and the last term for diamagnetism.

Now, for any operator $\hat{O}$ in quantum mechanics, the equality

$$\frac{d}{dt} < \hat{O} >= \frac{1}{\hbar} < i[\hat{H}, \hat{O}] > \tag{2.6}$$

is satisfied. Let us take first the non-commuting terms

$$\frac{d}{dt} < x >= \frac{i}{\hbar} < [\frac{\hat{p}_x^2}{2m} + \frac{qB_z}{2m}y\hat{p}_x, x] > . \tag{2.7}$$

Using the commutation relations

$$[\hat{p}_x, x] = -i\hbar$$

$$[\hat{p}_x^2, x] = -2i\hbar\hat{p}_x, \tag{2.8}$$

equation (2.7) becomes:

$$\frac{d}{dt} < x >= \frac{1}{m} < \hat{p}_x + \frac{1}{2}qB_z y > . \tag{2.9}$$

We will proceed now with the non-commuting terms for the momentum

$$\frac{d}{dt} < \hat{p}_x >= \frac{i}{\hbar} < [-\frac{qB_z}{2m}x\hat{p}_y + \frac{q^2B_z^2}{8m}x^2, \hat{p}_x] > . \tag{2.10}$$

Using in this case the commutation relations

$$[x, \hat{p}_x] = i\hbar$$

$$[x^2, \hat{p}_x] = 2i\hbar x, \tag{2.11}$$

equation (2.10) becomes:

$$\frac{d}{dt} < \hat{p}_x >= \frac{qB_z}{2m} < \hat{p}_y - \frac{1}{2}qB_z x > . \tag{2.12}$$

Using exactly the same technique for y and $\hat{p}_y$:

$$\frac{d}{dt} < y >= \frac{1}{m} < \hat{p}_y - \frac{1}{2}qB_z x > \tag{2.13}$$

and

$$\frac{d}{dt} < \hat{p}_y >= -\frac{qB_z}{2m} < \hat{p}_x + \frac{1}{2}qB_z y > . \tag{2.14}$$

In a magnetic field, the mechanical and canonical momenta are not the same, i.e. the relation $m\frac{d<\mathbf{r}>}{dt} \neq < \mathbf{p} >$ does not generally hold. However, from above:

$$\frac{d}{dt} < \hat{p}_x >= \frac{1}{2}qB_z\frac{d}{dt} < y >, \tag{2.15}$$

so, by differentiating:

$$m\frac{d^2}{dt^2} < x >= \frac{d}{dt} < \hat{p}_x > +\frac{1}{2}qB_z\frac{d}{dt} < y >= qB_z\frac{d}{dt} < y >$$

$$m\frac{d^2}{dt^2} < y >= \frac{d}{dt} < \hat{p}_y > -\frac{1}{2}qB_z\frac{d}{dt} < x >= -qB_z\frac{d}{dt} < x >, \tag{2.16}$$

which are the equations to be expected from the Lorentz force $\mathbf{F} = q(\mathbf{v} \times \mathbf{B})$.

Given that $\mathbf{L} = \mathbf{r} \times \mathbf{p}$, the Hamiltonian in equation (2.5) can be expressed as:

$$\hat{H} = \frac{\hat{\mathbf{p}}^2}{2m} - \frac{qB_z}{2m}L_z + \frac{q^2B_z^2}{8m}(x^2 + y^2) \tag{2.17}$$

which, generalized for a uniform magnetic field in any direction, becomes

$$\hat{H} = \frac{\hat{\mathbf{p}}^2}{2m} - \frac{q}{2m}\mathbf{B} \cdot \hat{\mathbf{L}} + \frac{q^2}{8m}[B^2r^2 - (\mathbf{B} \cdot \mathbf{r})^2]. \tag{2.18}$$

Once reached this point one can realize that the first magnetic term of the Hamiltonian ($-\frac{q}{2m}\mathbf{B} \cdot \hat{\mathbf{L}}$) could be considered as the interaction -$\hat{\boldsymbol{\mu}}_{\boldsymbol{L}} \cdot \mathbf{B}$ between the field and an operator which can be defined as the *magnetic moment*,

$$\hat{\boldsymbol{\mu}}_{\boldsymbol{L}} = \frac{q}{2m}\hat{\mathbf{L}}. \tag{2.19}$$

Let us leave it at this point for a moment and focus on the classical case described in figure 2.1. Here, a particle of charge q and mass m moves in a circular orbit with radius r, angular velocity ω and, therefore, has an angular momentum $L = mr^2\omega$.

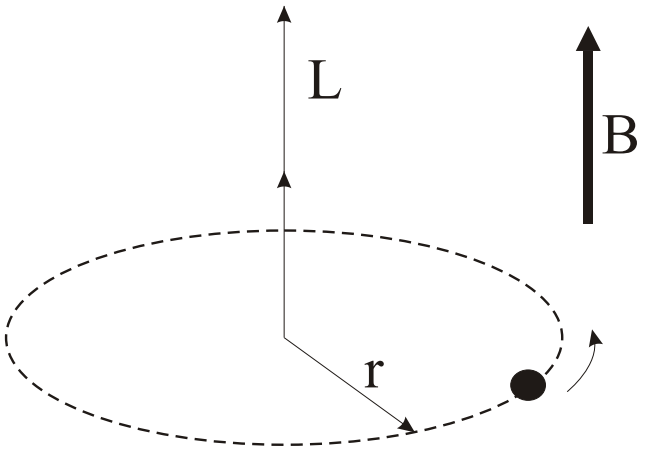

Figure 2.1: Sketch of a particle of mass m and charge q orbiting around a line of the magnetic field $\mathbf{B}$.

On the other hand, from the definition of the magnetic dipole moment ($\mu = IA$, being I the current in the loop created by the moving charge and A the area of the loop) and taking into account that the period T of the particle is $T = \frac{2\pi}{\omega}$, we get

$$\mu = \frac{qr^2\omega}{2}. \tag{2.20}$$

Inserting now the angular momentum, the magnetic dipole moment becomes

$$\mu = \frac{q}{2m}L. \tag{2.21}$$

This relation, which was defined classically, also holds in quantum mechanics when we replace the angular momentum vector with the angular momentum operator (equation 2.19). The details of the orbit are not important, only that there is some nett angular momentum.

The particular case of an atom with an electron in an orbit with angular momentum represents a small current loop, which implies that it is also a magnetic dipole. Then, the magnetic moment will be

$$\hat{\boldsymbol{\mu}}_{\boldsymbol{L}} = -\frac{e}{2m_e}\hat{\mathbf{L}} = -\frac{\mu_B\hat{\mathbf{L}}}{\hbar}, \tag{2.22}$$

with e the elementary charge, m_e the electron's mass and μ_B the Bohr magneton

$$\mu_B = \frac{e\hbar}{2m_e}. \tag{2.23}$$

To find out how the interaction with a magnetic field affects the energy levels of an electron orbiting an atom (we will take a hydrogen atom for simplicity), let us consider a magnetic field oriented along the z-axis. The potential energy is then

$$V = -\hat{\boldsymbol{\mu}}\cdot\mathbf{B} = -\hat{\mu}_z B_z = \frac{e}{2m_e}\hat{L}_z. \tag{2.24}$$

Since $< \hat{L}_z >= m_l\hbar$, where $m_l = -l, -l+1, \ldots, l-1, l$ are the usual quantum numbers, we can derive

$$< V >= -\mu_B B m_l. \tag{2.25}$$

Therefore, the energy degeneracy with respect to the magnetic quantum number m_l is broken with the application of an external magnetic field. It is possible to experimentally see the effect of the quantization of angular momentum, since the energy levels will be split into $2l+1$ different levels giving rise to multiple lines in the spectra.

2.2 Spin and the *g-factor*

It was not until 1925, three years after O. Stern and W. Gerlach performed their famous experiment [Ger22], that the intrinsic magnetic moment or spin was discovered, giving birth to two new quantum numbers: s and m_s. Spin operators satisfy exactly the same relations as angular momentum operators:

$$\hat{S}^2\Psi = s(s+1)\hbar^2\Psi = \frac{3}{4}\hbar^2\Psi$$

$$\hat{S}_z\Psi = m_s\hbar\Psi = \pm\frac{\hbar}{2}\Psi. \tag{2.26}$$

However, the magnetic moment is in this case:

$$\mu_s = -\frac{e\hbar}{m_e}m_s = -2\mu_B m_s = -g\mu_B m_s \tag{2.27}$$

where the 2 has been substituted by the gyromagnetic or *g-factor*. This indicates that spin is twice as effective in creating a magnetic moment than angular momentum, and that classical physics as well as Schrödinger's quantum mechanics predict (wrongly) a *g-factor* of 1.

It was known that a value of 2 for the *g-factor* could not come from the motion of currents inside the electron, which would yield a value of 1. This problem was solved when P.A.M. Dirac provided a relativistic treatment of quantum mechanics and derived the Dirac equation[2], which would become the successor of the Schrödinger equation. One of the triumphs of the Dirac equation was its explicit connection to the electron spin. Reduction of the Dirac equation for an electron in a magnetic field to its non-relativistic limit yields the Schrödinger equation with a correction term which takes account of the interaction of the electron's intrinsic magnetic moment with the magnetic field.

2.3 *g-factor* of an electron bound in a hydrogenlike system

From this point until section 2.6 the corrections for the *g-factor* known until today will be dealt with. The first one to take into account comes from the fact that, in the kind of systems we are interested in, the electron is subject to both spin and orbital angular momentum, so it will have a total angular momentum[3] $\mathbf{J} = \mathbf{L} + \mathbf{S}$. This problem was first solved by G. Breit in 1928 [Bre28]. In short, if one starts from the expression that generally defines the *g-factor* of the electron,

$$\boldsymbol{\mu} = -g\frac{e}{2m_e c}\mathbf{J} = -g\mu_B\frac{\mathbf{J}}{\hbar}, \tag{2.29}$$

the energy shift of a state $|a_n\rangle$ due to an external magnetic field (for simplicity assumed to point along the z-axis) is given by

$$\Delta E = -\langle a_n|\boldsymbol{\mu}\cdot\mathbf{B}|a_n\rangle = g\frac{\mu_B}{\hbar}B_z\langle a_n|J_z|a_n\rangle = \frac{1}{2}g\mu_B B_z \tag{2.30}$$

for an electron with $|a_n\rangle = |s_{1/2}\rangle$ and magnetic angular quantum number $m = 1/2$. This can also be written:

$$\Delta E = -\langle a_n|\boldsymbol{\alpha}\cdot e\mathbf{A}|a_n\rangle, \tag{2.31}$$

[2]In the static case:

$$[\beta mc^2 + c\boldsymbol{\alpha}\cdot(\hat{\mathbf{p}} - \frac{\mathbf{A}}{c}) + q\Phi]\Psi = E\Psi,$$

where m is the mass of the particle and q its mass, c the speed of light, Φ and $\mathbf{A}$ the scalar and vector potentials, respectively, E the energy and Ψ the wave-function. The matrices β and $\boldsymbol{\alpha}$ are:

$$\beta = \begin{pmatrix} I_{2\times2} & 0 \\ 0 & -I_{2\times2} \end{pmatrix}; \alpha_i = \begin{pmatrix} 0 & \sigma_i \\ \sigma_i & 0 \end{pmatrix} \tag{2.28}$$

where σ_i are the Pauli matrices,

$$\sigma_1 = \begin{pmatrix} 0 & 1 \\ 1 & 0 \end{pmatrix}; \sigma_2 = \begin{pmatrix} 0 & -i \\ i & 0 \end{pmatrix}; \sigma_3 = \begin{pmatrix} 1 & 0 \\ 0 & -1 \end{pmatrix}$$

[3]For this reason there is much literature concerned with *g-factors* that change the notation from g to g_j. In this work this distinction will not be made.

where $\boldsymbol{\alpha}$ is as defined in equation (2.28). Using the definition of the vector potential (equation 2.2), one gets to

$$g = \frac{e}{\mu_B}\langle a_n|(\mathbf{r}\times\boldsymbol{\alpha})_z|a_n\rangle = 2[\frac{1+2\sqrt{1-(Z\alpha)^2}}{3}]. \tag{2.32}$$

The last equal sign is valid only for an electron bound to a point-like nucleus, and the α is in this case the fine-structure constant.

This expression for the *g-factor* does not account yet for QED corrections, which will be dealt with from next section on.

2.4 QED corrections to the *g-factor* of a free electron

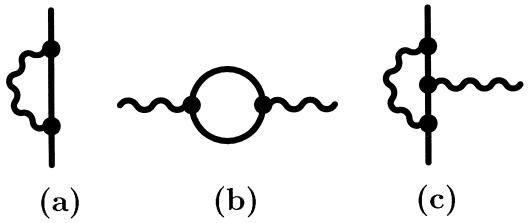

Figure 2.2: The basic quantum-electrodynamical processes, depicted as Feynman diagrams. The plain lines denote free electrons or positrons, the wavy lines denote photons. (a) Self-energy: emission and reabsorption of a virtual photon by an electron. (b) Vacuum polarization: creation and reannihilation of a virtual electron-positron pair by a photon. (c) Vertex correction: modification of a basic electron-photon interaction by an additional virtual photon.

To account for all QED corrections to the *g-factor*, the first one to consider is the change in the value coming from a non-bound electron. The computation of the leading correction in (α/π) (see figure 2.2) was performed by J. Schwinger in 1947 [Sch48]; contributions of order $(\alpha/\pi)^2$ (see figure 2.5) were considered by R. Karplus and N.M. Kroll [Kar50] and evaluated analytically by A. Petermann [Pet57] and C.M. Sommerfield [Som58]; the corrections of order $(\alpha/\pi)^3$ comprise already 72 Feynman diagrams, which have been evaluated analytically since 1996 [Lap96]; and, finally, an overview is given by T. Kinoshita in [Kin06]. The terms of order $(\alpha/\pi)^4$ add up to 891 diagrams and have been evaluated only numerically. The anomalous g value[4] defined as $a_e = \frac{g-2}{2}$ yields:

$$\begin{aligned} a_e(th) = \;& 0.5(\tfrac{\alpha}{\pi}) - 0.328\;478\;965\ldots(\tfrac{\alpha}{\pi})^2 \\ & +1.181\;241\;456\ldots(\tfrac{\alpha}{\pi})^3 \\ & -1.509\;8(384)(\tfrac{\alpha}{\pi})^4 \\ & +4.393(27)\cdot 10^{-12} \end{aligned} \tag{2.33}$$

[4]The reason for which the anomalous g value is a more convenient quantity than the *g-factor* itself is double: on the one hand, it is the simplest quantity theoretically calculable to an arbitrary precision; on the other, the measurement and theory of a_e have become so precise that it gives the most stringent test of QED if α is known precisely.

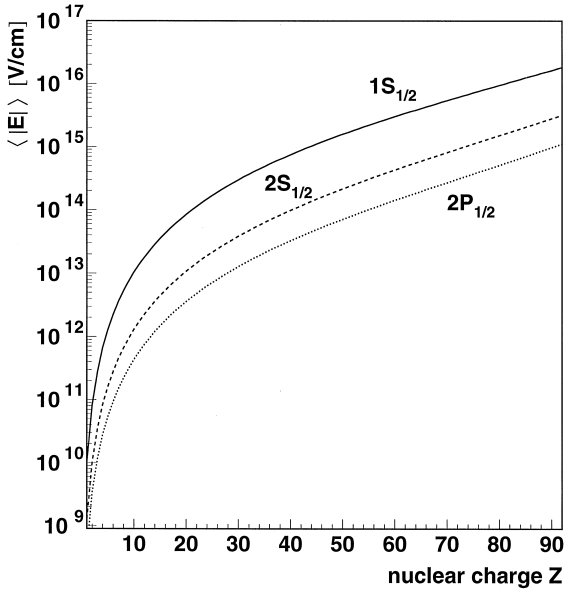

Figure 2.3: Expectation value of the electric field strength for the lowest-lying states of hydrogenlike ions for $Z = 1 \ldots 92$. Figure from [Bei00a].

where the last term includes the contributions from vacuum-polarization loops involving muons and taus, and from hadronic and weak interactions.

The final values for a_e in equation (2.33) depend on the number taken for the fine-structure constant, which at the same time depend on the experiment from which they are derived[5]. They are all less than 3 standard deviations away from the value measured by B. Odom *et al.* in 2006 [Odo06]

$$a_e(exp) = 0.001\ 159\ 652\ 180\ 85(76). \tag{2.34}$$

This is the most accurate measurement performed until the moment and also represents the setup that serves as the basis for the experiment used for the measurements presented in this thesis.

2.5 QED corrections to the *g-factor* of a bound electron

For bound systems, quantum-electrodynamical calculations are much more difficult due to the presence of a strong electric field, at the position of the electron, which is of the order of $10^9\,\mathrm{V/cm}$ for the helium ion ($Z = 2$) and reaches $10^{16}\,\mathrm{V/cm}$ for hydrogenlike uranium ($Z = 92$) (see figure 2.3).

The next step to take into account for the theoretical calculation of the *g-factor* of a bound electron includes the effects coming from the binding of the electron

[5]The most precise measurements of the fine-structure constant not directly having to do with *g-factors* all have relative uncertainties below the 10^{-7} level (see [Kru95], [Kin96], [Jef97] and [Liu99]).

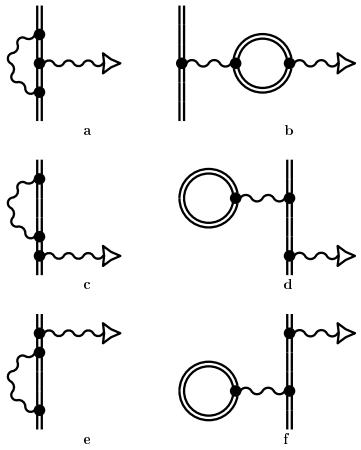

Figure 2.4: Feynman diagrams representing the QED contributions of order (α/π) to the *g-factor* of a bound electron. In each diagram there is one photon mediating the interaction with the magnetic field (triangle) and one virtual photon. The solid double line indicates the bound electron and, on the right side, also virtual leptons in the electron-positron loops. The diagrams on the left are the self-energy-like corrections and those on the right side the vacuum-polarization-like corrections.

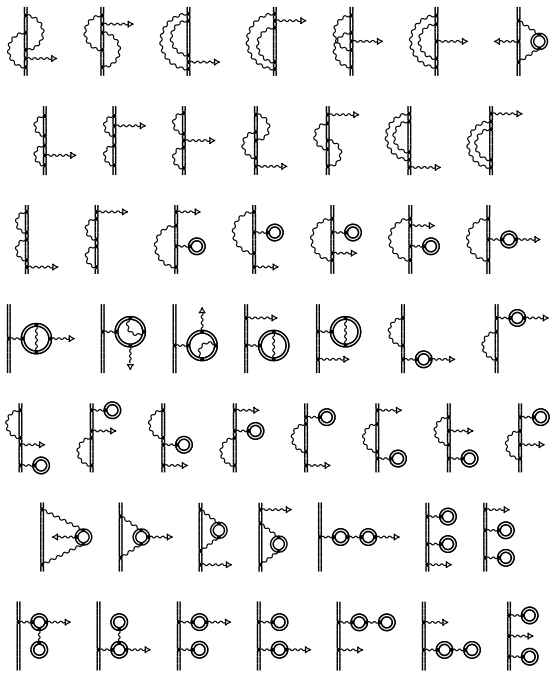

Figure 2.5: Feynman diagrams contributing to order $(\alpha/\pi)^2$ to the *g-factor* of a bound electron. Only seven diagrams of this order have to be considered for the free electron, those of the first row but without the double line indicating the bound state.

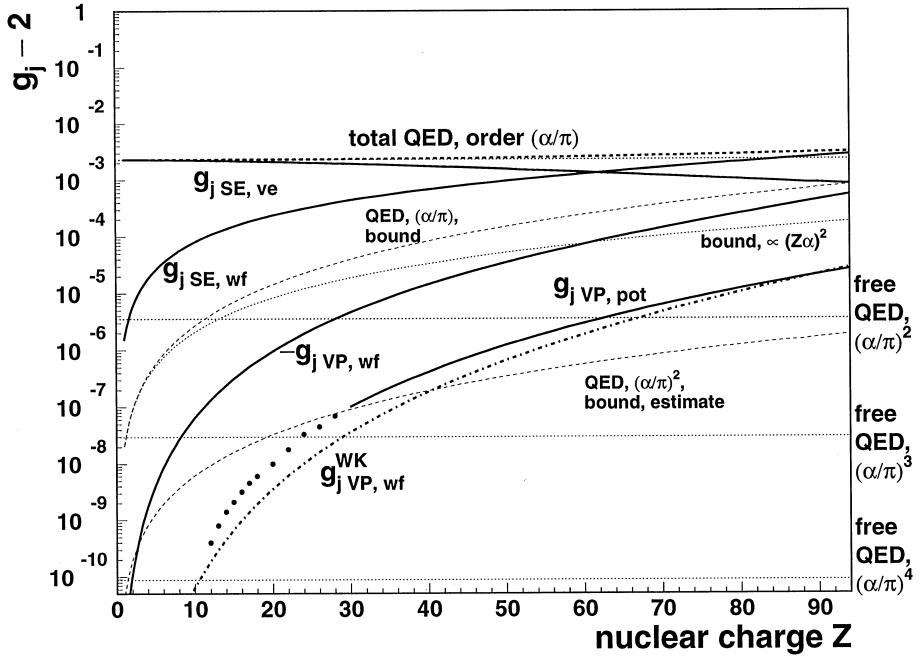

Figure 2.6: The QED contributions to the *g-factor* (written in this figure as g_j), including the contributions from free QED up to order $(\alpha/\pi)^4$. SE stands for self-energy, VP for vacuum polarization, ve for vertex terms, wf for wave-function terms and *pot* for potential terms. WK stands for the "Wichmann-Kroll" term, which will not be explicitly explained here, but is a term coming from a vacuum polarization potential. The binding contribution of order (α/π) is indicated separately, as well as the value of the $Z\alpha$ expansion due to [Gro71] ("*bound* $\propto (Z\alpha)^2$") and the estimate for the bound-state effects of order $(\alpha/\pi)^2$. For $g_{j,\ VP,\ wf}$, the negative value of this contribution is given. Results for $g_{j,\ VP,\ pot}$ for $Z < 30$ are not connected by a straight line due to the visible numerical uncertainty for these values. Figure from [Bei00a].

to the nucleus. A thorough and detailed calculation was performed by T. Beier in [Bei00a].

QED bound-state corrections of first order in (α/π) are depicted in figure 2.4 and have been evaluated to all orders. The correction of second order in (α/π) has been investigated only in the first term of the $Z\alpha$ expansion[6]. The whole set of 50 diagrams for the order $(\alpha/\pi)^2$ is shown in figure 2.5 and has also been evaluated in [Bei00a]. The sum of all different contributions are shown in figure 2.6.

[6]For all orders of (α/π) the leading term of the corresponding $Z\alpha$ expansion is given by $2 \times A^{(n)} \times (Z\alpha)^2/6$, where $A^{(n)}$ is the expansion coefficient for the nth power of (α/π) in the series for $g_{free}/2$ [Cza01].

2.6 Recoil and nuclear corrections to the *g-factor* of a bound electron

The last set of corrections relevant in the level of accuracy which can be presently achieved experimentally are those coming from a realistic treatment of the nucleus to which the electron is bound. In that sense, effects arising from the mass, size and shape of the nucleus have been investigated, as well as those originated by nuclear structure, namely from the nuclear magnetic moment, from the extended magnetization distribution and from nuclear polarization. For a complete overview on the calculations involved in these corrections, see [Bei00a]. The recoil correction is revisited in more detail in section 2.8, due to its direct effect on the value of the *g-factor* for two different hydrogenlike isotopes.

Figure 2.7 shows the contributions from all different effects relevant and discussed in this section, while in table 2.1 the values for the special case of hydrogenlike calcium are displayed. The most recent theoretical value for the *g-factor* is [Pac05]:

$$g_{theo}(^{40}\mathrm{Ca}^{19+}) = 1.988\ 056\ 946\ 6(100) \tag{2.35}$$

and it is the goal of this work to test it experimentally. Figure 2.8 shows the theoretical uncertainties to the calculation of the *g-factor* as a function of the nuclear charge.

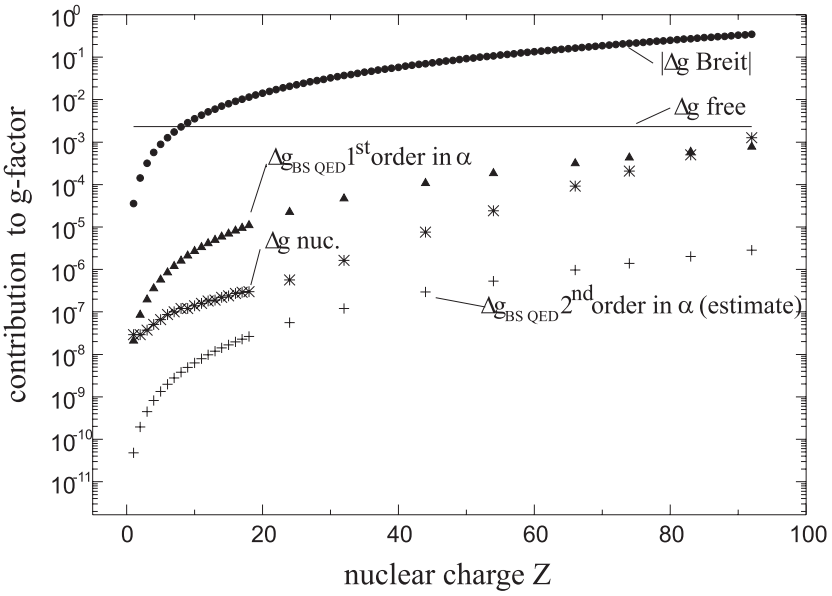

Figure 2.7: All relevant contributions to the *g-factor* of a bound electron: QED (free and bound-state), recoil and nuclear effects.

The stringency of a corresponding test of bound state-QED depends both on the experimental uncertainty and on the BS-QED contribution to the calculated *g-factor*, given in the bottom line of table 2.1. They result from a subtraction of the free electron's anomalous magnetic moment from the corresponding value of the total QED contributions.

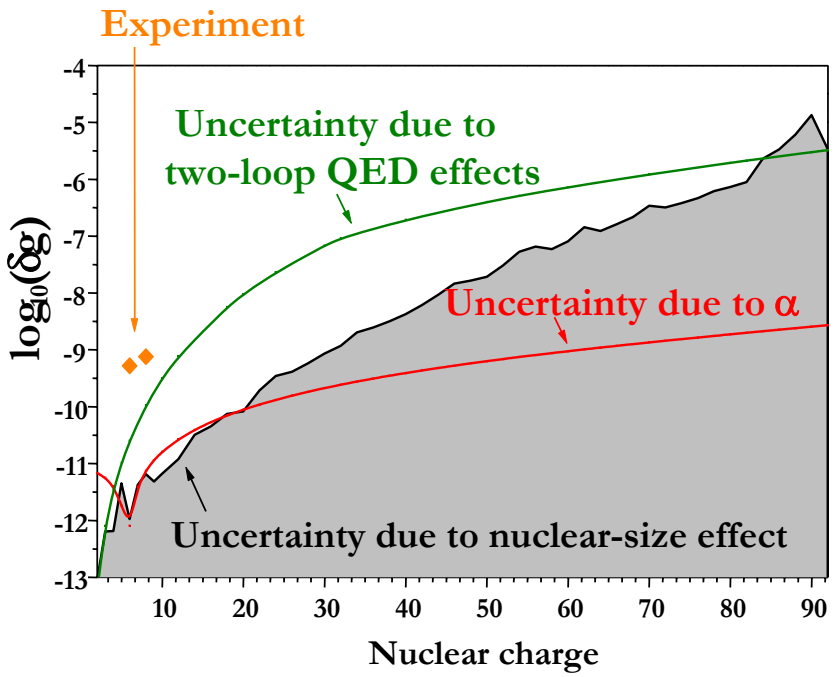

Figure 2.8: Relevance of the uncertainties of the theoretically-calculated *g-factor* as a function of the nuclear charge Z. The experimental uncertainty of the measurements performed on hydrogenlike ^{12}C and ^{16}O is also included for comparison [Häf00b, Ver04a]. Courtesy of V.M. Shabaev, V.A. Yerokhin and U.D. Jentschura.

A measurement of the electronic *g-factor* of $^{40}Ca^{19+}$ with the same experimental accuracy as obtained previously in [Ver04a], will improve the sensitivity to BS-QED contributions by a factor of about 8 when compared to $^{16}O^{7+}$. This improvement arises from the fact that the BS-QED term for hydrogenlike oxygen is 8 times smaller than that for hydrogenlike calcium (see figure 2.6). In other words, the presently reached combined experimental uncertainty of $5{\cdot}10^{-10}$ represents roughly 0.03% of the bound state-QED contributions of 14 058 ppb to the theoretical value of the *g-factor* of $^{40}Ca^{19+}$. For more details, refer to [Vog04].

2.7 The *g-factor* of lithiumlike ions

In this section we will shift our attention from hydrogen- to lithiumlike ions, where the latest theoretical calculations, regarding *g-factors*, were performed by V.M. Shabaev *et al.* in the last years [Sha02a, Gla04].

Exactly as in the case of hydrogenlike ions, the deviation of the *g-factor* value from that of a Dirac, point-like particle comes from QED, recoil and nuclear structure effects, but with an additional term introduced by electron-electron interactions (see table 2.2 for the particular case of lithiumlike calcium).

As motivated above, the interest in lithiumlike ions comes from the fact that one may expect that the uncertainty due to the nuclear size effect can be significantly reduced in a combination of measurements of the *g-factors* of hydrogen- and lithiumlike ions. In addition, the investigations of the *g-factor* of lithiumlike ions

Contribution	$^{40}Ca^{19+}$
Dirac value (point)	1.985 723 203 7 (1)
Finite size correction	+0.000 000 113 0 (1)
One-loop QED, order $(Z\alpha)^0$	+0.002 322 819 5
One-loop QED, order $(Z\alpha)^2$	+0.000 008 246 2
One-loop QED, order $(Z\alpha)^4$	+0.000 002 510 6
One-loop QED, h.o. SE	+0.000 003 107 7 (2)
One-loop QED, h.o. VP-EL	+0.000 000 172 7
One-loop QED, h.o. VP-ML	+0.000 000 014 6
Two-loop QED, order $(Z\alpha)^0$	-0.000 003 515 1
Two-loop QED, order $(Z\alpha)^2$	-0.000 000 012 5
Two-loop QED, order $(Z\alpha)^4$	-0.000 000 010 9
Two-loop QED, h.o.	+0.000 000 000 0 (100)
Recoil correction, (m/M)	+0.000 000 297 3
Recoil correction, h.o.	-0.000 000 000 3
Theory total	1.988 056 946 6 (100)
BS-QED only	0.000 014 057 7 (100)

Table 2.1: Summary of the numerical contributions to the theoretical calculation of the *g-factor* of hydrogenlike calcium, taken from [Pac05]. *h.o.* stands for higher orders, *SE* for self-energy corrections, *VP-EL* for electric-loop vacuum polarization, *VP-ML* for magnetic-loop vacuum polarization, m for the electron mass and M for the mass of the nucleus.

can serve as a very good test for various methods that are employed in relativistic calculations of many-electron systems [Yan01], because all the contributions to the $g-2$ value for an ns state are of pure relativistic origin.

Contribution	$^{40}Ca^{17+}$
Dirac value (point)	1.996 426 011
Finite size correction	+0.000 000 014
Interelectronic interaction	+0.000 454 450 (140)
QED, order α	+0.002 325 555 (5)
QED, order α^2	-0.000 003 517 (2)
Screened QED	-0.000 000 330 (100)
Recoil correction	+0.000 000 610 (20)
Theory total	1.999 202 240 (170)

Table 2.2: Summary of the numerical contributions to the theoretical calculation of the *g-factor* of lithiumlike calcium, taken from [Gla04].

2.8 Isotopic effects in *g-factors*

The importance of measuring the *g-factor* for two different hydrogenlike isotopes lies on the theoretical evaluation of the nuclear-recoil correction. The fact that the

nuclear mass is finite was historically dealt with from two different approaches. On the one hand, H. Grotch [Gro70a, Gro70b] made an expansion of the corresponding two-particle Dirac equation (electron and nucleus); on the other, R.N. Faustov [Fau70] employed an effective potential method. Their results provided an expression for the recoil correction:

$$\Delta g_{recoil} = (Z\alpha)^2[\frac{m}{M} - (1+Z)(\frac{m}{M})^2] + (Z\alpha)^2(\frac{\alpha}{\pi})[-\frac{1}{3}\frac{m}{M} + \frac{3-2Z}{6}(\frac{m}{M})^2], \quad (2.36)$$

where m/M is the ratio of the electron mass to the mass of the nucleus.

In 2002, the theoretical calculations were in such an advanced state that the $Z\alpha$ expansion of the nuclear recoil correction actually determined the uncertainty of the prediction of the *g-factor*. V.M. Shabaev and V.A. Yerokhin eliminated this source of errors by providing the contributions in first order in m/M, calculated to all orders in $Z\alpha$ [Sha02b]. The value given in table 2.1 for the nuclear recoil include these corrections and known corrections of orders $(m/M)^2$ and $\alpha(m/M)$ given in [Fau01].

Experimentally, if one measured the *g-factors* of two different isotopes, a direct comparison of the resulting values would provide an unambiguous test of the theoretical methods and calculations. Such a test has never been carried out until the moment. Thus, the experiment which has been set up in the scope of this work has been doted with the possibility of measuring the *g-factor* of the two most abundant isotopes of calcium: ^{40}Ca and ^{48}Ca. A similar experiment was proposed in 2003 for ^{24,26}Mg in [Ber03].

2.9 The relation between the *g-factor* and fundamental constants

All the contributions to the theoretically determined expression for the *g-factor* englobe many other quantities, which are known only with a certain precision. This means that the uncertainties in the calculation come not only from the numerical methods employed, but also from the uncertainties of fundamental constants. This implies that, assuming that the theoretical and experimental values of the *g-factor* agree, one can trust the theoretical value and use the experimental measurement to determine these quantities more accurately, depending on how they are related to the *g-factor*.

Actually, the theoretical determination of the *g-factor* makes use of the fine-structure constant α, of the nuclear size, via the Compton wavelength of the electron also of Planck's constant $\hbar$ and the speed of light c (fixed by definition), as well as the masses of electron and nucleus. The quantities which are subject to be known more accurately are:

- *The fine structure constant,* α: The uncertainty of α follows (from equation 2.33):

$$\frac{\delta\alpha}{\alpha} \sim \frac{1}{(Z\alpha)^2}\frac{\delta g}{g}, \quad (2.37)$$

  which means that a precise determination of α is possible from heavy systems.

- *Nuclear radii*: The effect of the nuclear size on the *g-factor* in carbon amounts to $4 \cdot 10^{-10}$ [Bei00a]. For uranium, the nuclear-size effect amounts to $1.3 \cdot 10^{-3}$ [Bei00b]. The uncertainty for this value imposed by the current error margin of the nuclear size, measured by J.D. Zumbro *et al.* [Zum84], $< r^2 >^{1/2}(^{238}\mathrm{U})$=5.8604(23) fm, amounts to 10^{-7}. From the theoretical side, it is not difficult to take into account an arbitrary distribution for the nuclear electric charge, provided it is well known. Therefore, also here the arguments can be turned around and a precise measurement of the *g-factor* serves as a sensible probe for the nuclear size and shape.

- *Nuclear magnetic moments (μ_I)*: Most of the tabulated values [Fir96] are obtained either by NMR (nuclear magnetic resonance) measurements on ions in a solution or by atomic spectroscopy. In both cases, the measured value has to be corrected for the effect of the electronic cloud, which is known as "diamagnetic-shielding correction". In addition, some of the measurements taking place in solutions seem to point to an environment-sensitive effect, the so-called chemical shift. The necessary corrections to obtain the "pure" magnetic moments have caused some inconsistencies in the literature. A recent overview about the problem is given by [Gus98]. A "cleaner" method is provided again by a *g-factor* measurement. For ions with nuclear spin, the total g_F*-factor* is given by:

$$\begin{aligned} g_F = \; & g\frac{F(F+1)+J(J+1)-I(I+1)}{2F(F+1)} - \\ & \frac{m_e}{m_p} g_I \frac{F(F+1)+I(I+1)-J(J+1)}{2F(F+1)}, \end{aligned} \tag{2.38}$$

  where g is the electronic *g-factor* which was discussed so far and g_I the nuclear *g-factor*. Electronic, nuclear, and total angular momentum are denoted by J, I, and F, respectively, and m_p stands for the proton mass. If g_F is measured with a precision of the order 10^{-9} and g is known at the same level from theory or from experiments on an isotope of the same element with $I = 0$, this still leaves a precision of 10^{-6} for g_I which is competitive to most of the tabulated values. In addition, no further corrections would have to be performed and diamagnetic shielding and chemical shift could be experimentally checked for the first time.

- *The mass of the electron*: In the setup used for this work, the *g-factor* of the electron bound in hydrogenlike calcium is determined from equation (3.3), which can be rearranged into

$$m_e = \frac{g}{2}\frac{e}{q}\frac{\omega_c}{\omega_L} m_{ion}. \tag{2.39}$$

  Here, q is the charge state of the ion and m_{ion} its mass, ω_c stands for the cyclotron frequency of the ion in a magnetic field and ω_L for the Larmor spin precession frequency. Note that g is the theoretically calculated *g-factor*. Two measurements of the Larmor-to-cyclotron ratio have been so far performed from which the electron's mass has been derived. The first one was performed by H. Häffner *et al.* [Häf00b] on hydrogenlike carbon, and the second one by J. Verdú *et al.* [Ver04a] on hydrogenlike oxygen. T. Beier *et al.* used both values to obtain the, so far, most accurate determination of the mass of the electron

[Bei02]: a factor of 4 times better than the one then accepted by CODATA and the most important contribution to the current CODATA-value [Moh05]. It is also expected that high-precision measurements of the *g-factor* of lithiumlike ions, combined with the related measurements for hydrogenlike ions and with the corresponding theoretical investigations, will provide a yet more accurate determination of the electron mass.

Chapter 3

Experimental requirements for *g-factor* measurements

"In theory, there is no difference between theory and practice; In practice, there is."

Chuck Reid.

Figure 2.7 showed a plot of the relevance of the different contributions to the *g-factor*. After a short glance at it, it becomes clear that an experimental relative uncertainty of $5 \cdot 10^{-10}$, as already achieved in previous measurements on hydrogenlike carbon and oxygen [Häf00b, Ver04a], would result for a heavier ion in a much more important test of all contributions in general and of bound state-quantum electrodynamics in particular, since the two-loop QED corrections have a theoretical uncertainty two orders of magnitude higher than one-loop corrections (table 2.1).

In order to achieve such low experimental uncertainties, it is necessary to access the bound system through observables which: are intrinsically stable at that level; are measurable with devices reliable at that level; and allow for techniques applicable down to the required accuracy. The first two conditions provide the natural division of this chapter, while the experimental procedures to carry out a *g-factor* measurement have been summarized in appendix A.

3.1 *g-factor* determination

3.1.1 Larmor spin-precession frequency

The *g-factor* can be regarded as a quantity which determines the energetic separation between the spin states of a system which would be degenerate in absence of a magnetic field. Indeed, for an electron[1] this gap is given by equation (2.30), which can be rewritten in terms of a frequency associated to the difference in energy between both levels:

[1] In the general case, the energy separation between two states for any system with a quantum magnetic number m_j is $\Delta E = \mu_B \cdot B \cdot g \cdot m_j$, only for an electron bound to a hydrogenlike ion in its ground level, $m_j = 1/2$.

$$\Delta E = g\mu_B B = \hbar\omega_L, \tag{3.1}$$

where $\omega_L = g\frac{\mu_B B}{\hbar}$ is the so-called Larmor (spin-precession) frequency. From the definition of the Bohr magneton given in equation (2.23), we get an expression for the *g-factor* which depends only on the Larmor frequency, the magnetic field and the charge-to-mass ratio of the electron:

$$g = 2\frac{\omega_L}{B}\frac{m_e}{e}. \tag{3.2}$$

Thus, the first experimental requirement has appeared: the measurement of the Larmor frequency of an electron bound to a hydrogenlike ion immersed in a strong[2], homogeneous magnetic field.

Larmor frequency measurement

Let us assume that we have a single hydrogenlike ion confined and sitting in a magnetic field. If it is irradiated with an electromagnetic excitation matching the Larmor frequency, a jump from a spin-up/down state to a spin-down/up state can occur. If this is the case, it is said that a *spin-flip* has taken place.

Since the Larmor frequency is unknown, a scan will have to be performed, sweeping the frequency of the excitation until a maximum in the spin-flip probability is found. The excitation frequency at which this happens will coincide with the Larmor frequency looked for. For our particular case, in which the magnetic field strength is close to 4 T, the Larmor frequency amounts to ∼100 GHz, so the excitation can be carried out with the use of microwave radiation.

There are several considerations to take into account now, regarding the determination of the *g-factor*:

- It has been assumed that an ion has been stripped out of all of its electrons except for one. The ionization (charge breeding) process is described in chapter 5.

- It has been assumed that a single ion has been confined. The main experimental tool used for this purpose in this work is the so-called *Penning trap*, and it is described in detail in chapter 4.

- It has been assumed that spin-flips can be detected. The detection procedure is described in section 7.6.

- Since the magnetic field enters directly equation (3.2), it has been assumed that it is known accurately enough, this is, with a relative uncertainty in the order of 10^{-9}. This difficulty will be dealt with in the next section.

[2]The reason for the magnetic field to be strong (in the order of a few tesla) is that the stronger the field, the bigger the separation between the energy levels (see equation 3.1), and therefore the more accurate the Larmor frequency can be determined.

3.1.2 Magnetic field measurement

Although there exist a few commercial probes which can measure a magnetic field with accuracies as high as required in order to carry out ultrahigh-precision experiments (like the NMR teslameters from GMW Associates, for instance), it would be of course impossible to place them exactly at the position where the ion sits, as would be necessary since the magnetic field fluctuates and drifts with time. In particular slight variations in pressure and temperature result in changes in the magnetic field which are specially distasteful, and big efforts have been made in order to stabilize both parameters [Dje04a, Mar06]. So measuring the magnetic field in one point and in one instant, and assuming that it is the magnetic field the ion is seeing would yield a wrong contribution to equation (3.2) and therefore to the final value of the *g-factor*.

Hence, another technique of monitoring the magnetic field is necessary. In high-precision experiments, it is common to use as a magnetic probe an ion itself, since due to the fact that it has a charge and a mass, the magnetic field causes it to circle around the field lines, with a cyclotron frequency $\omega_c = \frac{q_{ion}}{m_{ion}} B$. If one were able to measure this frequency, he would immediately have a value for the magnetic field which could be plugged into equation (3.2), assuming the mass to be well known. Or, in other words, one can rearrange the equation into

$$g = 2\frac{\omega_L}{\omega_c}\frac{q_{ion}}{e}\frac{m_e}{m_{ion}} \tag{3.3}$$

as long as the spin-flips, which determine the Larmor frequency, and the cyclotron frequency of the ion are measured simultaneously.

Thus, a new concern will have to be dealt with in order to perform a *g-factor* determination: the measurement of the cyclotron frequency of an ion. A detailed description of how such measurement is performed is given in section 7.4.

Figure 3.1 shows a typical resonance curve from which the Larmor-to-cyclotron frequency ratio can be extracted by following exactly the procedure described above, as was done for the *g-factor* measurements on hydrogenlike carbon and oxygen [Häf00b, Ver04a].

3.2 Overview of experimental setup

The objective of this section is to give an overview of the components of the experimental setup and to motivate the practical requirements which have led to the design of each part. However, the more technical developments like detection systems, biasing supplies and others will be covered in a more detailed way as their relevance becomes critical, within the specialized sections of the topics to whom they really belong.

As can be seen in figure 3.2, there are four distinguishable parts to the experiment developed in Mainz. The first and most important one is the cryogenic setup inserted into the magnet bore (section 3.2.1). That is where the *g-factor* will actually be measured. In order to carry out the measurement, some experimental procedures will have to be followed which require external influence on the cryogenic setup. That will be performed via electronic devices sitting outside the magnet, in a rack where also the microwave system for the induction of spin-flips is placed (section

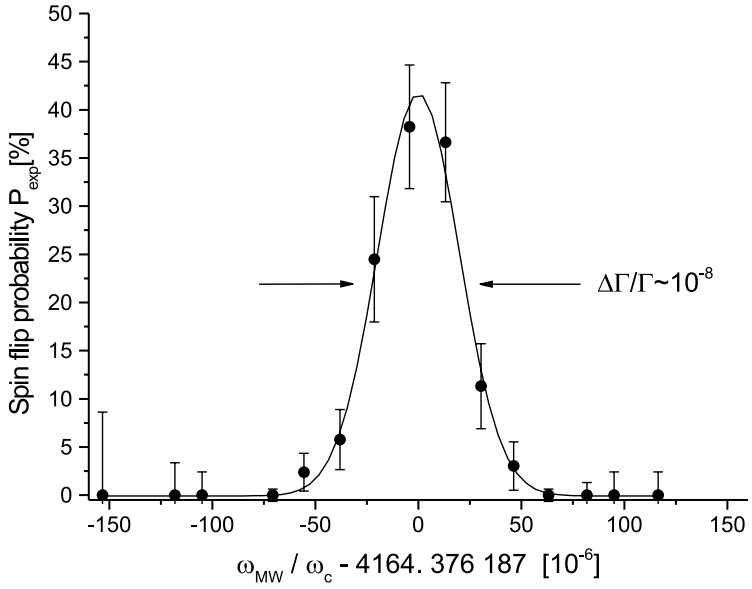

Figure 3.1: Spin-flip probability as a function of the ratio between the irradiated microwave frequency (the Larmor frequency is ∼100GHz at the magnetic field strength at which the measurement was performed) and the cyclotron frequency of a hydrogenlike-oxygen ion, from which the Larmor-to-cyclotron frequency ratio yields 4164.376 187 8(31).

3.2.2). A personal computer equipped with a self-made software code based ion LabView plays the role of the control system, both for the electronics required in the cryogenic environment and for the room-temperature home-made electronics and commercial devices (section 3.2.3). Finally, the vacuum and temperature conditions requested for an ultrahigh-precision measurement of the *g-factor* are met with a combination of conventional pumps and cryo-pumping (section 3.2.4).

3.2.1 Main setup

The heart of the experiment is the triple-Penning-trap setup. Although it will be presented in detail in chapter 6, there are some conditions which need to be fulfilled and which determine the overall structure of the experiment already at this point. The two most important requirements to be matched are a strong and homogeneous magnetic field and a cryogenic environment.

The need for a strong magnetic field is twofold: to ensure a large enough Zeeman-splitting of the levels in order to be able to measure the Larmor frequency with a resolution high-enough, as can be deduced from equation (3.2); and to guarantee the radial confinement of charged particles as required in a Penning trap (see section 4.2).

On the other hand, the ion's motion in the trap must be as harmonic as possible if one wants to have a well-defined frequency in order to perform the magnetic field measurement as outlined in section 3.1.2. The larger the volume the ion flies through, the larger the inhomogeneities in the fields it will see; so, in general terms, it is necessary to keep the energy of the ion as low as possible, which means that

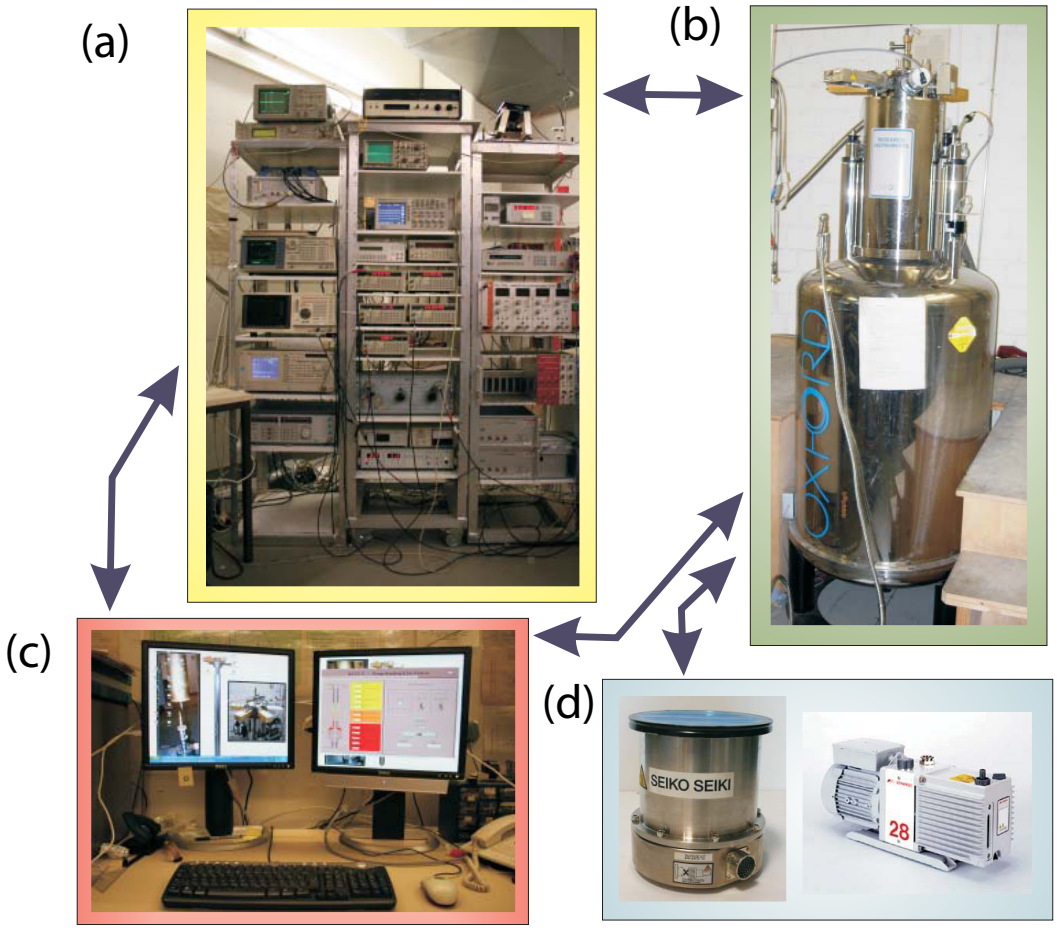

Figure 3.2: Overview of the four parts of the experimental setup: (a) the electronics rack with a variety of devices dedicated to biasing and excitation, read-out and post-analysis, as well as the microwave system; (b) the magnet and the cryogenic setup inserted into its bore; (c) the control system for both the setup in the magnet and part of the electronics in the rack; and (d) the vacuum system.

the temperature of the environment with which it is in thermal contact must be kept as low as possible. In addition, the Johnson noise U in the electronics required, like the detectors, for instance, depends on the temperature T as $U \propto \sqrt{T}$ [Joh28, Nyq28]. Therefore, a cryogenic environment for the trap setup and the electronics of the detection system is not only convenient, but necessary in a high-precision experiment.

Figure 3.3 is the solution found to fulfill the requirements explained above. The trap chamber and cryogenic electronics are in thermal contact with a liquid-helium reservoir which cools them to 4.2 K, and this construction is inserted into the bore of a magnet which provides the magnetic field. In the following, a closer inspection on each component of the main setup will be made.

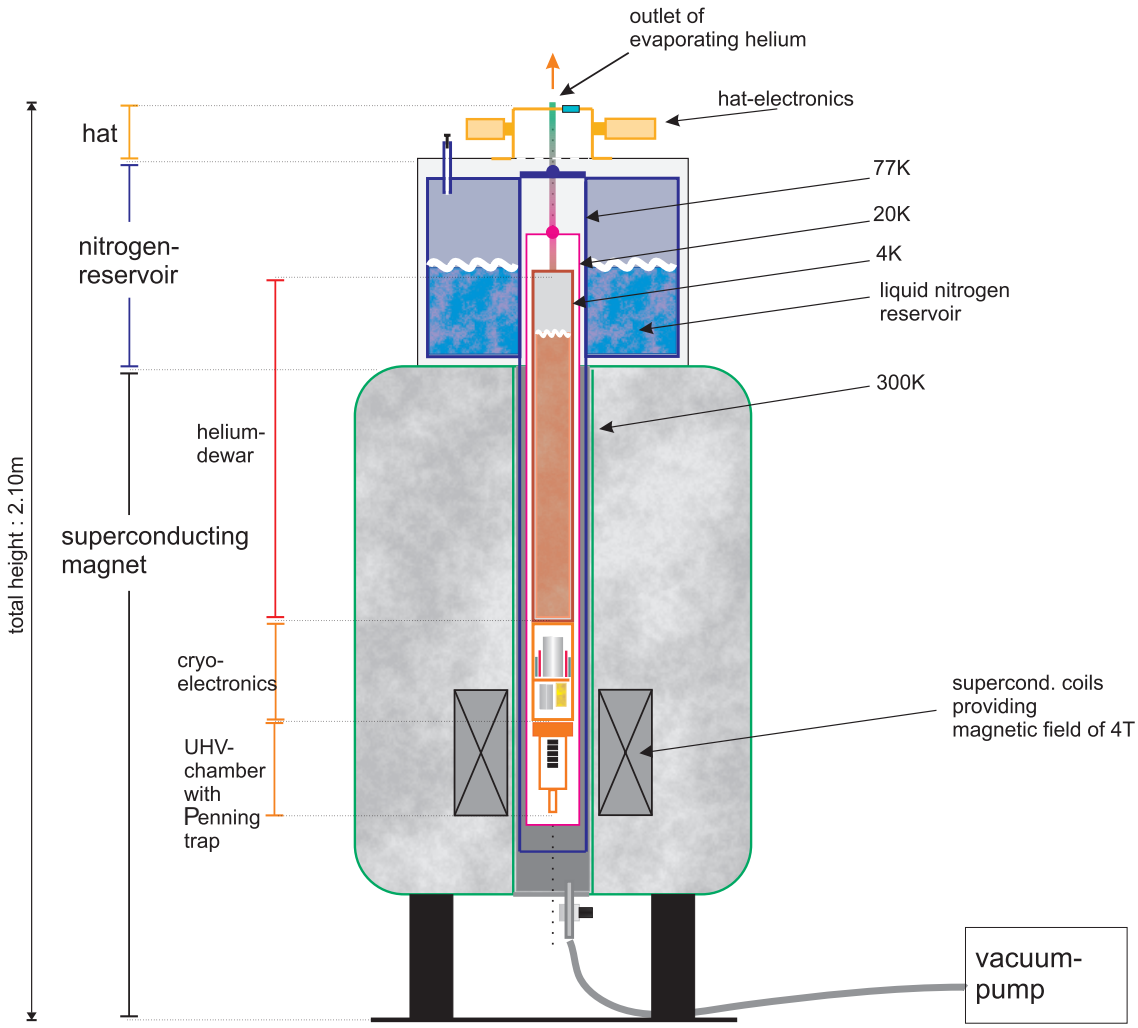

Figure 3.3: Scheme of the main experimental setup including the superconducting magnet, the cryogenic reservoirs and the trap chamber and electronics needed for the *g-factor* measurement.

The superconducting magnet and the cryostat

In order to ensure a strong, homogeneous magnetic field, a superconducting-NMR[3]-magnet from Oxford Instruments was the best option available (figure 3.3). The magnet is speared by a 127 mm-diameter bore and can yield a maximum field of 6 T in the vertical direction. It is equipped with a liquid-nitrogen tank coupled to a fixed cylindrical aluminum shield of 104 mm of diameter, which is meant to serve as a thermal-decoupling stage between the helium dewar and the external world (77 K-shield in figure 3.3).

This is the same magnet with which the *g-factor* measurements on hydrogenlike carbon and oxygen were performed [Häf00b, Ver04a] and, since then, the magnetic field has been left unchanged, other than the natural drift that all such supercon-

[3]NMR stands for Nuclear Magnetic Resonance. The magnet presented here is a standard, commercial magnet for NMR applications such as matter research or structure analysis.

ducting magnets experience [Kel03]. The magnetic field was set to 3.765 T more than a decade ago, because at that field strength the Larmor frequency for $^{12}C^{5+}$ ions was expected to be at 105 GHz, which was achievable by the microwave system available. This still holds for highly-charged calcium ions.

The magnetic field itself is created by the cylindrical, superconducting (NbTi) main coil shown in figure 3.3. There are several other smaller coils tuned for optimization of the homogeneity of the field. Finally, a special compensation coil stabilizes the magnetic field and protects the main coil from external influences or changes.

The setup (sometimes referred as the *apparatus*) shown in figure 3.4 is inserted into the magnet bore and it consists of the elements described in the following.

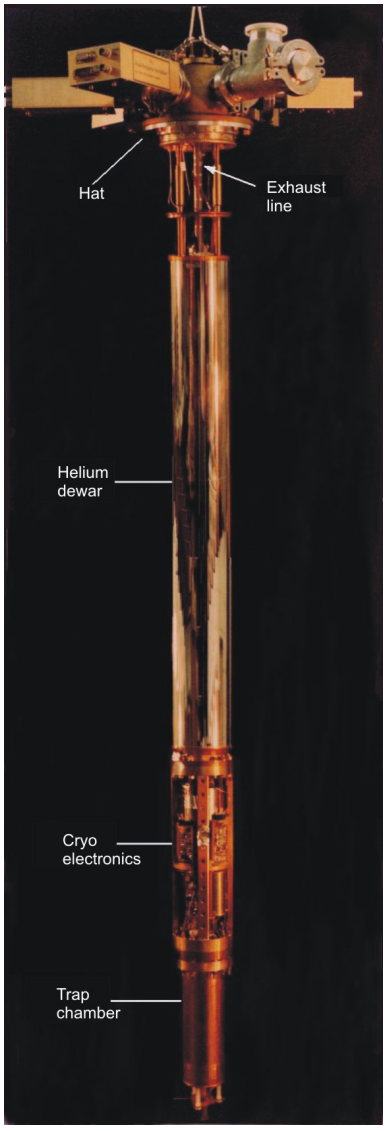

Figure 3.4: Picture of the setup inserted into the magnet bore, including the trap chamber where the *g-factor* is to be measured, the cryogenic electronics for detection, cooling and filtering, the helium reservoir which acts as refrigerator, and the hat where the room-temperature electronics are sitting.

(Ultrahigh-vacuum) trap chamber

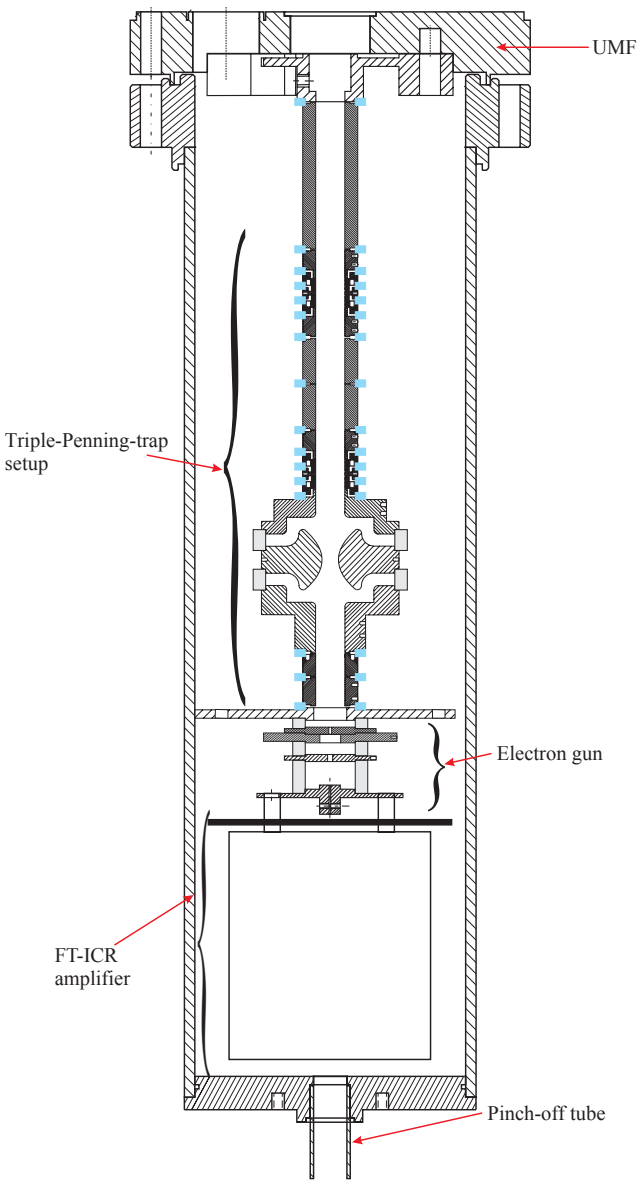

Figure 3.5: The trap chamber and its sealing parts: the UMF and the pinch-off tube.

The storage time of a single, highly-charged ion directly depends on the background pressure in its space of confinement. To the end of not losing the ion in a time as long as possible, an ultrahigh-vacuum chamber was designed and built which serves as container for the triple-Penning-trap setup. It is manufactured out of gold-plated[4] OFHC[5]-copper and an identical design has been tested to be able to reach pressures below 10^{-16} mbar [Häf03].

[4]Gold-plating is a common technique used when parts want to be prevented from oxidation, and also for homogenizing the surface of a material to reduce electric patch effects.

[5]OFHC stands for Oxygen-Free High Conductivity. It is certified at a minimum purity of 99.99%, which guarantees an extremely small amount of contaminants which could disturb the magnetic field, as well as a high thermal conductivity.

The drawing in figure 3.5 includes the inset to be placed inside the ultrahigh-vacuum chamber, consisting of the triple-Penning-trap setup (chapter 6), the electron gun (section 5.3) and the FT-ICR detection electronics (section 7.4.2).

The sealing of the chamber was performed via non-conventional techniques due to the required vacuum and temperature conditions. On the upper part, the UMF[6]-flange is fixed to the chamber body with an indium sealing (figure 3.6, left). On the bottom side, the tube is used for evacuating the chamber at room temperature and then pinched off (figure 3.6, right).

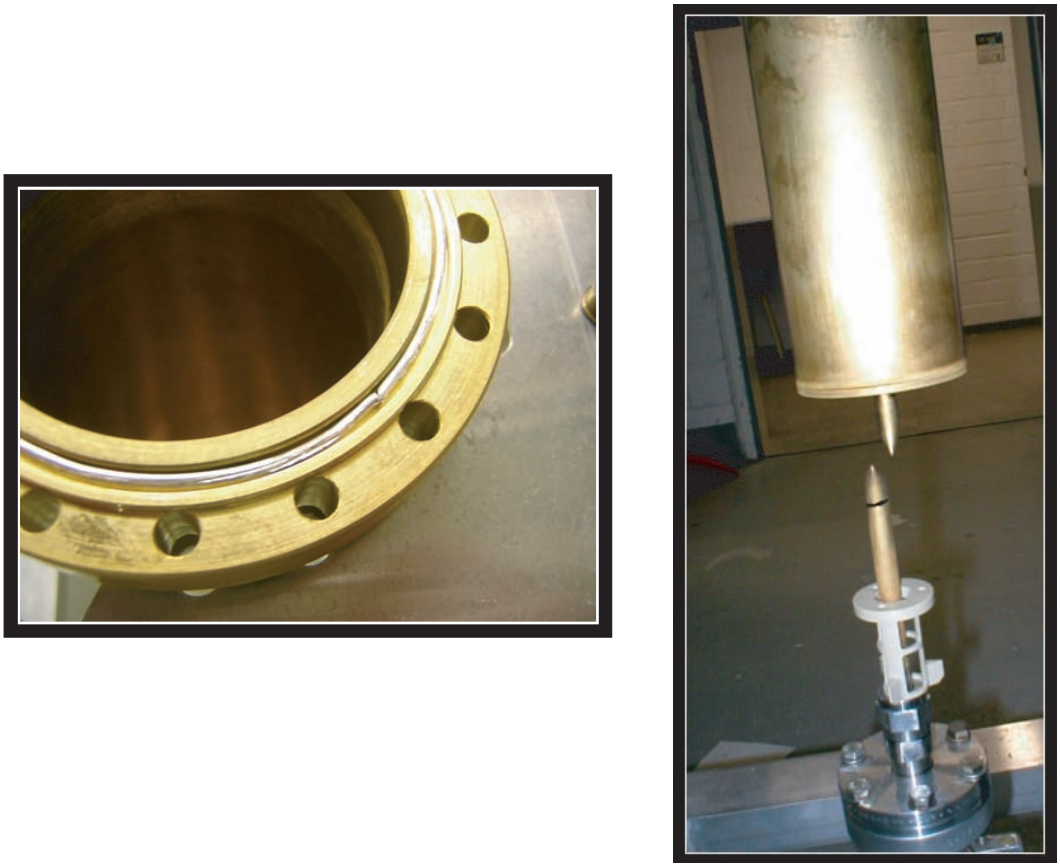

Figure 3.6: Left: indium sealing between the chamber body and the UMF (the inset was still not inside). Right: Pinch-off tube directly after performing the cut.

Once closed the vacuum chamber and before pinching off, a pumping system was attached to the pinch-off tube and started. The evolution of the pressure in the chamber can be seen in figure 3.7. After some days a heating jacket was installed around the chamber in order to accelerate the desorption of material. The temperature in the chamber should never exceed 100 °C, since there is a risk that the cables (isolated with shrinkable hoses) might get stuck to the walls of the chamber. Another reason not to go to higher temperatures is to avoid that the different expansion rates of the materials in the chamber might derive in unwanted electrical contacts. In order to always remain on the safe side, the heating jacket was first turned on

[6]UMF stands for Unterer Montageflansch, name which was kept for historical reasons in German (see figure 3.13).

to a temperature of 70 °C and soon later increased to 90 °C, which explains the two sudden increases in the pressure that can be observed in the figure.

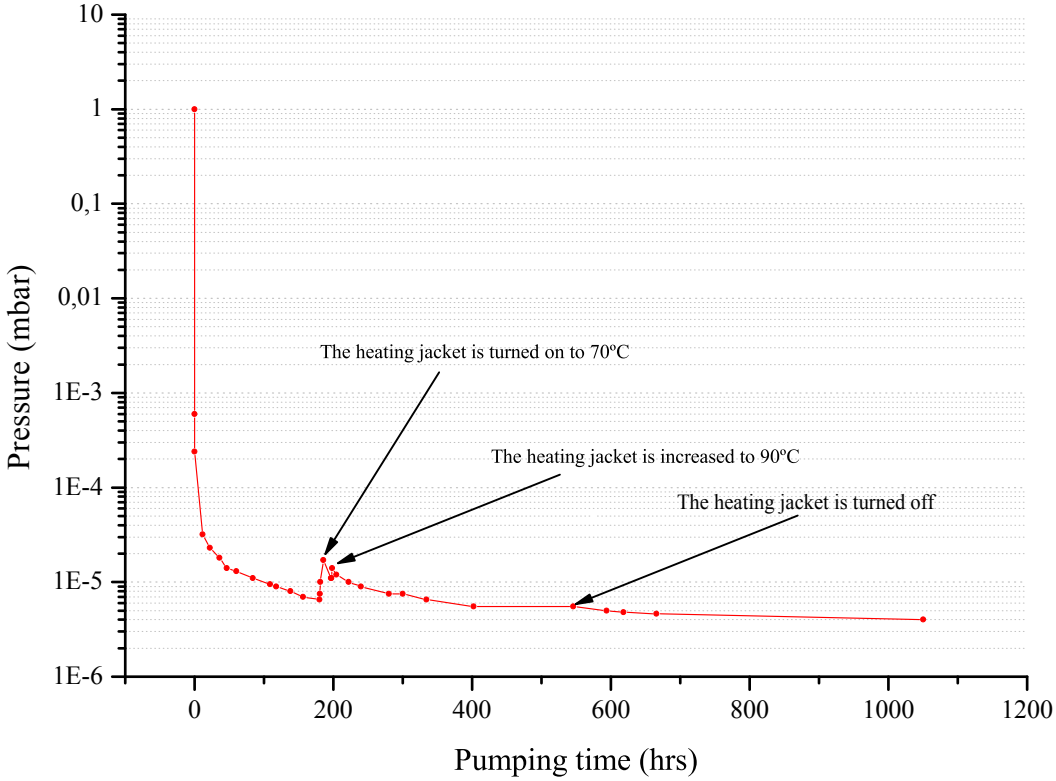

Figure 3.7: Evolution of the pressure in the vacuum chamber as a function of the pumping time.

For the pressure to go down the remaining ten orders of magnitude, the cryo-pumping power of liquid helium is utilized. When the time comes to insert the whole setup into the magnet, a so-called isolation vacuum is realized to the magnet's bore, and only then will liquid nitrogen and helium filling be done to cool down the experiment. This means that the cryo-pumping does not start immediately after the pinch-off, so it is also important that the pressure in the chamber does not rise enormously during this time. That is the reason that the outgassing of the materials in the vacuum chamber was monitored. In order to do so, the pumping is stopped (a valve is closed) for three minutes and the pressure evolution is noted. After these three minutes, the valve is opened so that the chamber is again pumped, and the recovery of the vacuum is also noted during the next minute. Figure 3.8 shows the results of these measurements.

Cryogenic-electronics region

As shown in figure 3.4, the cryogenic electronics are placed directly above the trap chamber and the UMF. There are mainly two kinds of electronics in the cryogenic region: those devoted to signal detection and amplification; and those devoted to noise filtering and excitation.

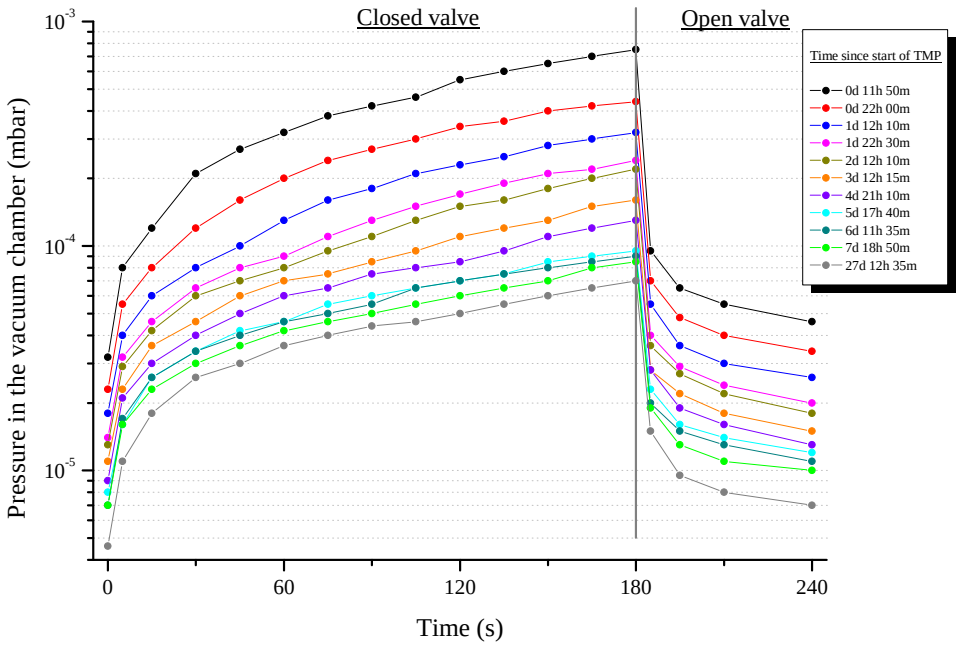

Figure 3.8: Outgassing tests in the vacuum chamber. While the valve is closed, the chamber is not being pumped and the pressure rises. As soon as the valve is opened, the vacuum is recovered. Each curve represents a measurement taken at a different time. Note: TMP stands for turbo-molecular pump.

The detection electronics and amplifiers have been designed to be able to cool and detect the motional frequency of a single ion, as well as to detect its spin direction relative to the external magnetic field. They have to be placed close to the trap setup because otherwise the parasitic capacitance of the cables would become large enough to spoil the quality factor of the resonant circuits, described in section 7.1, and hence diminish the signal-to-noise ratio of the measurement and increase the cooling time constant. All the detection electronics are explained in depth in chapter 7.

In the case of the cryogenic filters, their function is to prevent any radio-frequency (rf) signal picked up by the lines going from the cryo-electronics region to the hat from reaching the trap setup. They are conventional low-pass RC-filters as the one shown in figure 3.9 (left), with a corner frequency determined by the relation:

$$f_{corner} = \frac{1}{2\pi RC}. \tag{3.4}$$

Actually, the design of the filters is made in such a way that there are two resistors in parallel so that, in case one breaks or does not have a good electrical contact, there is another one preserving the line. Also, in the very sensitive lines, there are two capacitors in parallel and of different value. The reason is that capacitors are not ideal capacities, but rather show a frequency-dependent inductive behavior. By placing two different capacities in parallel, one makes sure that the parasitic

inductance does not happen for both at the same time, thus solving the problem.

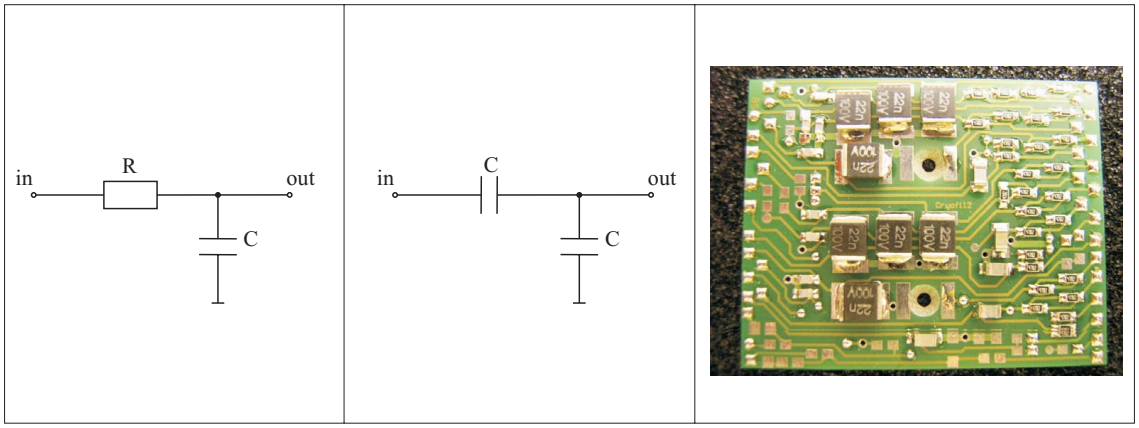

Figure 3.9: Left: schematic of a low-pass RC-filter. Middle: schematic of an ac-voltage divider. Right: picture of the new cryogenic filter board.

In the filter board shown in figure 3.9 (right) there are also ac-voltage dividers or CC-filters, with a scheme identical to that in the middle part of the figure. These are for coupling in rf-excitations meant either to heat the ions or to apply noise above the thermal equilibrium at the resonant circuits, as required by the experimental techniques involved in the measurement of *g-factors*.

Helium dewar

Below the hat and above the cryogenic electronics region in figure 3.4 is the long, cylindric helium dewar. It serves as container for the liquid helium which actually conforms the cryostat. It can hold up to 5 L of ^{4}He at normal pressure, conditions under which it is in equilibrium at 4.2 K.

The liquid refilling is done through a thin, stainless-steel tube marked as exhaust line in the figure because it also serves as outlet for the evaporated helium gas. This tube ends in a complex fixation system to the hat and plays the role, in addition, of mechanical suspension.

The hat

The *hat* (figure 3.10) is the name assigned to the room-temperature part of the apparatus which remains outside the magnet and where a big portion of the required electronics are attached to. The main reason to count on the hat at all is that in an ultrahigh-precision experiment it is of vital importance to have a well-defined electrical ground with no loops. Ground loops are caused by the non-vanishing resistance between the ground lines. Turning devices on and off, for instance, cause currents to flow through these loops and, thus, electronic contamination which limits the signal-to-noise ratio. Therefore, the setup will be electrically disconnected from the rest of the world, and everything will be fed by a car battery.

A second reason to have the hat is that it enables the opportunity of adding low-pass RC-filters, as those described in the left part of figure 3.9, to prevent electrical

Figure 3.10: Picture of the hat directly after insertion of the apparatus in the magnet bore.

rf-noise from getting to the cryogenic electronics and the trap[7].

The hat has six vacuum-accesses distributed uniformly around its structure. Each of them is a KF-40 flange, and connected to them are the following devices:

- **DC box:** Holds the electronics used to supply the voltages to the electrodes of the triple-trap setup. The supplied voltages are produced in two modules which can be plugged directly onto the box: an ultra-precise, low-voltage supply for the electrodes of the Analysis and Precision traps described in sections 6.4 and 6.3, respectively (the UM 1-14 module); and a medium-voltage supply capable of going down to -200 V for the electrodes of the Creation trap described in section 6.5 (the HVM module).

- **Amplifier box:** Holds the room-temperature amplifiers described in sections 7.5 and 7.4. It can be equipped with the BS 1-12 module, used to supply the bias voltages of the cryogenic electronics and part of the room-temperature electronics located in other boxes of the hat.

- **HV box:** Supplies the high voltages (down to -8 kV) required for turning on the electron gun described in section 5.3 and used for the creation and charge breeding of ions.

- **Excitation box:** Counts on a board which couples the external rf-excitations that need to be fed to the cryogenic region and serves as an ac-voltage divider at the same time.

[7] In an ultrahigh-precision experiment as the one described throughout this work, all filter stages are welcome and there are never too many.

- **Temperature-measurement box:** Gives access to two different temperature sensors located on top of the 20 K-shield and just above the UMF (see figure 3.4), and also to a helium levelmeter used to monitor the amount of liquid helium remaining in the dewar described above.
- **Vacuum gauge:** For controlling the pressure at the isolation vacuum described in section 3.2.4.

3.2.2 Microwave setup and external electronics

There are three main objectives that have to be accomplished by the electronics sitting in the rack shown in figure 3.3:

- generate the microwave radiation required to induce spin-flips which need to be detected in order to measure the Larmor frequency,
- generate the rf-excitations necessary to excite the ion's motion and to raise the noise level at the tank circuits, and
- analyze the ion signal.

Microwave setup

The microwave setup was designed and mounted in the frame of S. Stahl's doctoral thesis [Sta98] and M. Tönges' diploma thesis [Tön96] in 1996. Since the *g-factor* of the electron keeps its value close to 2 regardless of the nucleus to which it is bound, and since the magnetic field strength has not been modified along the past years, the Larmor frequency continues to be close to 105 GHz and the microwave setup has, thus, been left basically unchanged.

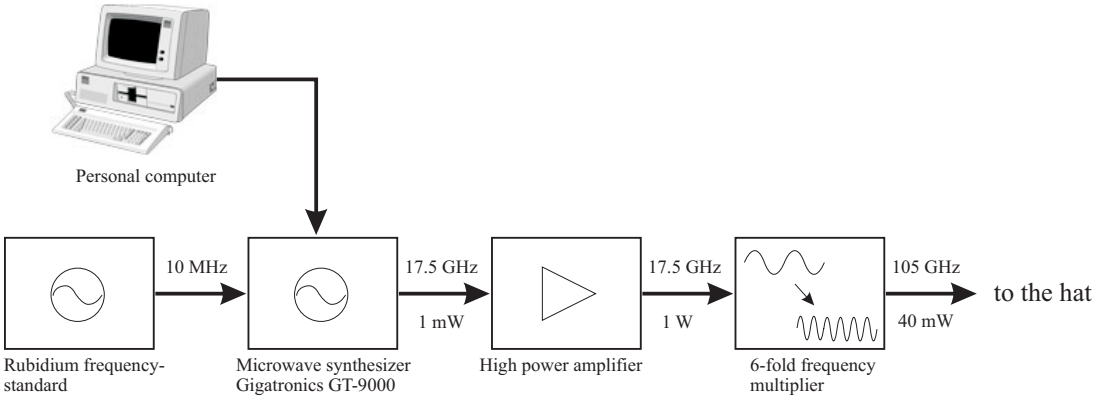

Figure 3.11: Schematic overview of the microwave setup. There is a 30 dB loss in signal power at the microwave guide from the frequency multiplier to the hat. The further damping of the power at the microwave-guide in the isolation vacuum (∼17 dB), at the teflon window connection (∼7 dB) and at the trap chamber transition (∼9 dB) brings the total power at the trap setup to ∼2.5 µW.

The setup is shown schematically in figure 3.11. The spectral cleanness of the outputted microwave radiation has to be remarkable, so not any standard klystron,

Gunn-element or IMPATT-diode would suffice, although they would be able to deliver high enough frequency. Hence, a Gigatronics microwave synthesizer (GT-9000) was chosen and coupled to a rubidium frequency-standard to maintain the center frequency as constant as possible. The synthesizer is only capable of outputting frequencies up to 20 GHz, so a six-fold passive multiplication stage conformed by non-linear GaAs-semiconductors (varactor diodes) delivers the desired frequency by an input coming from the GT-9000 module of ∼17.5 GHz. Since the frequency-multiplication stage yields a very poor power ratio, a high-power amplifier stage is inserted between the GT-9000 module and the 6-fold multiplier. The frequency-multiplied signal is wave-guided towards the hat and from there coupled into the isolation vacuum through a teflon window of 35 mm in diameter and approximately 3 mm in thickness. From there it is wave-guided again towards the UMF, where it is coupled into the trap setup via a quartz window transparent to microwaves. At this point, the remaining microwave power is around 2.5 µW if the power outputted by the GT-9000 module is 1 mW, which is enough to saturate the spin-flip transition.

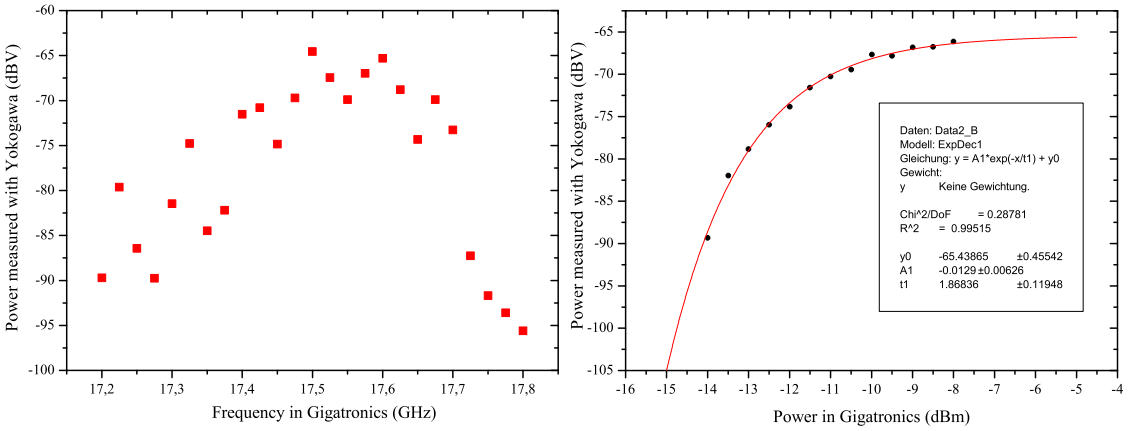

Figure 3.12: Characterization of the complete microwave setup. The left plot shows the power delivered after the six-fold frequency multiplier as a function of the frequency outputted by the Gigatronics GT-9000 synthesizer, keeping its delivered power constant. The plot at the right was measured at a fixed frequency at the GT-9000 of 17.5 GHz and shows the power delivered by the complete setup with respect to the power delivered by the GT-9000 module. The measurements were downmixed with a second microwave synthesizer (Systron Donner) and FFT-analyzed in the Yokogawa SA 2400.

Figure 3.12 is the result of test measurements performed on the GT-9000 with the objective of characterizing the output power dependence on the settings applied.

Radio-frequency excitations

Radio-frequency excitations are to be performed for two main reasons: first, the eigenmotions of the ion in the traps will be excited and coupled among each other (see section 4.4) for several experimental techniques like the phase sensitive detection (section 7.3) or the double-dip method (section A.1); second, the resonant tank circuits can be excited above the thermal noise level in order to reduce the averaging

time required to obtain a clear signal in the FFT[8]-analysis of the signal induced by the ion in the trap [Sta98].

All in all, four rf-generators are necessary simultaneously at some points, and six of them for a comfortable setup. For that reason we count with two extremely clean devices (a Rohde & Schwarz SMY 01 and a Schomandl SG 1000), and a battery of six signal generators from Stanford Research Systems (SRS DS 345) plus an Agilent 332208.

Analysis of the ion signal

As seen in equation (3.3), the *g-factor* measurement implies the determination of the ion's cyclotron frequency in a magnetic field. A detailed explanation on how to determine this frequency is given in chapter 7, including the required analysis of the detected and amplified electrical ion signal. However, a short glance upon the necessary electronic devices is now convenient.

The mostly used devices in our setup are FFT-spectral analyzers. They convert a time signal into a frequency spectrum, and the ones used in this experiment are able to do it in real time, unlike analog spectral analyzers or lock-in amplifiers. The FFT-analyzers used are the SA 2400 from Yokogawa and an 8-channel OR35 from Oros.

The limitation of these analyzers comes from the fact that they are not able to work on signals above a certain frequency, which is in the case of the devices mentioned above 400 kHz and 40 kHz, respectively. Since the frequencies which need to be measured are rather in the order of 1-40 MHz, it is necessary to perform a downmixing of the signals beforehand. Implemented at the hat there are several downmixer boards performing exactly this task, but worth of special mention is the FSA 40 from Stahl Electronics, an 8-channel downmixer with two independent inputs (1-40 MHz) and 8 independent outputs (0-40 kHz) which, in combination with the OR35, is used to follow the ion-creation process online (see section 7.4.2).

3.2.3 Control system

The control of the complete experiment is realized from a personal computer. It is a software code based on LabVIEW and developed mainly by the author. The whole of appendix B is dedicated to the development and functionality of the code, called M.I.R.C.O.[9], so for further reading it is recommended to go there.

3.2.4 Vacuum and cryo-technical design

As already motivated along this chapter, it is extremely important to achieve a vacuum as good as possible and to keep the setup at cryogenic temperatures. To that end, great care was taken during the mechanical design, which led to a non-negligible investigation of the materials and geometries to be chosen.

[8]FFT stands for Fast Fourier Transform, which is a digital Fourier transformation. For details on how it operates and its characteristics, see [Ope89].

[9]M.I.R.C.O. stands for Multiple Ionization Routines and COntrol system and keeps its name from its origin even though it has been extended to control processes other than the creation of ions.

Pump system and cryo-cooling

The main objective to accomplish at this point is to obtain a vacuum as low as 10^{-16} mbar in the ultrahigh-vacuum chamber. The first step, that is, evacuating the chamber at room temperature, has been described already and the results are shown in figures 3.7 and 3.8. The UMF (figure 3.13) serves as the upper flange of the chamber and took a remarkable amount of technical design. Its complication lies in the many feedthroughs necessary to connect electrically the trap electrodes and in-trap electronics with the external world, the quartz window required to couple the microwave radiation into the trap system to induce the spin-flips, and the limited space available.

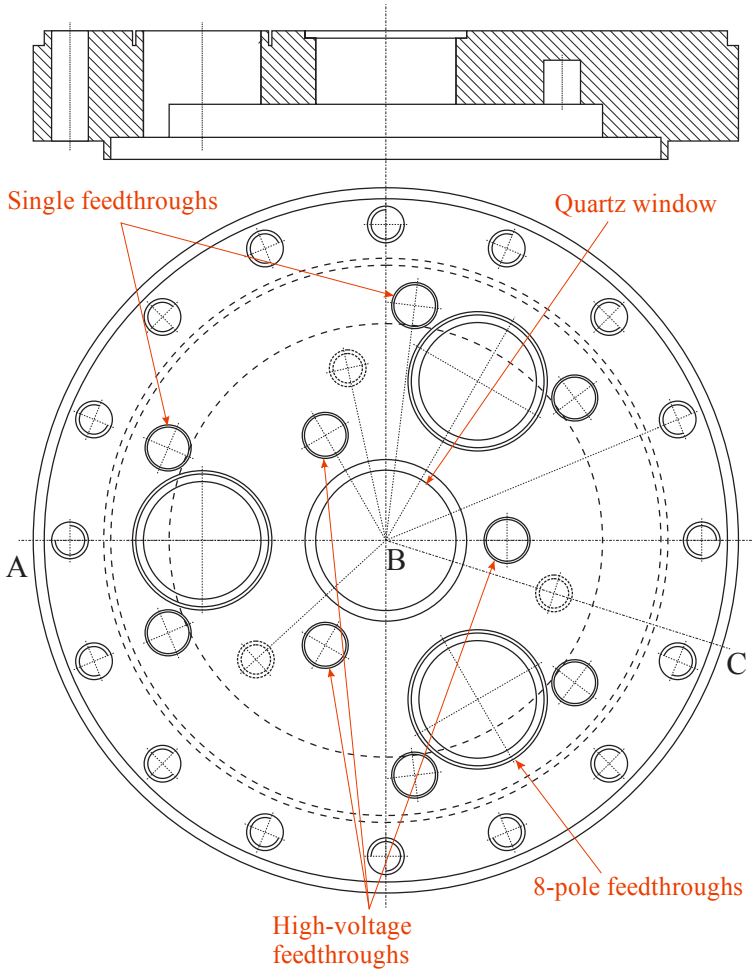

Figure 3.13: Technical design of the UMF-flange (Unterer Montageflansch).

After pinching off at a pressure in the level of 10^{-6} mbar, the complete inset is placed in the magnet bore, which is itself evacuated with a combination of a conventional turbo-molecular pump (TMP) and a rotary vane prepump system, as shown in figure 3.3. This is the so-called isolation vacuum, realized in the volume limited by the bottom part of the magnet bore and the hat. Once reached a pressure around 10^{-4} mbar, liquid nitrogen is filled into the dewar above the magnet. As the overall temperature goes towards the 77 K at which the liquid nitrogen is in equilibrium with the gas phase at atmospheric pressure, the isolation vacuum rapidly

gets better by around an order of magnitude. After some hours, liquid helium can be filled into the helium tank. This is the clue to obtain such low pressures as achieved: the liquid helium is in thermal contact with the cryogenic-electronics region and the trap chamber, cooling them down to close to 4 K. At that temperature, any atom or molecule other than hydrogen (whose abundance is insignificant in an unbound state) which gets in contact with the chamber walls will immediately freeze, leading to a negligible rest gas pressure. This technique is known as *cryo-pumping* [Gab90]. Meanwhile, since the overall temperature in the magnet bore also diminishes due to the influence of the liquid helium, the isolation vacuum goes down to a pressure of $\sim 1 \cdot 10^{-7}$ mbar at the position of the gauge attached to the hat.

Thermal shielding

Due to the extremely small vaporization heat of liquid helium of only 2.6 J/ml, it is crucial to properly isolate all those parts lying at 4 K. The so-called heat-load, that is, the energy flow on the cooled region, must be minimized. There are three different contributions:

- convection, or heat transport via the rest gas, which is negligible due to the isolation vacuum;
- thermal radiation, or the incoming power emitted by a surface because of the mere fact of being at a certain temperature;
- and heat conductivity, or the incoming power flowing through the solids due to the unavoidable temperature gradient between the cold region and room temperature.

Again, the main design was already carried out for the previous *g-factor* measurements. Here, the most significant considerations will be given.

In order to compensate for the huge evaporation rate that would occur in case the helium dewar was directly surrounded by the 300 K bore of the magnet, the first measure is to place intermediate shields in thermal contact with temperature focuses at 20 K and 77 K (see figure 3.14). The heat power P emitted by a body by thermal radiation is known to depend on the fourth power of the temperature T at which it lies, according to Stefan-Boltzmann's law [Ste79, Bol84]:

$$\frac{dP}{dS} = \epsilon \cdot \sigma \cdot T^4, \tag{3.5}$$

where S is the surface of the body, ϵ the emissivity[10] and $\sigma = 5.67 \cdot 10^{-8}\,\mathrm{W/m^2K^4}$ the Stefan-Boltzmann constant. In absence of thermal shields, the 2 m-long magnet-bore with emissivity close to 0.1 (matt-finished surface of a mirror-superinsulation foil) would mean a direct transfer of 32 W of heat to the helium dewar, so the liquid helium would evaporate in around seven minutes. Just by placing in the middle the 77 K-shield shown in figure 3.14 (in thermal contact with the liquid nitrogen dewar above the magnet), the power transmission is reduced by a factor of $\left(\frac{300}{77}\right)^4 \approx 230$, which brings the consumption time of the 5 l-dewar to more than 26 hours. In order

[10] The emissivity ϵ is a dimensionless constant between 0 and 1 determined by the material out of which the body is made, being 1 if it emits as a black body, and 0 if it does not emit at all.

to enhance the life-time further, the evaporated helium gas is forced to flow through an additional thermal shield, the so-called 20 K-shield, which improves by another factor of $\left(\frac{77}{20}\right)^4 \approx 220$ bringing the autonomy to close to 8 months.

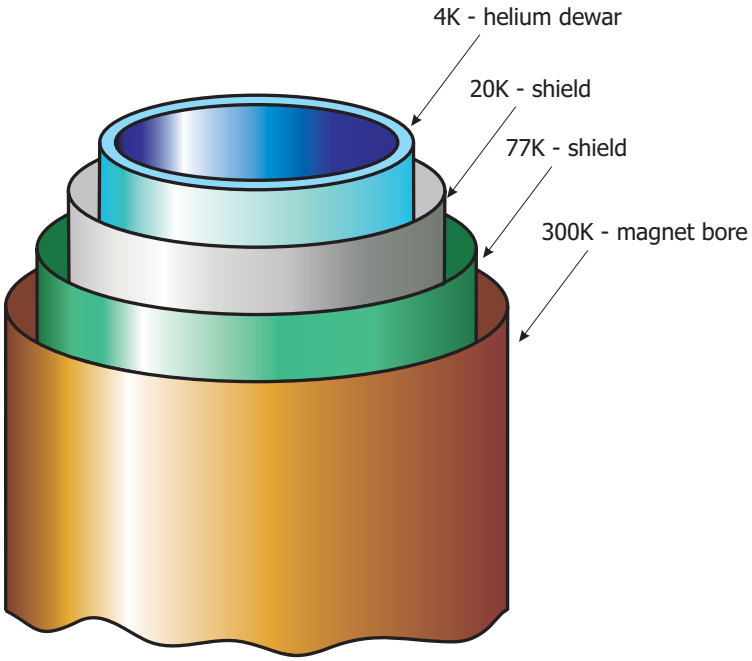

Figure 3.14: Thermal-shield configuration in the magnet bore.

In reality, the tank has to be re-filled with liquid helium every 4 days. The reason is that the biggest part of the power is lost in the transition between 4 K and 300 K through thermal conductivity. Every cable and line going from the UMF up to the hat represents a heat load, as well as the transitions between the shields and in the helium-exhaust line, which has one end directly on the helium dewar and the other at room temperature. So, in the sum, out of the 35 mW loaded onto the helium tank, less than 1 mW is in the form of thermal radiation.

As example of the care with which the thermal contacts between shields have to be made, shown in figure 3.15 is the piece serving as a spacer and centering part for the ultrahigh-vacuum chamber, and thus, the triple-Penning-trap setup. The importance of this design is that the part sets in contact the 4 K region with the 20 K-shield. The material was finally chosen to be PEEK (Polyetheretherketone) due to its values of the three parameters which are extremely important to know for cryogenics applications: the thermal conductivity, which defines the thermal input; the specific heat, which defines the cool-down time; and the integrated thermal contraction, which defines, with a proper mechanical design, the mechanical stability of the apparatus. Also an important aspect was its machinability.

A worst case estimation of the heat load is calculated next. The spacer can be divided into two: the three fins which actually make the contact to the 20 K shield, and the hollow tube. Both are made out of PEEK, which shows an integrated thermal conductivity between 20 K and 4 K of $\sigma \sim 4\,\mathrm{mW/mm}$. The heat power consumed by

a piece of conductivity σ, length l and section S is:

$$W = \sigma \frac{S}{l}. \tag{3.6}$$

Then, for the three fins:

$$\frac{1}{W_{fins}} = \frac{1}{3} \times \frac{1}{4} \frac{\text{mm}}{\text{mW}} \frac{9.45\text{mm}}{8\text{mm} \times 3\text{mm}} = 0.03\text{mW}^{-1}, \tag{3.7}$$

and for the tube:

$$\frac{1}{W_{tube}} = 3 \times \frac{1}{4} \frac{\text{mm}}{\text{mW}} \frac{35\text{mm}}{\pi(10^2 - 8^2)\text{mm}^2} = 0.23\text{mW}^{-1}, \tag{3.8}$$

where the factor of 3 comes from all the material removed from the tube. This results, when added in series the consumption of both parts, in:

$$\frac{1}{W_{tot}} = \frac{1}{W_{fins}} + \frac{1}{W_{tube}} \Rightarrow W_{tot} = 3.8\text{mW}, \tag{3.9}$$

which is around 10% of the total heat load.

For more details about the cryo-technical design, refer to [Sta98] or [Her96].

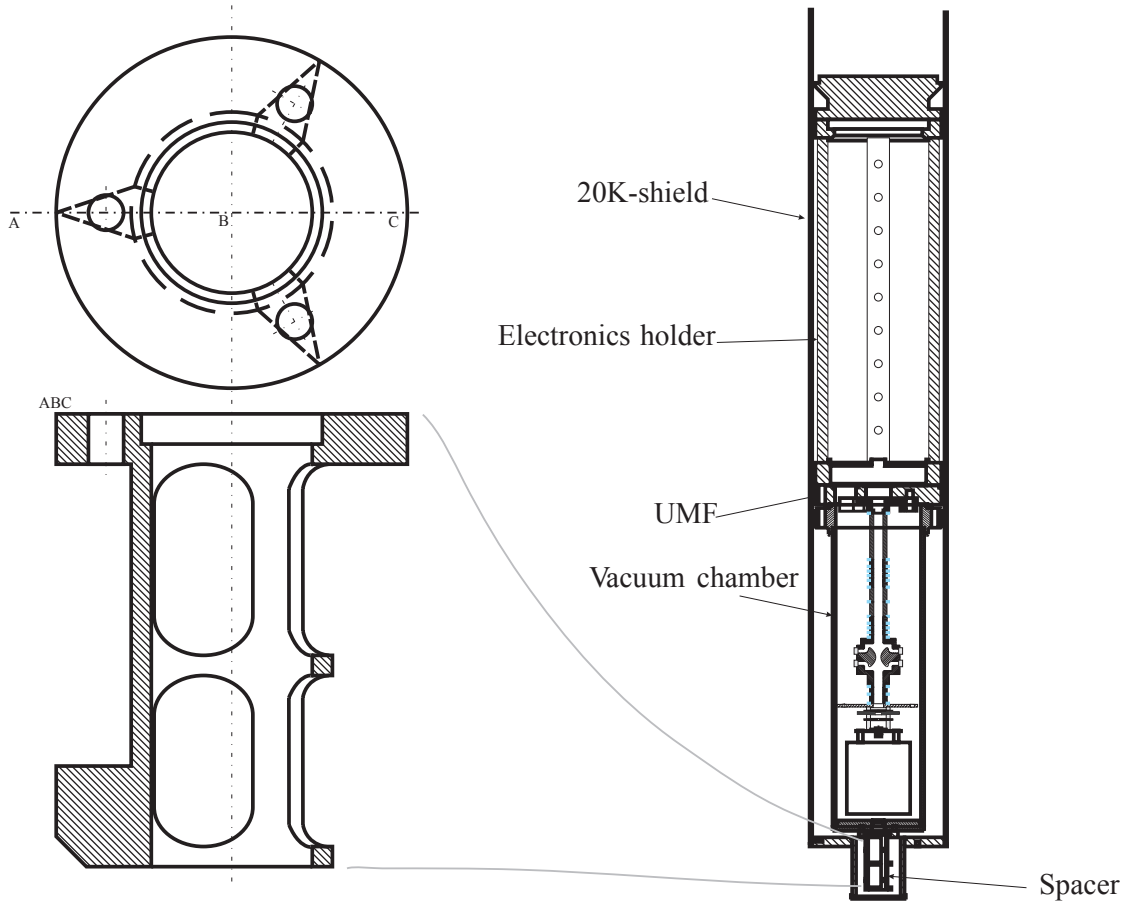

Figure 3.15: Technical design of the spacer (left) located between the vacuum chamber and the 20K shield (right).

Chapter 4

Trapping of charged particles

"... And the Raven, never flitting, still is sitting, still is sitting
on the pallid bust of Pallas just above my chamber door..."

Edgar Allan Poe, The Raven.

4.1 The origin of ion traps

The idea of trapping charged particles developed from studies on electrical discharges and has continuously evolved from extensive research in the fields of mass filters and particle accelerators. Investigation of the properties of an electrical discharge between a very thin filament cathode and a cylindrical anode led to the earliest trap called the Kingdon trap [Kin23], named after K.H. Kingdon. The study of the properties of the electrical discharges between coaxial cylinders in the presence of an axial magnetic field by F.M. Penning in 1936 led to the important result that the electron path between the two electrodes could be very long due to the tendency of the magnetic field to force the electrons into circular orbits around the axis [Pen36]. In 1953 W. Paul investigated the non-magnetic quadrupole mass filter, which revolutionized mass spectrometry [Pau55]. His studies led to the development of the Paul trap (also called radiofrequency trap) for charged particles and ions. Since then, various kinds of ion traps have been built which cater to specific investigations on the ions, such as Penning-Malmberg traps [Mal80] or electron beam ion traps (EBIT)[Lev88].

But coming back to Penning's idea, J.R. Pierce realized, in 1956, that by the combination of a magnetic field and a set of hyperbolical electrodes one could achieve the confinement of charged particles [Pie54]. With this, the Penning trap was invented. During the following years, H.G. Dehmelt studied it in detail, perfected it and obtained remarkable results from it [Deh67, Deh69, Deh68].

4.2 Principles

As mentioned before, a Penning trap is a device used to confine the motion of charged particles by use of the combination of an electrostatic and a magnetic field.

It typically consists of three electrodes: one ring and two endcaps, all of them hyperbolically shaped, as shown in figure 4.1.

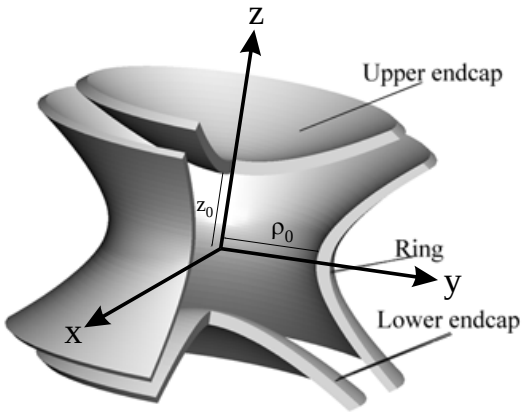

Figure 4.1: Hyperbolical Penning trap.

This special configuration guarantees that if a dc-voltage is applied between the endcaps and the ring, the field induced in the trap will be, ideally, completely quadrupolar. Thus, if a charged particle is on the trap axis (typically the z-axis) with a sufficiently low energy, it will see a harmonic potential and oscillate. It is, therefore, trapped axially.

However, it can still be lost radially to the ring. That is the reason that the magnetic field is applied in the axial direction: it will disable the possibility of movement normal to the field lines, trapping the charged particles radially, too. Nevertheless, this is a so-called metastable confinement, since any perturbation will shift the particle's motion into bigger radii, giving need to artificial centering mechanisms to avoid the loss of the particles. For further information on this topic see [Bro86].

4.3 Ion movement in an ideal Penning trap

The hyperbolically-shaped Penning trap is very convenient because the equations of motion can be solved analytically. Indeed, if we consider the setup in figure 4.2, we have an homogeneous magnetic field[1]

$$\mathbf{B} = (0, 0, B) \tag{4.1}$$

and an axial quadrupolar electric field

$$\mathbf{E} = \frac{U}{2d^2}(x, y, -2z), \tag{4.2}$$

obtained by application of a voltage difference U between the ring electrode obeying the surface equation

$$z^2 = \frac{1}{2}(\rho^2 - \rho_0^2) \tag{4.3}$$

[1]Bold characters denote vectors.

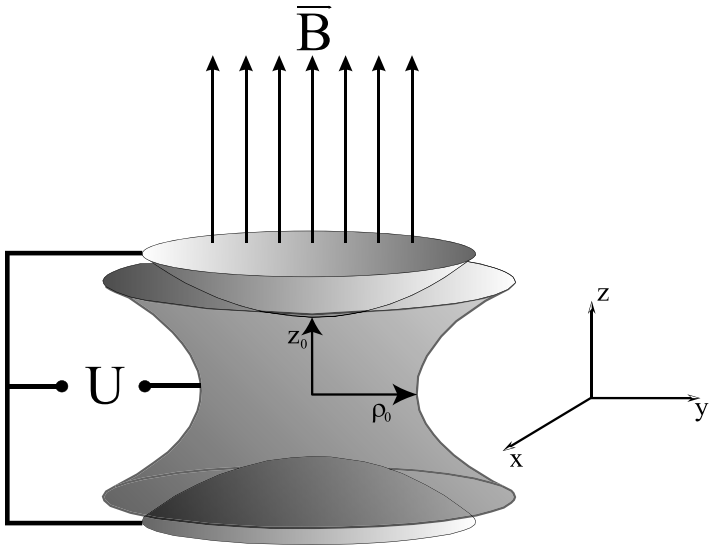

Figure 4.2: Sketch of the applied fields to the Penning trap.

and the two endcap electrodes with the surface equation

$$z^2 = z_0^2 + \frac{\rho^2}{2}, \tag{4.4}$$

where ρ_0 and z_0 are the shortest distances from the electrode surfaces to the trap center.

For ease of discussion and calculation, a convenient parameter, the trap dimension d, is defined as

$$d = \sqrt{\frac{1}{2}(\rho_0^2 + 2z_0^2)} \tag{4.5}$$

and also ideality of the Penning trap will be supposed.

The configuration described above originates the field lines shown in figure 4.3, which exert a Lorentz force leading to the following set of differential equations for the motion of an ion of mass m and charge q in the trap:

$$\begin{aligned} m\ddot{x} - qB\dot{y} - \frac{qU}{2d^2}x &= 0 \\ m\ddot{y} + qB\dot{x} - \frac{qU}{2d^2}y &= 0 \\ m\ddot{z} + \frac{qU}{d^2}z &= 0. \end{aligned} \tag{4.6}$$

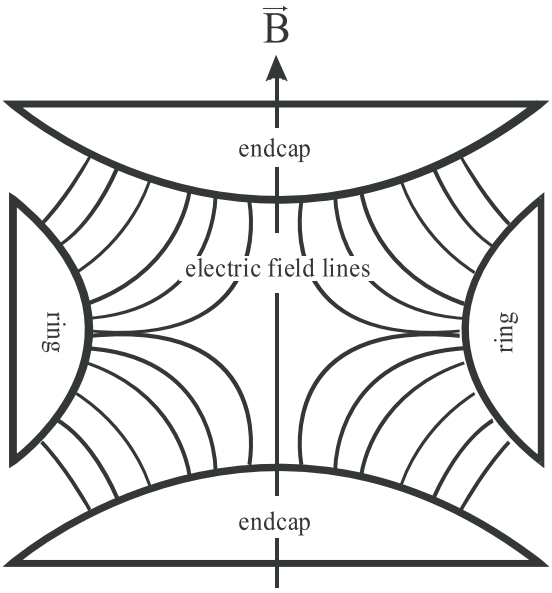

Figure 4.3: Electric and magnetic field lines in a Penning trap.

These may be rewritten as:

$$\begin{aligned} \ddot{x} - \omega_c \dot{y} - \frac{\omega_z^2}{2} x &= 0 \\ \ddot{y} + \omega_c \dot{x} - \frac{\omega_z^2}{2} y &= 0 \\ \ddot{z} + \omega_z^2 z &= 0, \end{aligned} \tag{4.7}$$

where the cyclotron frequency (in absence of an electric field)

$$\omega_c = \frac{q}{m} B \tag{4.8}$$

and the axial frequency

$$\omega_z = \sqrt{\frac{qU}{md^2}} \tag{4.9}$$

have been introduced.

The last line in the set of equations (4.7) obviously describes an harmonic oscillator of angular frequency ω_z, decoupled from the radial ion motion in the XY-plane.

One can now define two useful parameters which will provide a very compact solution to the set of equations (4.7). These are ω_+ and ω_-, which are defined as

$$\omega_\pm = \frac{\omega_c}{2} \pm \sqrt{\frac{\omega_c^2}{4} - \frac{\omega_z^2}{2}} \tag{4.10}$$

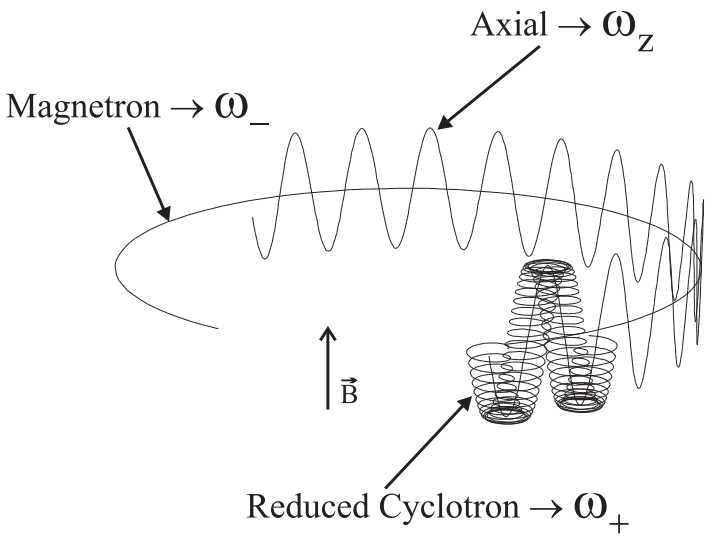

Figure 4.4: Orbit of a charged particle in a Penning trap.

and therefore fulfill the conditions:

$$\begin{aligned} \omega_+ + \omega_- &= \omega_c \\ \omega_+\omega_- &= \frac{\omega_z^2}{2}. \end{aligned} \tag{4.11}$$

The equations of motion of the charged particle in the trap are, finally:

$$\begin{aligned} x &= \rho_+ sin(\omega_+ t + \varphi_+) + \rho_- sin(\omega_- t + \varphi_-) \\ y &= \rho_+ cos(\omega_+ t + \varphi_+) + \rho_- cos(\omega_- t + \varphi_-) \\ z &= \rho_z sin(\omega_z t + \varphi_z), \end{aligned} \tag{4.12}$$

which can be seen as the superposition of three harmonic oscillations (figure 4.4) of angular eigenfrequencies and motional amplitudes ω_z, ρ_z in the axial direction and ω_+, ρ_+ and ω_-, ρ_- in the radial dimensions.

The motions associated to ω_+ and ω_- are called "reduced" (or "modified") cyclotron motion and magnetron motion, respectively. Note, that they are decoupled in their amplitudes, but not so in their frequencies.

4.3.1 Quantum and relativistic limits

The solution for the motion of a charged particle in a trap as given above is treated in a purely classical, non-relativistic manner. The objective is to justify such a treatment, and to do so it must be kept in mind that, for our experiment, the typical frequencies inside the trap are $\nu_+ \sim 25\,\mathrm{MHz}$, $\nu_z \sim 1\,\mathrm{MHz}$ and $\nu_- \sim 20\,\mathrm{kHz}$[2].

[2]These are the frequencies obtained for an ion with a charge-to-mass ratio close to $1/2$ in a trap with a dimension of $d \sim 2.5\,\mathrm{mm}$ with a voltage depth of $\sim 12\,\mathrm{V}$ immersed in a $4\,\mathrm{T}$ magnetic field.

One could think of dealing with the problem from a quantum-mechanical point of view. Actually, an extensive study can be found in [Bro86]. However, if we consider that the trapped ion is in thermal equilibrium with the environment, cooled to liquid helium temperature (4.2 K), it will have an energy $E = k_B T \simeq 3 \cdot 10^{-4}$ eV, where k_B is the Boltzmann constant[3]. Even if we look upon the reduced cyclotron motion, which is the fastest one, the quantum of energy is $h\nu_+ \simeq 1 \cdot 10^{-7}$ eV for a hydrogenlike ion in a magnetic field of 4 T. Thus, the quantum number is around 3000 for the cyclotron motion, and even higher for the magnetron and axial degrees of freedom, which justifies a non-quantum-mechanical treatment.

Another important question is whether a relativistic formulation is required or not. Let us consider a single $^{40}Ca^{19+}$ ion, in thermal equilibrium with its environment at 4 K, and let us consider again its fastest motion, $\omega \simeq 2\pi \cdot 25$ MHz. The amplitude A of the motion of an oscillator of energy E and mass m is given by

$$A^2 = \frac{2E}{m\omega^2} \tag{4.13}$$

and the linear velocity by

$$v = 2\pi A \cdot \nu = \omega A. \tag{4.14}$$

With the conditions described above, this yields an amplitude of $A = 300$ nm and $v = 40$ m/s, giving a $\beta^2 = (v/c)^2$ of $2 \cdot 10^{-14}$, which is very far from being relativistic.

4.4 Motional excitation: sideband coupling and avoided crossing

In the previous section it was derived that the motion of a charged particle inside a Penning trap is composed of three harmonic oscillators. One can excite each motion separately by applying the correct dipolar electrical signal into the trap, namely an ac-excitation at the frequency of the motion to be excited.

4.4.1 Sideband coupling

There is also the possibility of sideband coupling [Bro86, Cor90, Kre99], which relies on the fact that an ion with two eigenfrequencies ω_1 and ω_2 can absorb photons with frequencies ω_1, ω_2 *and* $\omega = \omega_1 \pm \omega_2$ (sidebands).

As an illustration of the process of sideband coupling, one can imagine that an ion absorbs a photon of frequency $\omega_+ - \omega_z$. This will lead to the loss of one quantum number in the axial motion and a gain of one quantum number in the reduced cyclotron motion, which for simplicity will be called only cyclotron motion from now on[4]. But it could also happen that there is stimulated emission, with opposite consequences. Let us suppose now that one of the motions, for example the axial one, is cooled by some mechanism. Then coherence will be lost and the result is that energy is dissipated from one of the motions to the other so that, in the average, the quantum levels of both tend to compensate.

[3]The Boltzmann constant is $k_B = 1.3806503 \cdot 10^{-23}\,\mathrm{m^2 \cdot kg \cdot s^{-2} \cdot K^{-1}}$.

[4]In order to avoid confusion, w_c will be referred to as *free* cyclotron frequency and the eigenmotion to which it is related, *free* cyclotron motion.

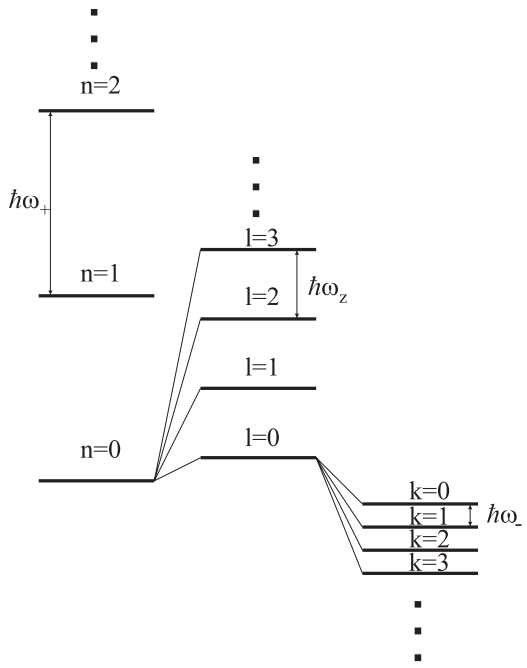

Figure 4.5: Energy levels of, from left to right, the cyclotron, the axial and the magnetron motions.

For the magnetron motion, sideband coupling does not work exactly in the same way, since it is a metastable motion: for higher quantum numbers the energy is lower (figure 4.5). Therefore, to reduce the magnetron orbit one has to apply an excitation not at the lower but at the upper axial-magnetron sideband, $\omega_z + \omega_-$.

This is important because of experimental reasons: away from the center of the trap, the magnetic field is less homogeneous, so the ion's oscillation is not completely harmonic. Such an anharmonicity would lead to an undesired coupling between the motions that would limit the accuracy of the measurements. For more details on anharmonicities and their effects on trapping see section 4.5.3.

4.4.2 Avoided crossing

Let us consider now a system that can be reasonably well described in terms of just two levels, labelled 1 and 2.

We suppose that this system is irradiated by an electromagnetic field with a frequency ω that is close to the excitation frequency

$$\omega_{21} = \frac{E_2 - E_1}{\hbar} \tag{4.15}$$

and the detuning from resonance is

$$\delta\omega = \omega - \omega_{21}, \tag{4.16}$$

with $|\delta\omega| \ll \omega_{21}$. It can then be shown [Sak85] that E_1 can take on two values, E_+ and E_-, separated by $\hbar\Omega$, where Ω is the Rabi frequency. Suppose that initially

the system is in the unperturbed state 1, and that a negatively-detuned field is slowly turned on. Suppose that, after the field has reached its maximum strength, the frequency is slowly increased. Then $|\delta\omega|$ decreases and the quasienergies E_+ and E_- approach one another. However, these levels do not cross; rather, they undergo an avoided crossing, with a minimum separation at $\delta\omega = 0$. As the frequency is increased further, into positive territory, $\delta\omega$ increases and the quasienergy levels move away from one another, until the coupling finally vanishes and the unperturbed level E_1 reappears.

A worthwhile, illustrative example is the procedure followed to measure the magnetron frequency of an ion in a Penning trap. When one excites the ion with a signal of frequency $\omega_z - \omega_-$, the axial signal is symmetrically split into two. To excite with such a sideband, one must know ω_-, which is, of course, not the case. It is not difficult to get an estimate of its value, though. This means that the excitation applied actually includes a small detuning and the coupling is catalogued as non-resonant. Figure 4.6 shows the splitting into two dips when the excitation is left- and right-detuned. One can clearly see the asymmetry of the splitting. For a known axial frequency, one can immediately obtain the magnetron frequency when both dips look perfectly symmetrical (resonant coupling). Thus, the measurement sequence is done as follows: first, an axial frequency measurement is performed without coupling field. Then the radiofrequency drive is applied (in this case left-detuned) and the splitting is recorded. An integration of the peaks is carried out in order to obtain the area they contain and a weighed average between the two is calculated. Next, the frequency of the excitation is increased in small steps of 50 mHz and the same process is repeated until the splitting is as right-detuned as it was left-detuned in the beginning. One can now plot all the four frequencies for every measurement (left signal, right signal, average of the two and axial) as seen in figure 4.7. At the point where the difference between the signals is minimum (which coincides with the point where the averaged signal crosses the axial frequency), one subtracts from the excitation frequency the axial one and obtains the final value for the magnetron frequency. By making use of the avoided crossing, the magnetron frequency was measured to a value $\nu_- = 17458.235 \pm 0.005\,\mathrm{Hz}$ for a $^{12}C^{5+}$ ion [Alo03].

4.5 The cylindrical Penning trap

The heart of the experiment is the triple-Penning-trap system, presented in chapter 6. It consists of a stack of cylindrical electrodes, forming three different cylindrical Penning traps. The simplest cylindrical trap (figure 4.8) comprises three electrodes, two endcaps and a ring, as in the case of a hyperbolical trap. There are several advantages to the cylindrical configuration when compared to the hyperbolically-shaped electrodes:

- it allows for an open setup, accessible from the outside with lasers or microwave radiation,
- it is easy to load particles in the trap,
- electrodes are easily machined to greater precision in less time,

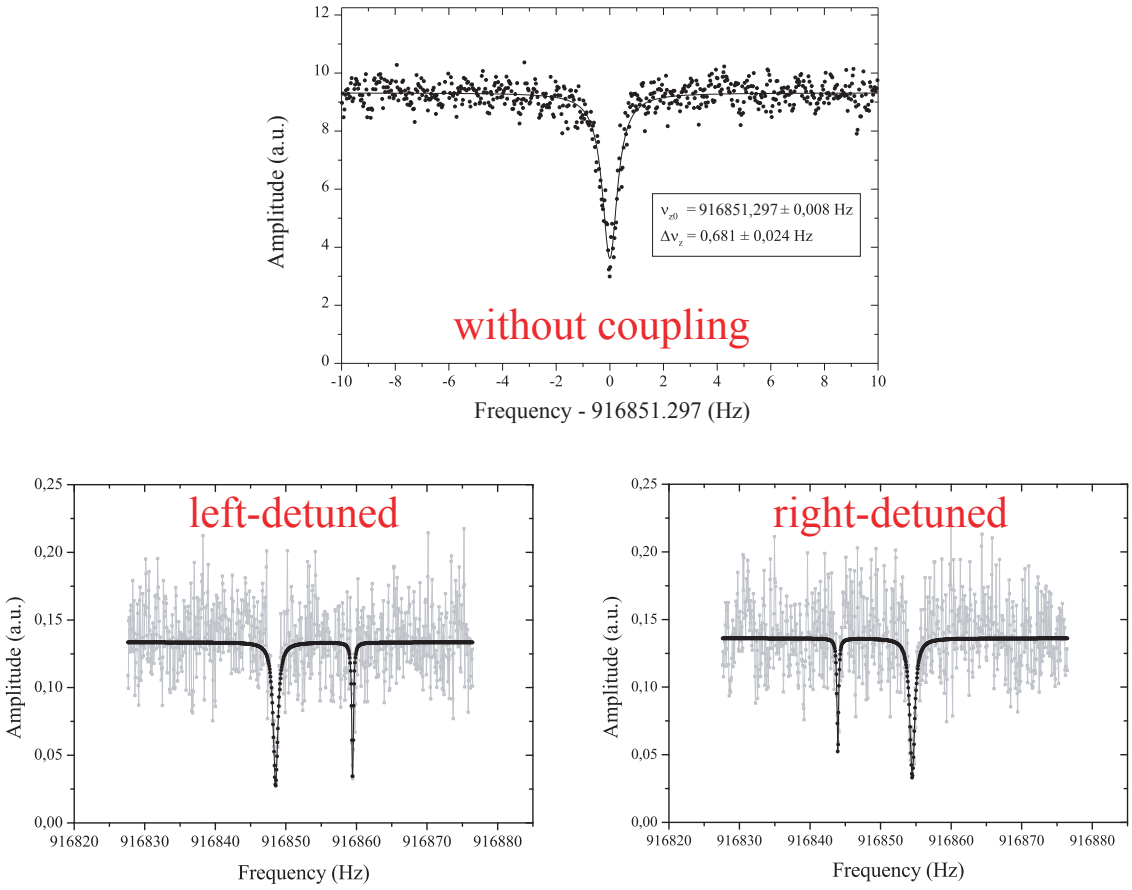

Figure 4.6: Top: axial signal of a single $^{12}C^{5+}$ ion without a coupling rf-excitation. The two bottom plots show the splitting of the signal into two for a left- and right-detuned coupling close to the $\omega_z - \omega_-$ sideband (left plot and right plot, respectively.)

- aligning the trap is easier, both the electrodes with respect to themselves, and of the whole trap with respect to an outer reference (like a magnet),
- the potential in the trap can still be calculated analytically,
- it can be better pumped.

The cylindrical Penning trap with open endcaps was for the first time studied by G. Gabrielse [Gab89], and the first purpose it served was enabling the most precise mass measurement of the antiproton until the moment [Gab95].

At first sight, it might seem that the main disadvantage of the cylindrical Penning trap comes from the shape of the electric potential inside the trap. The relevance of this problem is actually diminished due to the small amplitudes of the motion of the ion in the trap (see section 4.3.1). However, if the aim is to perform high-precision measurements, the imperfections in the potential still play a role. The easiest way to overcome this problem is by placing two additional electrodes, the so-called correction electrodes, between the ring and the endcaps. A dc-voltage can be applied to them in order to emend the lack of harmonicity of the electric potential.

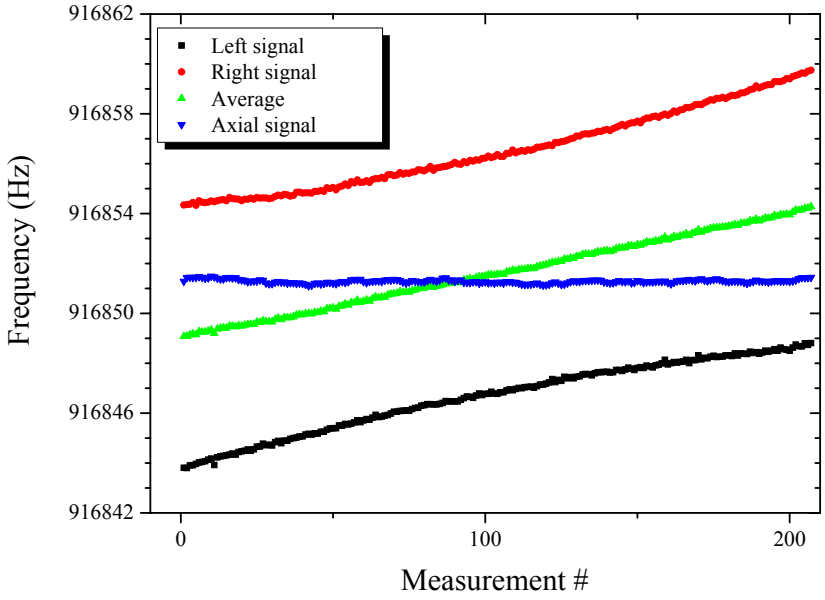

Figure 4.7: Avoided crossing: plot of the evolution of the four different frequencies involved in the determination of the magnetron frequency (center frequency of the left and right signals, average pondered by the areas of both and axial signal in absence of excitation).

An exhaustive modelling of such a 5-pole cylindrical Penning trap (figure 4.9) was realized by J. Verdú [Ver03].

In the ideal case, i.e. when the electric field is perfectly quadrupolar and the magnetic field is constant, the motion of a charged particle in a cylindrical Penning trap is exactly the same as in the case of the hyperbolical trap (figure 4.4). However, the potential ϕ will, of course, not be ideal. One can expand it in a Taylor series:

$$\phi(r,z) = \sum_{k=0}^{\infty}(\sum_{i=0}^{k} C_{i,k} r^i z^{k-i}), \tag{4.17}$$

with

$$C_{i,k} = \begin{pmatrix} k \\ i \end{pmatrix} \left.\frac{\partial^{i+k}\phi}{\partial r^i \partial z^k}\right|_{(0,0)}. \tag{4.18}$$

For our purpose, the only important coefficients are the $C_{0,k}$, which can be renamed to $C_k = \frac{1}{k!}\left.\frac{\partial^k \phi}{\partial z^k}\right|_0$, and normalized to $c_k = C_k/U_0$.

4.5.1 Optimization of a 5-pole cylindrical Penning trap

The double symmetry of the system in figure 4.9 (the rotational symmetry and the symmetry under reflection on the radial plane at $z = 0$, the center of the ring), has two consequences on the potential. First of all, the potential will be symmetric under rotation, and second, the influence of the odd terms cancel out.

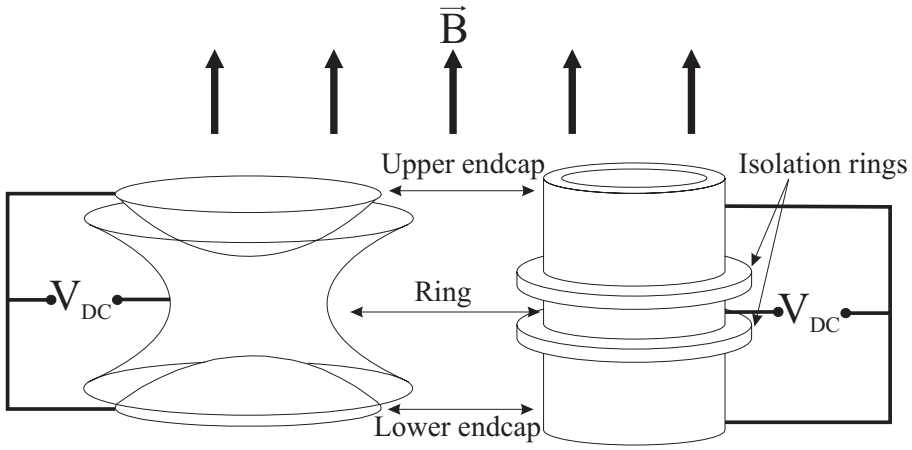

Figure 4.8: Geometric structure of a hyperbolical Penning trap (left) and a cylindrical trap (right).

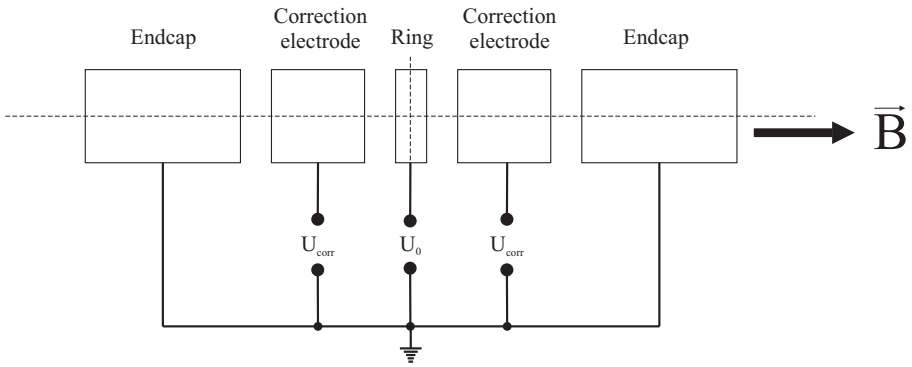

Figure 4.9: 5-pole cylindrical Penning trap in its typical voltage configuration for trapping positively charged particles.

In order to get a potential as harmonic as possible, one has to apply the correct compensation voltage to the correction electrodes. It is convenient to define at this point the *tuning ratio* as the ratio of the voltage applied to the correction electrodes to the one applied to the ring, $TR = U_{corr}/U_0$. In the ideal case, the potential will take the form

$$V = U_0 c_2 (z^2 + \frac{r^2}{2}), \tag{4.19}$$

yielding an expression for the axial frequency analogous to equation (4.9), but for a cylindrical trap:

$$\omega_z = \sqrt{\frac{q}{m} 2 c_2 U_0}. \tag{4.20}$$

In reality there are higher order terms which one has to care about. However, there are two considerations which come in very handy:

- by applying a special voltage configuration to the ring and the correction electrodes, one can manage to make the c_4 and c_6 terms of the electrostatic potential vanish simultaneously[5];
- by choosing a certain geometrical configuration of the electrodes, it is possible to *orthogonalize* the trap.

The c_4 and c_6 terms are minimized by setting an optimized tuning ratio, which experimentally requires measuring the axial frequency of the trapped ion for different excitations (different energies) and tuning the voltage applied to the correction electrodes until the dependence of the frequency on the energy of the ion is minimized.

Orthogonalization was shown in [Gab89]. By setting the dimensions of the electrodes carefully, one can achieve an independence between the axial frequency and the tuning ratio. Experimentally, working with an orthogonal trap ensures that if one sets always the same voltage to the ring, U_0, the ion will be found always at the same frequency, regardless of the voltage applied to the correction electrodes. The mathematical conditions needed to be fulfilled are:

$$\frac{z_c}{z_0} = 0.835 \text{ and } \frac{r_0}{z_0} = 1.0239, \tag{4.21}$$

where z_c is the length of the correction electrodes and z_0 and r_0 remain to be the distance from the center of the trap to the beginning of the endcaps and the ring, respectively.

4.5.2 The invariance theorem

It is straightforward to see from equations (4.8) to (4.10) that the relation

$$\omega_c^2 = \omega_+^2 + \omega_z^2 + \omega_-^2 \tag{4.22}$$

holds.

This is the so-called *invariance theorem*. It is of great use when one tries to find out the magnetic field which the ion is "feeling" in the trap, since by measuring

[5]For an extreme case, where c_6 does play a role, refer to the work described in [Ver05, Ulm06a].

the three observables (ω_+, ω_z, ω_-), equation (4.22) holds true even if there is a tilt between the magnetic field and the trap axis, a small break of the rotational symmetry or even low order perturbations on the trapping potential.

As explained in chapter 3, the precise determination of the free cyclotron frequency is of crucial importance for the computation of the *g-factor*. By inspecting the influence that the uncertainties on the measurements of the observables have on the uncertainty on the free cyclotron frequency, it becomes clear that specially the reduced cyclotron frequency has to be measured with a very high precision, since for our typical configuration:

$$\Delta\nu_c = \frac{\nu_+}{\nu_c}\Delta\nu_+ + \frac{\nu_z}{\nu_c}\Delta\nu_z + \frac{\nu_-}{\nu_c}\Delta\nu_- \simeq 1\cdot\Delta\nu_+ + 0.04\cdot\Delta\nu_z + 0.0007\Delta\nu_-. \quad (4.23)$$

4.5.3 The real cylindrical Penning trap

Despite the possibility of orthogonalizing the trap and optimizing it by compensating the electric potential with correction electrodes, and despite the invariance theorem, too, when one wants to perform a measurement in the 10^{-9} level successfully, several secular perturbations have to be taken into account.

In a general way, the frequencies in the trap (even the Larmor frequency), depend on the energies of the ion's motions: $\nu_{+,z,-,L} = \nu_{+,z,-,L}(E_{+,z,-})$.

In the electrostatic case, the dependence of the frequencies on the energies comes from a non-vanishing c_4 term. It can be shown [Ver03], in a matrix-representation, that

$$\begin{pmatrix} \frac{\Delta\omega_+}{\omega_+} \\ \frac{\Delta\omega_z}{\omega_z} \\ \frac{\Delta\omega_-}{\omega_-} \\ \frac{\Delta\omega_L}{\omega_L} \end{pmatrix} = \frac{6c_4}{qU_0} \begin{pmatrix} \frac{1}{4}(\frac{\omega_z}{\omega_+})^4 & -\frac{1}{2}(\frac{\omega_z}{\omega_+})^2 & -(\frac{\omega_z}{\omega_+})^2 \\ -(\frac{1}{2}\frac{\omega_z}{\omega_+})^2 & \frac{1}{4} & 1 \\ -(\frac{\omega_z}{\omega_+})^2 & 1 & 1 \\ 0 & 0 & 0 \end{pmatrix} \cdot \begin{pmatrix} \Delta E_+ \\ \Delta E_z \\ \Delta E_- \end{pmatrix}. \quad (4.24)$$

The effect of an inhomogeneous magnetic field acts only through the axial component of the field. This means that, although it can be expressed in terms of an axial and a radial contribution as $\mathbf{B} = B_r\mathbf{u_r} + B_z\mathbf{u_z}$, in the Precision and Analysis traps (see chapter 6) their ratios, B_r/B_z, have been calculated and measured to be $-8\cdot10^{-12}$ and $-4\cdot10^{-8}$, respectively [Ver03]. So the radial part of the magnetic field can be safely disregarded.

Similarly to the electrostatic potential ϕ, $B_z = B_z(r,z)$ can be expanded in a Taylor series:

$$B_j = \frac{1}{j!}\frac{\partial^j}{\partial z^j}B_z(r,z)\bigg|_{(0,z_0)}. \quad (4.25)$$

In this series, the non-secular perturbation introduced by the B_1 term will not be considered, since its effect has been shown to be of less importance than that from B_2 [Ver03], whose contribution is of the form:

$$\begin{pmatrix} \frac{\Delta\omega_+}{\omega_+} \\ \frac{\Delta\omega_z}{\omega_z} \\ \frac{\Delta\omega_-}{\omega_-} \\ \frac{\Delta\omega_L}{\omega_L} \end{pmatrix} = \frac{B_2}{B_0}\frac{1}{2m\omega_+\omega_-} \begin{pmatrix} -(\frac{\omega_z}{\omega_+})^2 & 1 & 2 \\ 1 & 0 & -1 \\ 2 & -1 & -2 \\ -(\frac{\omega_z}{\omega_+})^2 & 1 & 2 \end{pmatrix} \cdot \begin{pmatrix} \Delta E_+ \\ \Delta E_z \\ \Delta E_- \end{pmatrix}. \quad (4.26)$$

4.6 The magnetic bottle

It was just shown that the influence of B_2 is not negligible at the level of precision aimed by these measurements. Let us first study its effect and later make some considerations on its possible application.

For a non-vanishing B_2 term, the magnetic field takes the form shown in figure 4.10. Mathematically,

$$B_z = [B_0 + B_2(z^2 - \frac{r^2}{2})]. \tag{4.27}$$

The trapped particle's magnetic moment interacts with the magnetic field to give a magnetic potential energy $V = \boldsymbol{\mu} \cdot \mathbf{B}$, which becomes

$$V = \mu_z B_0 + \mu_z B_2(z^2 - \frac{r^2}{2}). \tag{4.28}$$

The first term is a constant and produces, therefore, no force. The second term, however, is of relevance. A direct comparison with the electric potential energy in equation (4.19) reveals that the effect of B_2 takes on a quadrupolar form. Thus, the particle will feel a total effective potential composed by both the magnetic and the electric contributions:

$$U_{eff} = U_e + U_m = (q \cdot V_e + \mu_z B_2)(z^2 - \frac{r^2}{2}). \tag{4.29}$$

This modified potential changes the solution for the axial frequency from $\omega_{z,0} = \sqrt{\frac{q}{m} 2 c_2 U_0}$ to

$$\omega_z = \sqrt{\frac{2qU_0c_2}{m} - \frac{2\mu_z B_2}{m}} \simeq \omega_{z,0} - \frac{\mu_z B_2}{m\omega_{z,0}}. \tag{4.30}$$

The magnetic moment in equation (2.29) can take on two different values depending on the spin direction with respect to the magnetic field, $\mu_z = -\frac{g\mu_B}{\hbar}(\pm\frac{\hbar}{2})$, which lead to two different effective potentials (see figure 4.11) and, thus, two different axial frequencies. This is the so-called *continuous Stern-Gerlach effect*.

What has just been shown is of great relevance, since it implies that by measuring the axial frequency of an ion in the trap, one can determine its spin-direction, as long as there is a non-vanishing B_2 term. The challenge of such a determination lies in the fact that a typical axial-frequency difference is in the order of 200 mHz for an absolute frequency of ∼1 MHz.

Figure 4.10 shows a magnetic bottle, a magnetic-field configuration like the one in equation (4.27). Experimentally, one can replace a conventional ring-electrode by a ferromagnetic one (typically, made out of nickel or cobalt-iron), to magnify the distortion of the magnetic field lines, i.e. creating a B_2 term as big as possible. This would make the axial frequency jump between the spin up and down states as large as possible, and therefore easier to detect (section 7.6). Such a technique will be employed to measure the Larmor frequency of the ion, which, in turn, is used to calculate the *g-factor*.

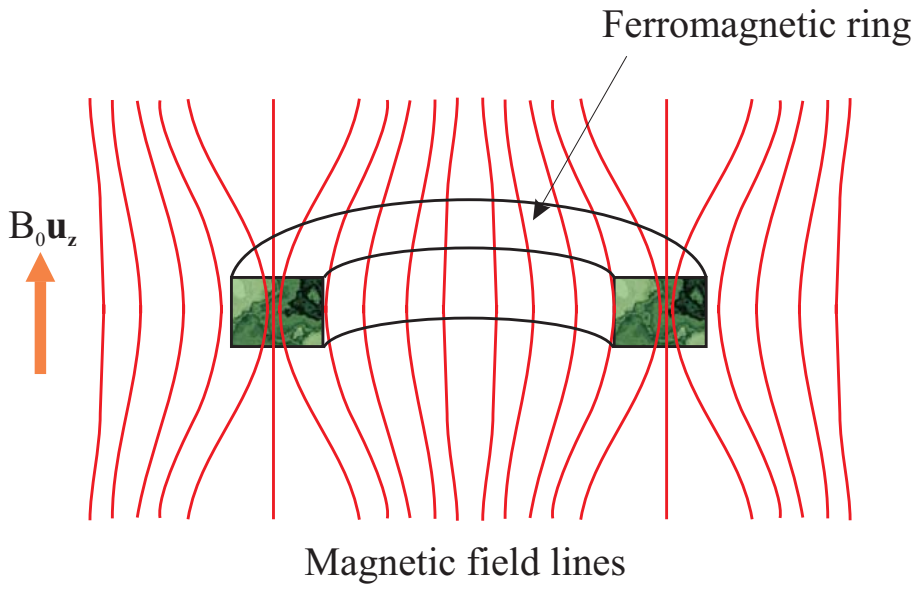

Figure 4.10: Magnetic bottle: distortion of the magnetic field lines created by a ferromagnetic ring electrode.

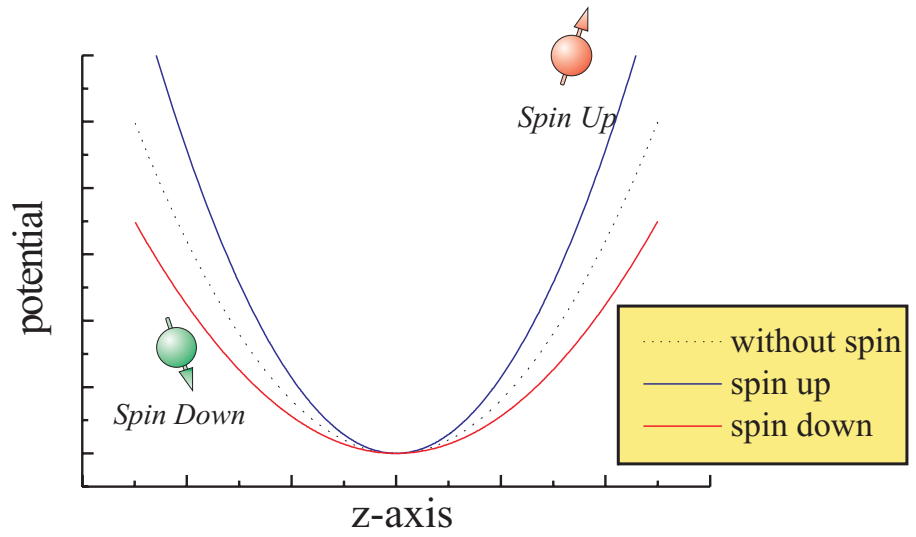

Figure 4.11: Schematic view of the variation of the potential seen by the ion immersed in a magnetic bottle depending on its spin state.

Chapter 5

Charge breeding of highly-charged ions

"Hopscotch is played with a small pebble one pushes with the tip of the shoe. Ingredients: a sidewalk, a pebble, a shoe and a beautiful chalk drawing, preferably in colors. (...) Heaven is on top, Earth on the bottom, it is is very difficult to reach Heaven with the pebble, almost every time one calculates wrong and the pebble falls beyond the drawing. Slowly, however, one acquires the necessary skills to overcome the different sections (snail hopscotch, rectangular hopscotch, fantasy hopscotch, rarely used) and one day one learns to part from Earth and carry the pebble up to Heaven..."

Julio Cortázar, Rayuela (Hopscotch).

Due to reasons which will be discussed along this chapter, the most convenient ion source to implement in the setup is one using accelerated electrons for achieving the creation and ionization of the desired species via electron-ion collisions. A configuration is chosen where the ions are at rest (trapped in a Penning trap, see chapter 4) and a beam of electrons travels through the ions and interacts with them in a confined volume. This idea describes exactly an Electron Beam Ion Source (EBIS), introduced in section 5.1.

As a source of electrons, a cathode capable of emitting at cryogenic temperatures a high-enough current is needed, which rules out immediately the possibility of relying on thermal emission. Thus an electron gun was developed consisting in an array of metallic nanowires out of which electrons tunnel when applied a strong-enough electric field. The physics of field emission will be dealt with in a detailed manner in section 5.2, along with numerous tests performed on the array of field-emission points. The implementation into an electron gun compatible with the experimental setup described in the chapter 3 will be seen in section 5.3.

5.1 Electron Beam Ion Sources / Traps

5.1.1 Introduction to EBIS/T

An EBIS is an instrument designed for the creation of highly-charged ions, and the first one was invented by E.D. Donets in 1968 [Don68, Don69]. If the EBIS is used not only for the creation of highly-charged ions, but also for their trapping and study, then it changes its name to Electron Beam Ion Trap or EBIT [Lev89, Gon05].

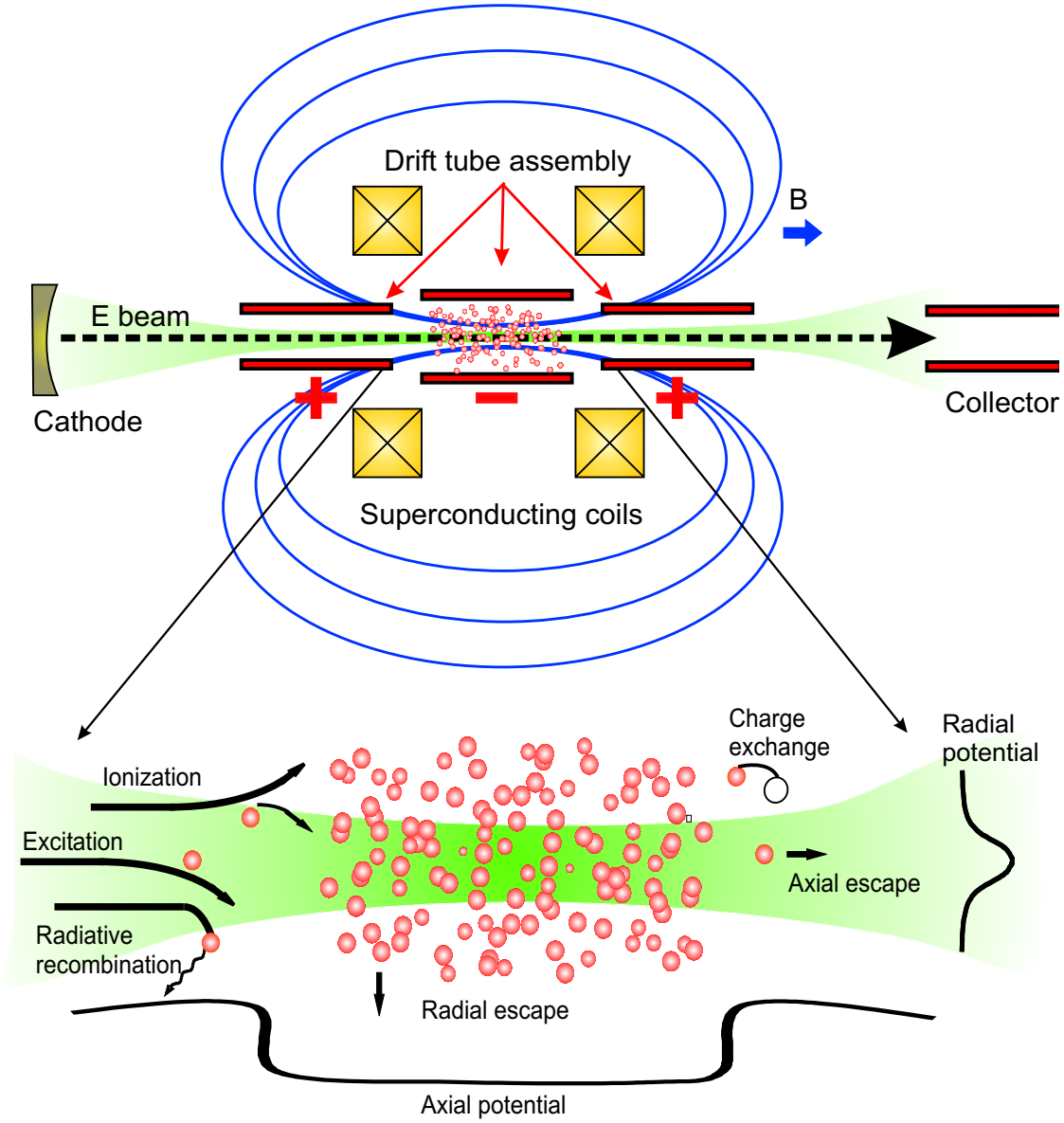

Figure 5.1: Sketch of the working principle of an electron beam ion trap (applicable also to an electron beam ion source). An electron beam is emitted from a hot cathode and compressed by a strong magnetic field in order to produce the current densities required to ionize the high charge states of the trapped particles. Courtesy of Antonio Javier González Martínez and Rosario Soria Orts.

The general structure of an EBIS/T is shown in figure 5.1. The electron beam

works as the ionizing element, but it also helps to trap charged particles. Its negative space charge can keep the positive ions confined. Therefore, the high electron density is the main ingredient of an EBIS. A strong magnetic field focuses the electrons and can compress the beam to extremely-high current densities of $\sim$10000 A/cm^2. The other main component of an EBIS/T is the trap, consisting of a set of electrodes to which static voltages are applied to create a potential minimum, as in the case of a Penning trap (chapter 4).

Originally, the label EBIS applied when the main objective of the device was to serve as an ion source from which the ions were to be extracted and transported to other experimental setups, while it was called EBIT if the experiments were realized directly in the electron beam. Now, this distinction can no longer be applied so strictly, since most of the EBI-traps count with an extraction line, and on most of the EBI-sources one can perform experiments. However, it is true that in an EBIT the magnetic field is usually provided by a short split coil in a Helmholtz configuration instead of a single long and closed solenoid, in order to allow for easy access to the trap volume. Also, the trap length of an EBIT is usually shorter than that of an EBIS, because that helps to reduce the plasma instabilities.

In what respects to this work, the main purpose of our electron-beam setup is to serve as an ion source, so it will be referred to as EBIS or mini-EBIS. The prefix "mini" is sometimes added because the operating parameters are in the order of some keV and µA for the electron energy and current, respectively, instead of a few hundred keV and hundreds of mA, which characterize most of the EBIS [Don68, Don69]. Note that with the currents mentioned for this setup, the trapping capability of the electron beam is negligible, so the electrons are confined only through the influence of the Penning trap, whose main purpose motivated its name, the Creation trap (section 6.5).

5.1.2 Evolution of ion charge-state distributions in an EBIS/T

There is a surprising lack of experimental knowledge on the cross sections of electron-impact-ionization processes (see figure 1.1). That, along with an experimental setup in which the ion-charge-state distribution can be observed on-line, motivated the possibility of using the tools developed during this work for the determination of such cross sections [Alo06]. In order to do so, a proper theoretical study of the physical processes responsible for the charge and energy balance in the EBIS/T (shown in the lower part of figure 5.1) needs to be carried out.

The large amount of particles involved make such a study extremely hard, but B.M. Penetrante *et al.* provided a very useful summary of how to perform it, as well as the basics of an algorithm with which to do simulations in a numerical way [Pen91]. In the following, their procedure will be adopted and the cross sections for all relevant processes will be investigated. Later, in section 5.1.2, they are all used within the equations of evolution which will enable the determination of the cross sections of electron-impact-ionization processes.

Ionization by electron impact

Let us start with the main process, ionization by electron impact (sketched in figure 5.2), whose cross sections are planned to be determined. It is one of the most

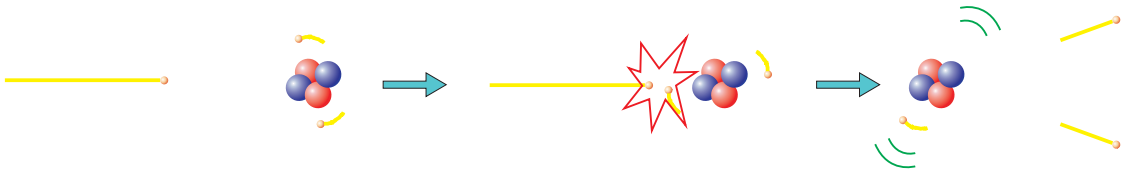

Figure 5.2: Cartoon of the ionization process by electron impact.

fundamental collision processes in atomic and molecular physics. Seen from a very simplistic point of view, when an incident electron interacts with an electron bound to an atom or ion, if enough energy is transferred during the interaction, the bound electron will be removed from the nucleus, leaving it in a higher (more positive) charge state.

Ionization by electron impact is a crucial process in many fields of physics and chemistry. It sustains gas discharges and plasmas, leads to most of the chemistry in radiation effects, plays a major role in planetary upper atmospheres and is the basis for a large fraction of mass-spectrometry experiments. This basic and practical importance has propitiated experimentalists to search for the cross-sections of electron-impact-ionization processes since the earliest days of atomic collision physics [Ble29, Com30, Smi30]. However, one can conclude, from the most important collections of data available [NIFS, NIST], that a new measurement on almost any species and charge state would be very welcome by the scientific community. This need is enhanced by the fact that there exist a large number of theoretical models which most often agree in their predictions only partially.

Such models provide individual values for the cross sections of electron-impact ionization through complex numerical computation or through semiempirical or empirical expressions which would fit the experimental data, such as the formulae developed by Lotz [Lot67], Deutsch *et al.* [Deu98], Casnati *et al.* [Cas82] and Jakoby *et al.* [Jak87].

In 1994, Kim and Rudd [Kim94] proposed the binary-encounter dipole (BED) model for the singly-differential ionization cross-section $d\sigma(T)/dW$ as a function of the secondary electron energy W and the incident electron energy T. The total ionization cross-section is obtained by integrating over W. The BED model requires knowledge of the differential dipole oscillator strengths for each atomic or molecular orbital. When unknown, Kim and Rudd approximated it by a simple analytic function which emulated the hydrogenic case, thus obtaining a compact, analytic expression for the total ionization cross section. This simplified version is referred to as the binary-encounter Bethe (BEB) model, also described in [Kim94]. The BED/BEB model has been used with great success to calculate total ionization cross-sections of neutral atoms and molecules for non-relativistic incident electron energies.

Photo-recombination

A very important hindering process in the way to full stripping of the ions is recombination with the electrons from the beam (figure 5.3). The electron is captured into a bound state of the ion, causing the emission of a photon. In fact, the radiative recombination (RR) of ions, known also as the radiative electron capture (REC) of

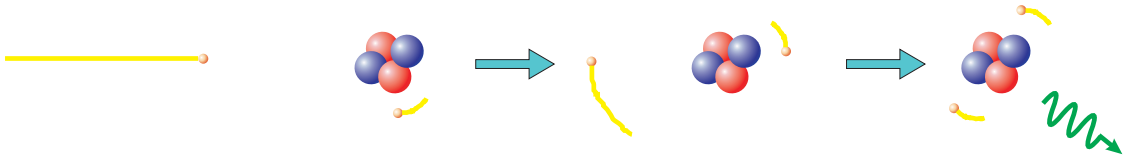

Figure 5.3: Cartoon of the radiative-recombination process with an incident electron.

loose electrons is the time-reversed photo-ionization process and frequently occurs in almost all types of plasmas.

A simple expression for the cross-section of atomic ions of nuclear charge Z and ionic charge Z_i was derived by Kim and Pratt [Kim83], assuming it interacts with an electron of energy E_e:

$$\sigma_{i\to i-1} = \frac{8\pi}{3\sqrt{3}}\alpha\lambda_e^2\chi\ln\left(1+\frac{\chi}{2(n_0)_{eff}^2}\right), \tag{5.1}$$

where α is the fine-structure constant[1], λ_e the Compton wavelength of the electron[2], and

$$\chi = 2Z_{eff}^2\frac{I_H}{E_e}, \tag{5.2}$$

being I_H the ionization potential of the hydrogen atom and $Z_{eff} = (Z + Z_i)/2$ the effective charge. Finally,

$$(n_0)_{eff} = n_0 + (1 - W_{n_0}) - 0.3 \tag{5.3}$$

is the effective quantum number, where n_0 is the valence shell number and W_{n_0} the ratio between the number of unoccupied states and the total number of states in the valence shell n_0.

For another calculation of the cross sections of radiative-recombination processes, refer to [Bec01] since Kim's formula is suspected to underestimate the energy dependence.

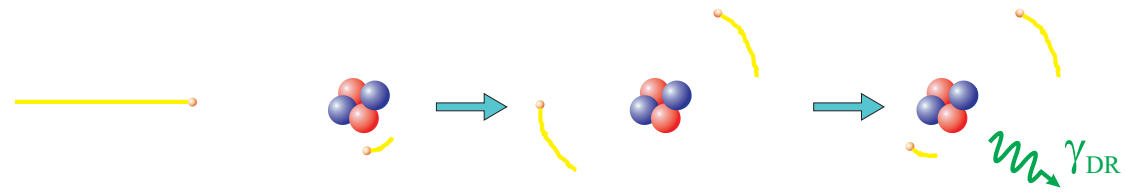

Figure 5.4: Cartoon of the dielectronic-recombination process with an incident electron.

[1] $\alpha \cong \frac{1}{137}$.
[2] $\lambda_e \cong 3.861 \cdot 10^{-11}$ cm.

There is yet another process of photo-recombination, which can take place between an electron in the continuum of energies and an ion (but not a bare nucleus), sketched in figure 5.4: dielectronic recombination. It works as follows: the free electron is captured into a vacant excited state of the ion A^{q+}, transferring non-radiatively the energy difference to a core electron with energy E_1, which is simultaneously promoted to a higher laying excited state, with energy E_2, of the ion. Hence, an intermediate (singly, doubly or multiply) excited state is formed:

$$A^{q+} + e^- \rightarrow [A^{(q-1)+}]^* \rightarrow A^{(q-1)+} + \hbar\omega_{DR}. \tag{5.4}$$

Here, the $[\,]^*$ indicates an excited state and ω_{DR} the frequency of the photon emitted. This resonant process can only happen when the energy difference between the core-electron state and the state in which the second electron is excited is equal to the kinetic energy of the free electron E_e plus the binding energy I_p of the recombined state. This resonance condition is written as

$$\Delta E = E_2 - E_1 = E_e - I_p. \tag{5.5}$$

The cross sections of dielectronic recombination can be huge if the electron-beam energy matches the resonance, but are negligible otherwise. Thus, for the determination of the cross sections of electron-impact ionization, it is important to be aware of the resonances. For an extensive review of dielectronic and photo-recombination processes, see [Hah97].

Charge exchange

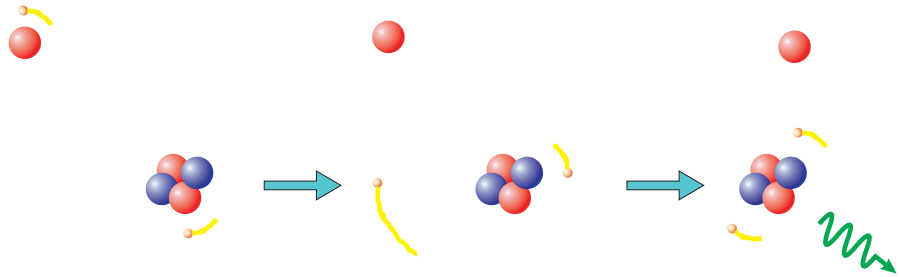

Figure 5.5: Cartoon of the charge-exchange process with a rest-gas atom.

Charge exchange (figure 5.5) is the generic name given to collisions between multiply-charged ions and neutrals where there is a transfer of electrons. These neutrals are generally rest-gas atoms or molecules. The expressions for the cross sections of charge-exchange processes, as was the case for the processes seen before, differ depending on the method used for deriving them. A widely-used semi-empirical formula is due to Müller and Salzborn [Mül77]:

$$\sigma_{i\rightarrow i-1} = 1.43 \cdot 10^{-12} Z_i^{1.17} P_0^{-2.76}, \tag{5.6}$$

where Z_i is the charge state of the ion and P_0 the ionization potential of the neutral target.

There are more sophisticated formulas, purely theoretical models, and there are even formulas for multiple-charge-exchange terms ($\sigma_{i\to i-2}$ through $\sigma_{i\to i-4}$). However, the ultrahigh-vacuum under which the experiment presented in this work is performed (the pressures are below 10^{-16} mbar, see section 3.2) keeps the charge-exchange rates so small that this process can be safely neglected.

Heating of ions by the electron beam

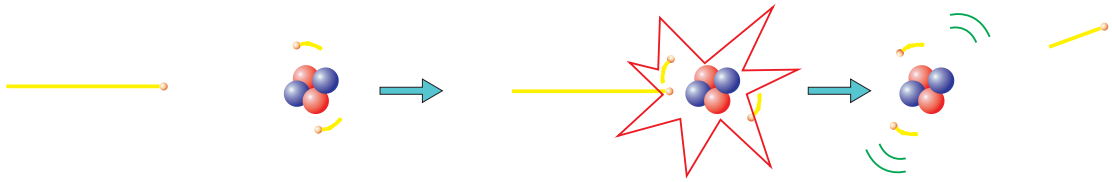

Figure 5.6: Cartoon of the ion-excitation process by electron impact.

While the ions and the electron beam overlap, the ion-electron Coulomb collisions result in a nett gain of energy for the ions (figure 5.6). This energy then redistributes among the rest of the ions by ion-ion collisions. In the end, the energy acquired by each ion determines the confinement time and also the fraction of time during which they are within the beam.

I.P. Shkarofsky [Shk66] derived the equations for the rate at which the energy is transferred in a very general case (from a first charged species of mass m, charge Z', speed distribution f_0 and density n, to a second charged species characterized by M, Z, F_0 and N):

$$\begin{aligned} \frac{dE}{dt} &= \int \frac{mv^2}{2}\left(\frac{\delta f}{\delta t}\right) d^3v \\ &= (4\pi)^2 \frac{m}{M} Y \left[-\int_0^\infty mv f_0 dv \int_0^v F_0 u^2 du + \int_0^\infty MuF_0 du \int_0^u f_0 v^2 dv \right], \end{aligned} \tag{5.7}$$

where

$$Y = 4\pi \left(\frac{ZZ'e^2}{m}\right)^2 \ln\Lambda \tag{5.8}$$

and $\ln\Lambda$ is the Coulomb logarithm[3].

First, the energy transfer from the electron beam to the ions will be investigated. Since the electrons move much faster than the ions, the speed distribution functions f_0 and F_0 reduce to a delta and a maxwellian function, respectively. Thus, the energy-transfer rate obeys:

[3]The Coulomb logarithm is the natural logarithm of the ratio of the maximum to minimum impact parameters for Coulomb "collisions", a very relevant parameter in plasma physics. Thus, in a general case where two particles of masses $m_{1,2}$, charges $q_{1,2}$ and kinetic energy T in the center-of-mass reference, $\ln\Lambda_{12} = \ln(d_{max}/d_{min})$, being $d_{max} = \sqrt{\epsilon_0 T/nq_1q_2}$ (the Debye length) and $d_{min} = q_1q_2/4\pi\epsilon_0 T$. Here, n is the number density of particles, assumed to be the same for both species for simplicity.

$$\frac{3}{2}\left[\frac{d}{dt}(N_i k T_i)\right] \simeq N_i N_e Y \frac{m}{M_i}\frac{m}{v_e}, \tag{5.9}$$

and

$$Y = 4\pi\left(\frac{Z_i e^2}{m}\right)^2 \ln\Lambda_i. \tag{5.10}$$

T_i is the temperature of the ith ionic state, N_e the electron-beam density and N_i the average ion density. Equation (5.9) is equivalent to the simple energy-loss rate expressed in terms of the electron-ion Coulomb-collision frequency ν_i and the average elastic energy loss ΔE:

$$N_e \nu_i \Delta E = N_e(N_i \sigma_i v_e)\left(2\frac{m}{M_i}E_e\right), \tag{5.11}$$

where the Coulomb cross-section is

$$\sigma_i = 4\pi\left(\frac{Z_i e^2}{m}\right)^2 \frac{\ln\Lambda_i}{v_e^4}, \tag{5.12}$$

being Λ_i the electron-ion Coulomb logarithm for the ith ion.

Ion-ion energy exchange

Coming back to equation (5.7), one has to assume this time two maxwellian distributions to study the energy-transfer rate among the ions. This time, there will be no cross sections involved, since the ion-ion energy exchange affects the equations of evolution only indirectly. The proper mathematical development can be seen in [Spi56], yielding, for the energy gain of the ith species due to collisions with the jth species:

$$\frac{d}{dt}(N_i k T_i)_j = 2\nu_{ij} N_i \frac{M_i}{M_j}\frac{k(T_j - T_i)}{\left(1 + \frac{M_i T_j}{M_j T_i}\right)^{3/2}}, \tag{5.13}$$

where ν_{ij} is the Coulomb-collision rate between the ith and the jth ionic species,

$$\nu_{ij} = \frac{4}{3}\sqrt{2\pi} N_j \left(\frac{Z_i Z_j e^2}{M_i}\right)^2 \left(\frac{M_i}{k T_i}\right)^{3/2} \ln\Lambda_{ij} \tag{5.14}$$

and $\ln\Lambda_{ij}$ are the ion-ion Coulomb logarithms.

Ion escape from the trap

The rate at which ions escape from the trap was studied in detail by E.D. Donets *et al.* as an approximated solution of the Fokker-Planck equation [Don81]:

$$\frac{dN_i}{dt} = -N_i \nu_i \left[\frac{e^{-\omega_i}}{\omega_i} - \sqrt{\omega_i}[\mathrm{erf}(\omega_i) - 1]\right], \tag{5.15}$$

where

$$\nu_i = \sum_j \nu_{ij} \tag{5.16}$$

and

$$\omega_i = \frac{eZ_iV_w}{kT_i}, \tag{5.17}$$

being V_w the potential depth of the electrostatic trap. The error function is defined as $\mathrm{erf}(x) = \frac{2}{\sqrt{\pi}} \int_0^x \exp(-t^2)dt$.

The rate of energy loss due to the escaping ions can be similarly derived from the Fokker-Planck equation as:

$$\frac{d}{dt}(N_i kT_i) = -\left(\frac{2}{3}N_i\nu_i e^{-\omega_i} - \frac{dN_i}{dt}\right) kT_i, \tag{5.18}$$

where dN_i/dt is given by equation (5.15).

Equations of evolution

At this point, a basis has been established which allows for a proper study of the equations of evolution of the ion densities and the ion temperatures.

Evolution of the ion densities

It is time to put side by side all processes described in the previous sections related to the change in the amount of ions in a certain charge state[4]: ionization, radiative recombination, the escape rates of the ions from the trap, both axially and radially, and finally the rate at which neutrals are injected from the source. Then, the evolution in the density N_i of ith charge state is given by:

$$\frac{dN_i}{dt} = R^{ioniz}_{i-1\to i} - R^{ioniz}_{i\to i+1} + R^{recomb}_{i+1\to i} - R^{recomb}_{i\to i-1} - R^{axesc}_i - R^{radesc}_i + R^{source}_i. \tag{5.19}$$

The effective ionization rate is

$$R^{ioniz}_{i\to i+1} = \frac{J_e}{e} N_i \sigma^{ioniz}_{i\to i+1}(E_e) f(r_e, r_i), \tag{5.20}$$

where J_e is the electron-beam-current density, $\sigma^{ioniz}_{i\to i+1}(E_e)$ the ionization cross-sections at beam energy E_e and $f(r_e, r_i)$ a factor that takes into account the spatial overlap between the electron beam of radius r_e and the ion distribution of characteristic radius r_i (see section 5.1.3).

In a completely analog way,

$$R^{recomb}_{i\to i-1} = \frac{J_e}{e} N_i \sigma^{recomb}_{i\to i-1}(E_e) f(r_e, r_i), \tag{5.21}$$

[4]In this work, three important conditions will be assumed: first, that ionization occurs in a stepwise manner thus neglecting the $\sigma_{i\to i-2}$ and higher order terms; second, that the electron-beam energy will be kept away from dielectronic-recombination resonances; and third, that there is no charge exchange with the rest gas due to the remarkable vacuum.

where $\sigma_{i\rightarrow i-1}^{recomb}(E_e)$ is the radiative-recombination cross-section for an energy of the beam E_e, given in equations (5.1) through (5.3).

The axial-escape rate was given by equations (5.15) through (5.17) if V_w is the voltage applied to the electrodes of the EBIS. The radial escape is given by the same equations, but replacing V_w with the effective radial potential V_{eff} given by:

$$V_{eff}(r) = V(r) + \frac{eZ_iB^2r^2}{8M_i}, \tag{5.22}$$

where $V(r)$ is the radial-electrostatic potential due to the electron beam, which is negligible at the current densities at which the experiment described in this work is run, and B is the magnetic-field strength.

Regarding the injection of neutrals, the source term is

$$R_1^{source} = \frac{J_e}{e} N_0 \sigma_{0\rightarrow 1}^{ioniz} \tag{5.23}$$

and $R_i^{source} = 0$ for $i > 1$.

Evolution of the ion temperatures

There are four terms to take into account when describing the energetic balance in the plasma: the heating of the ions by the electron beam, its redistribution among the ions and the amount of energy lost due to ions escape, both axially and radially. Thus,

$$\begin{aligned} \frac{d}{dt}(N_i k T_i) &= \left[\frac{d}{dt}(N_i k T_i)\right]^{heating} + \sum_j \left[\frac{d}{dt}(N_i k T_i)\right]_j^{exchange} \\ &\quad - \left[\frac{d}{dt}(N_i k T_i)\right]^{axesc} - \left[\frac{d}{dt}(N_i k T_i)\right]^{radesc}, \end{aligned} \tag{5.24}$$

where the first two terms are given by equations (5.9,5.10) and (5.13,5.14), respectively, and the axial and radial energy-escape rates are given by equation (5.18), using the corresponding axial and effective-radial potentials in equation (5.17).

5.1.3 Determination of the cross-sections of electron-impact ionization

In order to perform a cross-section measurement as the one planned, there are several aspects to consider. Here, only the theoretical points will be dealt with, and not the details about how to perform the analysis of the measurement, since the experimental-detection scheme will be introduced in chapter 7.

Once clarified that issue, let us assume that we count with a tool with which we are able to follow online the charge-state densities during the charge-breeding process, such as the one described in section 7.4.2. In that case, in equations (5.19) through (5.24):

- N_i and dN_i/dt would be observables;

- E_e is an experimentally-controlled parameter;
- J_e is an extremely difficult parameter to calculate, but it would cancel out if the measurement performed were not aiming for an absolute cross-section determination, but rather for one which would be later normalized to a known value;
- $f(r_e, r_i)$ can be approximated by the overlap in the volumes occupied by the various ions and it can be evaluated using the ion characteristic radius r_i, which, for $eZ_iV(r_e) > kT_i$, is

$$r_i = r_e \sqrt{\frac{kT_i}{eZ_iV(r_e)}} \tag{5.25}$$

  and, for $eZ_iV(r_e) < kT_i$,

$$r_i = r_e \exp\left[\frac{1}{2}\left(\frac{kT_i}{eZ_iV(r_e)} - 1\right)\right]; \tag{5.26}$$

- σ^{recomb} is given in equations (5.1) through (5.3);
- N_0 can be experimentally extracted by setting the electron-beam energy to a small value just below a shell-closure so that virtually all ions survive in the trap and can be counted, from which a good estimation of the injection of neutrals should be possible;
- and, finally, R^{ioniz} would be the only unknown variable, yielding the possibility of extracting σ^{ioniz}.

5.2 Field emission from a cryogenic electron source

In this section, the topic of field emission will be dealt with from both a theoretical and an experimental point of view. The motivation for such a detailed study is that the ionization and charge-breeding process represents a first, crucial step towards the isolation of a single highly-charged calcium ion on which the *g-factor* measurement can be performed. To this end, an electron source is needed which fulfills several requirements, like being capable of supplying an electron current of at least a few nA, as well as emitting at 4 K and in a 4 T magnetic field.

The free-electron-gas model will be introduced first. Second, a fully-quantum-mechanical derivation of the probability for an electron to tunnel out from a metal under the influence of an externally-applied, strong electric field will be motivated and discussed. Then, both points will be combined to find out the current density of electrons extracted through tunnel effect.

Regarding experimental results, numerous measurements of the emitted current versus the applied voltage have been carried out with a simple experimental setup which models the electron gun presented in section 5.3. It was designed to fit in a pulsed-tube cooler, capable of bringing the temperature down to a few kelvin, in order to perform temperature-dependent measurements and to check that there is still emission in a cryogenic environment [Ulm06a]. The last point will show the dependence of the extracted current on the magnetic field.

5.2.1 The free-electron-gas model

The simplest approximation to model a metal is to assume that the potential seen by the electrons remains constant along the whole of it, ignoring everything about the structure of the material. If one assumes, in addition, that the electrons do not interact with each other (independent-electron approximation), then the free-electron-gas model is brought forth [Bub92].

In spite of it simplicity, this model is widely used because it succeeds in explaining and predicting important features of metals such as density of states, binding energies, the shape of heat-capacity curves and electrical conductivities. However, it fails in explaining many other points like band gaps, why certain crystalline structures are favored with respect to others, or predicting Hall coefficients. But since the mentioned drawbacks are not needed in the derivation made in the following, one can stick to it without loss of validity in the results.

Density of states

Since the potential $V(r)$ will be considered as constant, one might as well set it to 0. Then, the Schrödinger equation becomes simply

$$-\frac{\hbar^2}{2m}\nabla^2\Psi = \varepsilon\Psi, \tag{5.27}$$

where m is the mass of the electron, ε its energy and Ψ its wave-function:

$$\Psi_k(\mathbf{r}) = \frac{1}{\sqrt{\mathcal{V}}}\exp(\imath\mathbf{k}\cdot\mathbf{r}). \tag{5.28}$$

Here, $\mathcal{V}$ is the volume of the material and $\mathbf{k}$ the wave-vector. In this simple case, the energy depends only on $k = |\mathbf{k}|$:

$$\varepsilon = \frac{\hbar^2k^2}{2m} = \frac{\hbar^2}{2m}(k_x^2 + k_y^2 + k_z^2). \tag{5.29}$$

It is possible to show that the lattice-vibrations density of states depends on k as $\rho(k) = \mathcal{V}k^2/2\pi^2$, where the cubic lattice is given in k-space by (k_x, k_y, k_z) by the fact that periodicity is assumed on the structure of the volume. One can relate the density of states, $\rho(k)$, to the density of states with respect to the energy, $D(E)$. But, since there are two electrons for every value of k, one for each spin-state, $2\rho(k)fk = D(\varepsilon)d\varepsilon$ holds true. From equation (5.29), it is obvious that $d\varepsilon/dk = \hbar^2k/m$, so

$$D(\varepsilon) = \frac{\mathcal{V}km}{\pi^2\hbar^2} = \frac{\mathcal{V}m}{\pi^2\hbar^3}\sqrt{2m\varepsilon}. \tag{5.30}$$

The Fermi-Dirac distribution

The distribution of energy levels, denoted as $n(\varepsilon, T)$, is defined as the probability that the level of energy ε is occupied by an electron if the metal is at a temperature T. Thus, at 0 K, the level distribution is

$$n(\varepsilon, 0) = \begin{cases} 1 & \epsilon \leq \epsilon_F \\ 0 & \epsilon > \epsilon_F \end{cases}, \tag{5.31}$$

being ϵ_F, the Fermi energy, the point at which the discontinuity occurs (see figure 5.7).

If the temperature is increased, the kinetic energy of the electrons increases and some levels are occupied which were empty at 0 K. A very simple derivation yields the Fermi-Dirac distribution [Fey72]:

$$n(\varepsilon, T) = \frac{1}{\exp\left(\frac{\varepsilon-\mu}{k_B T}\right) + 1}, \tag{5.32}$$

where μ is the chemical potential, which can be approximated by the Fermi energy for low temperatures, and k_B the Boltzmann constant. The left part of figure 5.7 shows a plot of the distribution for several temperatures. The right is a plot, also for several temperatures, of the product between the distribution and the density of states. This quantity will be of importance for the derivation of the electron-current density in the coming sections.

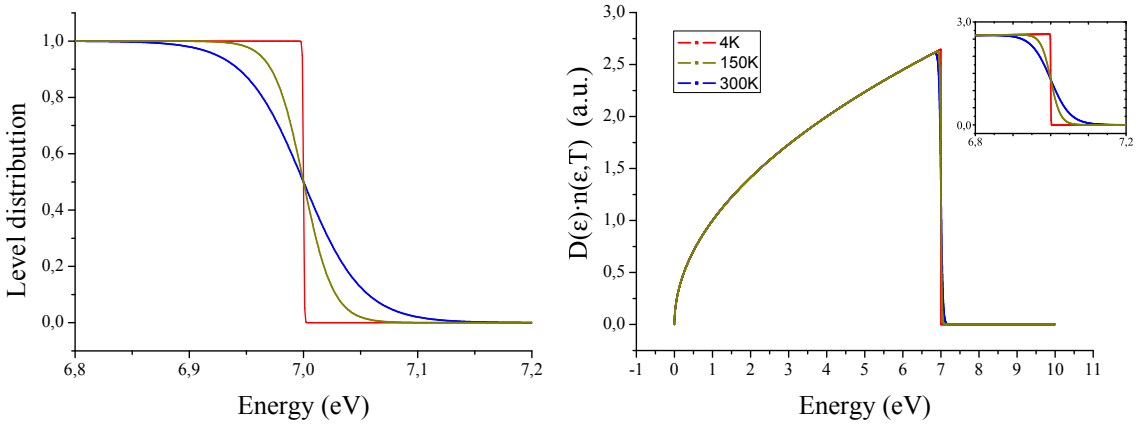

Figure 5.7: Plots of the Fermi-Dirac distribution $n(\varepsilon, T)$ (left) and of its product with the density of states (right) for a Fermi energy of 7.0 eV (coinciding with the ε_f of copper) and three different temperatures: 4 K (red), 150 K (dark yellow) and 300 K (blue). The inset zooms in the region close to ε_f.

5.2.2 Transmission probability

The objective of this point is to obtain the probability for a single electron to tunnel through the potential barrier when an external electric field is applied. Let us part from the Hamiltonian for an electron of momentum p in a metal, considering the free-electron-gas model:

$$H_0 = \frac{p^2}{2m} + V(x), \tag{5.33}$$

where, in the most general case, the one-dimensional potential (figure 5.8) is described by:

$$V(x) = \begin{cases} -W_a & \text{for } x \leq 0 \\ V_0 - eFx - \frac{me^2}{2\hbar^2}\frac{1}{x} & \text{for } x > 0 \end{cases}, \tag{5.34}$$

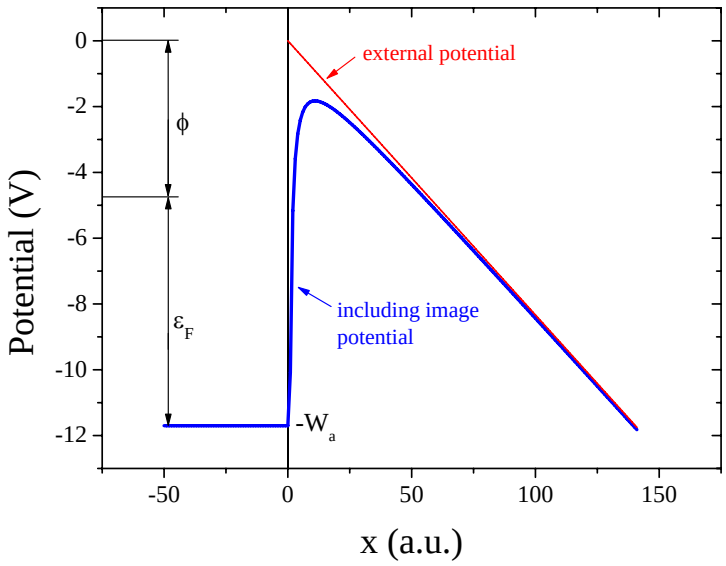

Figure 5.8: Representation of the potential seen by an electron in a metal (according to the free-electron-gas model), added to the externally-applied electric field and the image-charge term. The position x has been given in arbitrary units and the potential in volts, where the work function ϕ has been set to 4.7 eV and the Fermi energy ε_F to 7 eV (realistic numbers for copper). V_0 is 0 in this example.

being F the electric field applied externally. V_0 vanishes under normal circumstances, yielding a potential-barrier height equal to the work function ϕ, if one neglects the image potential. The term eFx is due to the electric field and the term $\frac{me^2}{2\hbar^2}\frac{1}{x}$ accounts for the image potential the electron induces in the phase transition between the metal and the external vacuum [Nor28].

Then, the Schrödinger equation reads:

$$\Psi''(x) + \frac{2m}{\hbar^2}[\varepsilon - V(x)]\Psi(x) = 0, \tag{5.35}$$

It is useful to introduce the variables α, ϵ and β for a more compact derivation:

$$\begin{aligned} \alpha &= \frac{2meF}{\hbar^2}, \\ \epsilon &= \frac{2m(\varepsilon - V_0)}{\hbar^2}, \\ \beta &= \frac{me^2}{2\hbar^2}, \end{aligned} \tag{5.36}$$

reducing the Schrödinger equation to

$$\Psi''(x) + (\epsilon + \alpha x + \frac{\beta}{x})\Psi(x) = 0. \tag{5.37}$$

Also for convenience, a variable change can be applied from x to $\xi = (x+\epsilon/\alpha)\alpha^{1/3}$, which yields the following form for the Schrödinger equation [Lan91]:

$$\Psi''(\xi) + \left(\xi + \frac{\overline{\alpha}}{\xi - \overline{\epsilon}}\right)\Psi(\xi) = 0, \tag{5.38}$$

where $\overline{\alpha} = \beta\alpha^{-1/3}$ and $\overline{\epsilon} = \epsilon\alpha^{-2/3}$. This may be rewritten as

$$\Psi''(\xi) + \left[\frac{(\xi - \lambda_+)(\xi - \lambda_-)}{\xi - \overline{\epsilon}}\right]\Psi(\xi) = 0, \tag{5.39}$$

with $\lambda_\pm$ as two newly defined variables:

$$\lambda_\pm = \frac{1}{2}\left(\overline{\epsilon} \pm \sqrt{\overline{\epsilon}^2 - 4\overline{\alpha}}\right). \tag{5.40}$$

Let us focus now on the region very close to the top of the potential barrier, where $\lambda_\pm \simeq \overline{\epsilon}/2$, in particular close to the origin $x = 0$, where $\xi_0 = \overline{\epsilon}$. Then,

$$\Psi''(\xi) + \frac{(\xi - \frac{\overline{\epsilon}}{2})^2}{\xi - \overline{\epsilon}}\Psi(\xi) = 0. \tag{5.41}$$

Since in this region[5] $\xi - \overline{\epsilon} \ll \overline{\epsilon}$, one can perform a new change of variable from ξ into $y = \xi - \overline{\epsilon}$, converting the Schrödinger equation in

$$y\Psi''(y) + \left(y + \frac{\overline{\epsilon}}{2}\right)\Psi(y) \simeq y\Psi''(y) + \frac{\overline{\epsilon}}{2}\Psi(y) = 0. \tag{5.42}$$

The solution to such equation can be written through the Hankel function of first order[6]. After undoing the variable change, it reads:

$$\Psi(\xi) = \exp\left(\imath\frac{\pi}{4}\right) \cdot \sqrt{\frac{\pi}{2}} \cdot \overline{\epsilon} \cdot \sqrt{\xi - \overline{\epsilon}} \cdot H_1^1(\overline{\epsilon}\sqrt{\xi - \overline{\epsilon}}). \tag{5.43}$$

The transmission amplitude[7] derived from this wave-function can be shown to be

$$\mathcal{T} = \frac{2\overline{\epsilon}k_0^{1/3}}{|\Psi(\xi_0)|^2 + \epsilon^2 k_0^{1/3} + k_0^{2/3}|\Psi'(\xi_0)|^2}, \tag{5.44}$$

where

$$\Psi'(\xi) = \exp\left(\imath\frac{\pi}{4}\right) \cdot \sqrt{\frac{\pi}{8}} \cdot \overline{\epsilon}^2 \cdot H_0^1(\overline{\epsilon}\sqrt{\xi - \overline{\epsilon}}) \tag{5.45}$$

and $k_0^{1/3} = \frac{\alpha^{1/3}}{k}$, with

$$k = \sqrt{\frac{2m(\varepsilon + W_a)}{\hbar^2}}. \tag{5.46}$$

[5]For a typical configuration where $V_0 = 0$, $\varepsilon = \phi = 1\,\text{eV}$ and $F = 100\,\text{V}/\mu\text{m}$, $\overline{\epsilon} \simeq 10$ and $\overline{\alpha} \simeq 10^{-9}$.

[6]The Hankel functions of the first kind are defined as $H_n^1(z) = J_n(z) + \imath Y_n(z)$ where $J_n(z)$ is a Bessel function of the first kind and $Y_n(z)$ is a Bessel function of the second kind.

[7]The transmission $\mathcal{T}$ and reflection $\mathcal{R}$ coefficients are related to the tunnelling probabilities associated to the wave-functions. They are normalized in such a way that $\mathcal{T} + \mathcal{R} \equiv 1$. In order to obtain them mathematically in the problem described, one takes the portion of the wave-function outside the metal, $\int_0^\infty dx\Psi^\dagger\Psi$, the portion which remains inside, $\int_{-\infty}^0 dx\Psi^\dagger\Psi$, and makes them match at the origin, being $\Psi^\dagger$ the complex-conjugate of Ψ.

The normalization condition $\mathcal{T} + \mathcal{R} = 1$ can be shown to be fulfilled, meaning that the essential features of the theory have been properly picked up. Nevertheless, the transmission coefficient according to equation (5.50) yields a vanishing probability for emission from the metal at the origin ($x = 0$). The reason is the weak singularity of $1/x$ in Ψ' close to the origin. However, one may write

$$\mathcal{T} \simeq \frac{4\pi}{\overline{\epsilon}^{3/2} \ln^2(\delta^{1/2}\overline{\epsilon})}, \tag{5.47}$$

being δ a renormalization constant with a value much smaller than that from $\overline{\epsilon}$. The physical explanation for this renormalization to be there at all is that the electron and its image charge cannot coincide in the same position in the transition surface. Rather, there must be a minimum distance in the order of atomic dimensions. If one assumes that the closest approximation is, for instance, 1 Å, then $\delta = 10^{-4}F/\phi$, where F is given in V/µm and ϕ in eV.

If one now moves the attention to the area close to the top of the potential barrier, but not directly on top, then we can approximate equation (5.40) by

$$\lambda_{\pm} \simeq \frac{\overline{\epsilon}}{2}(1 \pm \sigma), \tag{5.48}$$

where $\sigma = \sqrt{1 - 4\overline{\alpha}/\overline{\epsilon}^2}$. Since $\overline{\epsilon}$ is large, equation (5.39) can be turned into

$$y\Psi''(y) + \gamma^2\Psi(y) = 0, \tag{5.49}$$

with $\gamma = \frac{1}{2}\overline{\epsilon}\sqrt{1 - \sigma^2}$. This time, the transmission amplitude is given by

$$\mathcal{T} = \frac{8\gamma^2 k_0^{1/3}}{|\Psi(\xi_0)|^2 + 4\gamma^2 k_0^{1/3} + k_0^{2/3}|\Psi'(\xi_0)|^2}, \tag{5.50}$$

the wave-function by

$$\Psi(\xi) = \exp\left(\imath\frac{\pi}{4}\right) \cdot \sqrt{\frac{\pi}{2}} \cdot 2\gamma \cdot \sqrt{\xi - \overline{\epsilon}} \cdot H_1^1(2\gamma\sqrt{\xi - \overline{\epsilon}}) \tag{5.51}$$

and its primitive by

$$\Psi'(\xi) = \exp\left(\imath\frac{\pi}{4}\right) \cdot \sqrt{\frac{\pi}{8}} \cdot (2\gamma)^2 \cdot H_0^1(2\gamma\sqrt{\xi - \overline{\epsilon}}). \tag{5.52}$$

At this point, it is worth taking a look at the solution reached by Fowler and Nordheim through a WKB[8]-formalism [Fow28, Nor28, Goo56], which approximates the wave-function as

$$\Psi_{FN}(\xi) = \frac{1}{\sqrt{p(\xi)}} \exp\left[\imath \int_{\min\{\lambda_+,\lambda_-\}}^{\xi} p(\xi')d\xi' + \frac{\imath\pi}{4}\right], \tag{5.53}$$

where

[8]The WKB (Wentzel-Kramers-Brillouin) approximation is the most familiar example of a semi-classical calculation in quantum mechanics in which the wave-function is recast as an exponential function, semiclassically expanded, and then either the amplitude or the phase is taken to be slowly changing.

$$p(\xi) = \sqrt{\frac{(\xi - \lambda_+)(\xi - \lambda_-)}{\xi - \overline{\epsilon}}}. \tag{5.54}$$

If one plugs Ψ_{FN} into equation (5.50), above a certain value of the electric field of around 700 V/µm for $\phi = 1\,\text{eV}$ and $V_0 = 0$, the transmission amplitude becomes greater than unity, which is non-physical (see figure 5.9). What the figure also shows is that, according to the Fowler-Nordheim formalism, $\mathcal{T}$ drops exponentially as F diminishes, as opposed to the purely quantum-mechanical solution.

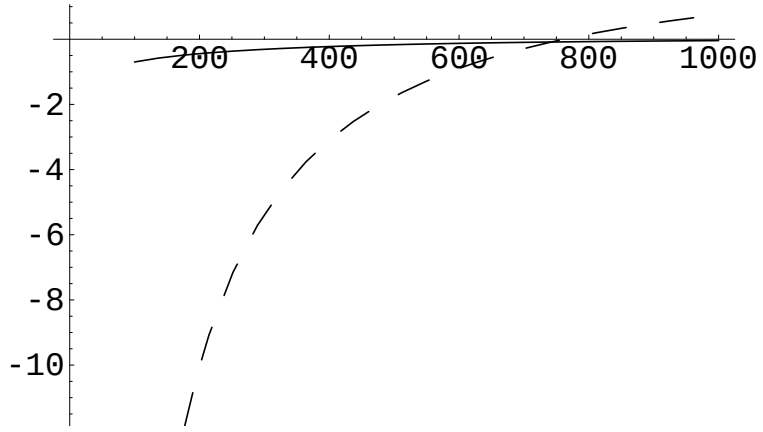

Figure 5.9: Plot of the transmission coefficient derived quantum-mechanically (equation 5.50, solid line) versus the Fowler-Nordheim formula less the prefactors in the full image case (dashed line). F is in units of V/µm. Figure taken from [Cho03].

5.2.3 Electron current tunnelling from a metal

The total electron-current density J is given by

$$J = \int_0^\infty e \cdot v \cdot \rho \cdot D(\varepsilon) \cdot n(\varepsilon, T) \cdot \mathcal{T} \cdot d\varepsilon, \tag{5.55}$$

where e is the charge, $v = \sqrt{2\varepsilon/m}$ the velocity and ρ the particle density of the electrons. Neglecting thermal effects and assuming that the temperature is well below the Fermi energy divided by the Boltzmann constant, $\varepsilon_F/k_B \simeq 60000\,\text{K}$, one obtains

$$J = \frac{4\pi me}{(2\pi\hbar)^3} \int_{-W_a}^{\varepsilon_F} \mathcal{T}(\varepsilon)(\varepsilon_F - \varepsilon)d\varepsilon. \tag{5.56}$$

This equation cannot be solved analytically, but it is possible to apply a numerical-approximation method, which yields [Cho03]:

$$J \simeq \frac{\kappa c_A \phi^{-3/2}}{\ln^2\left(\frac{c_B\phi}{\sqrt{eF}}\right)} \sqrt{\frac{\varepsilon_F}{\phi}} (eF)^3 \ \text{A/cm}^2, \tag{5.57}$$

where, $c_A = 9.924 \cdot 10^{-2}\,\mathrm{eV}^{-3/2}\cdot\mu\mathrm{m}^3$ and $c_B = 51.231\,\mathrm{eV}^{-1/2}\cdot\mu\mathrm{m}^{-1/2}$. Since the lowering of the potential barrier has been shown to be of relevance, the factor $\kappa \in [0, 1]$ can be used to take into account the screening effects which changes the effective field seen by the electron from F to κF.

5.2.4 Experimental setup for field-emission investigation

Equation (5.57) indicates that the probability of an electron tunnelling out from a metal grows with the third power of the electric field it sees. A widespread choice in order to make use of this feature are *field-emission points* (FEP), whose main characteristic is a much smaller diameter than length or, in other words, a very large aspect ratio. Just at the tip, the curvature radius is sometimes as small as 100 nm, so for a small voltage the electric field can be huge. Therefore, the electron gun was mounted with the FEP shown in figure 5.10.

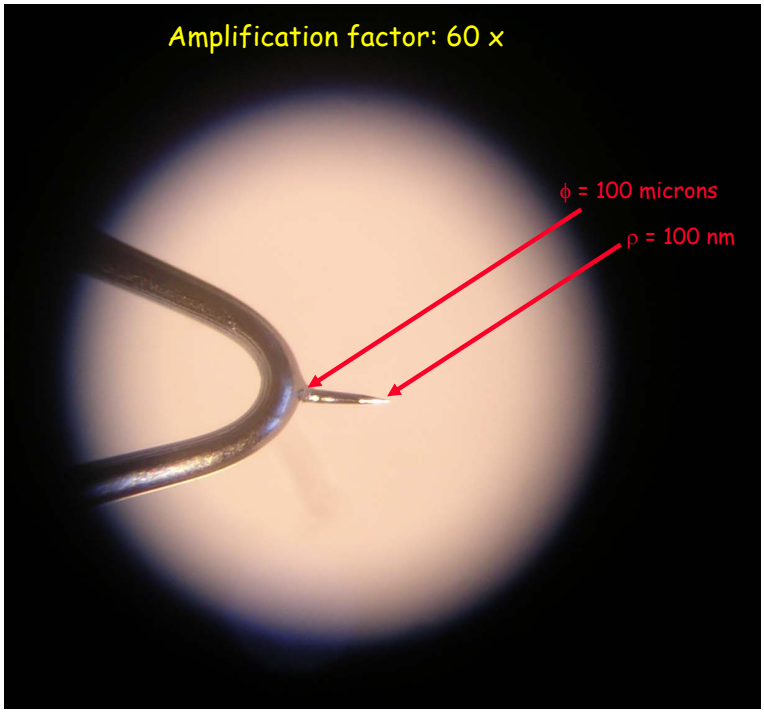

Figure 5.10: Photograph of a single field-emission point taken through a microscope. The amplification of the microscope was set to 60×. The FEP is point-soldered to the supporting structure.

However, when immersed in a strong magnetic field and cooled down to cryogenic temperatures, no electrons were ever seen to tunnel out from it. This could be mainly due to three reasons: the voltage applied to it was not high enough, the electrical contact was lost, or the fragile tip was simply destroyed.

So the decision was made to use as a cathode an array of field-emission points (FEPA) rather than a single tip. The array, shown in figure 5.11, was manufactured in collaboration with F. Maurer and C. Trautmann from the TU-Darmstadt and GSI-Darmstadt, respectively. A polycarbonate foil (MAKROFOL N, Bayer Leverkusen) of 30 µm thickness was irradiated with ^{238}U ions of energy of 11.1 MeV

per nucleon at the UNILAC accelerator (GSI-Darmstadt), as described in [Mau06]. Prior to the chemical track etching, all samples were exposed to UV light to enhance the etching rate along the tracks and thus favor the formation of cylindrically shaped pores. Etching was performed at 50°C in a 6 M NaOH solution during less than 10 min. A ∼100 nm gold film was sputtered onto one side of the membrane to establish a conductive substrate for wire growth. The gold layer was mechanically strengthened by electrodeposition of ∼10 µm copper, using a commercial electrolyte solution (Cupatierbad, Riedel Company). The potentiostatic deposition of copper into the etched pores of the template was accomplished at 50°C with an electrolyte solution of 238 g/l $CuSO_4 \cdot 5H_2O$ and 21 g/l H_2SO_4. The voltage applied was kept constant during wire growth at around 100 mV. The wires were separated from the template by dissolving the polymer in CH_2Cl_2, and the array of field-emission points was thus grown on a copper substrate.

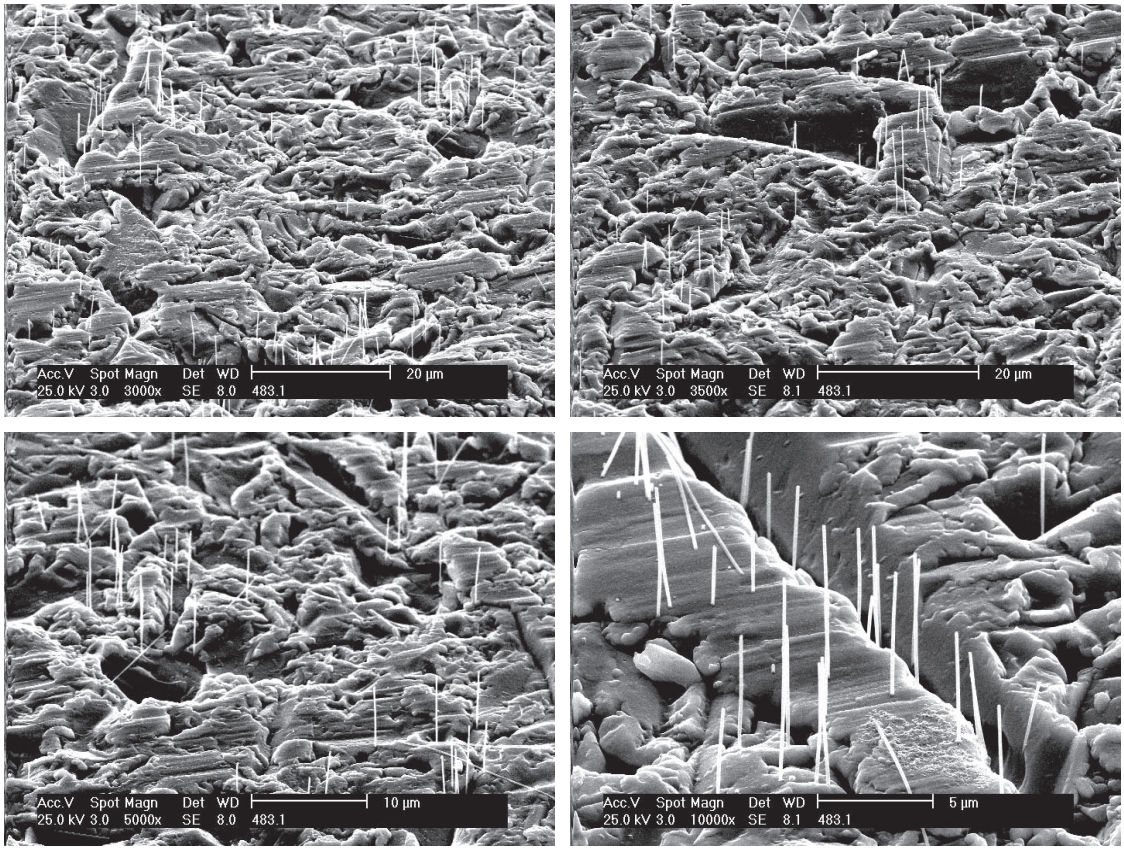

Figure 5.11: Field-emission-point array of copper nanowires seen through a scanning electron microscope (amplifications factors of 3000×, 3500×, 5000× and 10000×). The diameter of the nanowires is 150±6 nm, the length 10±3 µm. The large deviation of the length is due to breaking of wires. The maximal length (which should be the length for all standing wires) is about 15 µm. The number density of the wires is around $1.7 \cdot 10^7\,\mathrm{cm}^{-2}$.

A portion of the FEPA was cut and stuck to a cathode holder with a carbon sticky pad (Plano-EM G304). The electrical resistance of these pads is very small at room temperature, but they are barely conducting under cryogenic conditions.

Hence, the holder, the pad and the FEPA were gold-covered with a layer of ∼10 nm to ensure conductivity at a few kelvin.

The emission of electrons is achieved by applying a voltage between the FEPA and an extraction electrode, which creates the required, high electric field (see figure 5.12). The extraction electrode is located ∼280 µm above the array, electrically isolated from the FEPA holder by a MACOR ring.

The electron current emitted is measured directly as the current supplied by the voltage source to the cathode in order to compensate for the loss of electrons at the tips. This current produces a measurable voltage drop at the inner 11 MΩ resistance of a Fluke voltmeter type 189. The 1 GΩ resistance shown in the figure is there only for protection purposes.

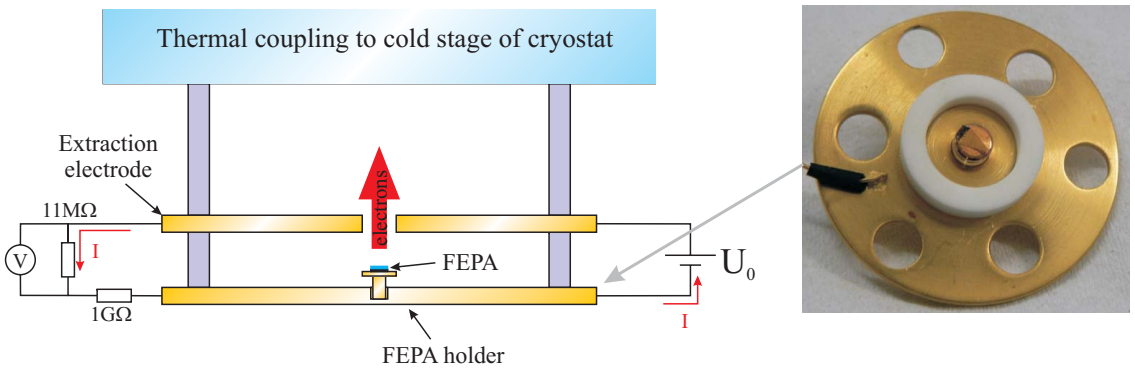

Figure 5.12: Setup for testing the electron gun (left) and a photograph of the holder of the FEPA, including an isolator ring made out of MACOR (right).

In order to measure the temperature characteristics and cryogenic properties of the FEPA, the setup was thermally anchored to the colder stage of a two-stage Gifford-MacMahon pulse-tube cooler from VeriCold. In such a cooler, the cryogenic temperatures are achieved via pulsed-gas expansion of a closed, high-purity helium circuit pumped by a Leybold COOLPAK 4000 compressor. The stage temperatures have been measured with Lake Shore CX-1050-Cu thermometers mounted directly on the setup. To achieve FEPA temperatures around 4 K, the cold-stage setup has been surrounded with a radiation shield coupled to the first stage of the cooler (50 K). The complete setup is then mounted in a vacuum chamber, where pressures of $\sim 1 \cdot 10^{-7}$ mbar at 4 K were achieved [Ulm06a].

5.2.5 Current-vs-voltage measurements and comparison to theory

Current-vs-voltage measurements

The characteristic of the electron source most important to us is the extracted electron-current behavior with respect to the voltage applied, an I-V curve. Many such measurements were performed, where the emitted current was monitored, as explained above, for different values of the extraction voltage U_0. The curve in figure 5.13 was taken at a temperature of 5.4 K and shows a typical result, where one can easily distinguish three operating regions:

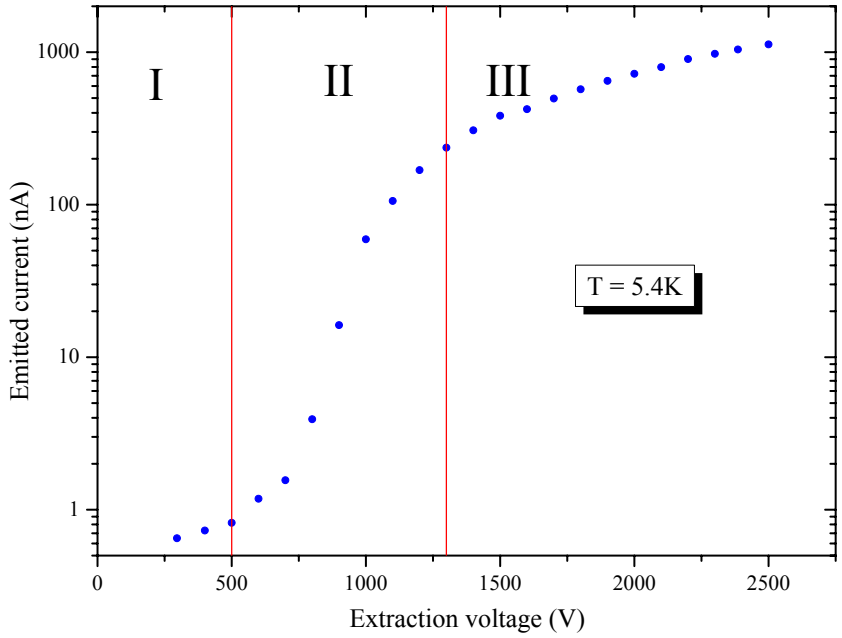

Figure 5.13: *I-V* curve taken at 5.4 K. The three operating regions are: I - non-emitting regime; II - electron emission; III - saturation. The voltage is plotted, rather than the electric field, since that is the experimentally-controlled variable and is known to be constant within the whole conducting array.

- **I - Non-emitting regime:** at low voltages, the electric field at the tips is not large enough to make the electrons tunnel through the potential barrier of the metal. There are, however, small leak currents measured with the voltmeter. These arise from the fact that the setup is, of course, not ideal; there are finite resistances at the output of the voltage supply, the MACOR rings are not perfect isolators, currents can also leak through the vacuum feedthroughs, etc. The slope is of around 1 nA/100 V, which corresponds to a resistance of 100 GΩ, a very reasonable value.

- **II - Electron emission:** above a certain electric field which depends on many factors such as the material out of which the nanowires are grown, the density of nanowires, the temperature and others, electrons start to tunnel out from the field-emission points. In this case, the threshold is ∼3 V/µm, and above it the electron current is increased by several orders of magnitude.

- **III - Saturation:** which can be explained in terms of the decrease in work-function of the metal due to the heating effect during field emission [Pur02, Pat06], deformations at the tips [Kuz01], and space-charge and screening effects, which will be discussed later. This saturated regime is not predicted by the derivation of the emitted current density discussed before and given by equation (5.57).

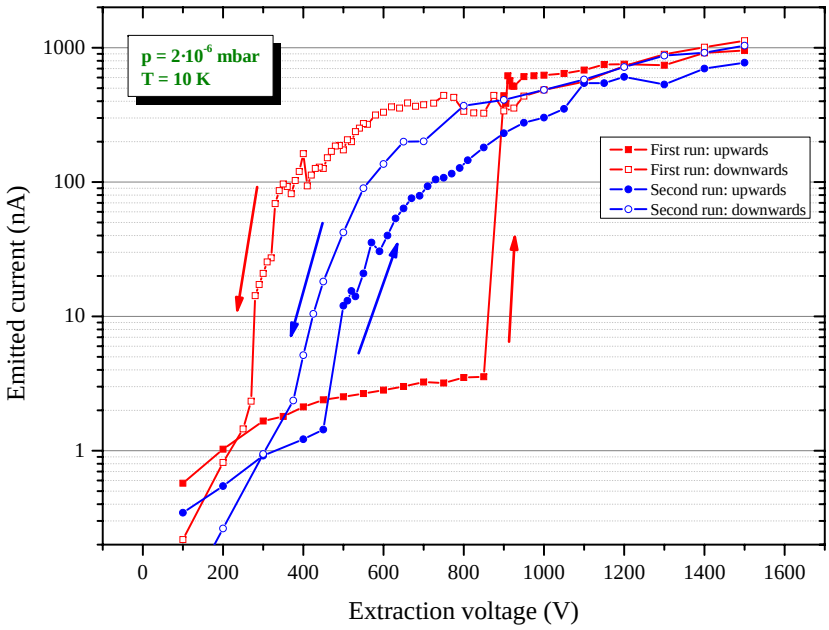

Figure 5.14: First two I-V measurements taken before training the system.

Conditioning of an array

Figure 5.14 shows the first two I-V curves measured. There is a clear hysteresis effect to observe, but, moreover, the second plot differs significantly from the first one. This result has also been reported by other groups (see, for instance, [Pat06]), and it is believed to be well understood. The principal underlying cause is the existence of a contaminant layer situated on the array of field-emission points, specially at cryogenic temperatures. The contaminants can be removed by scanning several times the voltage up and down. After a number of runs which depends on the system but which are usually no more than 20, the emission from the nanowires becomes stable and reproducible: the system has been *trained* or *conditioned*. All results presented in this work are from measurements performed once the system was already trained.

Comparison to theory: screening and space-charge effects

It is interesting to compare the experimental I-V curves to the theoretical predictions in order to test the model used for field-emission calculations. This is particularly true since the model presented in this work and derived by T.C. Choy in [Cho03] is still used only by a small minority of the field-emission community. The reason is that the semi-classical approach, that is, the Fowler-Nordheim formula [Fow28, Nor28], fits extremely well with the experimental results at the low electric fields (below 50 V/µm) usually present in the experiments with nanowires.

Figure 5.15 shows a fit using the expression obtained previously for the current density extracted as a function of the electric field at the position of the tips (equation 5.57). The observable accessible experimentally is the total emitted cur-

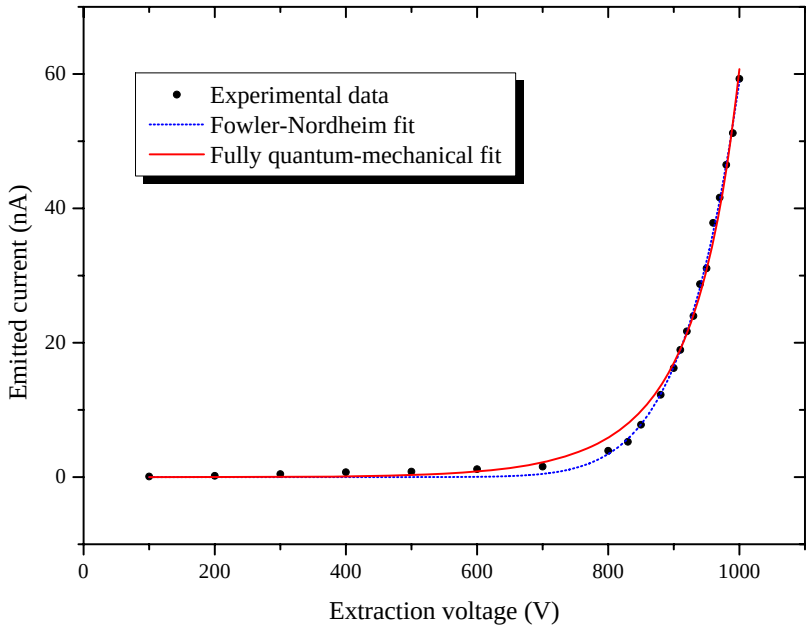

Figure 5.15: Theoretical fit to an experimental I-V measurement in regions I and II. Note: the y-axis is this time linear for clarity.

rent rather than the current density, but if one assumes that current emission is homogeneous all over the array, then the surface is just a constant. The formula obviously reproduces correctly the behavior of the system, and the Fowler-Nordheim prediction fits also properly [Ulm06a, Ulm06b]. Note that only zones I and II are included in the figure, before saturation comes into play. At higher voltages, both the fully quantum-mechanical treatment and the Fowler-Nordheim semiclassical approximation fail to explain the observed data. There are several aspects which seem, thus, need to be taken into account but have not been included in the theoretical description derived above.

The first, and probably most important one comes from the assumption of homogeneity in the emitted current along the surface of the array. Simulations performed in SIMION 7.0 assuming an array of 100 identical field-emission points equispaced on a plane show that, if an array is packed enough, screening effects can become crucial. The results of these simulations are shown in figure 5.16. The electric field strength is plotted for the whole plane just above the tips. The screening avoids the electric field from penetrating for those tips away from the edges. Figure 5.17 is a cut through the innermost row of points, and it shows that the field strength decreases exponentially as one gets closer to the center of the array. This effect has been already reported in [Koh04, Rea04, Sed06], for example.

Another effect which has not been taken into account by the theoretical model is space-charge. The negative potential created by the emitted electron current shields the electric field seen by the field-emission points. These effects were studied early in the 20^{th} century for thermionic emission [Chi11, Lan23], and the models derived

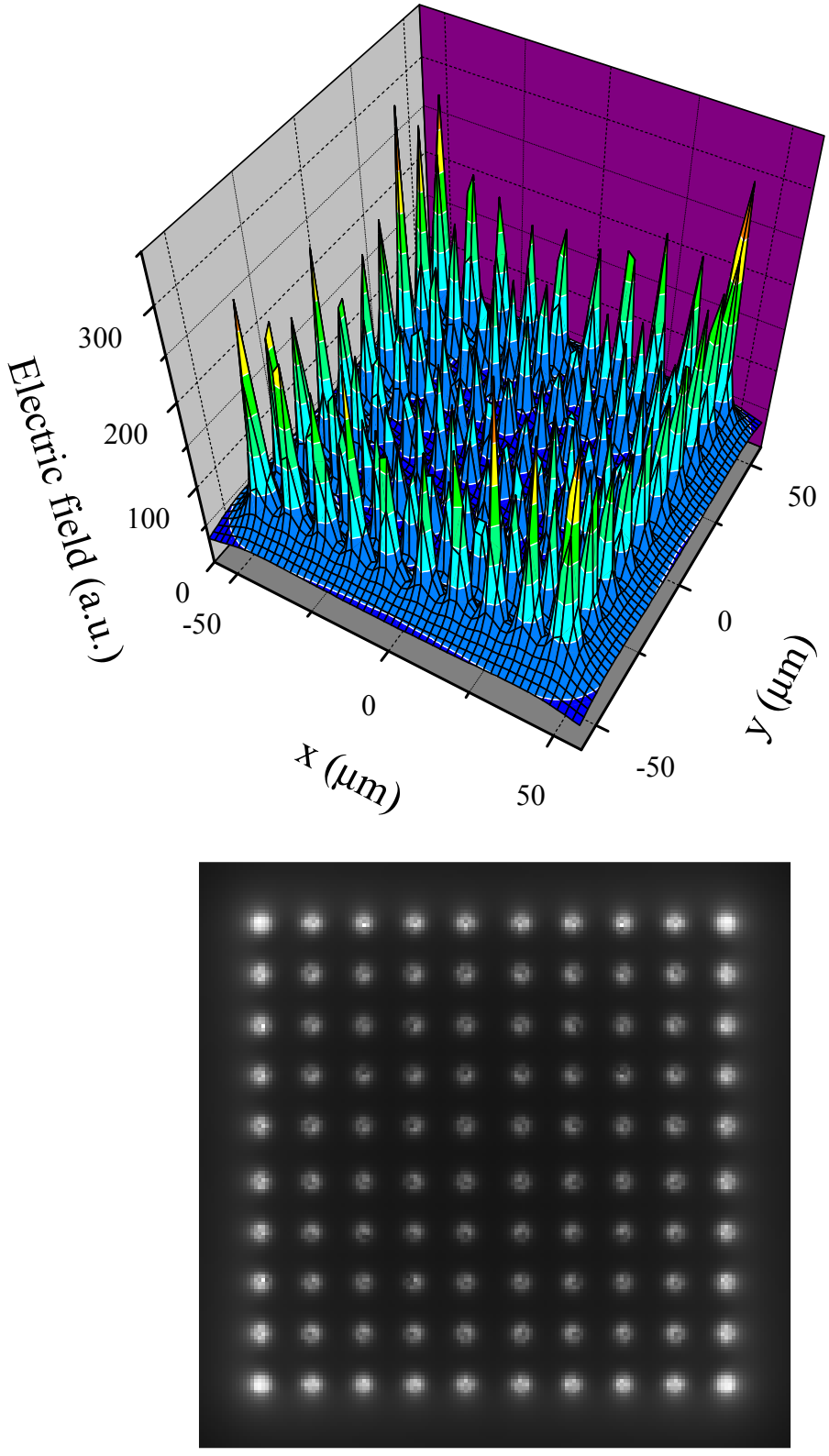

Figure 5.16: Simulation of the electric-field-strength distribution in an homogeneous field-emission-point array consisting of 100 identical points.

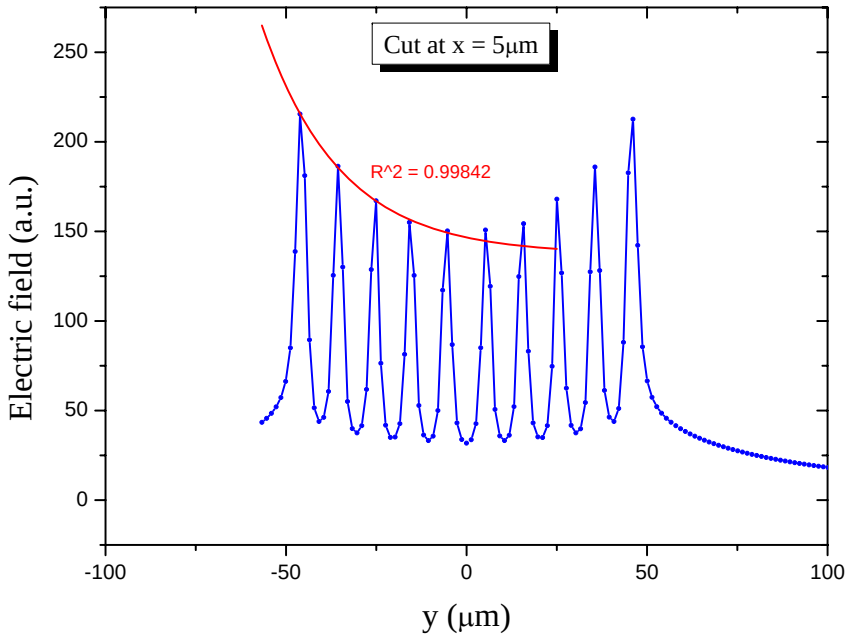

Figure 5.17: Electric-field strength as a function of the distance of the nanowire from the edge of the array. An exponential curve has been fitted along the tips.

then are used as a basis for calculations in the case of field emission [Lug96]. Both screening and space-charge effects can combine, leading to a point where, above a certain nanowire density, only the outermost tips are expected to fire. This has been seen experimentally with use of an electron microscope by J. Song *et al.* (figure 5.18).

Also temperature effects have been disregarded to obtain equation (5.57). The next subsection is dedicated to this topic.

5.2.6 Temperature effects on field emission

If the temperature is bigger than the absolute 0, then the Fermi energy ε_F must be substituted by the chemical potential μ in equation (5.57). For a free-electron gas, the temperature-dependent chemical potential is given by the expression [Gre95]:

$$\mu = \varepsilon_F \left[1 - \frac{\pi^2}{12} \left(\frac{k_B T}{\varepsilon_F} \right)^2 + \frac{\pi^4}{80} \left(\frac{k_B T}{\varepsilon_F} \right)^4 + \cdots \right]. \tag{5.58}$$

The chemical potential is not the only quantity which changes with the temperature in equation (5.57). The work-function ϕ does too, since, as can be seen in figure 5.8, $W_a = \mu + \phi$.

Hence, it is expected that, although there is no real thermionic emission [Mur56, Str62], there is a slight temperature dependence of the extracted current on the temperature. The results in figure 5.19 shows that, indeed, this is the case.

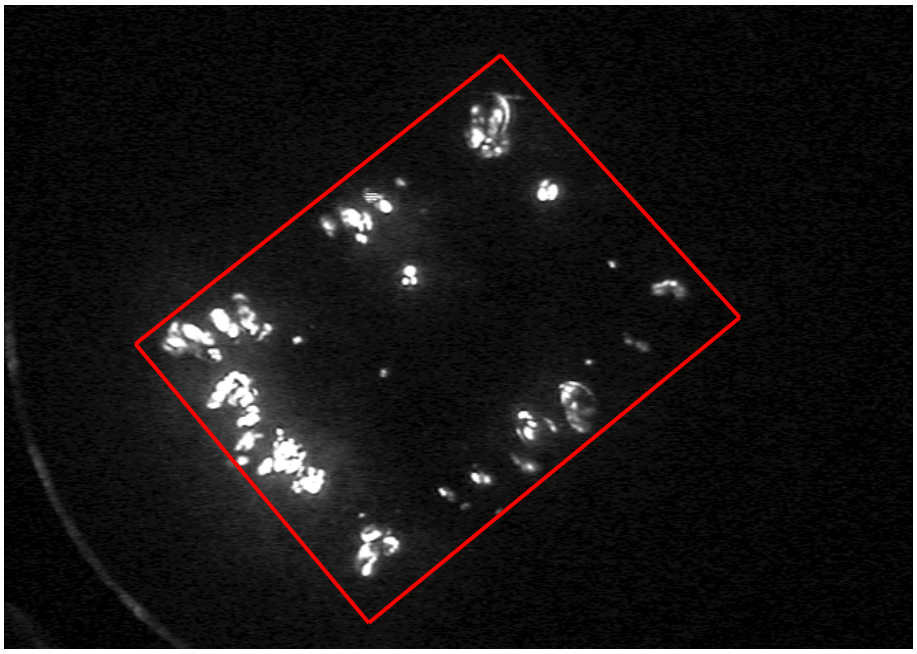

Figure 5.18: Picture of an array where only the outermost tips emit electrons. Figure taken from [Son04]. The rectangle has been added for the sake of clarity.

5.3 Ion creation and the electron gun

5.3.1 Overview

The first part of this chapter has been dedicated to the physics behind charge breeding with an EBIS/T and field emission from an array of nanowires. Now both techniques have to be put side by side in order to be able to achieve the two goals aimed for:

- ionizing calcium ions up to their hydrogenlike and lithiumlike states in order to further isolate a single ion on which to perform a *g-factor* measurement of the bound electron,
- and realize systematic studies of the charge-breeding process in order to extract the cross sections of ionization process by electron impact.

The setup shown in figure 5.20 is an overview of the realization of such combination. The electrode completely at the bottom (*cathode*[9]) is a holder for the field-emission-point array, exactly like the one used for measuring the I-V characteristics (figure 5.12). Just above the cathode is the so-called *acceleration electrode*. The voltage difference between the acceleration electrode and the cathode is responsible for the extraction of the electrons from the nanowires. Then comes the *target*, made out of graphite upon which a layer of isotopically-enriched calcium of $\sim$10µm was intentionally grown. The abundances of the different isotopes in the target are listed in table 5.1. After a spacer electrode, which is grounded and not used for the

[9]The cathode will be often referred to as *FEP*, name kept for historical reasons.

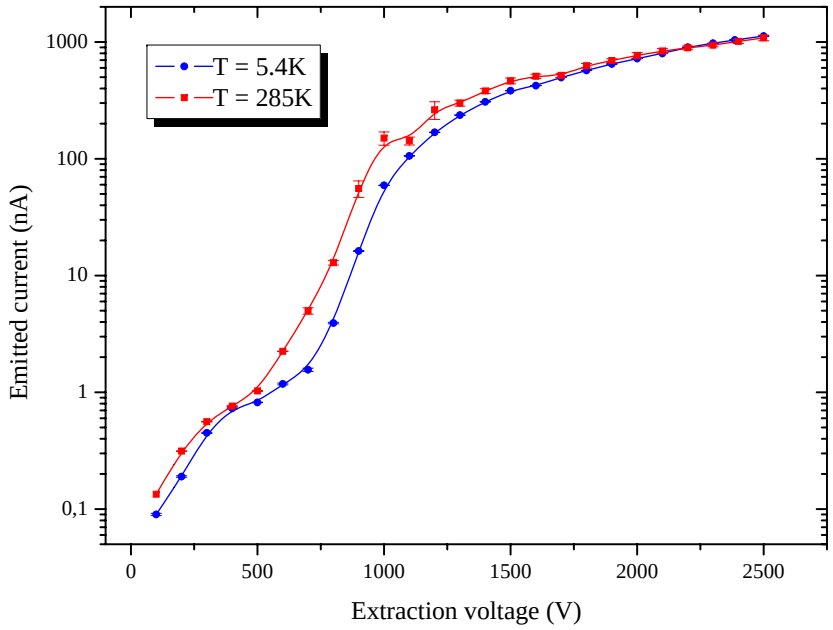

Figure 5.19: I-V measurements taken at 5.4 K and 285 K. As expected from the dominant power of ϕ with respect to ε_F in equation 5.57, the emitted current increases with increasing temperatures. Note: the solid line has been added to guide the line, it represents no fit.

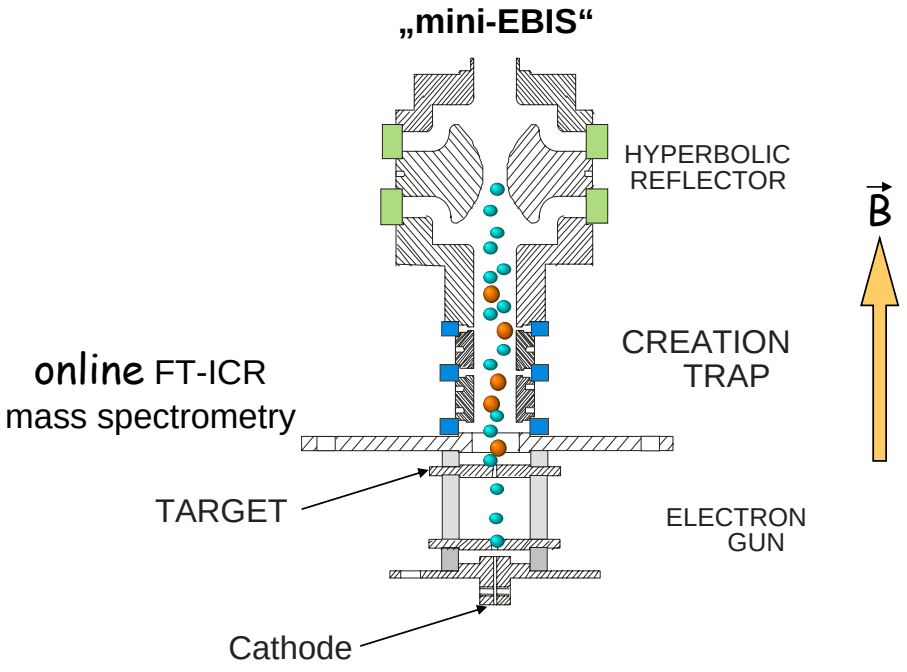

Figure 5.20: Overview of the electron gun and the Creation trap.

creation of ions, come the three electrodes conforming the *Creation trap*, described in detail in section 6.5, but whose relevant characteristic at this point is that it is able to store positively-charged particles. Finally, there is a hyperbolically-shaped *reflection electrode*, to which a high, negative voltage can be applied in order to create a potential wall from which the electrons coming from the cathode bounce back towards the target. The reason for such geometry is to maximize the electric-field gradient without physically blocking the path.

In order to properly understand the ion-creation process it is necessary to be familiarized with the voltage configuration in the setup. The target is always grounded via a 28 MΩ resistance. The rest of the voltages are negative, so the target represents a potential minimum for the negative electrons. The FEP is set to a negative voltage which determines the energy of the electrons as they pass through the target and, in very good approximation, through the Creation trap. Regarding the acceleration electrode, if the electron gun is off, it will lie at the same voltage as the FEP, while for turning it on it is set to a less negative voltage. The voltage difference between the FEP and the acceleration electrode determines the intensity of the electron beam. Thus, we count on a tool with which one can tune the energy and current of the electron beam. Finally, the voltage applied at the reflection electrode is always 10 % more negative than that at the FEP, ensuring that no electrons can overcome its barrier and that all of them are reflected back down.

So let us assume that the electron gun is suddenly turned on (the voltage at the acceleration electrode is suddenly increased). Then, electrons (drawn in blue in figure 5.20) start to tunnel out from the array. They follow the magnetic-field lines through the holes in the acceleration electrode and the target until the reflection electrode, where they feel the repulsive field and are forced to turn back. As they oscillate around the potential minimum at the target, more and more electrons tunnel out, increasing the Coulomb repulsive forces between the electrons and, therefore, making the diameter of the electron beam grow further. Once it is wide enough, it will hit the surface of the target, evaporating atoms and ions of calcium (marked in red), but also of carbon and impurities, into the Creation trap. There they will be confined and further ionized by the electron beam, and, so, the charge-breeding process takes place.

Isotope	Abundance
^{40}Ca	15.78 %
^{42}Ca	0.18 %
^{43}Ca	0.07 %
^{44}Ca	1.27 %
^{48}Ca	82.7 %±1.1 %

Table 5.1: Abundances of the different calcium isotopes in the target.

5.3.2 Required electronics

The main electronic tool required to drive the electron gun is a high-voltage supply capable of feeding the FEP, the acceleration electrode and the reflection electrode. Although there are many multichannel high-voltage-sources available in the market,

the special requirements of a setup with which to perform an ultrahigh-precision measurement of the *g-factor* led us to designing a home-made device. The main restriction comes from the fact that ground loops need to be avoided, and that lines need to be kept short in order to prevent them from picking up radiofrequency noise. Therefore, the high-voltage supply, or *HV-box*, is connected at the hat (see section 3.2.1).

Figure 5.21 shows the schematics of the supply board. It has two main components which create the high voltages out of two low voltage inputs: the C80N and the GP60 modules, both from EMCO.

The C80N has an output voltage ranging from 0 V to -8 kV, proportional to an input between 0 V and +5 V. This is the negative voltage supplied at the reflection electrode. Then, it is voltage divided to 90 % and sent to the FEP. A second voltage divider (50 %) provides the voltage to the so-called *auxiliary-voltage* line. This line is physically the outer conductor of the coaxial cable which travels through the isolation vacuum, from the hat to the UMF (figure 3.3). There are two arguments regarding the choice of high-voltage cables which act one against the other: on the one hand, the cable needs to withstand a high voltage without breaking up, so a thick cable is preferred in this sense; on the second hand, the thermal conductivity needs to be kept as small as possible in order to diminish the evaporation rate of the liquid helium, which requires a thin cable. The second condition is actually more stringent, since the outer conductor need not be grounded. Rather, it can be set to a negative voltage, making the voltage difference between inner and outer conductors smaller, but still being able to supply the maximum voltage and not representing a huge heat load. Finally, there is a last voltage divider of 1:1000 in order to monitor the voltage supplied at the high-voltage lines with any conventional voltmeter.

The GP60 outputs 0 V to +6 kV for an input voltage between 0 V and 12 V. This voltage is referenced to the voltage at the FEP, not to ground, and it is applied directly at the acceleration-electrode line in order to produce the voltage difference required to extract electrons from the array of field-emission points (see figure 5.21).

The HV-box was first characterized as a stand-alone device, disconnected from the hat, the lines and, thus, the high-voltage electrodes. Figures 5.22 through 5.24 show the behavior in this situation. Measuring high voltages in such a board is not trivial due to the enormous resistances in the order of hundreds of MΩ sputtered on it. Conventional voltmeters (e.g. Fluke 189 or Voltcraft VC820) have inner resistances of 10 MΩ or 11 MΩ in their maximum range, so placing them in parallel to any resistance in the board will effectively almost shortcut the connection. A 1 GΩ resistor was therefore added serial to the voltmeter, and then the voltages were calculated back as if no extra-resistors had been present.

First, the GP60 was off and voltages were applied at the 0..5 V input to the C80N (see figure 5.21). The voltages were measured at the four outputs: reflection electrode, FEP, acceleration electrode and auxiliary voltage. One can see in figure 5.22 the clearly-linear performance of the module and that everything is as expected: the voltage at the FEP and acceleration electrode is exactly the same and close to 90 % of the voltage at the reflection electrode; and the auxiliary voltage is around half of the reflection voltage.

In order to test the behavior of the GP60, now the 0..5 V input was kept at 0 V, while a biasing voltage was supplied to the 0..4.3 V input. This voltage is divided by a 1 kΩ and a 1.5 kΩ resistor combination in order to be able to disable the

voltage remotely and/or manually with the use of diodes. Then a transistor is added through whose base-emitter junction the voltage is further damped by V_{BE}. The characterization of the low-voltage part is shown in figure 5.23. The point at which V_{BE} saturates is when the transistor is conducting, and only then it is expected to see that the GP60 receives an input and, hence, outputs a high voltage. This is observed in figure 5.24, where now the high-voltage was measured at the line of the acceleration electrode.

5.3.3 Measurements and discussion

Connecting the HV-box to the electron gun

Once the performance of the HV-box has been delineated, it needs to be tested connected to the electron gun in the ultrahigh-vacuum chamber through the high-voltage lines standing in the isolation vacuum. At first sight, one would expect no significant changes in its behavior. Since all electrodes are isolated from ground and from each other through MACOR rings, basically no currents are expected to flow which could change the properties shown previously (figure 5.22). Actually, measurements were carried out where the voltage at the FEP was kept constant and the voltage at the acceleration electrode was ramped. A current was measured in the FEP line indicating that there was electron emission. The shape of the I-V curves resembled exactly the ones measured while testing the electron gun, so for a typical result, see figure 5.13.

However, after making use of the electron gun on a daily basis during several weeks, huge currents in the order of micro-amperes could be measured in the acceleration-electrode line. This happened even when the electron gun was off, this is, when the voltage at the FEP and at the acceleration electrode was exactly the same. In order to find out where these currents leaked through, a series of resistance measurements were done between all high-voltage electrodes and ground, and also between each other.

Leakage resistances

In order to measure resistances of up to 1 TΩ, one can make use of a picoammeter. For these measurements, a Keithley 6487 was chosen. A few voltages were set between the two electrodes under study and the current was measured with the picoammeter. From the slope of these data, a value for the resistance was obtained. The results are summarized in table 5.2.

Specially noteworthy is the low value of 350 MΩ between the acceleration electrode and ground, and which clearly explains the leakage currents observed. A very plausible explanation for this small resistance is that the electrons impacting on the lower part of the target could have evaporated carbon from it which could have then stuck to the MACOR isolator. This would happen due to the fact that the field-emission-point array is larger in area than the hole of the target[10]. Hence, a thin layer of carbon would be responsible for the high conductivity between the acceleration electrode and the grounded target.

[10]It is also larger than the hole in the acceleration electrode, which will be of importance further in the text.

Electrodes	Resistance (MΩ)
Reflection elec. vs ground	11100
FEP elec. vs ground	8400
Acceleration elec. vs ground	350
Auxiliary line vs ground	20500
Reflection elec. vs FEP	18700
Reflection elec. vs Acceleration elec.	19700
Reflection elec. vs Auxiliary line	12100
FEP elec. vs Acceleration elec.	11900
FEP elec. vs Auxiliary line	27900
Acceleration elec. vs Auxiliary line	7700

Table 5.2: Leakage resistances in the high-voltage setup.

As a consequence of this obstacle, the forthcoming measurements were performed with the acceleration electrode grounded. Otherwise, the leak currents would have posed a heat load which would have increased too much the liquid-helium consumption.

Performance of the electron gun

The next step was to switch on the electron gun for a time ranging from a few seconds up to a few minutes and systematically search for ions in the Creation trap as explained in section 7.4.2. While in that task, we noticed a strange behavior of the HV-box outputs. A direct measurement of the voltage at the output of the C80N module yielded the results given in the left plot of figure 5.25. When the voltage reached a value of ∼1550 V, the slope changed drastically. The same kink is visible in the voltage-divider output of the HV-box (right plot of figure 5.25), and it was absolutely reproducible.

This puzzling effect seemed to indicate that above a certain threshold in the voltage at the output of the C80N, a new resistance came into play which changed all the dividers, since further measurements exhibited the same pattern on all outputs, as reflected in figure 5.26. The only element in the setup which changes its property drastically as a function of the voltage is the FEPA. On the other hand, the voltage at which the kink appeared, ∼1550 V, was approximately the outset above which the electrons tunnelled out massively. So it was predicted that this ghost resistance could actually come from the current going directly from the FEPA to the acceleration electrode, since, as mentioned before, the surface of the array is bigger than that of the hole spearing the acceleration electrode.

This prediction could in fact be tested by calculating back the value the resistance should have in order to fix the voltage at the divider output which was experimentally measured. This analysis, which of course included the influence of the leakage resistances listed in table 5.2, gave the results shown in figure 5.27. While there is no electron emission, the resistance is in the order of many GΩ, but above the familiar voltage of 1550 V, the resistance markedly decreased to a minimum of ∼140 MΩ.

It is now possible to calculate the voltage at the FEP as a function of the voltage

supplied by the C80N. Again the shape looks linear between 0 V and 1550 V, and then seems to saturate, meaning that the flow of electrons between the FEP and the acceleration electrode tries to pull together the voltage difference. By simply dividing the voltages obtained by the resistances calculated, one can compute the current flowing through the FEP-line, which is, in a very good approximation, the current emitted by field emission, since the FEP is well isolated from the rest of the electrodes. The results are plotted in figure 5.29.

Finally, the current can be measured as it flows from the acceleration electrode towards ground. Figure 5.30 shows the outcome of measuring simultaneously the current emitted from the FEP and that impacting on the acceleration electrode. The slopes and the offsets are due to the finite resistances. Obviously, the biggest part of the electrons tunnelling out of the points head towards the acceleration electrode.

Discussion and outlook

It was already shown in section 5.2.5 that a densely-packed array of field-emission points could fire only from the outermost tips (see figure 5.18). The fact that the difference in currents seen at the acceleration electrode and at the FEP are negligible, along with the fact that no ion signal was found even though a huge amount of hours were dedicated to it, seem to prove that we might have run into a configuration where none of the field-emission points located directly under the hole of the target is firing.

A solution to this problem would be to treat electrically the array as proposed by X.H. Liang *et al.* in [Lia06]. The idea is simply to increase the extraction voltage to a value where the emitted currents are more than an order of magnitude higher than those required, and have it emitting for several minutes. This results in a more homogeneous site-emission distribution (see figure 5.31), and is something that can be realized without need of re-opening the ultrahigh-vacuum chamber the electron gun is sitting in. However, it was shown that the voltage at the FEP is physically limited to around 1400 V, which is not high enough to apply this technique efficiently.

Therefore, a new setup is currently being prepared where the field-emission-point array will be smaller in size than the hole of the target. This will prevent the undesired flow of currents from the FEP to the acceleration electrode, and it will ensure that the electrons travel the way they are expected to, regardless of the position of the tips firing in the array.

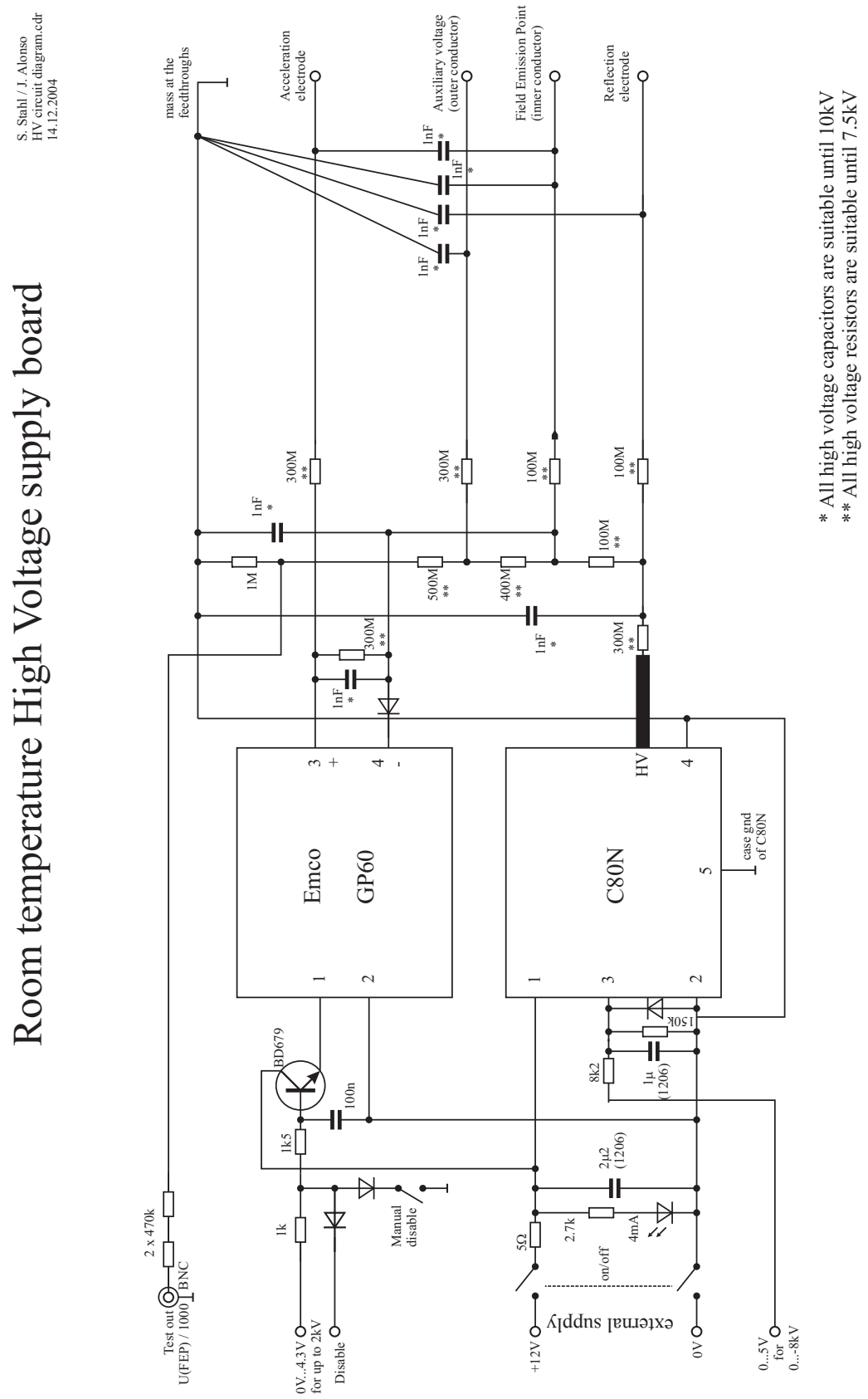

Figure 5.21: Schematics of the HV-box.

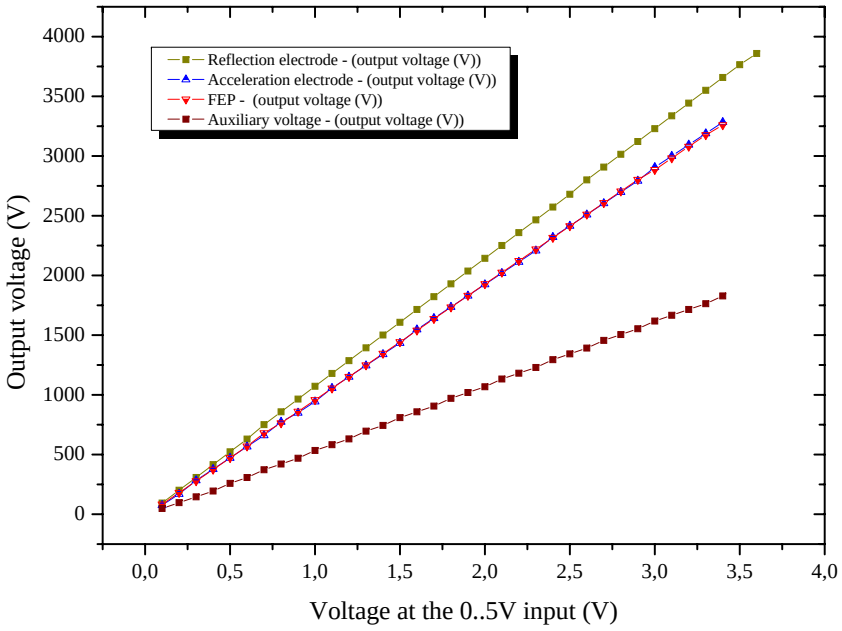

Figure 5.22: Characterization of the C80N module in the HV-box.

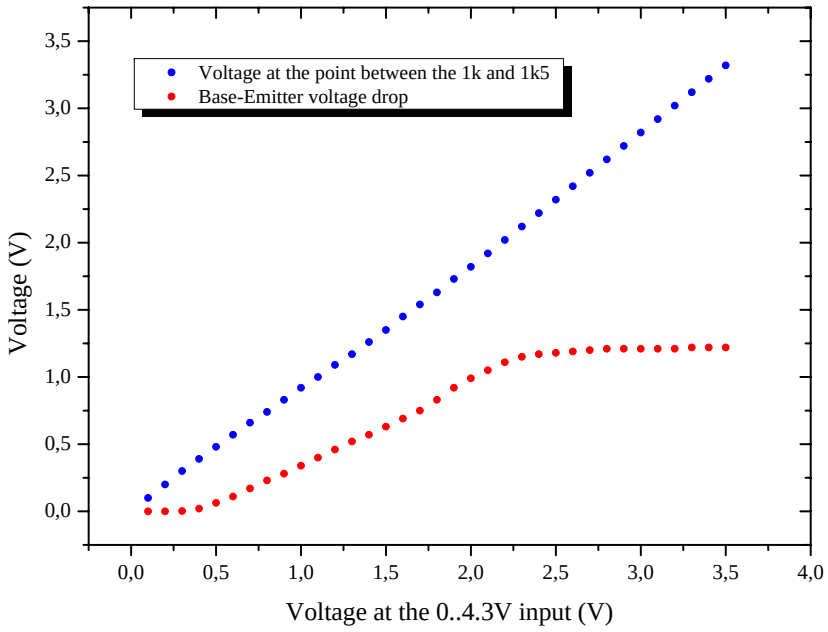

Figure 5.23: Characterization of the low-voltage side linked to the GP60 module in the HV-box. The saturation of V_{BE} occurs at an input voltage of $\sim$2 V.

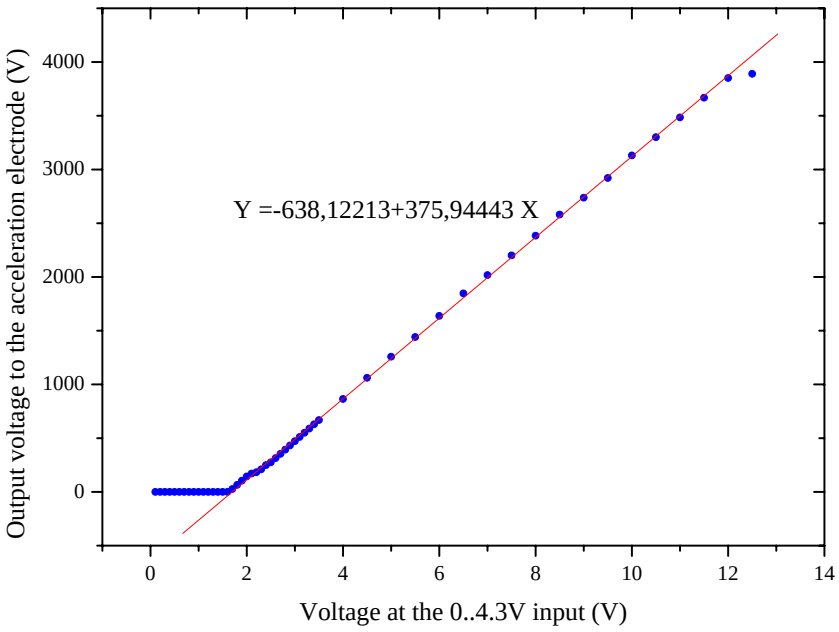

Figure 5.24: Characterization of the high-voltage side linked to the GP60 module in the HV-box. The GP60 starts to output a voltage when the saturation of V_{BE} is reached.

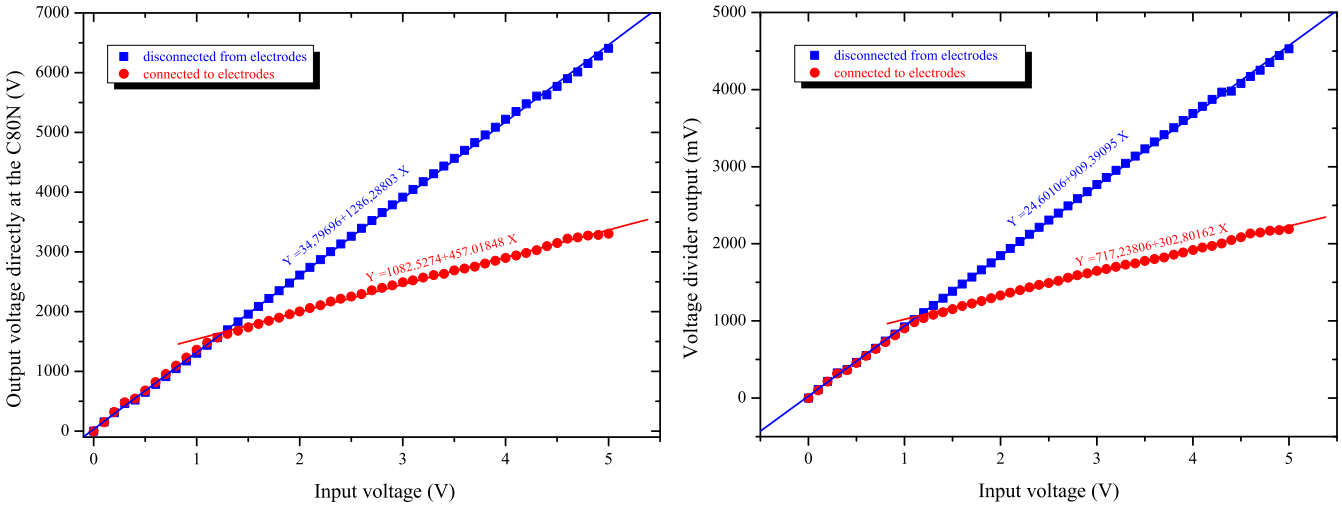

Figure 5.25: Characterization of the C80N module in the HV-box, once connected to the setup. The left plot shows the voltage directly at the output of the C80N as a function of the input voltage, while the right plot shows the voltage measured at the voltage-divider output.

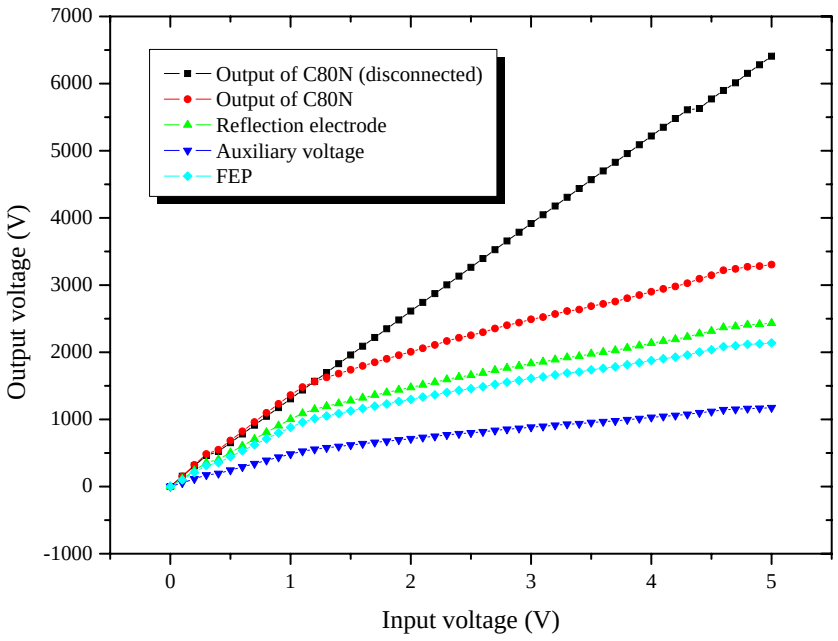

Figure 5.26: Characterization of all output channels from the C80N module in the HV-box, once connected to the setup.

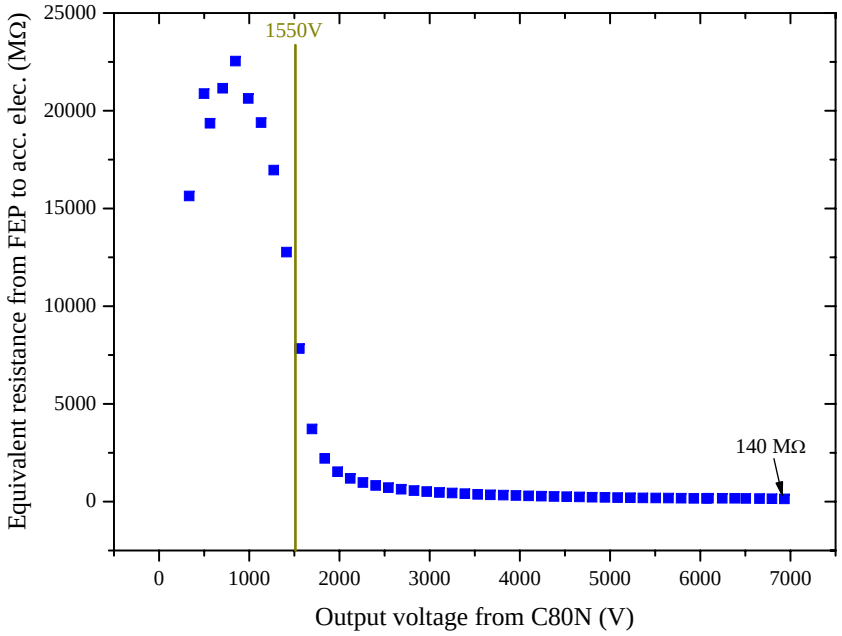

Figure 5.27: Equivalent resistance between the FEP and the acceleration electrode as a function of the voltage supplied by the C80N.

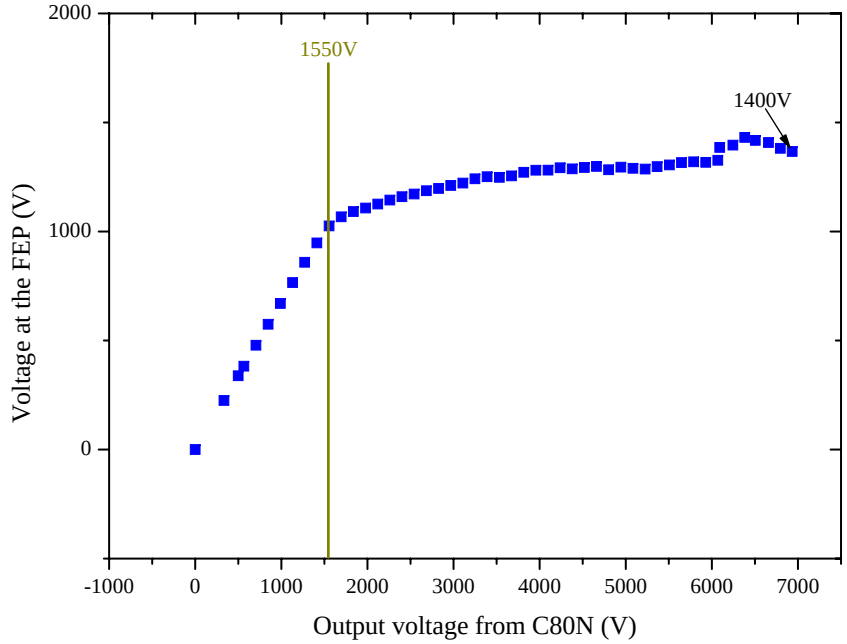

Figure 5.28: Voltage at the FEP during field emission.

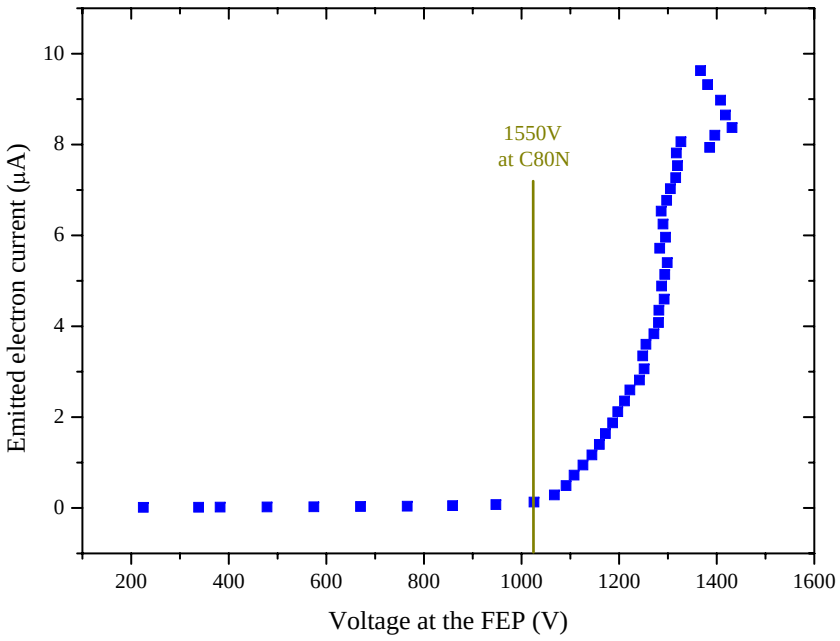

Figure 5.29: Current flowing through the FEP line during field emission.

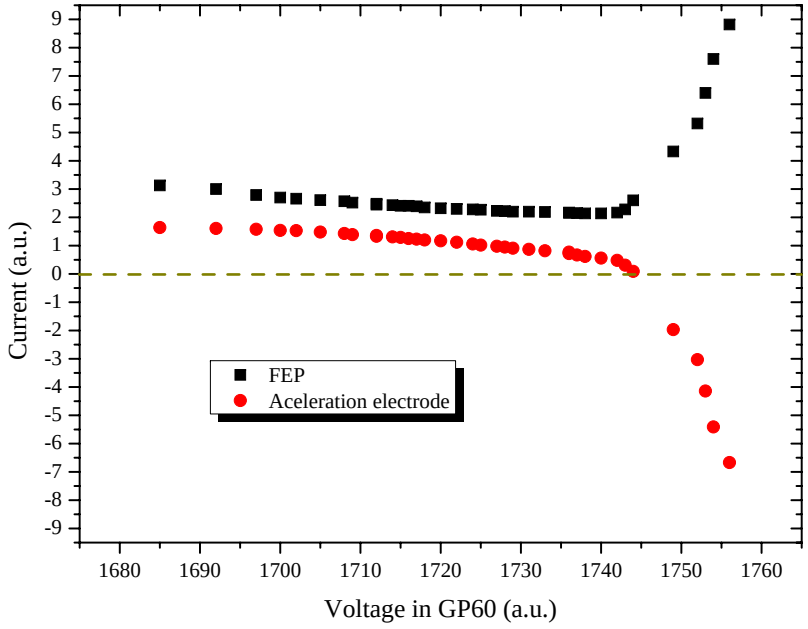

Figure 5.30: Current flowing through the FEP and the acceleration-electrode lines during field emission.

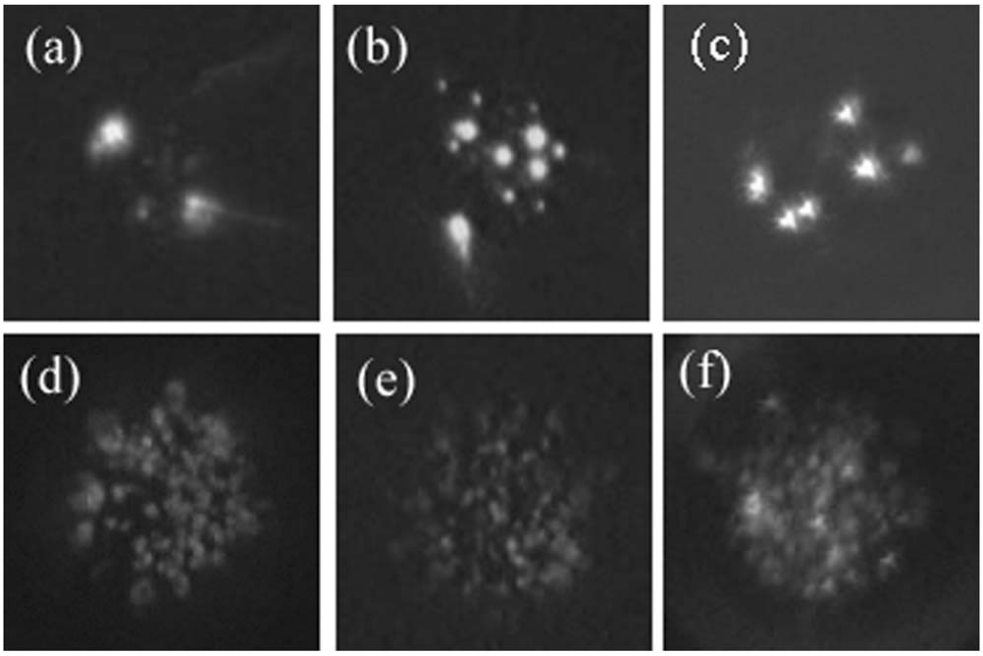

Figure 5.31: Array conditioning: emission site distributions in three FEPA. The measurements on (a)-(c) were taken before conditioning, each on a different sample, and (d)-(f) after conditioning. The treatment current was the same for all three cases. Picture taken from [Lia06].

Chapter 6

The triple-Penning-trap setup

"Any sufficiently advanced technology is indistinguishable from magic."

Arthur C. Clarke, Profiles of The Future (Clarke's third law).

6.1 Motivation

The pillars which determine the structure of the setup to perform a *g-factor* measurement have been already established:

- First, the magnetic field the ion is immersed in has to be obtained through the determination of the free cyclotron frequency, which, in turn, can be figured out from the measurement of the three eigenfrequencies of the ion in the Penning trap (see sections 3.1.2 and 4.5.2).

- Second, a mechanism with which spin-flips can be detected is necessary. In section 4.6 it was shown that a magnetic bottle, which couples the internal spin degree of freedom to the external axial frequency degree of freedom, would do the job.

- Third, the process of ion creation and charge breeding is an important issue, due to the high binding energy of the 1S-electrons, that can be tackled with an electron beam ion source, as described in chapter 5.

6.2 Overview

The three conditions given above can be fulfilled with three independent parcels in the setup:

- For a proper determination of the free cyclotron frequency a magnetic field as homogeneous as possible is required. The Penning trap for which this is the case in our setup is the so-called *Precision trap*.

- To facilitate a detection of the axial frequency jump due to a spin-flip in a magnetic bottle, the B_2 term needs to be enhanced as much as possible. This is achieved in the *Analysis trap* by placing a ferromagnetic ring.

- The charge breeding of ions with an electron energy up to 8 keV requires a deep-enough trap to hold the ions heated by the electron beam. Thus, the setup was provided with a *Creation trap*.

At this point, it is clear that the distinction of *triple-Penning-trap* setup is given for obvious reasons.

Figure 6.1 shows a technical overview of the setup. The UMF-flange is shown on top, and from it the stack of electrodes sprouts down. The first long electrode is used as a spacer to fix the center of the ring of the Precision trap exactly on the position of maximum homogeneity of the magnetic field. Then, the Precision trap is shown in blue. Below, two intermediate electrodes are placed with the function of separating the Analysis trap from the Precision trap so that the ferromagnetic ring of the first does not affect the homogeneity of the magnetic field in the latter. Later, in red, comes the Analysis trap, followed by the mini-EBIS conformed by an electron gun, the Creation trap and a hyperbolical reflector electrode, all of which are explained in a detailed manner in section 5.3. Also the relevant cryo-electronics are shown, including the detection and amplification electronics which will be introduced in chapter 7.

6.3 The Precision trap

The first natural remark is that a five-pole cylindrical configuration was chosen for the design of the Precision trap, for the reasons already justified earlier, in chapter 4. Actually, the electrode configuration has been left unchanged from that conceived for previous *g-factor* measurements and described in [Sta98]. Worth of mention are its two main characteristics: it is orthogonal, that is, it fulfills equations (4.21); and the c_4 and c_6 terms can be minimized by applying a tuning ratio between 0.87 and 0.90.

Regarding the machining, the decision of manufacturing all trap electrodes out of OFHC-copper and then gold-plating was taken upon the advantages that have been already mentioned in chapter 3. The correction electrodes were split into two halves in order to allow for the radial motion detection as described in section 7.1. Both parts are kept electrically separated by sapphire balls of 0.8 mm in diameter. Sapphire is a special modification of extremely pure aluminum-oxyde (Al_2O_3), and is also the material out of which the spacer rings used to isolate the electrodes in the stack from one another are made.

Both OFHC-copper and sapphire are diamagnetic in essence. Their magnetic susceptibilities are shown along with other characteristic properties in table 6.1. They are so small that their influence on the magnetic field is negligible when compared to the influence of the ferromagnetic ring of the Analysis trap. Also MACOR is shown for completion, since there are some isolators made out of it inside the trap chamber.

Further important requirements for the materials used in the trap chamber, other than a low magnetic susceptibility, are:

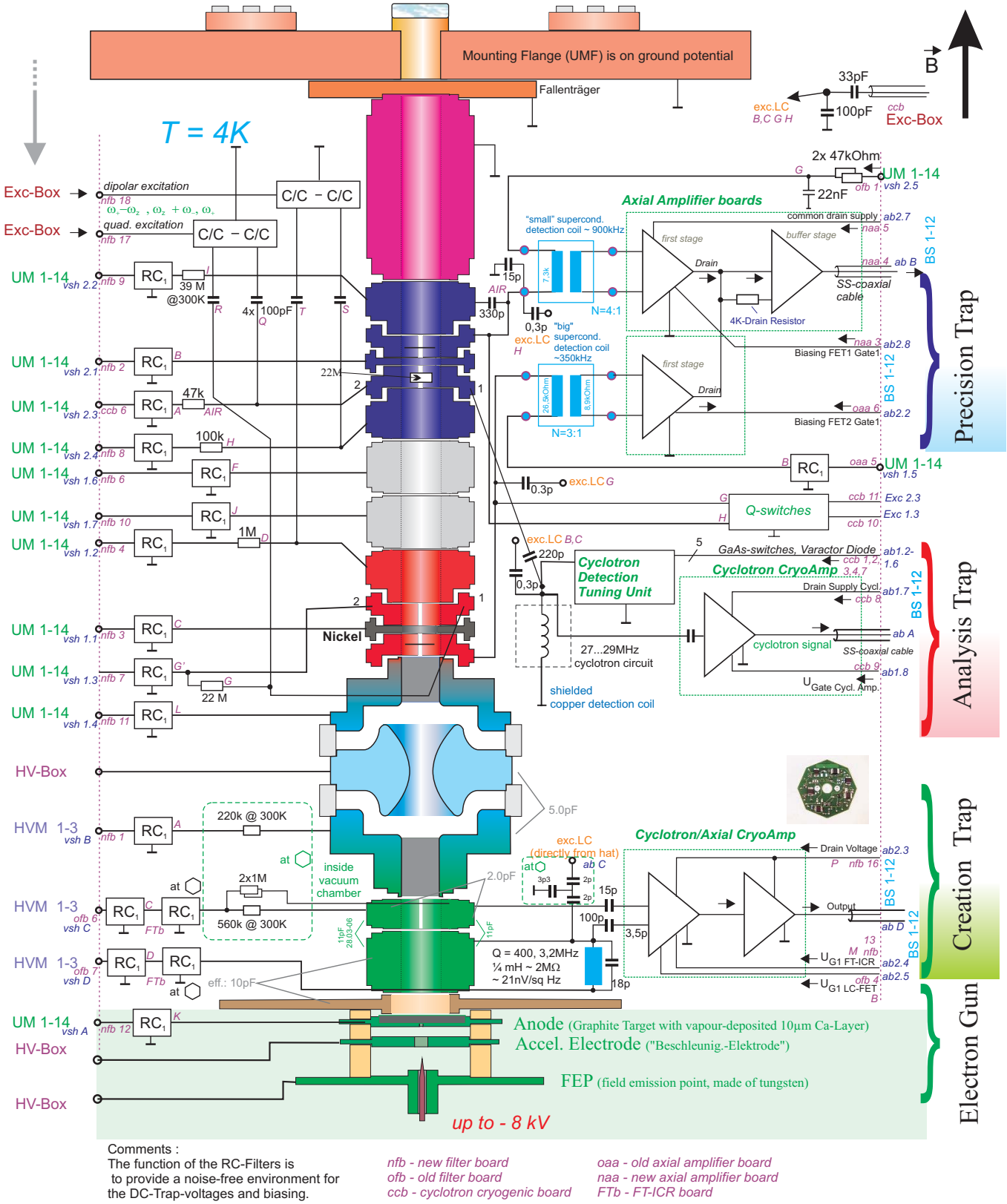

Figure 6.1: Overview of the triple-Penning-trap setup. The FT-ICR amplifier board and the detection coil, both sitting in reality inside the trap chamber, are not shown in this figure.

- a low dielectric constant in order to have small parasitic capacitances;
- a low resistivity for electrodes and cables and a very large one for isolators;
- the isolation between both parts of a split electrode must be harder than the electrode in order to avoid compression, and it must also contract less than the electrode when cooled down to 4 K to avoid possible shortcuts;
- a good thermal conductivity of all materials in order to ensure that all of them get cooled in a short time and that they all lie at the same temperature.

	ϵ_r	$\rho\,(\Omega{\cdot}\mathrm{m})$	Hardness	χ	$\alpha\,(\mathrm{K}^{-1})$	$\sigma\,(\mathrm{Wm}^{-1}\mathrm{K}^{-1})$
Copper	6	$16.78{\cdot}10^{-9}$	3	$-6.4{\cdot}10^{-6}$	$1.7{\cdot}10^{-5}$	400
Sapphire	10	10^{19}	9	$-2.1{\cdot}10^{-7}$	$8{\cdot}10^{-6}$	40
MACOR	6	$> 10^{19}$	4.5	$-3.8{\cdot}10^{-7}$	$7{\cdot}10^{-6}$	1.8

Table 6.1: Main mechanical, thermal, electrical and magnetic properties of copper, sapphire and MACOR: the dielectric constant ϵ_r; the resistivity ρ; the hardness according to the Mohs scale; the magnetic susceptibility χ; the thermal expansion coefficient α; and the thermal conductivity σ. All values are given for a temperature of 300 K. Although some properties change drastically, the ratio of the quantities between materials remains approximately the same.

6.4 The Analysis trap

The Analysis trap is, in essence, exactly the same as the Precision trap, since the frequencies of the ion in it have also to be very well defined. Thus, basically the same considerations in respect to design have to be taken into account. The difference is, of course, that the ring has to be ferromagnetic in order to create a strong enough magnetic bottle in the center of the trap. Nickel was chosen as the material it should be constructed out of, since the B_2 term it can induce on the magnetic field (for our configuration) amounts to $\sim 10\,\mathrm{mT/mm^2}$, producing an axial-frequency jump of $\Delta\nu_z \sim 190\,\mathrm{mHz}$ if the spin of a $^{40}\mathrm{Ca}^{19+}$ ion flips and $\Delta\nu_z \sim 160\,\mathrm{mHz}$ for $^{48}\mathrm{Ca}^{19+}$. The ring could have also been constructed out of a cobalt-iron alloy, whose saturation polarization is four times bigger than that of nickel[1]. This would have had the positive consequence that the axial jump would have been always larger than 600 mHz, much easier to detect, but jumps of 100 mHz are still detectable with the phase-sensitive technique (section 7.3) and this way the influence of the ring of the Analysis trap on the Precision trap is kept lower.

[1]The saturation polarization J_s of a material defines how much it can compress the magnetic field lines and, therefore, how strong the magnetic bottle can get. For nickel $J_s = 0.615\,\mathrm{T}$ and for cobalt-iron $J_s = 2.34\,\mathrm{T}$ [Kay].

6.5 The Creation trap

The need for a Creation trap is new with respect to previous *g-factor* measurements. Its design was carried out in the scope of J. Verdú's diploma thesis [Ver01] and its function is intimately linked to the electron gun and the reflection electrodes presented in section 5.3.

The purpose of the Creation trap is to have a volume for the ions to occupy while they are charge-bred by the electron beam. Thus, a superb harmonicity of the potential well is not required, in opposition to the case of the Analysis or the Precision traps. This allows for a 3-pole cylindrical trap instead of a 5-pole one.

As was the case for the correction electrodes of the other two traps, the ring of the Creation trap is segmented to be able to access it with an FT-ICR detection system (section 7.2) to make it possible to follow the charge-breeding process on real time.

Another important aspect of this trap is that it is sitting close to electrodes which will be set to high voltages of down to -8 kV. Hence, the endcaps have to be long enough so that the voltage minimum is properly protected by the 0 V to which they are set. Otherwise, the design of the Creation trap is straightforward.

Figure 6.2 shows a photograph of the electrode stack just after mounting and before cabling or adding the electronics which are attached below the electron gun and inside the ultrahigh-vacuum chamber. The upper conglomerate of electrodes is the Precision trap, separated from a second conglomerate (the Analysis trap) by the two bigger intermediate electrodes. The ferromagnetic ring of the Analysis trap is marked with a red flag. Below that, the bulkier part comprehends the lower endcap of the Analysis trap, the reflection electrode and the upper endcap of the Creation trap. Next come the remaining two electrodes of the 3-pole Creation trap and finally, completely at the bottom, the target and the electrodes of the electron gun.

6.6 Required electronics

There are mainly two kinds of electronic functionalities to be implemented regarding trapping: filtering the rf-noise, which could be picked up by the dc-lines travelling from the UMF to the hat, and supplying the required voltages to the stack of electrodes. The scheme shown already in figure 3.9 is used for the filtering purposes required, and not much needs to be added at this point. However, regarding the voltage supplies needed to feed the electrodes of the Precision and Analysis traps (which will have a maximum well-depth of 14.2 V) and of the Creation trap (which will be typically set to -100 V during charge breeding), an enormous amount of design and engineering work has been carried out in close collaboration with S. Stahl from Stahl Electronics.

6.6.1 Voltage supply for the Precision and Analysis traps - the UM 1-14

Figure 6.3 shows the main functionality that the voltage supply for the Precision and Analysis traps (and the intermediate electrodes) must have. On the one hand, ultrahigh-precision measurements as the ones planned for this setup must count on

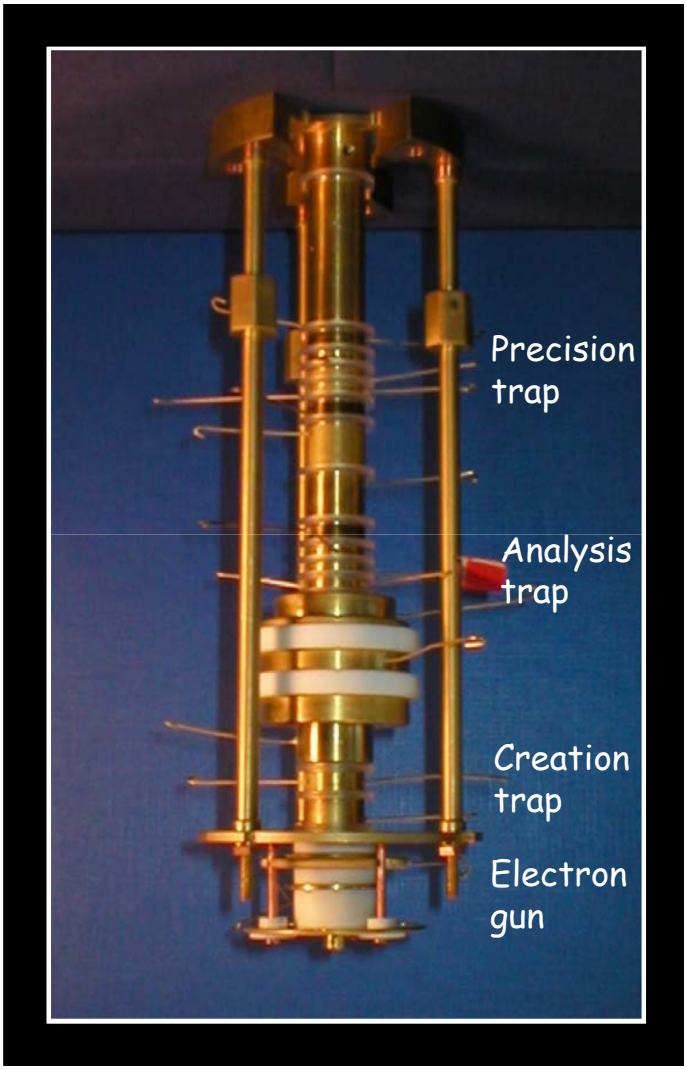

Figure 6.2: Picture of the triple-Penning-trap setup before cabling and implementing the in-chamber electronics.

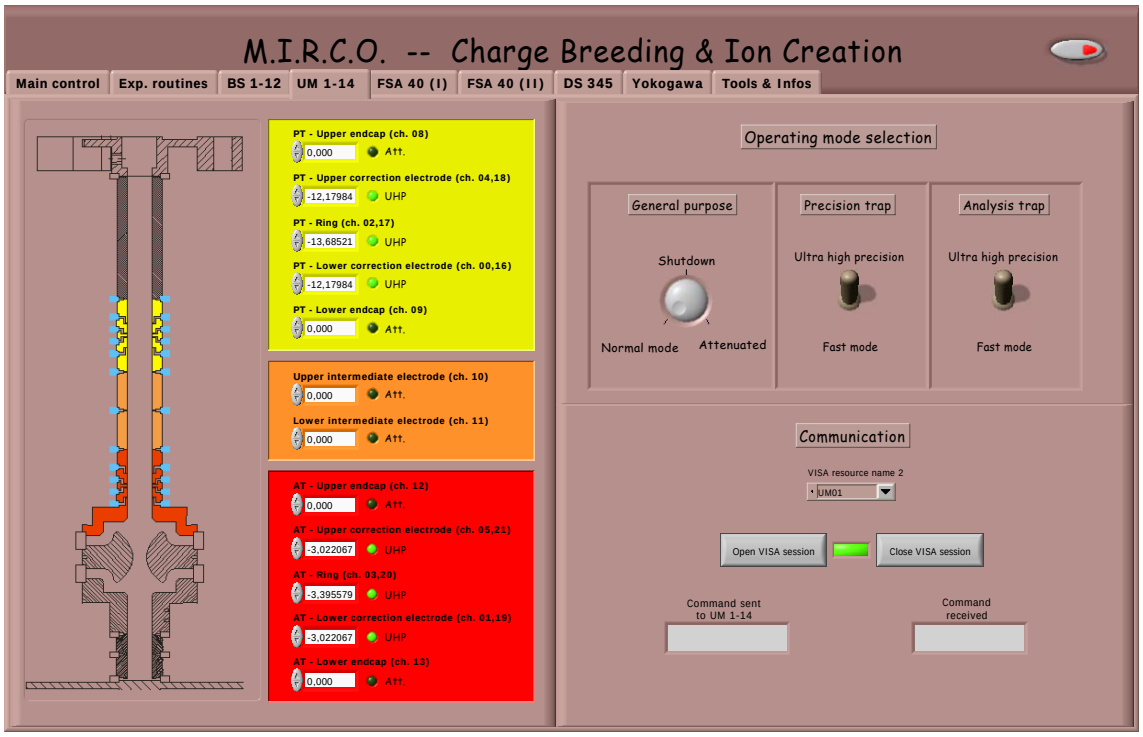

Figure 6.3: Capture of the control-software tab which handles the ultrahigh-stability 25-bit voltage supply for the trap electrodes (UM 1-14 from Stahl Electronics).

an extremely stable and accurate voltage source in order to ensure the proper control and reproducibility of the environment which surrounds the ion.

For the frequency of $\sim$ 1 MHz characteristic of the axial motion in the Precision trap, typically voltages of $\sim$-12 V must be applied at the ring electrode. To that end, the UM 1-14 was developed in a joint-collaboration with the company Stahl Electronics. It is equipped with six output channels with 25 bits of resolution each (30 ppb) giving a maximum of -14.2 V. These six channels cover the connections to the ring and correction electrodes of both traps. In reality, only three of these channels are independent, since during the experimental measurements it is of interest to control the trapping voltage of only one trap at a time. Thus, there are three highly-stable voltage dividers of a factor of 4.030303 between the channels going to the Precision trap and the ones going to the Analysis trap, where a lower axial frequency of $\sim$300 kHz is preferable to make the spin-flip detection easier, corresponding to a typical voltage of $\sim$-2 V.

On the other hand, the endcaps and intermediate electrodes will be typically grounded, so there is no need to apply an extremely stable voltage to them. The UM 1-14 counts, therefore, with 16 outputs each with a resolution of 16 bits and yielding a maximum voltage of -12 V. Four of these lines go to the already mentioned electrodes. Another six are to go to the rings and correction electrodes. The reason is that the 25-bit channels require a stabilization time of several seconds and are filtered with very low corner frequencies which make the time required to go from one voltage to another very large. This is inconvenient for the ion transport required during the *g-factor* measurement routine (see appendix A), for instance. Thus, there

are internal switches in the UM 1-14 to select between the ultrahigh-precision mode (UHP or 25-bit mode) and the fast (16-bit mode) in each of the traps (upper-right switches in figure 6.3). The remaining four lines are spare.

In the figure there is yet another control, a knob-selector situated left from the switches just described. This is for choosing an operational mode for the UM 1-14 between: normal, attenuated and shutdown. Normal mode will be the option usually selected. In shutdown mode, all 16-bit channels are grounded simultaneously, which reduces the consumption of the device. Finally, the attenuated mode can be selected if, as will be convenient for certain experimental procedures, one wants to shift slightly and in a controllable way the potential minimum from the center of trap. Then, instead of grounding the endcaps, they are connected via a big impedance to ground enabling the possibility of applying voltages from 0 to 28 mV in steps of 500 nV, with which the possibility of applying an asymmetric voltage configuration is opened. This brings about the opportunity to determine the B_1 and B_2 components of the magnetic field (equation 4.25) by shifting the position of the potential minimum in well-defined steps and measuring the cyclotron frequency. In addition, the high impedance versus ground diminishes the influence of the fluctuations of the latter on the potential seen by the ion.

6.6.2 Voltage supply for the Creation trap - the HVM-module

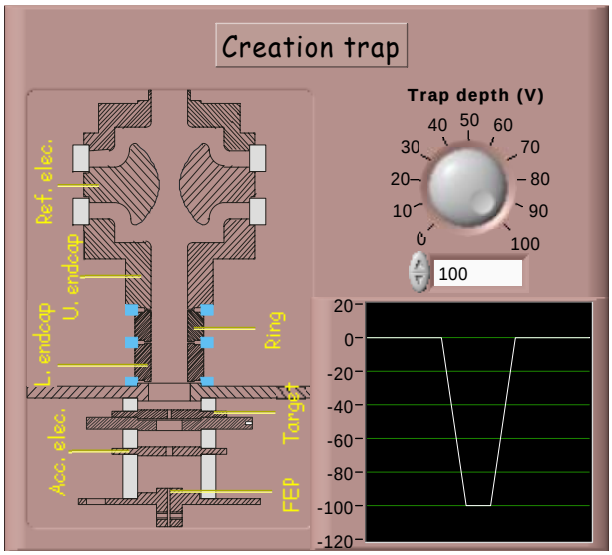

Figure 6.4: Capture of the control-software tab which handles the voltages at the Creation trap (HVM-module from Stahl Electronics).

The charge-breeding process requires a voltage depth in the Creation trap of around -100 V (see figure 6.4). Hence, a device other than the UM 1-14 is needed. To that end, the HVM-module from Stahl Electronics was developed. It is capable of delivering the three independent voltage outputs required for biasing each of the electrodes in the trap. In this case, it is a completely analog design, since there is no need for high harmonicity in the potential seen by the ions in the Creation trap,

based on three internal sub-circuits which amplify a low-voltage input (0 V to 10 V) to a negative medium-voltage output (0 V to -200 V).

6.6.3 Summary

Table 6.2 shows a summary of the modules used as supplies for the different electrodes of the triple-Penning-trap setup as well as of the voltages delivered by these modules and the resolution they can reach.

	P.&A. traps			**C. trap**		
	Ring	Corr. elec.	Endcaps	Int. elec.	Ring	Endcap
Module		UM 1-14		UM 1-14	HVM	HVM
V_{min} (V)	-14.2 / -12	-14.2 / -12	-12 / -0.028	-12	-200	-200
Resol. (bits)	25 / 16	25 / 16	16 / 16	16	an.	an.

Table 6.2: Characteristics of the voltages supplied to the electrodes of the triple-Penning-trap setup. For the ring and correction electrodes of the Precision and Analysis traps, the first number given is for the UHP-mode and the second for the fast-mode. For the endcaps, the first number given is for the normal mode and the second for the attenuated mode. Here, "an." stands for "analog".

Chapter 7

Detection of trapped charged particles

"You cannot depend on your eyes when your imagination is out of focus."

Mark Twain, A Connecticut Yankee in King Arthur's Court.

As in every other field of experimental physics, in trap physics the detection systems can be catalogued into *destructive* and *non-destructive*. In the first case, the particles are ejected from the trap (either by lowering the potential of one endcap electrode or by application of a voltage pulse of high amplitude) and then detected. A non-destructive detection scheme detects while the particles are orbiting. The main advantages of a non-destructive technique are the possibility of performing a continuous detection and, of course, that the ions are not lost, i.e. a reloading of the trap is avoided. One can get statistics by time-averaging, while with a destructive detection system the statistics are achieved by multiple repetition of the experiment, including loading the trap with ions. For an overview on the many detection systems used in the trap community around the world, see [Maj04].

A possibility to detect non-destructively is via the so-called *bolometric* detection. The idea was first described in [Deh62, Deh68], and it was successfully used in [Chu69]. A bolometric detection is based on the pick-up of the electric signal that the motion of the ion induces on the electrodes of the trap. Such a signal is very weak, so it needs to be amplified as close as possible from the trap to avoid external noise (already at the cryogenic stage shown in section 3.2). A very advantageous possibility is to use an electronic parallel resonant LC-circuit (or *tank circuit*), since it enables also the possibility of cooling the particle while detecting it, as will be discussed in section 7.1.

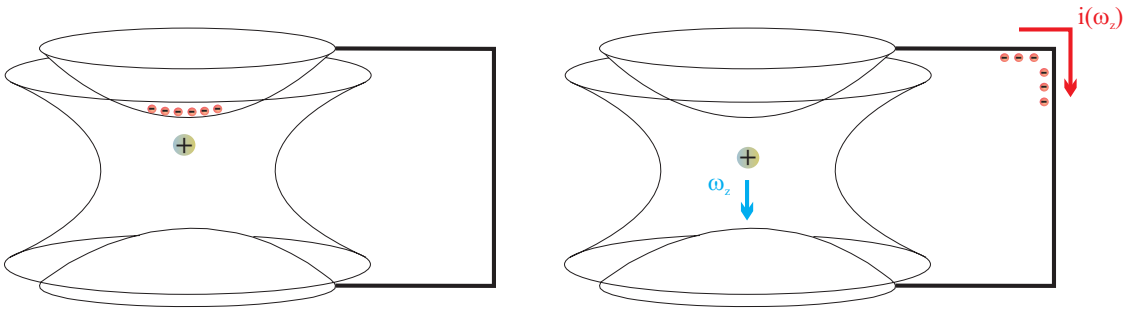

Figure 7.1: The axial oscillation of the ions induces an image charge current of the same frequency as that of the ion.

7.1 Narrow-band bolometric detection and resistive cooling

7.1.1 Interaction between a trapped ion and the attached electronics

Let us consider the circuit shown in figure 7.1, where the endcaps of a hyperbolical Penning trap are shortcut. The ion[1] is oscillating axially with a frequency ω_z due to the dc-voltage applied between the ring and the endcap electrodes, as was shown in chapter 4. When the ion approaches one of the endcaps, its positive charge will attract the negatively-charged electrons at the endcap. As the ion continues its way to the other endcap, the electrons will try to meet its positive charge, so they will travel through the cable until the other endcap. Hence, an oscillating charge in the trap creates a variable-induced image current, whose frequency is exactly that of the ion. This was already first studied by Shockley in 1938 [Sho38].

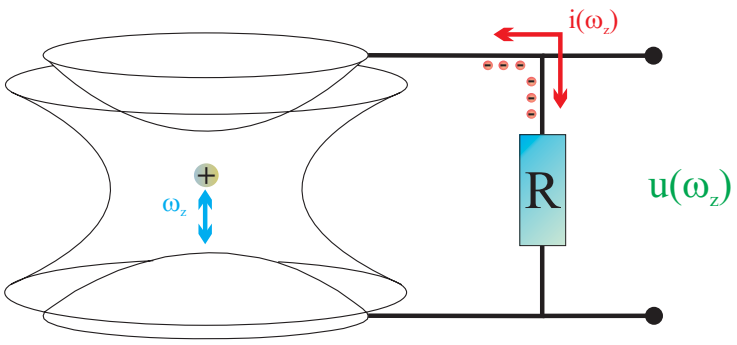

Figure 7.2: The induced image current will create a voltage difference when passing through an impedance. This voltage difference can be easily measured and Fourier-transformed to yield a visible signal at the ion's axial-oscillation frequency.

[1] Although the following argumentation will be inferred to an ion, it is straightforward to generalize it to any charged particle and also to a group of charged particles.

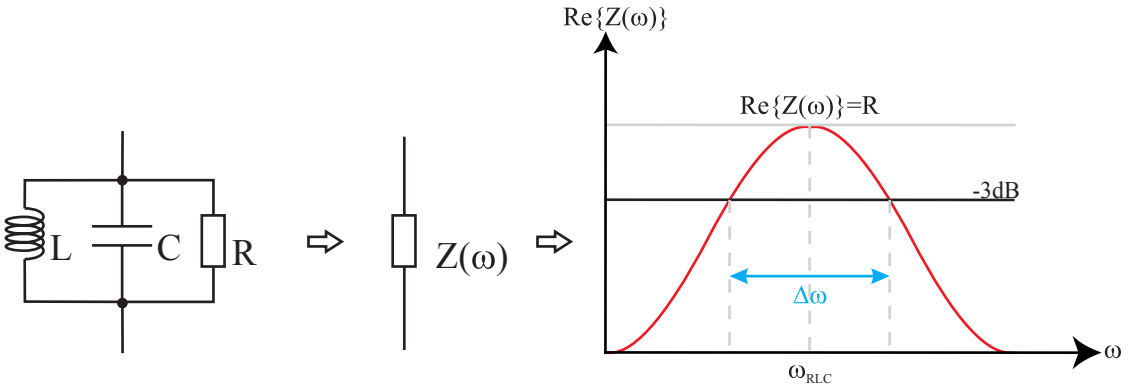

Figure 7.3: Equivalent circuit for a real tank circuit consisting of a resistor added in parallel to the capacitor and the inductance. At the right, the characteristic resonant shape for the real part of the overall impedance $Re\{Z(\omega)\}$ is shown. The characteristic parameter of the resonance $\Delta\omega$ is the width of the curve 3 dB below the maximum.

One can use this image current to create a detectable voltage simply by placing a resistance between the endcaps (figure 7.2). At this point, already one has built a very simple detector, but perhaps the most important characterizing quantity of any detector is the signal-to-noise ratio (S/N). A possibility to enhance the S/N of the bolometric detector in figure 7.2 is to implement a frequency-dependent resistor, which shows a very high resistance at the frequency of the ion which is to be detected, thus creating a big voltage drop for that frequency, and a very small impedance for any other frequency, which will damp the background noise level. A tank circuit (figure 7.3) shows exactly the desired behavior, and it is the basis upon which the bolometric detection is realized.

Although what has been shown until the moment applies to the axial degree of freedom, the radial components of the motion can be detected with an analogous setup if one splits an electrode as depicted in figure 7.4.

A suitable way of observing the detected signal is to perform a Fast Fourier Transform (FFT) of the time-dependent voltage measured at the tank circuit in the resulting frequency spectrum. This will yield a peak[2] at the ion's motional frequency. This technique is known as Fourier Transform - Ion Cyclotron Resonance (FT-ICR). For a complete review as well as an application for high-precision mass spectrometry, see [Bei95].

7.1.2 The trap as an effective capacity

In order to do a proper mathematical study of the interaction between the ion and the electronics attached to the trap, it is recommendable to first consider the trap endcaps as infinitely large planes separated by a distance D, so that the ion

[2] Actually, the signal can take either the form of a peak above the noise level or a dip shortcutting the background noise to ground at the ion's frequency. Whether one or the other is detected, depends on the ion's energy compared to the temperature of the tank circuit, as will be seen further in this section.

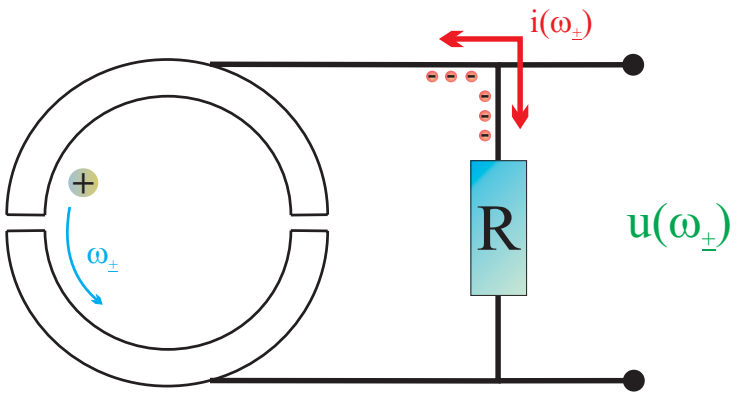

Figure 7.4: The radial oscillation of the ions induces an image-charge current of the same frequency as that of the ion.

would actually be oscillating inside a capacitor. The plates of the capacitor will be considered to be perfectly conducting. Then, the induced current, $I_{ind} = \frac{dQ}{dt}$, can be expressed as the change in the charge when the ion moves from one plate to the other ($dQ = q$) divided by the time it takes to perform this half-cycle at a velocity $\dot{z}$ ($dt = \frac{D}{\dot{z}}$).

The endcaps of a Penning trap are obviously not the plates of an ideal capacitor. Thus, in order to obtain D, one can calculate the effective distance that there would be between the plates of an infinite-ideal capacitor, assuming the electric field would be the same as in the real configuration (a 5-pole cylindrical trap). To that end, a set of simulations for the axial case had to be performed in our case. The axial electric field, E_z, is found out in the center of a trap (with the software code SIMION 7.0) for a certain disposition of potentials applied to the electrodes. Then, $D = V/E_z$, where V is the voltage applied to the electrode where the signal is picked up.

In the case of the Creation Trap (figure 7.5), two different configurations were studied. On the one hand, a voltage of 1V was applied to the upper endcap, and then again the same for the lower endcap. The results are shown in figure 7.6.

For the Precision trap, very similar studies were performed, with the only difference that now this trap is a 5-pole trap. This gives, in principle, more possibilities to find the optimum electrode to attach the tank circuit. However, this trap is absolutely symmetrical, so the three combinations in figure 7.7 were explored.

Let us come back to these results once the relevance of having an effective distance D as small as possible is justified.

7.1.3 Electronic equivalence of an ion-trap system

Wineland showed in 1975 that an ion-trap system can be modelled by passive electronic components [Win75], which allows for a purely electronical treatment of the interaction between the stored ion and the electronics attached to the Penning trap.

One can start by considering the circuit at the left of figure 7.8, where the ion oscillates between the ideal plates of a capacitor (separated by a distance D) with an axial frequency ω_z. There will be two different forces acting on the ion: the harmonic

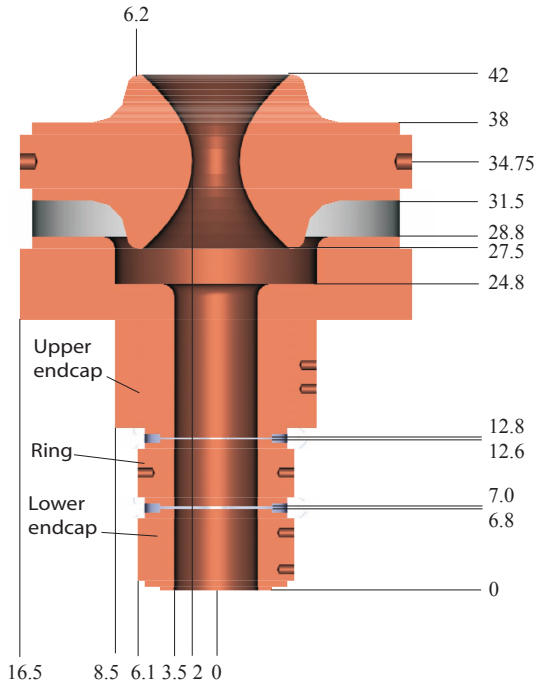

Figure 7.5: Scheme of the Creation trap. All distances in mm.

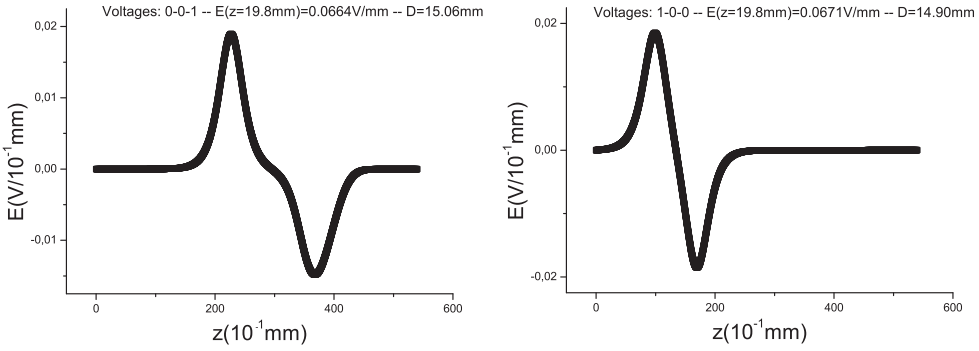

Figure 7.6: Axial component of the electric field in the Creation trap as a function of the axial position for a configuration where the lower endcap and the ring are grounded and 1 V is applied to the upper endcap (left) and where the upper endcap and the ring are grounded and 1 V is applied to the lower endcap (right). Note that the trap center is on z=19.8 mm for simulation convenience. The simulation yields D=15.06 mm and D=14.90 mm, respectively.

force which produces the axial oscillation (in the real configuration, the dc-potential applied between the ring and the endcaps), and the external drive depicted as $U(t)$ in the figure. Hence, the ion's equation of motion will be:

$$m\ddot{z}(t) = F_{U_0} + F_U(t) = -m \cdot \omega_z^2 \cdot z + \frac{q}{D} U(t). \tag{7.1}$$

As deduced before, the induced current is $I_{ind} = \frac{q}{D}\dot{z}$, so the external drive can be

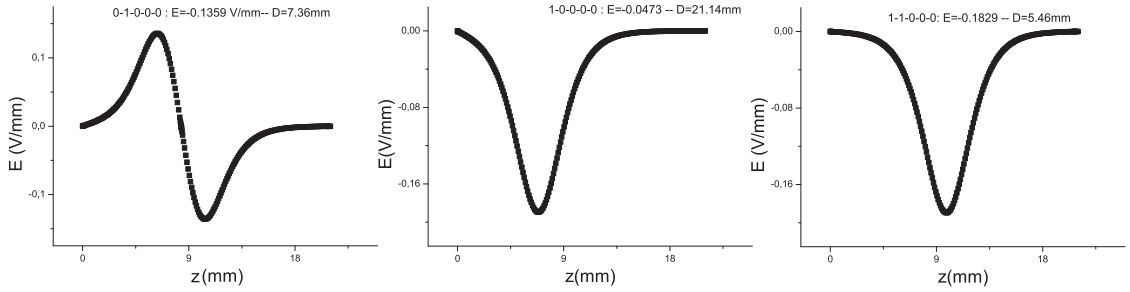

Figure 7.7: Axial component of the electric field in the Precision trap as a function of the axial position for a configuration where all electrodes are grounded except a correction electrode, where 1 V is applied (left); a configuration where all electrodes are grounded except an endcap, where 1 V is applied (center); and a configuration where all electrodes are grounded except a correction electrode and its adjacent endcap, where 1 V is applied (right). The simulation yields D=7.36 mm, D=21.1 mm and D=5.46 mm, respectively.

isolated, yielding

$$U(t) = m\frac{D^2}{q^2}\dot{I} + m\omega_z^2\frac{D^2}{q^2}\int I \cdot dt. \tag{7.2}$$

The first term corresponds formally to the voltage drop on a coil of inductance $l_{eq} = mD^2/q^2$ and the second one to a voltage drop on a capacitor of capacity $c_{eq} = m\omega_z^2 D^2/q^2$, so equation 7.2 is actually saying that an ion-trap system can be modelled by a serial LC-circuit, with a resonant frequency $\omega_z = \frac{1}{\sqrt{c_{eq} \cdot l_{eq}}}$.

To model real effects like the influence of the trapping potential inhomogeneities or the ion-ion interaction in case there is more than one ion in the trap (both of which result in a distribution of axial frequencies, $\Delta\omega_z$, rather than a Dirac-delta), one can add a serial resistance r (figure 7.8, right). For more details, refer to [Sta98].

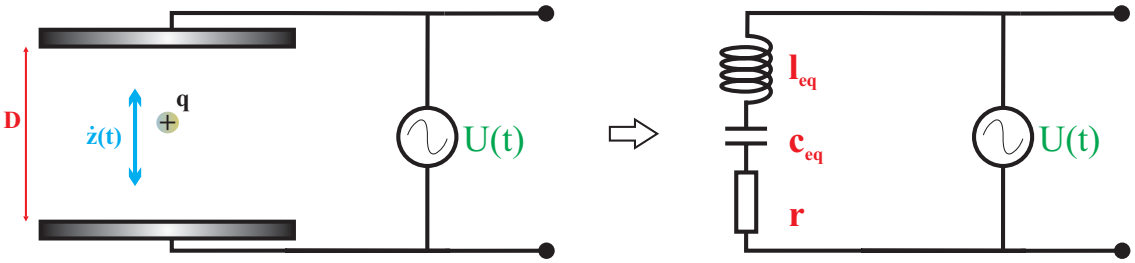

Figure 7.8: An ion-trap system can be electronically modelled by a serial RLC-circuit.

7.1.4 Resistive cooling of the ion motion

One should now consider how the equation of motion (equation 7.1) is affected by the presence of an impedance $Z(\omega)$, as sketched in figure 7.9. The current induced

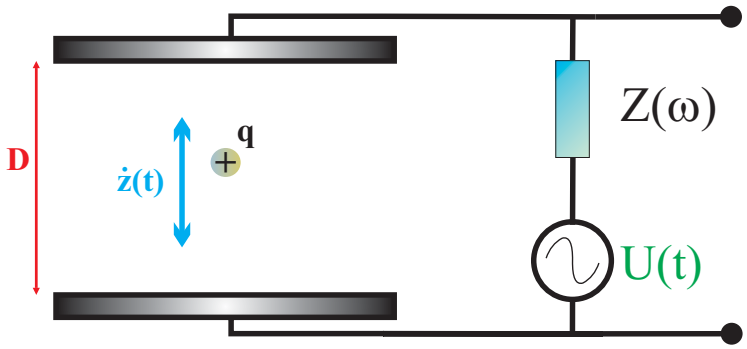

Figure 7.9: Ion-trap system connected to an impedance $Z(\omega)$.

by the ion will generate a voltage through the impedance, which will be fed back to the trap, generating a force on the ion:

$$F_{ind} = \frac{q}{D} I_{ind} Z(\omega) = \frac{q^2}{D^2} \dot{z}(t) Z(\omega). \tag{7.3}$$

Thus, equation (7.1) turns into

$$m\ddot{z}(t) = -m\omega_z^2 z(t) + \frac{q}{D} U(t) - \frac{q^2}{D^2} \dot{z}(t) Z(\omega), \tag{7.4}$$

which can be rewritten as

$$m\ddot{z} + \frac{q^2}{D^2} Z(\omega)\dot{z} + m\omega_z^2 z = \frac{q}{D} U. \tag{7.5}$$

This coincides with an equation for an harmonic oscillator of frequency ω_z driven by a force U and damped with a damping constant $\gamma = \frac{q^2 \mathrm{Re}\{Z\}}{mD^2}$. If one defines the cooling time constant as

$$\tau = \frac{1}{\gamma} = \frac{mD^2}{q^2 \mathrm{Re}\{Z\}}, \tag{7.6}$$

considers that there is no driving potential ($U(t) = 0$) and assumes that the ion is excited, after a few time constants it will have reached thermal equilibrium with the impedance Z, since power will be dissipated to the environment through Joule effect.

This process is called resistive cooling, and it can be used to lower the energy of the trapped particles to the physical temperature at which the impedance (the tank circuit) is[3].

The importance of being able to predict the value of the effective distance of the trap D has now become obvious, due to its influence on the time that the ions will

[3]Note that, throughout this work, the energy of a single particle will be often given in Kelvin. This might surprise the reader, since the temperature is a macroscopic magnitude and is, in principle, only defined for an ensemble of particles. However, if one measured many times the energy of an ion, the result would yield a Boltzmann distribution characterized by a temperature T which can be related to the energy E through the Boltzmann constant $k_B = E/T$. Therefore, one can talk about the energy of a single ion, and the ergodic principle sustains this possibility. For further details, read [Alo03, Dje04a, Dje04b].

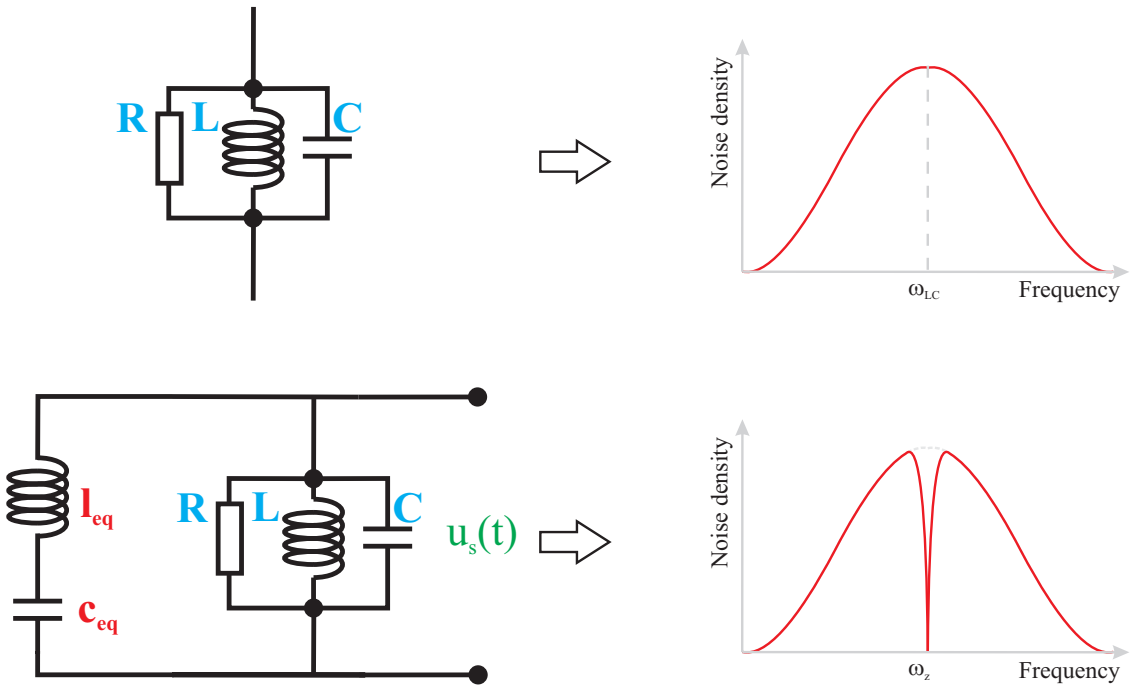

Figure 7.10: The Johnson thermal noise in a tank circuit takes a resonant shape (up). If there is a trapped ion in a Penning trap in thermal equilibrium with the tank circuit, then a dip appears in the spectrum at the frequency of the ion (down).

need to cool down (equation 7.6). At the view of the results in figures 7.6 and 7.7, it was decided to attach the detection and cooling tank circuits to the lower endcap in the case of the Creation trap, and to both an endcap and its adjacent correction electrode in the case of the Precision trap, very closely to the traps themselves.

7.1.5 An ion in thermal equilibrium with a tank circuit

The Johnson thermal noise in a resistor with resistance R at a temperature T can be approximated to be a white noise throughout the spectral bandwidth $\Delta\nu$ where the measurement is performed:

$$u_{R,eff} = \sqrt{4 \cdot k_B \cdot T \cdot \Delta\nu \cdot R}, \tag{7.7}$$

where k_B is the Boltzmann constant. This noise comes from the movement of the electrons in the resistor due to the fact that they are at a temperature above zero Kelvin [Joh28, Nyq28].

In the case of a tank circuit, the resistance is the real part of the impedance ($R = Re\{Z(\omega)\}$) and shows a resonant dependence with the frequency. Thus, the thermal noise will also be frequency-dependent (figure 7.10, up).

So let us go on to the circuit at the bottom of figure 7.10, which was demonstrated to be valid for an ion-trap system interacting with a tank circuit, and where the parasitic resistance r of the ion-trap system has been neglected for simplicity. The ion and the electronics are assumed to be in thermal equilibrium, and the ion's frequency ω_z is assumed to exactly match the resonance frequency of the tank circuit ω_{LC},

which can be achieved by properly tuning the trapping voltage. Since the voltage in a serial LC-circuit is the same as in a parallel LC-circuit but phase-shifted by π, at $\omega_z = \omega_{LC}$ the voltage u_s drops to zero. Therefore, a dip will be seen in the frequency spectrum of the voltage at the frequency at which the ion is oscillating. From now on, this technique will be referred to as *dip detection*. If $r \neq 0$, the spectrum will be very similar, only the dip will not fully reach the ground level.

7.1.6 An ion excited above the thermal equilibrium

If the driving voltage $U(t)$ in figure 7.9 is no longer turned off, but rather it is tuned to a frequency close to that of the trapped ion, there will no longer be thermal equilibrium between the ion and the attached electronics. The ion will deposit energy on the tank circuit, therefore producing a peak on top of the spectrum, at the frequency at which the ion is oscillating (figure 7.11). This detection technique has been baptized as *peak detection*.

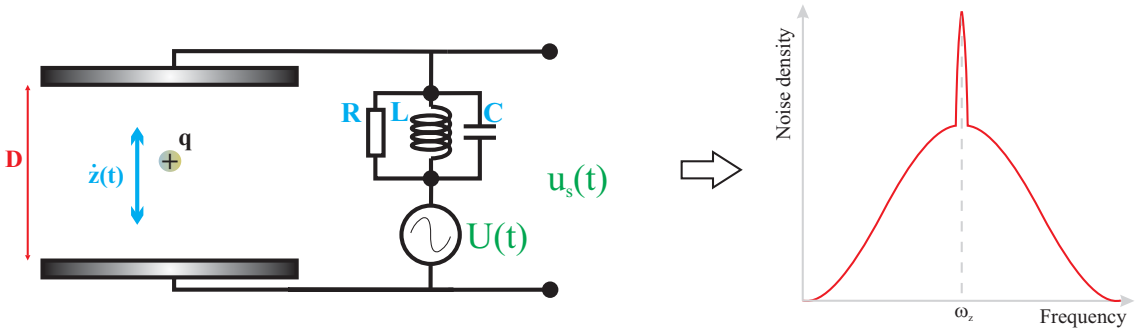

Figure 7.11: If the ion is not in thermal equilibrium with the tank circuit, the noise signal will yield a peak instead of a dip.

7.1.7 Considerations while designing a detection system based on a tank circuit

The detection electronics are dealt with in detail further in this chapter, but it is important to have in mind a few aspects concerning the necessities that have to be fulfilled by a detection system based on a tank circuit:

- If one wants to be able to use a dip-detection technique, the frequency of the ion needs to be very well defined, otherwise the parasitic resistance r in figure 7.8 would be too big and the dip would not be detectable. To have a well-defined frequency, the ion has to "see" an harmonic potential, which will be true if the amplitude of the motion is small enough. Therefore, the dip will be best seen if the temperature at which the trap and the electronics sit is low enough.

- To minimize the averaging time needed to see the dip appear in the spectrum, the ion has to be cooled to the temperature of the tank circuit as fast as possible. From equation (7.6) it is easily observed that the bigger the resistance

$R = Re\{Z(\omega)\}$ of the tank circuit, the faster the ion cools. That means that the LC circuit should be built with components which show very small parasitic losses.

- As was already stated above, a proper analysis of the effective distance D is necessary in order to find the best combination of electrodes to attach the tank circuit. The smaller D is, the smaller the cooling time constant.

- In order to achieve a big signal-to-noise ratio, the width of the resonance $\Delta\omega$ is required to be kept small, so the Q-value of the tank circuit needs to be as high as possible.

These conditions can be achieved experimentally by cryo-cooling the trap setup and the detection electronics (in this setup, to liquid helium temperature, 4.2 K). A high Q-value of the tank circuit is obtained by using a superconductive coil attached to the parasitic capacity between the two electrodes to which it is attached (or both parts of the split electrode in case a radial degree of freedom is to be detected).

7.2 Fourier Transform-Ion Cyclotron Resonance detection

If one needs a detector to observe a signal spread over a large frequency span, or several signals scattered in separated frequency regions, then tank circuits are not the option to go for. The width, in frequency, of a signal must be smaller than that of the tank circuit, otherwise the portion of the signal far from the resonance frequency would not be amplified, rather attenuated. On the other hand, as the number of interesting areas in the spectrum increases, so does the number of necessary tank circuits, reaching a point where it is no longer viable.

However, if the experiment does not require the ions to be in thermal equilibrium with the detector, one need not have a good quality factor of the detection electronics, since a small cooling time constant is not aimed for. Then, the detection would be a peak detection, as explained above. A hot enough ion would cease its energy to the detection electronics also if the Q-value were close to zero, meaning that, instead of a resonance, one would obtain virtually a flat response from the amplifier. If this were the case, one would no longer count on a tank circuit. Rather, it would be a resistor, whose amplification factor is the same regardless of the signal frequency and which would, therefore, serve as a broadband-detection system. This technique is well-known within the trapping community (refer, for instance, to [Bei95] and references therein), and it is named Fourier Transform-Ion Cyclotron Resonance or FT-ICR, in short.

7.3 Phase-sensitive detection

The last detection scheme needed for our *g-factor* measurement is the so-called *phase-sensitive* detection technique [Sta05]. It is most useful when trying to discern between two frequencies lying close one to the other, so it will be used to detect the small axial-frequency shifts due to spin-flips in the Analysis trap.

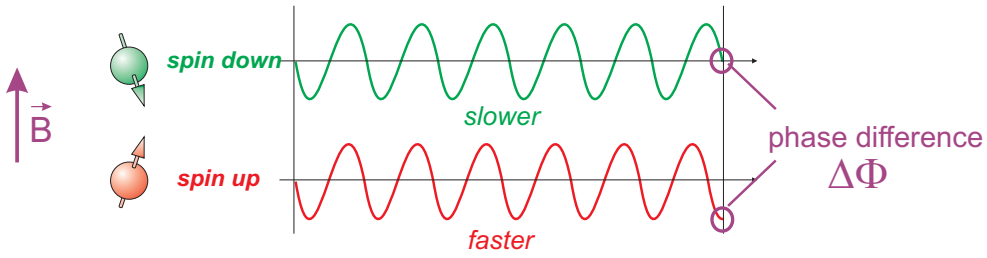

Figure 7.12: Principle of the phase-sensitive detection technique.

Its principle is sketched in figure 7.12. If two sinusoidal signals, of frequencies ν_1 and ν_2, are left to evolve, the difference between their phases $\Delta\Phi$ will increase with time:

$$\Delta\Phi = 2\pi t(\nu_2 - \nu_1) = 2\pi t\Delta\nu. \tag{7.8}$$

An FFT analysis of a time signal always yields two outputs, the amplitude and the phase, both frequency dependent. The detection time necessary to be able to resolve a frequency shift $\Delta\nu$ is $t_{det} = 1/\Delta\nu = 2\pi/\delta\Phi$, where $\delta\Phi$ is the uncertainty in the phase determination. A phase resolution smaller than 2π directly improves the time with respect to a direct measurement of the frequency, as long as $\delta\Phi < \Delta\Phi$, of course. Thus, in a sense, the Fourier limit, $\Delta\nu = 1/t_{det}$, is the worst case for a phase-sensitive measurement.

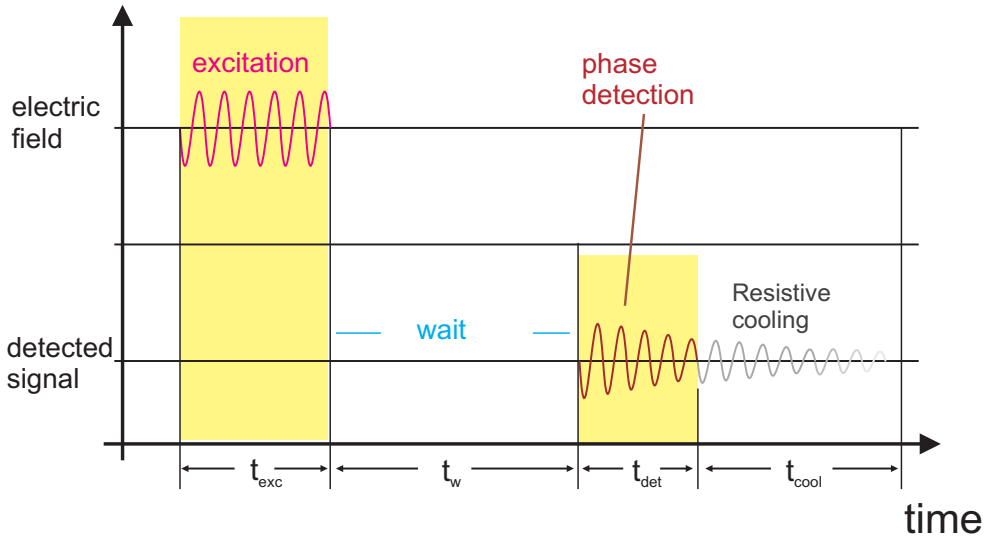

Figure 7.13: Time sequence of a phase-sensitive detection.

Figure 7.13 shows the time sequence of a phase-sensitive measurement. First, a well-defined excitation of duration t_{exc} is applied to the ion. This excitation must be strong enough to make sure that the initial phase of the ion is negligible and that the ion's motion is in phase with the burst. The ion is then decoupled from its environment. Then, it oscillates coherently and the phase evolves freely meanwhile. After a time t_w, the detection is performed. The detection system (a tank circuit,

for instance) interacts with the ion (t_{det}), and thus cools the ion. After performing the FFT analysis, the ion is further cooled due to the re-coupling to the cryogenic detection system.

The phase-detection technique has yet another important advantage compared to direct frequency measurements when trying to detect a small frequency jump. If this jump is really small, the frequency to be measured needs to be extremely well defined, meaning that the anharmonicities seen by the ion must be minimized. This is achieved, as described earlier in this chapter, by keeping the ion in thermal equilibrium with the tank circuit. And here is where the advantage of phase detecting shows up: the initial excitation burst heats the ion so much that the energy deposited in the tank circuit is very much above thermal contributions. Hence, the signal-to-noise ratio is increased by orders of magnitude, allowing for a much shorter observation time.

A similar detection technique was introduced by D. Pritchard *et al.* in [Cor89], the so-called PNP-technique.

7.4 Measurement of the cyclotron frequency in the Penning traps

Unlike the axial-frequency case, the cyclotron frequency needs not be measured in all three traps. It is important to know it in the Precision trap, since there all three eigenfrequencies have to be obtained in order to determine, via the invariance theorem (equation 4.22), the free-cyclotron frequency ω_c, needed to find out the *g-factor* in equation (3.3). The function of the Analysis trap is to serve as a means to detect spin-flips in their realizations as small axial-frequency jumps, so the cyclotron frequency is not a relevant observable there. Finally, in the Creation trap, the cyclotron frequency will play the main role within the FT-ICR scheme implemented in order to follow on-line the charge-breeding process during ion creation.

7.4.1 Precision trap

Signal pick-up

The electronic signal of the cyclotron motion in the Precision trap is picked up between the two parts of the split upper correction-electrode, following the procedure described in section 7.1.

It was pointed out in section 7.1.7 that the higher the Q-value of the tank circuit attached to the trap, the shorter the cooling time constant and the faster the characteristic dip of the signal becomes visible. Actually, if the cooling time constant is not short enough, the dip might never appear because the fluctuations in the frequency in a longer-term scale washes it out, leaving the only option of peak-detecting.

This is exactly the case of the cyclotron eigen-motion in the Precision trap. The quality factor of the tank circuit is intentionally limited. The reason is that, in order to be able to detect the cyclotron motion at all, the ion's frequency has to match the resonance frequency of the LC-circuit. However, the tuning possibilities when speaking about the cyclotron degree of freedom are negligible, since the magnetic

field is fixed and the voltage conforms only a minor part in the order of 1 ‰ of the absolute frequency.

Actually, there is a way of tuning the resonance frequency in a small range by changing the value of the capacity with a varactor diode and/or switches, as will be shown further in this section, but the effect is also limited. Therefore, the way of ensuring that the frequencies of the ion and the tank circuit match is by widening the resonance of the LC-circuit.

The physical way of limiting the quality factor is by using a normal-conducting material for the manufacture of the coil, instead of superconducting wire, such as niobium-titanium. Niobium-titanium is a type II superconductor whose critical temperature is close to 9.2 K and which can work in magnetic fields of up to 10 T [Tur89]. Hence, the cyclotron coil is wound 14 times with copper wire of 0.8 mm diameter and 99.99 % purity. The core is manufactured out of teflon, and everything is inserted into a metallic housing in order to minimize inductive as well as radiation losses [Gra97, Gra99]. The optimum ratio between the diameters of housing and coil body is of 0.55 [Sch94]. The reason for choosing teflon for the body is its small dielectric constant of $\epsilon_r = 2.1$ and small dielectric losses in the coil body. All in all, the coil is 8 mm×19 mm and the housing is 35 mm×69 mm (diameter×length). This construction yields a resonance frequency of 23.29 MHz and 24.28 MHz, and a quality factor of 65 and 304 at room temperature and 4 K, respectively (figure 7.14).

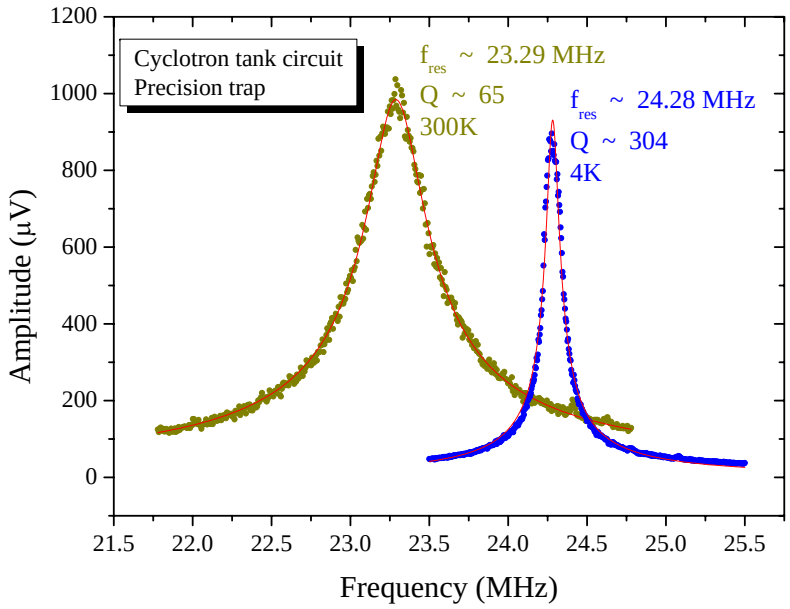

Figure 7.14: Resonance of the cyclotron LC-circuit at 4 K and 300 K.

Frequency selection

It was already mentioned above that trying to tune the cyclotron frequency of the ion is in vain since the magnetic field is fixed. In order to make a matching between the frequencies of the ion and the LC-circuit, the capacity of the latter can be varied. To

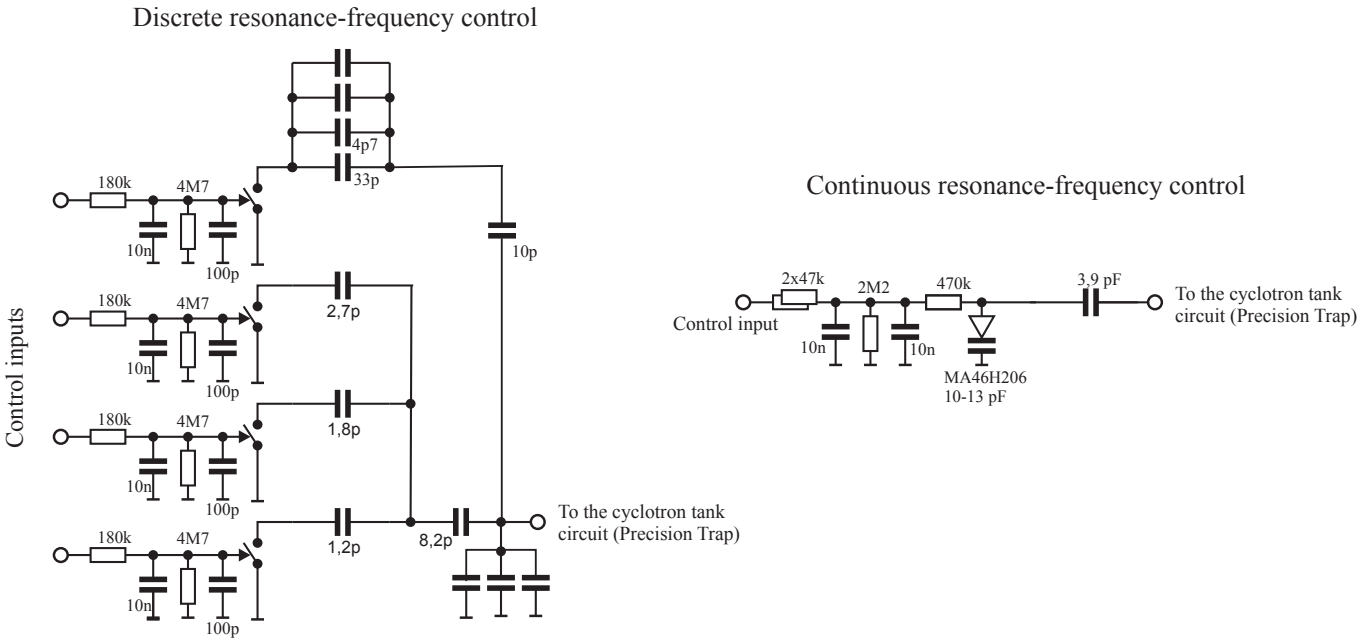

Figure 7.15: Schematic of the cryogenic GaAs switches for discrete control of the resonance frequency of the cyclotron tank circuit (left), and of the varactor diodes for continuous control (right).

that end, the setup has been equipped with a set of four different capacities (figure 7.15, left) which can be switched on or off by means of four GaAs (gallium-arsenide) transistors. This gives a discrete control over a range of ∼390 kHz (see table 7.1).

In order to fine-tune the frequency, two varactor diodes, whose capacities depend on the voltage across their respective poles, were added. This way, the resonance frequency can be continuously changed in a range of more than 200 kHz. The circuitry needed for their implementations is shown on the right part of figure 7.15, and figure 7.16 shows the resonance for several different voltages applied.

As a consequence of counting on both a discrete and a continuous control of the resonance frequency of the cyclotron tank-circuit, any frequency in a range of over 400 kHz can be tuned. In addition, there is a fourth switch which can produce a jump big enough to account for the frequency difference between a $^{40}Ca^{17+}$ and a $^{40}Ca^{19+}$ ion. For a summary of the effects achievable, see figure 7.17 and table 7.1.

Cryogenic amplification

The electronic scheme of the cryogenic cyclotron amplifier is sketched in figure 7.18. The signal picked up by the tank circuit is conducted to gate 1 of a dual-gate GaAs MESFET[4] 3SK166 from Sony. The circuit is implemented as a high-ohm common-source configuration.

Due to the high frequency of the cyclotron motion, an impedance matching between the output of the 3SK166 and the coaxial line which will take the signal to the room-temperature amplifier is necessary. This is achieved with a GaAs single-

[4]MESFET stands for Metal-Semiconductor Field Effect Transistor.

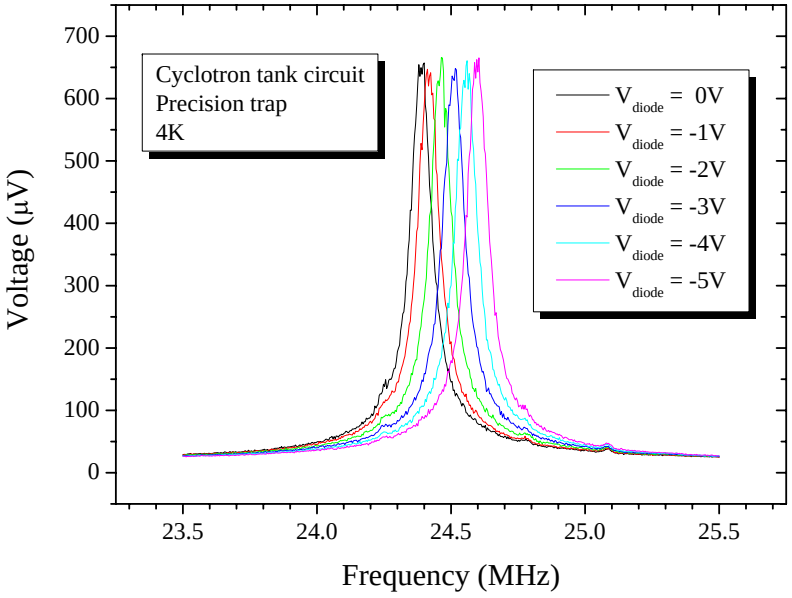

Figure 7.16: Cyclotron-LC resonance for different voltages applied to the varactor diodes.

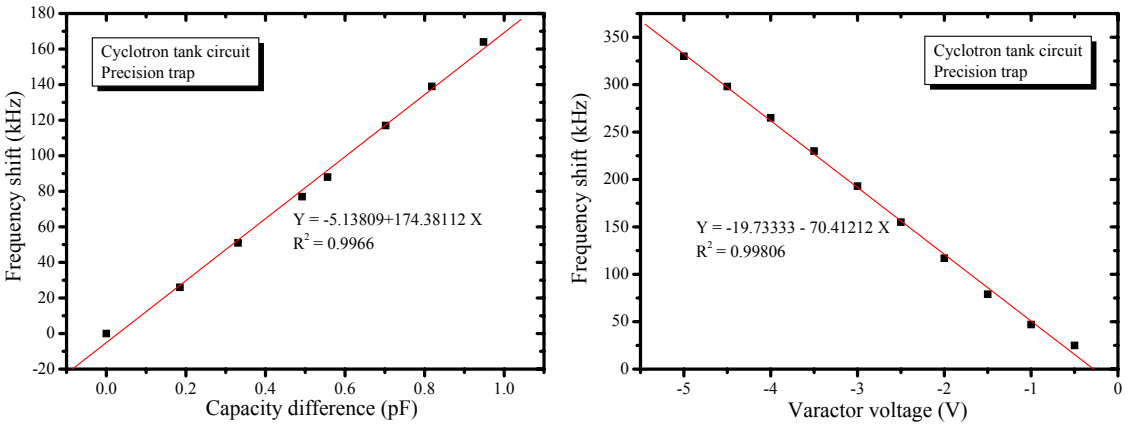

Figure 7.17: Cyclotron-LC resonance frequencies as a function of the switches turned on (left) and of the voltage applied to the varactor diodes (right).

gate HEMT[5], an ATF 35143 from Agilent.

Tuning properly the biasing voltages and currents of the transistors is crucial in order to obtain an optimized amplification and noise behavior of the circuit. As an example to illustrate this importance, figure 7.19 shows the resonance of the tank circuit given for different gate voltages supplied at the 3SK166. If the drain voltage is 0 V or very close, the drain-source channel is basically shortcut, so the drain output

[5]HEMT stands for High-Electron-Mobility-Transistor.

Switch	$\Delta\nu$ (kHz)
none	0
1	76
2	137
1+2	203
3	208
1+3	288
2+3	334
1+2+3	386
varactor	0-113

Table 7.1: Frequency shifts in the cyclotron tank circuit due to the effect of switching the different GaAs transistors on and off (discrete control) and of tuning the varactor diode (continuous control).

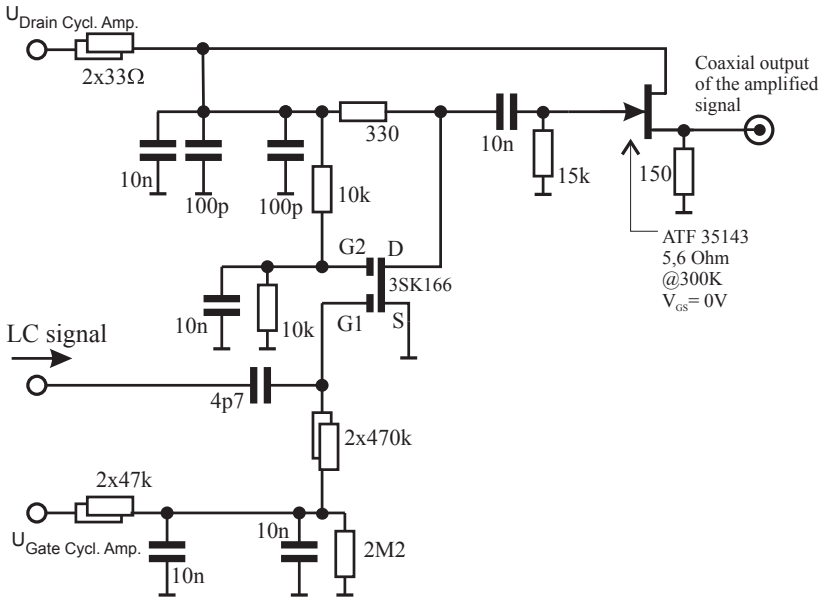

Figure 7.18: Schematic of the cryogenic cyclotron amplifier.

is grounded and does not amplify. As the gate voltage becomes more negative, the amplification improves until, at a voltage of ∼-0.9 V, it starts to become worse again, meaning that the drain-source channel has closed too much.

Room-temperature amplification and analysis

The signal, pre-amplified in the cryogenic stage, travels to the hat in a stainless-steel coaxial cable. There, it is further amplified by a room-temperature amplifier from Stahl Electronics (figure 7.20). This board consists actually of two independent channels. On the second one, the FT-ICR signal from the Creation trap is input, as will be explained below.

The output of the hat amplifier is converted from time-domain to frequency-domain by an FFT-analyzer, typically the SA 2400 from Yokogawa, where the evo-

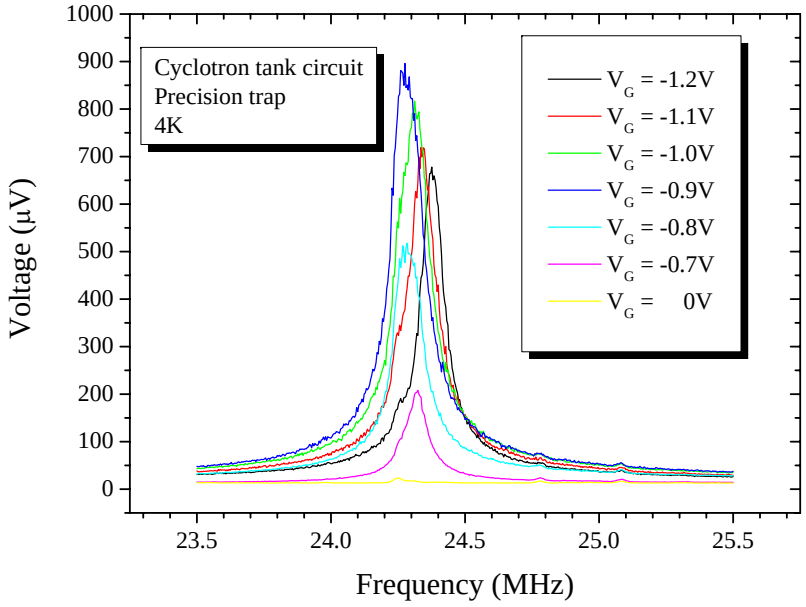

Figure 7.19: Resonance of the cyclotron tank circuit as a function of the gate voltage applied at the 3SK166 transistor.

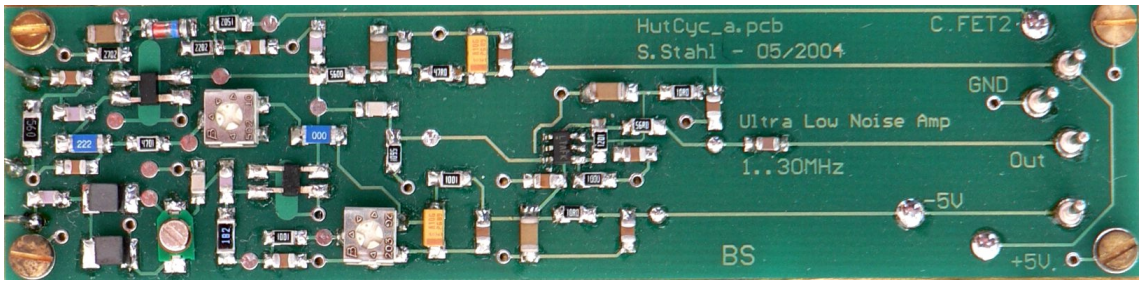

Figure 7.20: Picture of the room-temperature cyclotron amplifier.

lution of the signal can be followed on real-time.

7.4.2 Creation trap

Signal pick-up

After a frequency down-conversion, the cyclotron detection in the Creation trap is performed in order to follow on-line the charge breeding of the ions by means of a broadband FT-ICR detection technique. Since the cyclotron frequency is different for every charge-to-mass ratio, it can be used to determine the intensities of the coexisting species in the trap.

This time the ring electrode was chosen to be split in order to maximize the strength of the signal picked up. The feature of the detector is that there is no resonant circuit attached, since the frequencies of the different charge states span

between 0 and 40 MHz. Rather, the signal coming from the trap is amplified equally for all frequencies within the mentioned span, as required by broadband FT-ICR detection.

Although no ion signal has been yet recorded, the results shown in figure 7.21 represent a proof of principle that the detection works. The background-noise level increases considerably as the electrons from the electron gun fly through the trap. The noise distribution induced is white, and what is shown in the figure is in a span of 40 kHz close to 5 MHz.

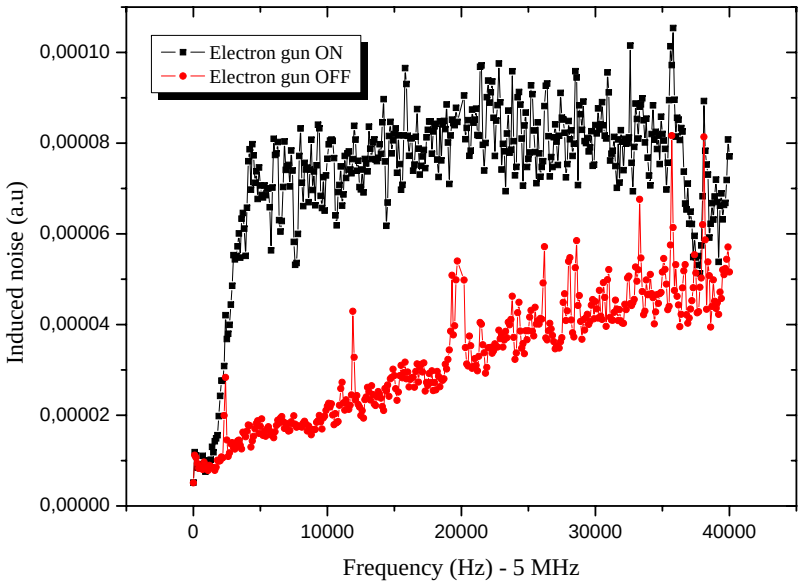

Figure 7.21: Background noise picked up at the split ring electrode of the Creation trap with and without electrons from the electron gun.

Actually, the noise induced by the electrons while the beam is on is strong enough to cover the ions' signal. Therefore, the FT-ICR detection in the Creation trap is sequenced in time as follows (figure 7.22):

- the electron beam is turned on and the charge breeding takes place;
- the electron beam is turned off and all electrons are given time to disappear;
- the detection takes place;
- the electron gun is turned on again.

One complete iteration will take, typically, from 500 ms to 1.5 s, depending on the rate at which the signals induced by the different ion species need to be updated.

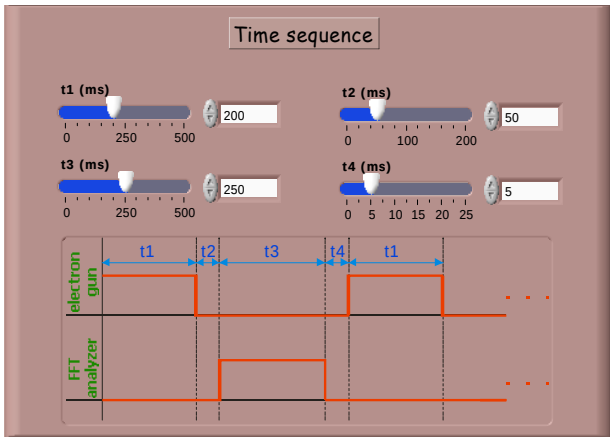

Figure 7.22: Timing sequence of the broadband FT-ICR detection during charge breeding in the Creation trap.

Cryogenic amplification

The circuit shown in figure 7.23 is in charge of amplifying the cyclotron signal coming from the different ions in the Creation trap. Both parts of the segmented ring are connected to the board, and, as in the case of the cyclotron amplifier connected to the Precision trap, the current induced there is guided to a high-ohm first stage. In this case this stage consists of two dual-gate MESFET's (CF739 from Siemens), connected in a parallel, common source configuration.

The pre-amplified signal is then superposed to the axial contribution, since this board contains also the axial amplifier of the Creation trap. The composition of both signals is then buffered and impedance-matched with the coaxial line going to the hat with a an ATF 35143 HEMT from Agilent, exactly as in the case of the Precision trap.

Room-temperature amplification and analysis

The room-temperature amplifier for the FT-ICR and axial signals coming from the Creation trap is located in the same board as the cyclotron amplifier for the Precision trap (figure 7.20).

In the case of ^{40}Ca, every charge state is separated from the next one by roughly 1.5 MHz, and the width of the peaks can be as narrow as some hundreds of mHz. Hence, if one wants to observe several peaks, i.e. charge states, simultaneously, the possibility of a single FFT-analyzer is ruled out. Therefore, an 8-channel frequency-downconverter was developed in collaboration with Stahl Electronics (FSA-40), which is used in combination with an 8-channel signal analyzer from Oros (OR35). The FSA-40 can read from two independent inputs of frequencies between 0 and 40 MHz, take 8 different windows with 8 different local-oscillator frequencies, and mix them down. These downmixed signals can then be given as an input to the OR35, which will perform an FFT-analysis of its contents between 0 and 40 kHz. With this, a system capable of displaying a high-resolution FFT-analysis of the signal induced by 8 different ionic charge states is available.

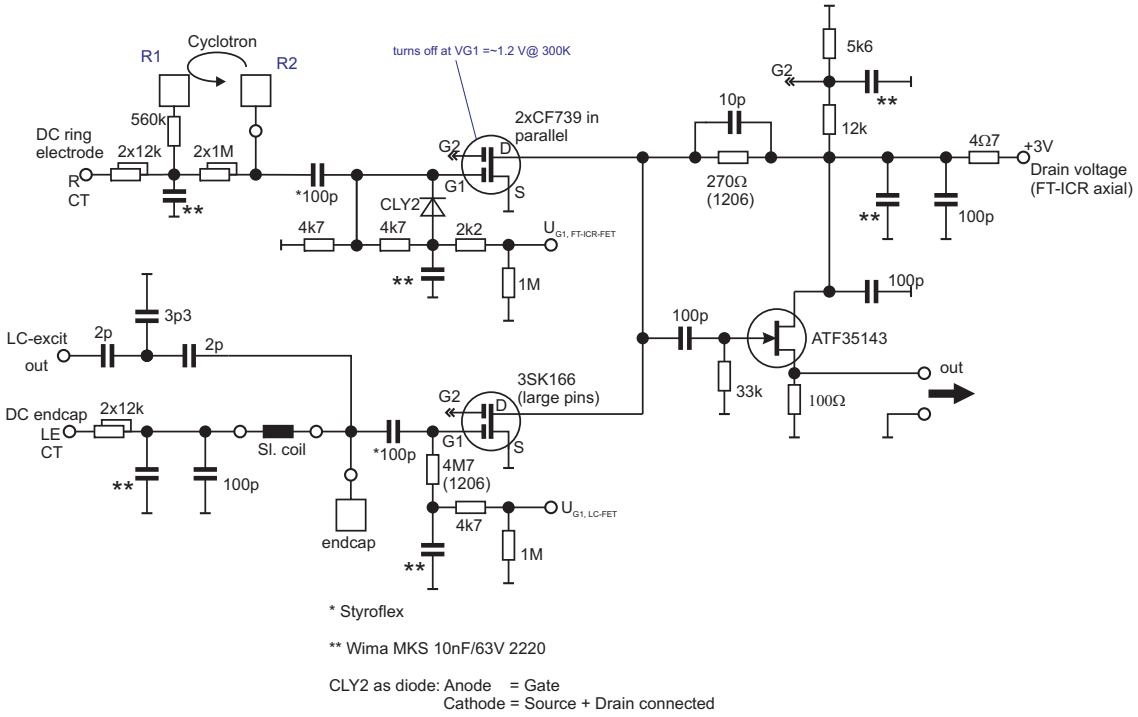

Figure 7.23: Schematic of the cryogenic FT-ICR and axial amplifier of the Creation trap.

7.5 Measurement of the axial frequency in a Penning trap

7.5.1 Precision and Analysis traps

The measurements of the axial frequencies in the Precision and the Analysis traps work under exactly the same principles and will, therefore, be dealt with together.

Signal pick-up

The induced image currents of the ion are picked up simultaneously at the upper correction electrode and endcap, in the case of the Precision trap, and at the lower correction electrode for the Analysis trap.

Both axial tank circuits count on superconducting coils for a maximized Q-value of the resonance, enabling cooling-time constants well below 500 ms for highly-charged ions. The 51 µm-NbTi wire is isolated with kapton, giving a total diameter of 76 µm. The coil bodies are made out of teflon, as in the cyclotron case, and they are both housed in NbTi housings. The disadvantage of this configuration is that thermal contraction is stronger for teflon than for NbTi, so, at 4 K, the wire would have loosened had it not been wrapped with a teflon band to stabilize it mechanically. For a summary of the dimensions and main characteristics of the axial coils, see table 7.2.

Regarding the performance of the tank circuits, figures 7.24 and 7.25 show the resonances of the Precision and Analysis trap, respectively. For further details on

the technical design, see [Sta98].

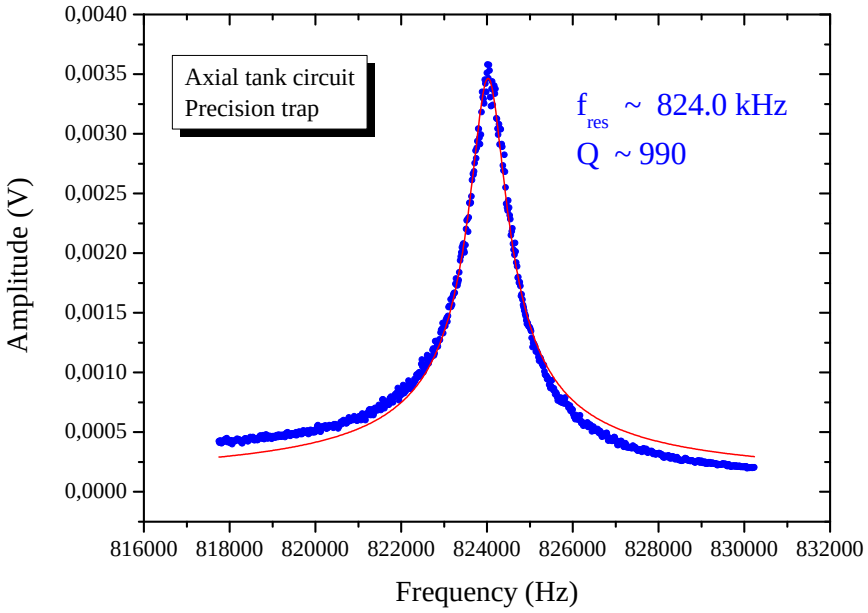

Figure 7.24: Resonance of the axial LC-circuit attached to the Precision trap.

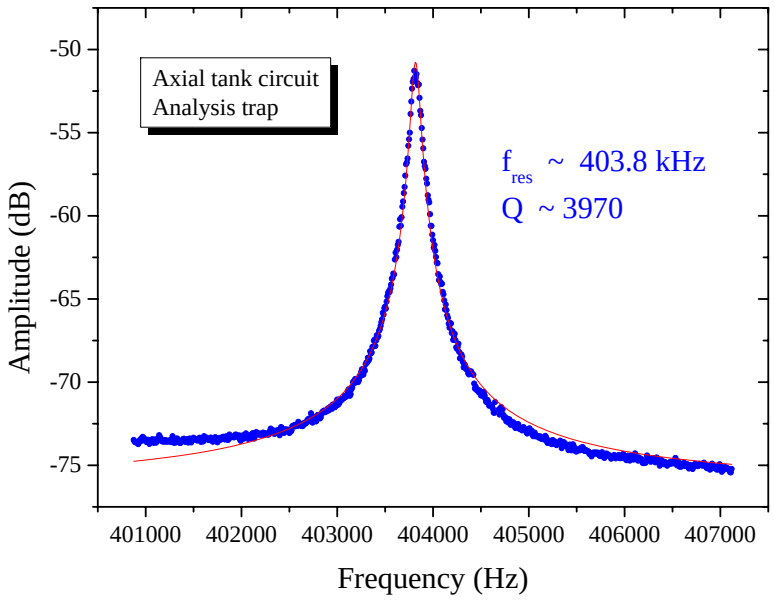

Figure 7.25: Resonance of the axial LC-circuit attached to the Analysis trap.

	Precision trap	Analysis trap
Length of housing (mm)	65	105
Number of windings	700	920
Resonance frequency (kHz)	824.0	403.8
Q-value (max.)	990	3970
Wire diameter (µm)	51	51
Wire + isolation diameter (µm)	76	76

Table 7.2: Main characteristics of the axial tank circuits attached to the Precision and Analysis traps.

Cryogenic amplification

There are two cryogenic boards for the first amplification stage of the axial signals (figures 7.26 and 7.27). The so-called "old" amplifier board is connected to the secondary side of the coil connected to the Analysis trap. This signal is amplified by a 3SK166 MESFET (Sony) in a common-source configuration, analogous to that described already for the cyclotron cryogenic amplifier of the Precision trap. For the axial signal coming from the Precision trap, the first stage is identical, but implemented in the "new" amplifier board. In this very board, a second buffer stage takes the combined signals from both traps to the coaxial line going to the hat post-amplifier. The buffering is achieved with a CF739 HEMT from Infineon, which, as discussed for the cyclotron case, also serves for impedance matching to the coaxial cable.

Q-switches

The phase-sensitive detection technique described in section 7.3 needs the phase of the signals to evolve coherently after the initial excitation burst (figure 7.13). Thus, the ion must not suffer from any interaction with its environment in general and with the tank circuits in particular. Therefore, the tank circuits need to be switched off. This is achieved by small circuits based on GaAs transistors (figure 7.28) which can connect or disconnect big capacitors in parallel to the LC-circuits. These capacities result in two correlated effects: they shift the resonance frequency, and they diminish the quality factor. Hence the name of Q-switches.

When the capacitors are switched on, the resonances of the tank circuits change dramatically, as can be observed from figure 7.29. Note that, at the resonance frequency, the noise amplitude is basically at the background level, meaning that there is no coupling of the ion's axial motion to the LC-circuit.

Room-temperature amplification and analysis

The room-temperature board used for amplifying the signal coming from the cryogenic region was developed by Stahl Electronics. Its most special feature is that it has been equipped with a single-sideband down-converter stage used for mixing the signal down. Its advantage is mainly the improved S/N compared with a "normal" mixer used for down-conversion. Hence, the output can be directly guided to the SA

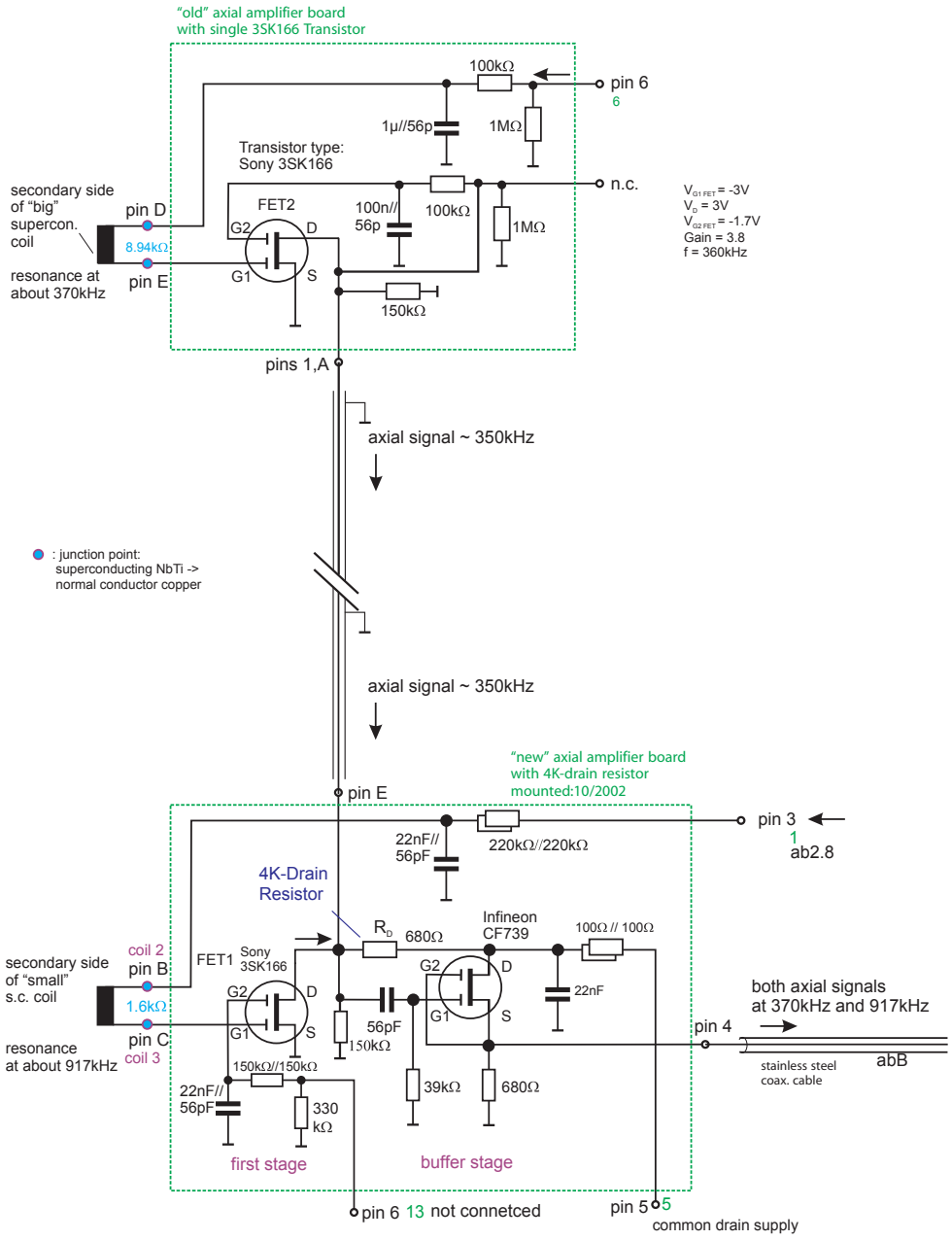

Figure 7.26: Schematic of the cryogenic axial-amplifier setup, consisting of the "old" (top) and "new" (bottom) axial-amplifier boards. Both boards are approximately the same in dimensions ($\sim 9 \times 4\,\mathrm{cm}^2$).

2400 signal analyzer to follow on-line the frequency spectrum of the signals induced by the ions.

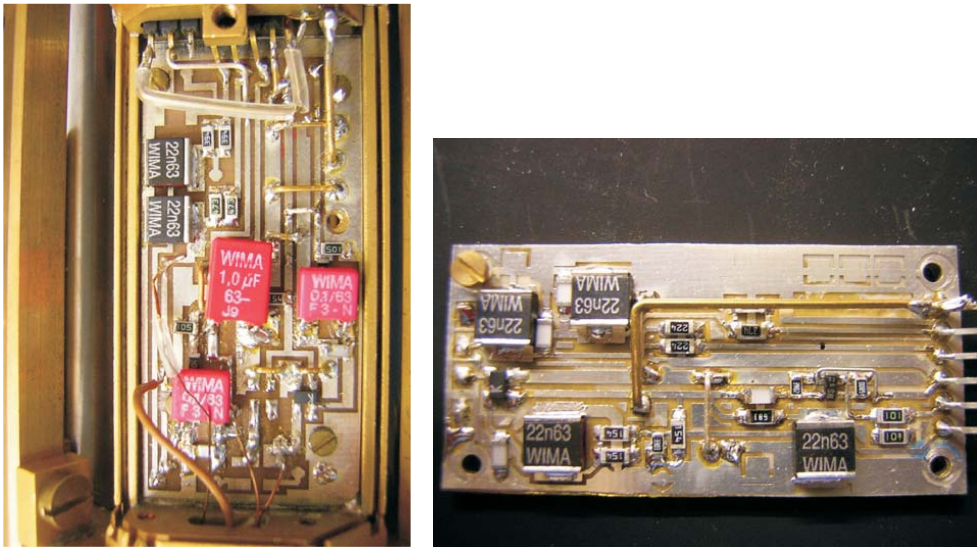

Figure 7.27: Picture of the "old" (right) and "new" (left) axial-amplifier boards.

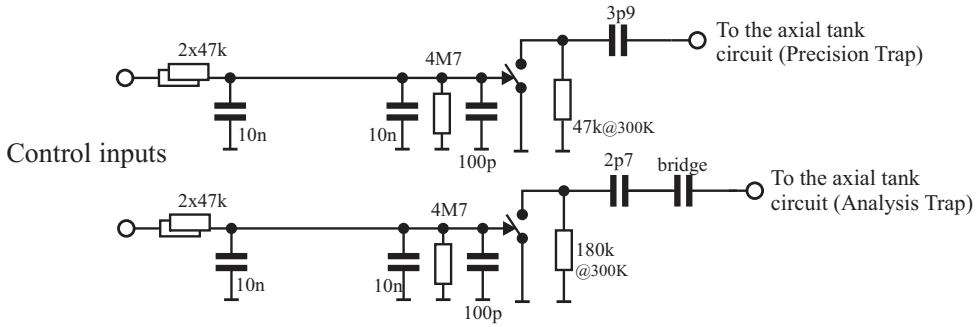

Figure 7.28: Schematic of the Q-switches.

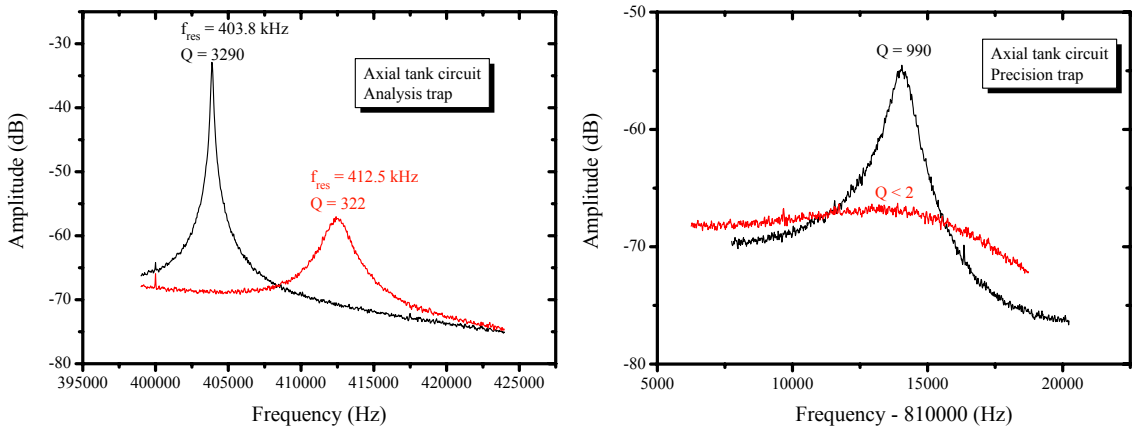

Figure 7.29: Effects of the Q-switches on the resonance curves of the axial tank circuits.

7.5.2 Creation trap

Signal pick-up

The purpose of the axial tank circuit is more to give the chance to do resistive cooling than to detect the ions' motions. However, there is an amplifier attached to be able to see and tune the tank circuit.

The reason to cool the ions resistively is that, during charge breeding, the ion cloud becomes very energetic. If there were no cooling, most of the ions would be lost from the trap, thus making it extremely hard to create a cloud of the desired species in the desired charge state.

The tank circuit is attached to the lower endcap of the Creation trap. The coil is made of NbTi and the resonance frequency lies at 2.763 MHz (figure 7.30). The quality factor of ∼180 is much smaller than that of the other two axial resonant circuits. The reason for this is that the housing is not of NbTi. Rather, it is the OFHC-copper of the ultrahigh-vacuum chamber itself, since this coil and the amplifier are *inside* the trap chamber. Therefore, the previously mentioned optimum factor of 0.55 for the ratio of the diameters between coil and resonator is not respected. Moreover, there is no real housing, since it is open on one side.

In principle, only one value of q/m will be in resonance and thus cooled, corresponding to Ca^{15+} for a typical trap depth of ∼100 V. However, during charge breeding, the voltage at the ring of the trap can be ramped slowly to make sure that all charge states interact with the tank circuit, give it their energy, and only then restart the electron gun.

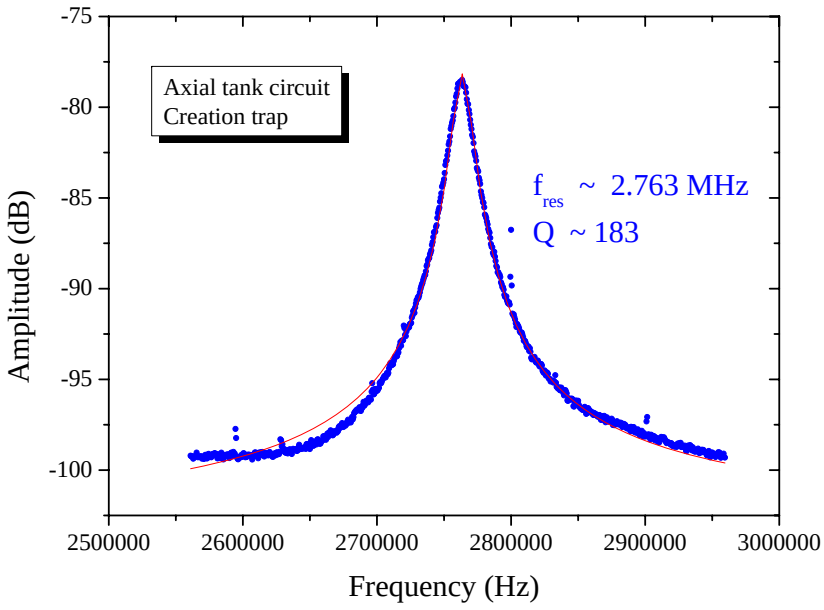

Figure 7.30: Resonance of the axial LC-circuit attached to the Creation trap. There is a slight asymmetry visible in the curve. The excitation applied for ease of visibility of the resonance is responsible for this.

Cryogenic amplification, room-temperature amplification and analysis

The cryogenic amplifier for the axial signal of the Creation trap is physically implemented in the same board as the broadband FT-ICR amplifier. The octogonal board is attached to the triple-trap setup, and the coil is held from the board. A picture of the system is shown in figure 7.31

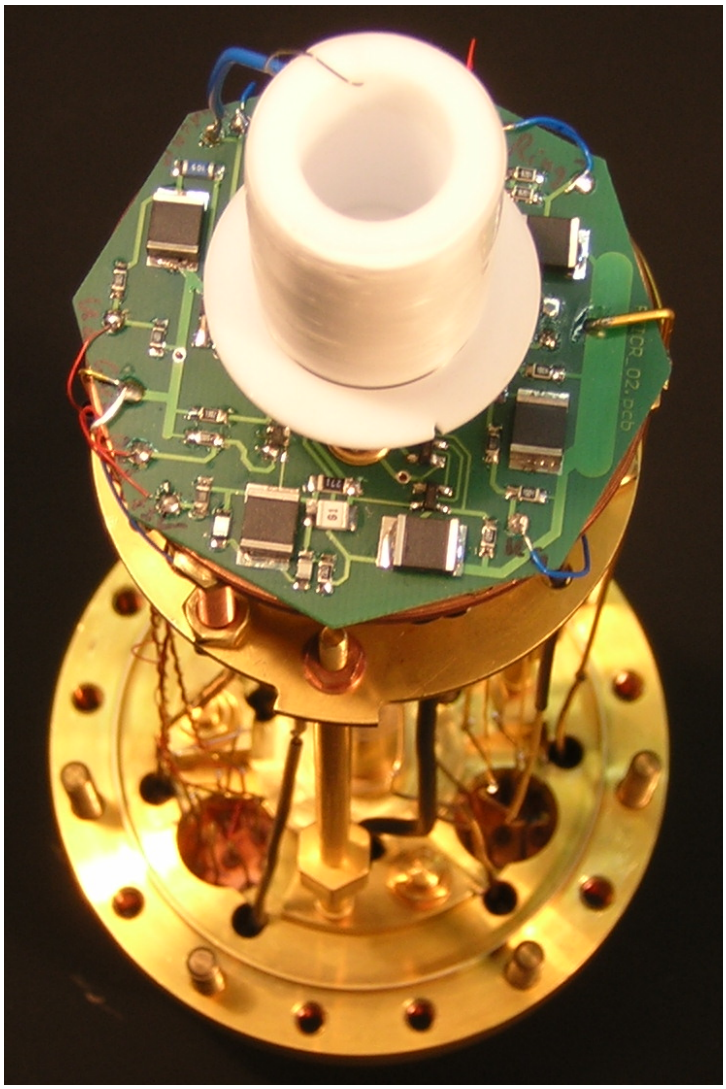

Figure 7.31: Picture of the axial coil and the FT-ICR boards attached to the Creation trap.

The amplification scheme is exactly the same as for the other two axial amplifiers (see figure 7.23), with the only peculiarity that the axial signal is combined with the cyclotron signal before being buffered, impedance matched and sent to the hat for further amplification.

The room temperature amplifier was also already introduced when presented the broadband cyclotron amplifier, so for details, refer to section 7.4.2. However, since the detection is narrow-band, there is no need for a multichannel spectrum analyzer, so the FFT is performed in the SA 2400 from Yokogawa after frequency

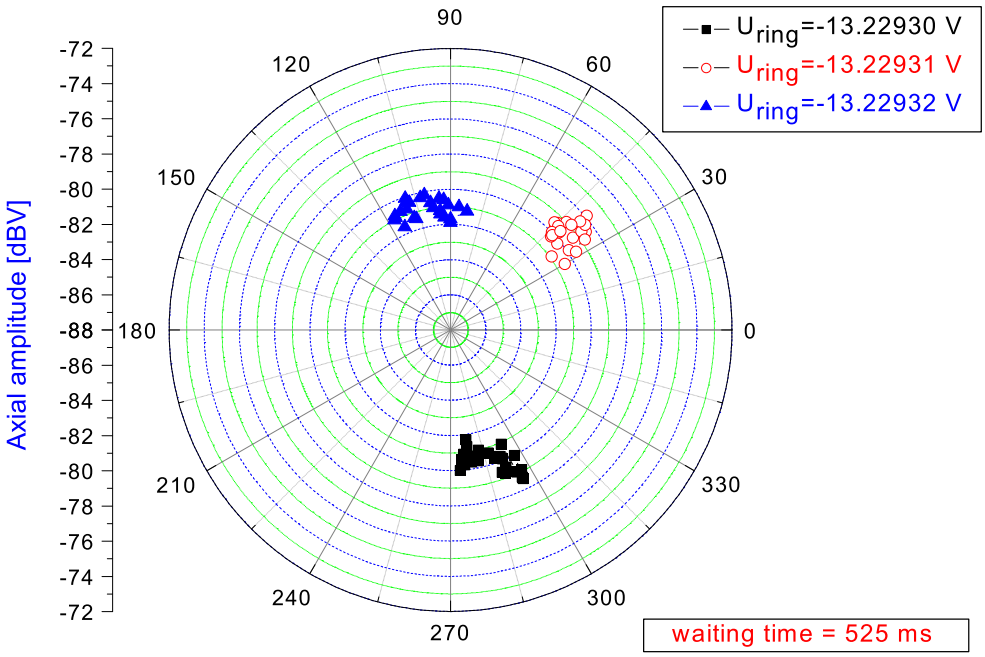

Figure 7.32: Phase-sensitive measurement: axial amplitudes and phases of a single ion measured successively 25 times in a total time of 1 min for three different ring voltages. The phase shifts between the data sets of roughly 90° are obtained for a waiting time of 525 ms, corresponding to frequency differences of roughly 0.5 Hz. Actually, the phase jump is not exactly the same between the three sets of data. The reason for this is the fact that the voltage steps of 10 µV were not well defined within the supply used. Figure taken from [Dje04a].

down-conversion.

7.6 Spin-flip detection in the Analysis trap

In order to judge whether a spin-flip has occurred or not, the axial frequency in the Analysis trap is studied. The small frequency shift due to the coupling of the spin state to the magnetic bottle can be detected by measuring directly the axial frequency, but it can also be measured with the phase-sensitive technique introduced in section 7.3. The advantages presented there can then be made use of.

The signal is picked up and amplified as explained previously for the axial degree of freedom of the Analysis trap. The difference now is the FFT-analysis performed in the Yokogawa SA 2400, since, instead of a power spectrum, the phase is plotted.

Figure 7.32 shows a result for a measurement where the axial frequency shift is of approximately 500 mHz. It was performed with a single hydrogenlike carbon ion in the Precision trap [Dje04a]. Since the B_2 term is very small there, the frequency shift was intentionally created by changing the trap depth by 10 µV. After letting the phase evolve for 525 ms, it shifts by approximately 90°. Of course, if the frequency shift between the spin-up and spin-down states differ in less than 200 mHz, the waiting time must be kept longer. Still, the overall time estimated to find out the spin direction of a single ion is in the order of a few seconds, instead of the several

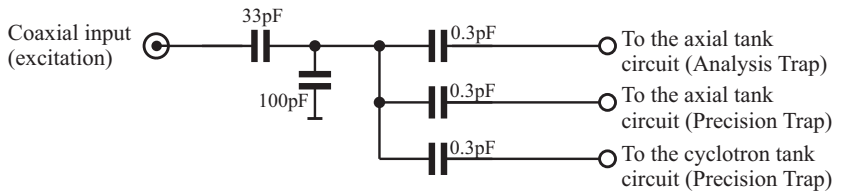

Figure 7.33: Schematic of the capacitive-coupling design for rf-excitations.

minutes needed when looking directly for the dip.

7.7 Further electronics

7.7.1 Radio-frequency filters and excitation

Every single line coming from the room-temperature region into the cryogenic region must count on a filter to prevent noise from getting into the trap and also from being detected and amplified. The low-pass filters are analogous to those shown in figure 3.9, and they are scattered around all cryogenic boards. There are even two boards dedicated exclusively to filtering purposes.

Also excitations need to be coupled in for several experimental applications. To that end, the setup counts on an input for feeding radio-frequency signals which are then split towards the different tank circuits, as sketched in figure 7.33.

7.7.2 Bias supply

All transistors upon which the cryogenic amplifiers are based need to be biased with dc-voltages. As has been mentioned several times throughout this thesis, avoiding electronic noise is a must in a *g-factor* measurement. Therefore, all required room-temperature electronics are attached directly at the hat and fed by a battery, so the experiment is galvanically decoupled from the rest of the world. Thus, a personalized multichannel voltage supply was developed in collaboration with Stahl Electronics, the BS 1-12. It is able of outputting 16 independent voltages ranging from -5 V to +5 V, with a 16-bit resolution. These voltages are used to bias not only the cryogenic amplifiers, but also the low-voltage inputs required by other devices, like the high-voltage or the HVM-boxes, are created in the BS 1-12 (figure 7.34).

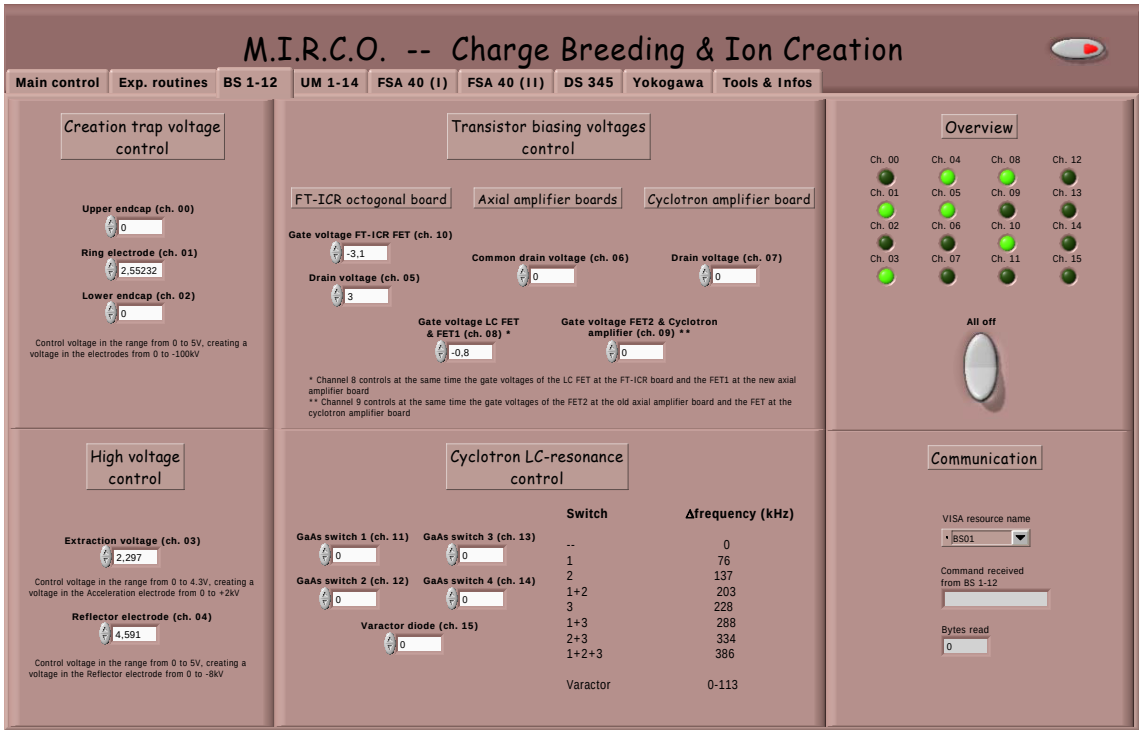

Figure 7.34: Capture of the control-software tab which handles the BS 1-12 bias supply for the trap electrodes.

Chapter 8

Summary and Outlook

"I may not have gone where I intended to go, but I have ended up where I needed to be."

Douglas Adams.

Summary

The work realized in the scope of this thesis is the required design, construction, simulation, remodelling, set-up, programming and first evaluations and verifications of an experiment dedicated to ultrahigh-precision measurements of the *g-factor* of medium-heavy, highly-charged ions.

The relevance of such measurements for testing a part of the Standard Model has been motivated along the first two chapters. The various parts of the experimental setup have been argued and discussed in detail throughout the rest of the work, supported as often as possible by measurements.

In addition, experimental techniques have been introduced, which have been proposed and tested before, but have still not been used in *g-factor* measurements. They will presumably allow for an improvement in the precision of at least a factor of 4.

An unavoidable obstacle, which needs to be tackled for such measurements with highly-charged ions, is the necessity of charge breeding. This reality, along with the fact that a completely-sealed setup is certainly preferable in order to satisfy the environmental conditions required, incentivized the inclusion of an electron-beam-ion source. Hence, a door to a completely new field of physics had been opened: solid-state physics in general and electron emission in particular. The underlying science has been introduced and applied to field-emission-point arrays, upon which the electron gun in charge of impact-ionizing the ions was based.

Current status

At this point, the experiment is in a status where everything is ready to start the production of ions in the Creation trap. Actually, thorough tests in that sense have been already carried out, as was presented in chapter 5. However, the fact that the field-emission point array is larger than the hole in the target, through which the electrons need to fly, seems to be preventing ions from being sputtered

from the target into the trapping potential. Therefore, a new electron gun has been designed and constructed in the scope of B. Schabinger's doctoral thesis, which will be implemented into the setup once it has passed the previous, necessary tests.

Otherwise, everything is ready to start with the measurements, including the large amount of personalized electronic devices required. Moreover, a modular control system already capable of conducting many devices and routines, but also easily expandable with further features, has been programmed (appendix B).

Ion creation studies

It has been emphasized several times in this thesis that the combination of the mini-EBIS and the broadband FT-ICR detection systems implemented in this experiment allows for cross-section determinations of electron-impact-ionization processes. Although the extraction of these data is not straightforward and the uncertainties in the measurements are large, there are, in many cases, *no* experimental results available, which makes it a very appealing possibility.

The difficulty of the measurement arises from the fact that in order to find out the abundance of a certain charge state, the strength of the induced signal needs to be analyzed. Actually, it is the area under the curve that matters, unlike in a frequency measurement, where it is the frequency itself. As shown in section 7.1.4, the amplitude of the signal induced by the ions in an electrode depends on its velocity. Thus, a proper estimation of the spatial and velocity distributions of the ions inside the Penning trap is required.

Nevertheless, although cross-section measurements are a highlight, they are not the only value of the setup. It must be kept in mind that yields as high as possible of the desired charge state of the desired ion species need to be obtained from the mini-EBIS. Thus, an intensive knowledge of the processes happening inside the Creation trap is essential, and the creation and detection systems included aid us in properly understanding them.

First *g-factor* measurement

Once a single, lithiumlike calcium ion has been created and isolated, the required measurements previous to the *g-factor* determination will be carried out. A compendium of these measurements for the case of hydrogenlike carbon can be found in [Alo03]. An important previous procedure to be performed is the optimization of the tuning ratios in both the Precision and the Analysis traps. Also specially relevant are the results from the tests aiming to find out if there is really a single ion in the Penning trap, or if, on the contrary, there are impurities. For instance a measurement of the cyclotron cooling-time constant helps to discern which is the case. If the behavior of the ion's cyclotron frequency, after an initial excitation, with respect to the time elapsed since the end of the burst follows a clean exponential law, then the ion is most probably isolated. Otherwise, when the impurity is close to the ion, its influence will result in sudden frequency jumps which spoil the exponential shape of the curve.

After these tests and further measurements, most of which are also given in [Alo03], the *g-factor* measurement on a $^{40}Ca^{17+}$ ion is planned.

Further possible *g-factor* measurements with this setup

With all probability, other measurements will follow. $^{40}Ca^{19+}$, $^{48}Ca^{17+}$, $^{48}Ca^{19+}$ and $^{12}C^{5+}$ ions can be procured by the existing setup without need of re-opening the ultrahigh-vacuum chamber. The interest of hydrogenlike carbon has to do with the mass of the electron, as will be discussed below. The rest of the ions are of relevance for further tests of QED, but also for nuclear effects which can give a deeper insight into a territory still immersed in fog when compared to the field of atomic physics.

In order to carry out these other measurements, slight modifications will have to be realized in the resonance frequencies of the detection systems, and also in the charge breeding routines. Otherwise, the setup is ready for all of them.

Electron mass

The triple-dip technique (appendix A) and the phase-sensitive detection (chapter 7) will shorten considerably the time and decrease the cyclotron energy required for the measurement. The reduction of the duration has a direct positive influence in the smaller fluctuations of the magnetic field. On the other hand, a smaller cyclotron energy (corresponding to a temperature of 4 K), improves the width of the *g-factor* resonance. The combination of both effects can improve considerably the precision of the *g-factor* determination. Therefore, a future possibility would be to re-measure the *g-factor* of a single $^{12}C^{5+}$ ion, from which an even more precise value for the electron mass can be extracted.

Other *g-factor* measurements

The heaviest stable element, uranium, represents an extremely valuable system in the sense that it allows for the most stringent test of BS-QED possible with a *g-factor* measurement. Therefore, huge efforts are being undertaken by the HITRAP collaboration from GSI-Darmstadt [Qui01, Bei05, Her06]. At the moment, they are already working on a design of a trap setup, based on the one used for the *g-factor* experiment in Mainz.

The collaboration between GSI-Darmstadt and the University of Mainz is also working on a setup for measuring the *g-factor* of the free proton [Ver05]. Such a measurement has never been carried out before, which is already an important motivation for the experiment. However, it is not the only one. The setup, which is in a very advanced state, can be also used to measure the *g-factor* of an isolated antiproton. A comparison between both values would yield an extremely stringent test of CPT-invariance (charge conjugation - parity inversion - time reversal), a pillar upon which the Standard Model is sustained.

Regarding the free electron, G. Gabrielse has improved by a factor of six the value measured by H.G. Dehmelt and unbeaten for almost two decades [Odo06]. Moreover, a new value for the fine-structure constant has been derived from that measurement [Gab06].

At the sight of this, one can conclude that high-precision *g-factor* measurements represent a very interesting benchmark for testing the Standard Model, its predictions, and its possible limits.

Appendix A

Experimental procedures to perform a *g-factor* measurement

In chapter 3 it was discussed which observables are related to the *g-factor* and make it experimentally accessible. Also, a setup has been designed and constructed in order to do so. Therefore, the remaining task is to describe the experimental techniques to be followed for carrying out the *g-factor* measurement itself.

In the previous measurements on light, hydrogenlike ions [Häf00b, Ver04a], the measurement of the cyclotron frequency in the Precision trap was peak-detected. This means that the number whose uncertainty affects the overall uncertainty of the measurement most (equation 4.22 and 4.23), was not measured in thermal equilibrium with the environment. Rather, in order to have a good signal-to-noise ratio, it was excited, shifting its frequency between 500 mHz and 5 Hz. If one keeps in mind that the width of the cyclotron peak is ∼30 mHz, one realizes that the effect is very strong. Therefore, several *g-factor* measurements had to be performed at different cyclotron energies, only to then extrapolate to 0 cyclotron energy. This is a major issue, as discussed in detail by J. Verdú in [Ver03].

A.1 Double-dip method

The very J. Verdú proposed the detection of the cyclotron frequency by sideband coupling to the axial degree of freedom. The principles behind this technique are given in section 4.4, and in more detail in [Val04]. With this method, the cyclotron motion is kept at the temperature of the tank circuit to which it is coupled: 4.2 K.

Figure 4.6 showed the splitting into two dips resulting from performing a sideband coupling between the axial and the magnetron degrees of freedom. If, instead of using the magnetron, one would couple the cyclotron motion to the axial one, the splitting would be analogous. From the frequencies and areas characterizing the two dips, the cyclotron frequency is obtained at an energy corresponding to 4 K. Hence the name of *double-dip* method.

A.2 Triple-dip method

Since the determination of the free cyclotron frequency requires the measurement of all three motional frequencies (equation 4.22), the axial dip, without splitting,

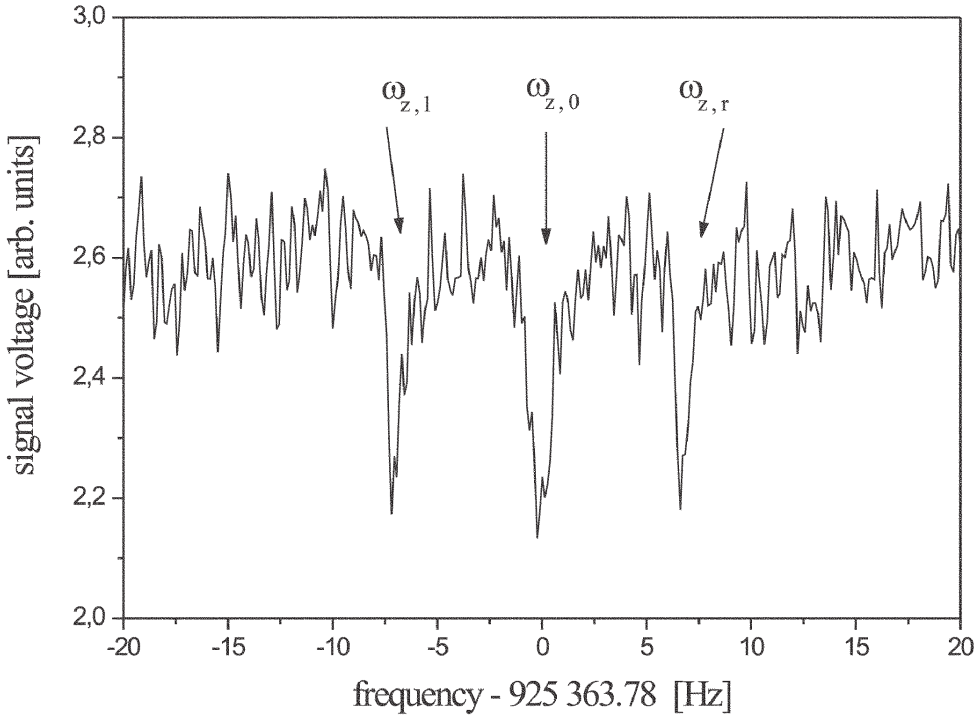

Figure A.1: Triple dip resulting from the superposition of an axial dip with the splitting due to sideband coupling. Figure taken from [Ver04b].

has to be observed as well. In the double-dip method described above, a separate measurement of the axial frequency was performed[1], without sideband coupling, of course. But, by modulating the coupling excitation itself, one can obtain a time-average of the signals with (split case) and without (single dip) coupling, resulting in three dips simultaneously (figure A.1). From such a spectrum, one obtains the axial and cyclotron frequencies at the same time, minimizing the measurement time and, therefore, unwanted shifts [Ver04b].

A.3 Measurement routine

The *g-factor* measurement routine should proceed as follows:

1. Find out spin direction in the Analysis trap:
   - measurement of the phase (ϕ_1)
   - saturating microwave irradiation
   - measurement of the phase (ϕ_2)
   - if $|\phi_2 - \phi_1| < \Delta\phi_{lim}$ go to 1
   - if $\phi_2 > \phi_1 \Rightarrow$ initial spin up
     if $\phi_2 < \phi_1 \Rightarrow$ initial spin down

[1] Actually, two measurements were performed: before and after measuring the cyclotron frequency by sideband coupling.

2. Transport from the Analysis to the Precision trap
3. Frequency measurement in the Precision trap
    - modulated sideband coupling and saturating microwave irradiation (simultaneous) $\Rightarrow \omega_z, \omega_+$
    - ω_{mw}/ω_c
4. Transport from the Precision to the Analysis trap
5. Find out spin direction in the Analysis trap
    - measurement of the phase (ϕ_1)
    - saturating microwave irradiation
    - measurement of the phase (ϕ_2)
    - if $|\phi_2 - \phi_1| < \Delta\phi_{lim}$ go to 5
    - if $\phi_2 > \phi_1 \Rightarrow$ final spin up
      if $\phi_2 < \phi_1 \Rightarrow$ final spin down
    - if final spin = initial spin $\Rightarrow$ spin-flip
      if final spin $\neq$ initial spin $\Rightarrow$ no spin-flip
    - go to 1

$\Delta\phi_{lim}$ has to be defined according to the phase-resolution during the measurement, but it can typically be chosen to be 180°. This procedure must be repeated many times for each value of ω_{mw}/ω_c in order to have enough data to properly quantify the spin-flip probability for each point.

Appendix B

M.I.R.C.O. - Multiple Ionization Routines and COntrol system

B.1 Introduction

M.I.R.C.O. is the name given to the software code programmed to control the *g-factor* experiment. Actually, in its very beginning, it was designed to take care of the ionization and charge breeding, hence its name.

M.I.R.C.O. is a LabView-based software, organized in a modular manner both in the front panel (user interface) and in the block diagram (programmer's view). The front panel is divided in tabs which contain the controls and pieces of information grouped according to the specific topic to which they are related. There are 9 tabs at the moment:

- main control, dedicated to ion creation and charge breeding;
- experimental routines, where typically the parameters required by other subprograms are set and, after, these are executed;
- BS 1-12, for direct control of the 16 voltage lines supplied by this source;
- UM 1-14, *idem* but for the 22 channels of the ultrahigh-precision voltage supply;
- FSA 40 (I), for communication and configuration of the 8-channel frequency downmixer;
- FSA 40 (II), where the digitized inputs of the downmixer can be fast-Fourier transformed (broadband);
- DS 345, for applying the proper settings to the battery of the signal generators from Stanford Research Systems;
- Yokogawa, with a display for plotting the spectra read from the SA 2400 signal analyzer;
- and tools and infos, with a compendium of applications and frequently needed data.

B.2 Main control - Ion creation

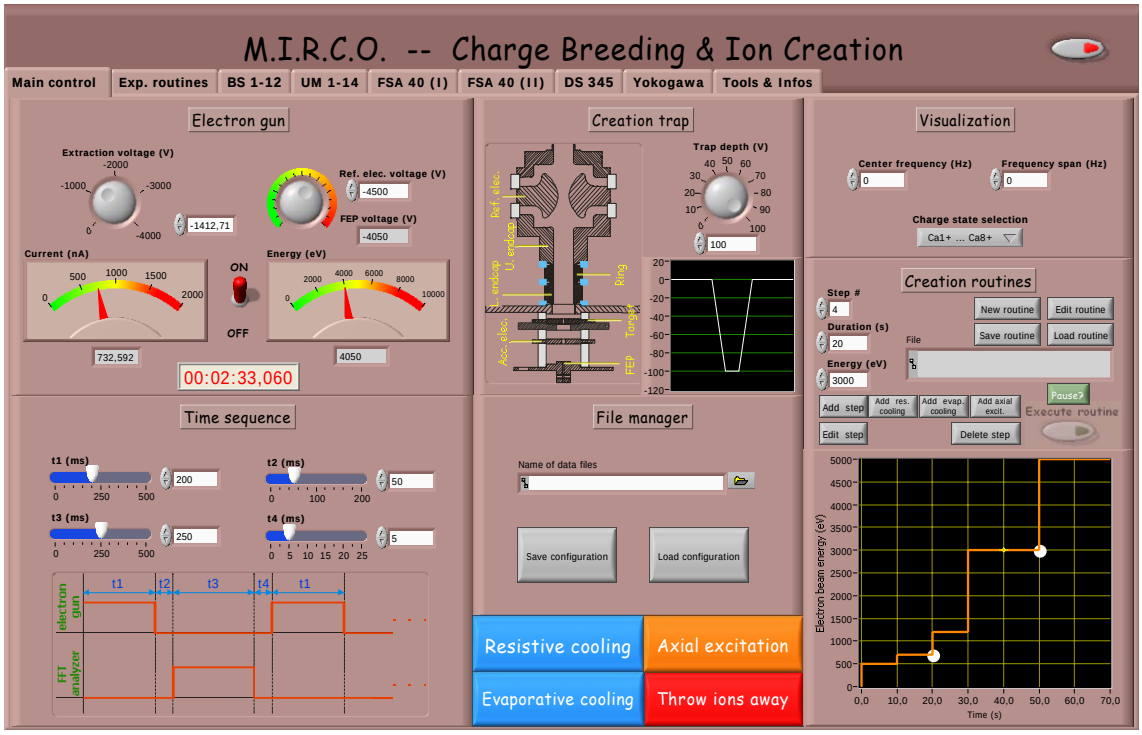

Figure B.1: Capture of the control-software tab which handles the ion creation.

The main control tab (figure B.1) is the console from which the electron gun, the Creation trap and everything related to the charge breeding of ions is managed:

- the electron-beam current and energy,
- the trapping voltage of the Creation trap,
- the timing configuration of the electron gun and the FT-ICR detection,
- the manipulation of the ions in the Creation trap (resistive and evaporative coolings, axial excitation and ejection of the ions)
- and, finally, a tool for automatizing the ion-creation process.

In addition, there is a tool for selecting which ion species want to be observed on-line (to what frequencies the local oscillators of the FSA 40 should be set), and a further control for managing the files. Regarding the evolution of the ions, it will be displayed by a software other than M.I.R.C.O., which will be able to communicate by the first, though.

B.3 Communication with devices

There is a number of home-made and personalized devices dedicated to very important tasks in the experiment and which need to be managed from the control-system

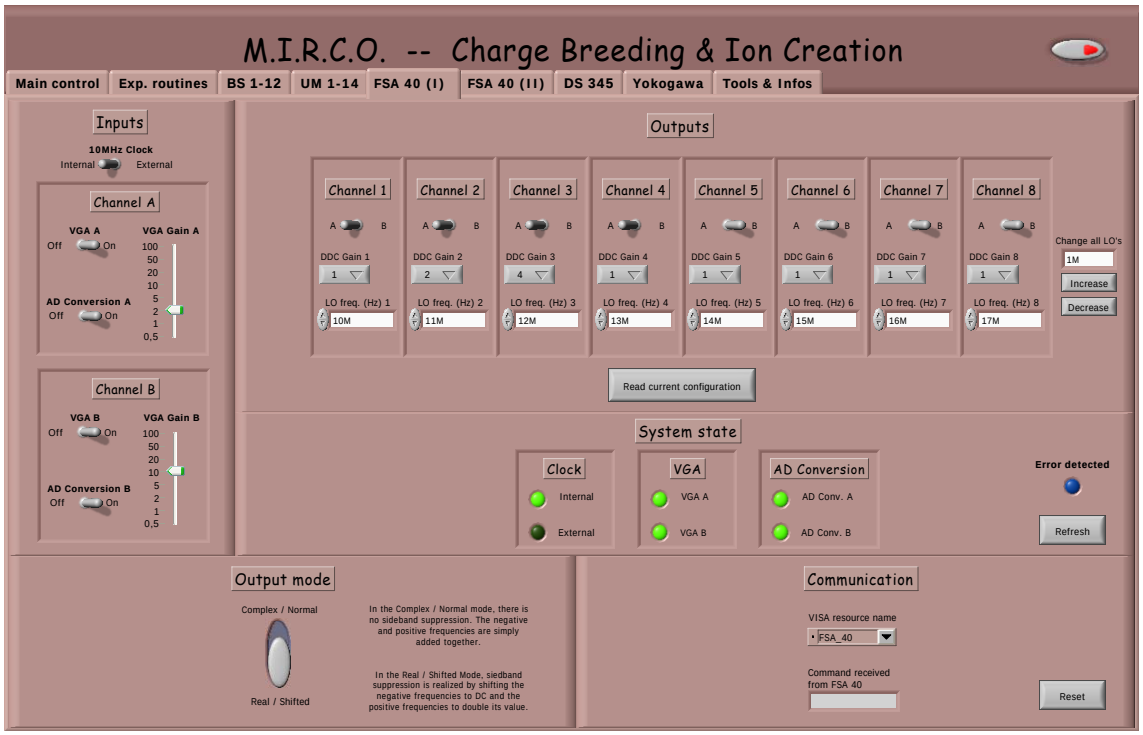

Figure B.2: Capture of the control-software tab which handles the configuration of the FSA 40.

software. Two voltage supplies from Stahl Electronics and a few other boards have already been mentioned along the text. Specially remarkable have been the efforts dedicated to the UM 1-14 and BS 1-12 supplies (figures 6.3 and 7.34, respectively.) Also the FSA 40 multichannel frequency-downmixer was demanding, as expected from the fact that it conforms two out of the nine tabs of M.I.R.C.O. (figure B.2).

Regarding the commercially-available devices, they were usually easier to implement into the program due to the fact that very intuitive drivers are provided. This was the case for the signal generators used for excitation and rf-coupling, both the DS 345's from SRS and the AG 332208 from Agilent.

B.4 Read-out of spectra

Another commercially-available device, heavily used in the *g-factor* experiment, is the SA 2400 signal analyzer from Yokogawa. Actually, it has been retired from the market, but it still holds true that the LabView drivers provided have been directly implemented into M.I.R.C.O.

The read-out of spectra from the SA 2400 is probably the most repeated action in the *g-factor* laboratory. To that end, a display simulating that of the SA 2400 was added into a control-system tab (figure B.3). From this tab, one can order the spectra to be displayed on the screen of the personal computer, save them to the hard disk, and load any saved spectrum.

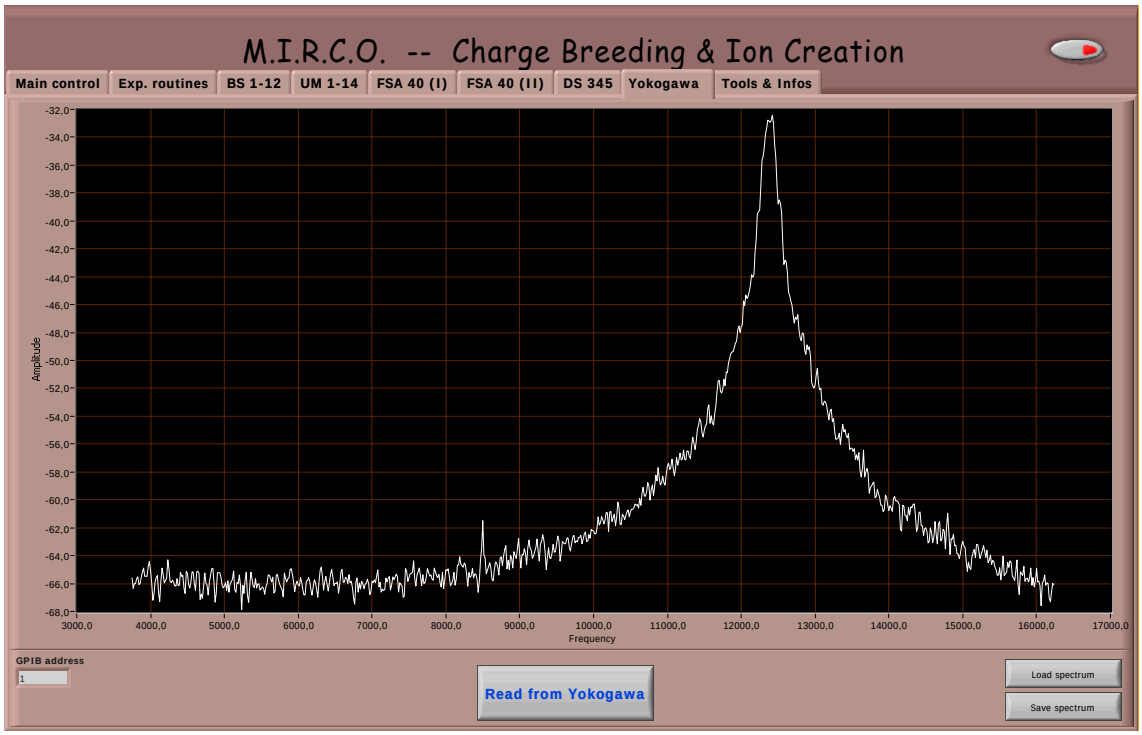

Figure B.3: Capture of the control-software tab which handles the read-out of spectra from the Yokogawa SA 2400.

B.5 Experimental routines

M.I.R.C.O. also counts on a tab from which the experimental routines can be called. These are typically subprograms, also LabView based, which automatize an experimental procedure or measurement. Until the moment, two subroutines have been implemented: one which automatically scans small frequency windows in the magnetron frequency region of the Creation trap in order to identify possible ion signals; and an ion-transport routine for moving the ions between the Precision and Analysis traps, but also to move clouds from the Creation trap to the other two Penning traps.

B.6 Further utilities

There are a number of tools, which do not require communication with external devices, which are useful to have implemented in the control system. An example are the frequency calculators which enable the user to find out the frequencies of an ion in a trap. The dimensional parameters of all three traps have been included, so, depending on the charge, mass, magnetic field strength and voltage applied, the axial and cyclotron frequencies are calculated. Furthermore, for a desired frequency, the voltage applied experimentally in order to get is calculated back.

Other pieces of information, such as the optimum biasing voltages for the transistors and amplifiers, or the binding energies of the electrons in calcium, along with several others, are also displayed in a separate tab (figure B.4).

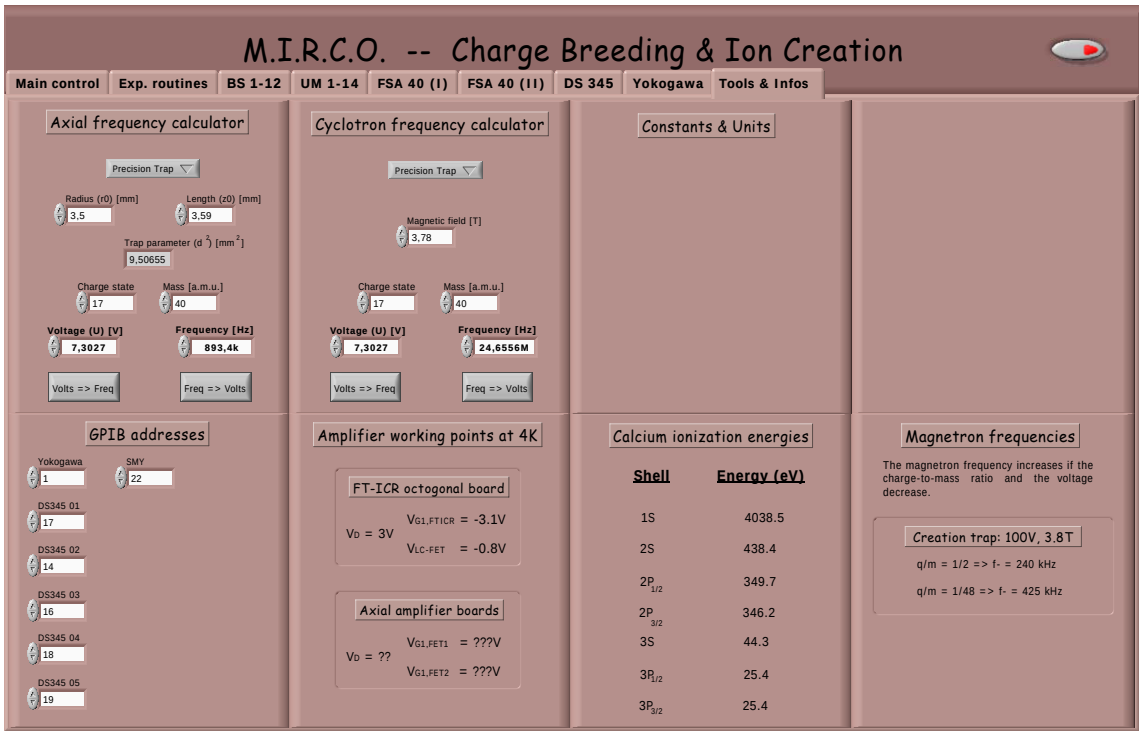

Figure B.4: Capture of the control-software tab where commonly-used tools and informations are located.

B.7 Expansion possibilities

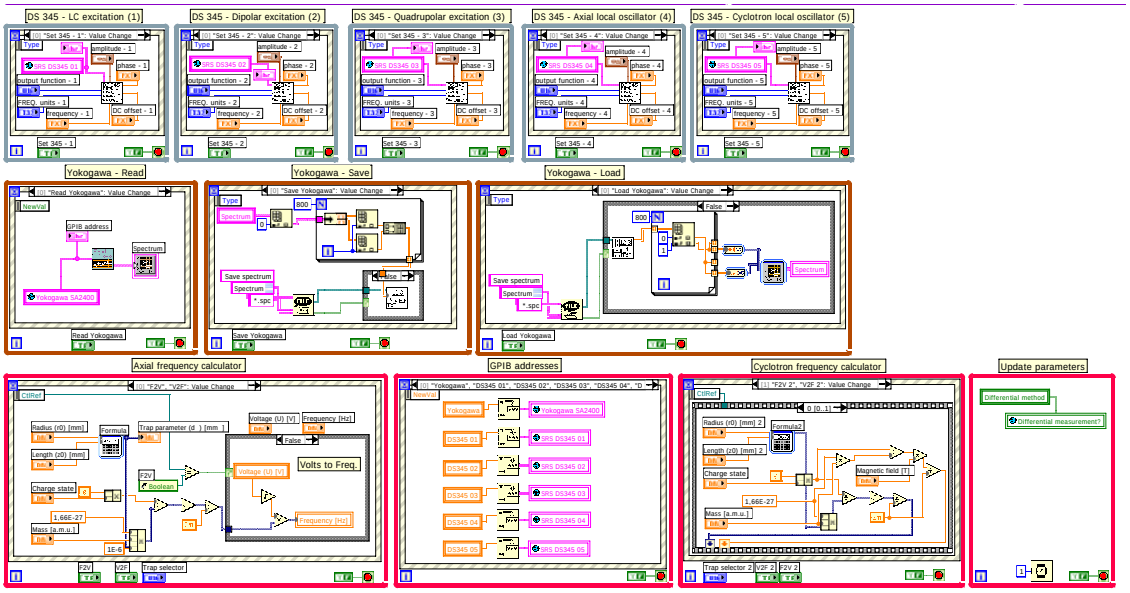

Figure B.5: Capture of the control-software source-code.

It has been already mentioned that M.I.R.C.O. is a modular program. Figure B.5 shows a screenshot of the source-code written in LabView. It represents a minor

portion of the complete code, since the overall program occupies 33 pages when printed, and there are many nested subroutines depicted by only an icon in them. Still, it is enough to show the modular configuration. Every one of the loops includes an interrupt-based functionality, which will be executed only in case the user triggers it with a button, knob, slide or any other control. Thus, by simply adding more of these loops, properly programmed so that it acts as an interrupt, the M.I.R.C.O. can be enhanced with new functions, routines and subprograms, which will be necessary for the next experimental stages.

Bibliography

[Alo03] J. Alonso
Axial temperature of a single hydrogenic carbon ion in a Penning trap.
Diplomarbeit Mainz (2003)

[Alo06] J. Alonso, K. Blaum, S. Djekic, H.-J. Kluge, W. Quint, B. Schabinger, S. Stahl, J. Verdú, M. Vogel and G. Werth
A miniature electron-beam ion source for in-trap creation of highly charged ions.
Rev. Sci. Instr., **77**(2006)03A901

[Bec01] R. Becker, O. Brinzanescu and T. Stöhlker
Limitation of EBIS/T ion yield by radiative recombination.
Proc. of the 8th International Symposium on EBIS/T 2000, Upton, New York 2000, AIP conference proceedings, **572**(2001)119

[Bei95] P. Beiersdorfer, St. Becker, B. Beck, S. Elliott, K. Widmann and L. Schweikhard
Fourier transform - ion cyclotron resonance mass spectrometry - A new tool for measuring highly charged ions in an electron beam ion trap.
Nucl. Instr. Meth. B, **98**(1995)558

[Bei00a] T. Beier
The g_j factor of a bound electron and the hyperfine structure splitting in hydrogenlike ions.
Phys. Rep., **339**(2000)79

[Bei00b] T. Beier, H. Häffner, N. Hermanspahn, I. Lindgren, H. Persson, S. Salomonson and P. Sunnergren
g_j factor of an electron bound in a hydrogenlike ion.
Phys. Rev. A, **62**(2000)032510

[Bei02] T. Beier, H. Häffner, S.G. Karshenboim, H.-J. Kluge, W. Quint, S. Stahl, J. Verdú and G. Werth
New determination of the electron's mass.
Phys. Rev. Lett., **88**(2002)011603

[Bei03] T. Beier, P. Indelicato, V.M. Shabaev and V.A. Yerokhin
New value for the electron's mass - theoretical foundations.
J. Phys. B: At. Mol. Phys., **36**(2003)1019

[Bei05] T. Beier, L. Dahl, H.-J. Kluge, C. Kozhuharov, W. Quint and the HITRAP collaboration.
Trapping ions of hydrogen-like uranium: The HITRAP project at GSI.
Nucl. Instr. and Meth. B, **235**(2005)473

[Ber03] I. Bergström, M. Björkhage, K. Blaum, H. Bluhme, T. Fritioff, S. Nagy and R. Schuch
High-precision mass measurements of hydrogen-like $^{24}Mg^{11+}$ and $^{26}Mg^{11+}$ ions in a Penning trap.
Eur. Phys. J. D, **22**(2003)41

[Bet57] H.A. Bethe and E.E. Salpeter
Quantum mechanics of one- and two-electron atoms.
Springer, Berlin, 1957

[Bla06] K. Blaum
High-accuracy mass spectrometry with stored ions.
Phys. Rep., **425**(2006)1

[Ble29] W. Bleakney
A new method of positive ray analysis and its application to the measurement of ionization potentials in mercury vapor.
Phys. Rev., **34**(1929)157

[Bol84] S. Boltzmann
Ableitung des Stefan'schen Gesetzes, betreffend die Abhängigkeit der Wärmestrahlung von der Temperatur aus der electromagnetischen Lichttheorie.
Ann. Phys. Chem., **22**(1884)291

[Bos89] M.G. Boshier, P.E.G. Baird, C.J. Foot, E.A. Hinds, M.D. Plimmer, D.N. Stacey, J.B. Swan, D.A. Tate, D.M. Warrington, and G.K. Woodgate
Laser spectroscopy of the 1S-2S transition in hydrogen and deuterium: Determination of the 1S Lamb shift and the Rydberg constant.
Phys. Rev. A, **40**(1989)6169

[Bre28] G. Breit
Magnetic moment of the electron.
Nature, **122**(1928)649

[Bro86] L.S. Brown and G. Gabrielse
Geonium Theory: Physics of a single electron or ion in a Penning trap.
Rev. Mod. Phys. 58, **1**(1986)233

[Bub92] R.H. Bube
Electrons in solids: an introductory survey.
Academic press Inc., Elsevier (1992)

[Cas82] E. Casnati, A. Tartari and C. Baraldi
An empirical approach to K-shell ionisation cross section by electrons.
J. Phys. B: At. Mol. Phys., **15**(1982)155

[Chi11] C.D. Child
Discharge from hot CaO.
Phys. Rev., **32**(1911)492

[Cho03] T.C. Choy, A.H. Harker and A.M. Stoneham
Field emission theory for an enhanced surface potential: a model for carbon field emitters.
J. Phys. C: Condens. Matter, **16**(2004)861

[Chu69] D.A. Church and H.G. Dehmelt
Radiative cooling of an electrodynamically contained proton gas.
J. Appl. Phys., **40**(1969)3421

[Com30] K.T. Compton and I. Langmuir
Electrical discharges in gases. Part I: Survey of fundamental processes.
Rev. Mod. Phys., **2**(1930)123

[Cor89] E.A. Cornell, R.M. Weisskoff, K.R. Boyce, R.W. Flanagan, Jr, G.P. Lafyatis and D.E. Pritchard
Single-ion cyclotron resonance measurement of $M(CO^+)/M(N_2^+)$.
Phys. Rev. Lett., **63**(1989)1674

[Cor90] E.A. Cornell, R.M. Weisskoff, K.R. Boyce and D.E. Pritchard
Mode coupling in a Penning trap: *pi* pulses and a classical avoided crossing.
Phys. Rev. A, **41**(1990)312

[Cza01] A. Czarnecki, K. Melnikov and A. Yelkhovski
Anomalous magnetic moment of a bound electron.
Phys. Rev. A, **63**(2001)012509

[Deh62] H.G. Dehmelt
Bull. Am. Phys. Soc., **7**(1962)470

[Deh67] H.G. Dehmelt
Radio-frequency spectroscopy of stored ions. I. Storage.
Adv. At. Mol. Phys., **3**(1967)53

[Deh69] H.G. Dehmelt
Radiofrequency spectroscopy of stored ions. II. Spectroscopy.
Adv. At. Mol. Phys., **5**(1969)109

[Deh68] H.G. Dehmelt and F.L. Walls
"Bolometric" Technique for the rf Spectroscopy of Stored Ions.
Phys. Rev. Lett., **21**(1968)127

[Deu98] H. Deutsch, K. Becker and T.D. Märk
Improved low-energy dependence of calculated cross sections for the K-shell ionization of atoms using the Deutsch-Märk formalism.
Int. J. Mass Spec., **177**(1998)47

[Dje04a] S. Djekic
Implementation of new techniques for high precision *g-factor* measurements.
Dissertation, Universität Mainz (2004)

[Dje04b] S. Djekic, J. Alonso, H.-J. Kluge, W. Quint, S. Stahl, T. Valenzuela, J. Verdú, M. Vogel and G. Werth
The temperature of a single ion in a Penning trap.
Eur. Phys. J. D, **31**(2004)451

[Don68] E.D. Donets, V.I. Ilyushchenko and V.A. Alpert
Electron Beam Multicharged Ion Source.
Preprint Joint Inst. Nucl. Res., **R7**(1968)4124

[Don69] E.D. Donets, V.I. Ilyushchenko and V.A. Alpert
Ultrahigh Vacuum Electron Beam Source Of Highly Stripped Ions.
Proceedings 1st International Conference on Ion Sources in Saclay, (1969)635

[Don81] E.D. Donets and V.P. Ovsyannikov
Investigation of ionization of positive ions by electron impact.
Sov. Phys. - JETP, **53**(1981)466

[Dyc87] R.S. Van Dyck, Jr., P.B. Schwinberg and H.G. Dehmelt
New high-precision comparison of electron and positron *g-factors*.
Phys. Rev. Lett., **59**(1987)26

[Eid95] M.I. Eides
New developments in the theory of muonium hyperfine splitting.
Proceedings of the Paris workshop on quantum infrared physics, June 6-10, 1994
ed. H.M. Fried and B.M. Mueller (World Scientific, Singapore, 1995)262

[Far99] S. Fardo and D. Patrick
Understanding ac Circuits.
Butterworth-Heinemann (1999)

[Fau70] R.N. Faustov
Magnetic moment of the hydrogen atom.
Phys. Lett. B, **33**(1970)422

[Fau01] A.P. Martynenko and R.N. Faustov
The *g-factors* of bound particles in quantum electrodynamics.
JETP, **93**(2001)471

[Fey72] R.P. Feynman
Statistical Mechanics, A Set of Lectures.
Addison-Wesley Publishing Company, (1972)

[Fir96] R.B. Firestone
Table of isotopes (8th edition).
John Wiley & Sons, New York, (1996)

[Fow28] R.H. Fowler and L.W. Nordheim
Electron emission in intense electric fields.
Proc. R. Soc. Lond., **A119**(1928)173

[Gab89] G. Gabrielse, L. Haarsma and S.L. Rolston
Open-endcap Penning Traps for High Precision Experiments.
Int. J. Mass Spectrom. Ion Processes, **88**(1989)319

[Gab90] G. Gabrielse, X. Fei, J. Haas, H. Kalinowsky, W. Kells, L.A. Orozco, R.L. Tjoelker and T.A. Trainor
Thousandfold improvement in the measured antiproton mass.
Phys. Rev. Lett, **65**(1990)1317

[Gab95] G. Gabrielse, D. Phillips, W. Quint, H. Kalinowsky, G. Rouleau and W. Jhe
Special relativity and the single antiproton; Fortyfold improved comparison of $\overline{p}$ and p charge-to-mass ratios.
Phys. Rev. Lett, **74**(1995)3544

[Gab06] G. Gabrielse, D. Hanneke, T. Kinoshita, M. Nio and B. Odom
New determination of the fine structure constant from the electron g-value and QED.
Phys. Rev. Lett, **97**(2006)030802

[Ger22] W. Gerlach and O. Stern
Z. Phys., **9**(1922)349 & 353

[Gla04] D.A. Glazov, V.M. Shabaev, I.I. Tupitsyn, A.V. Volotka, V.A. Yerokhin, G. Plunien and G. Soff
Relativistic and QED corrections to the *g-factor* of Li-like ions.
Phys. Rev. A, **70**(2004)062104

[Gon05] A.J. González Martínez
Quantum interference in the dielectronic recombination of heavy highly charged ions.
Dissertation, Universität Heidelberg (2005)

[Goo56] R.H. Good and L.W. Müller
Field emission.
Handbuch der Physik, vol. XXI, edited by S. Flugge, Springer, Berlin (1956)176

[Gra97] G. Grandi, M.K. Kazimierczuck, A. Massarini and U. Reggiani
Optimal design of single-layer solenoid air-core inductors for high frequency applications.
Proc. 40$^{\text{th}}$ Midwest Symp. on Circ. and Sys. (MWSCAS 97), Sacramento CA, **1**(1997)358

[Gra99] G. Grandi, M. K. Kazimierczuck, A. Massarini and U. Reggiani
Stray Capacitances of Single-Layer Solenoid Air-Core Inductors.
IEEE Trans. on Industry Applications, **35**(1999)1162

[Gre95] W. Greiner, L. Neise and H. Stöcker
Thermodynamics and statistical mechanics.
Springer-Verlag, (1995)349

[Gro70a] H. Grotch
Nuclear Mass Corrections to the Electron *g-factor*.
Phys. Rev. A, **2**(1970)1605

[Gro70b] H. Grotch
Electron *g-factor* in Hydrogenic Atoms.
Phys. Rev. Lett., **24**(1970)39

[Gro71] H. Grotch and R.A. Hegstrom
Hydrogenic atoms in a magnetic field.
Phys. Rev. A, **4**(1971)59

[Gus98] M.G.H. Gustavson and A.-M. Martensson-Pendrill
Need for remeasurements of nuclear magnetic dipole moments.
Phys. Rev. A, **58**(1998)3611

[Häf98] H. Häffner
Präparation einzelner hochgeladener Ionen in einer Penningfalle.
Diplomarbeit Mainz (1998)

[Häf00a] H. Häffner
Präzisionsmessung des magnetischen Moments des Elektrons in wasserstoffähnlichem Kohlenstoff.
Dissertation, Universität Mainz (2000)

[Häf00b] H. Häffner, T. Beier, N. Hermanspahn, H.-J. Kluge, W. Quint, S. Stahl, J. Verdú and G. Werth
High-accuracy measurements of the magnetic moment anomaly of the electron bound in hydrogenlike carbon.
Phys. Rev. Lett., **85**(2000)5308

[Häf03] H. Häffner, T. Beier, S. Djekic, N. Hermanspahn, H.-J. Kluge, W. Quint, S. Stahl, J. Verdú, T. Valenzuela and G. Werth
Double Penning trap technique for precise *g-factor* determinations in highly charged ions.
Eur. Phys. J. D, **22**(2003)163

[Hah97] Y. Hahn
Electron-ion recombination processes - an overview.
Rep. Prog. Phys., **60**(1997)691

[Her96] N. Hermanspahn
Aufbau eines Tieftemperaturkryostaten zum Betrieb einer Penningfalle.
Diplomarbeit Mainz (1996)

[Her99] N. Hermanspahn
Das magnetische Moment des gebundenen Elektrons in wasserstoffähnlichem Kohlenstoff (C^{5+}).
Dissertation, Universität Mainz (1999)

[Her06] F. Herfurth, T. Beier, L. Dahl, S. Eliseev, S. Heinz, O. Kester, C. Kozhuharov, G. Maero, W. Quint and the HITRAP collaboration
Precision measurements with highly charged ions at rest: The HITRAP project at GSI.
Int. J. Mass Spectrom., **251**(2006)266

[Jak87] C. Jakoby, H. Genz and A. Richter
A semi-empirical formula for the total K-shell ionization cross section by electron impact.
J. Physique Coll., **48**(1987)C9-487

[Jef97] A.-M. Jeffery, R.E. Elmquist, L.H. Lee, J.Q. Shields and R.F. Dziuba
NIST comparison of the quantized Hall resistance and the realization of the SI OHM through the calculable capacitor
IEEE Trans. Instrum. Meas., **46**(199)264

[Joh28] J.B. Johnson
Thermal agitation of electricity in conductors.
Phys. Rev., **32**(1928)97

[Kar50] R. Karplus and N.M. Kroll
Metrologia, **32**(1995)117

[Kay] Kaye & Laby
Table of physical and chemical constants
2.6.6 Magnetic properties of materials
http://www.kayelaby.npl.co.uk/general_physics/2_6/2_6_6.html

[Kel03] A. Kellerbauer, K. Blaum, G. Bollen, F. Herfurth, H.-J. Kluge, M. Kuckein, E. Sauvan, C. Scheidenberger and L. Schweikhard
From direct to absolute mass measurements: A study of the accuracy of ISOLTRAP.
Eur. Phys. J. D, **22**(2003)53

[Kim83] Y.S. Kim and R.H. Pratt
Direct radiative recombination of electrons with atomic ions: Cross sections and rate coefficients.
Phys. Rev. A, **27**(1983)2913

[Kim94] Y.-K. Kim and M.E. Rudd
Binary-encounter-dipole model for electron-impact ionization.
Phys. Rev. A, **50**(1994)3954

[Kin23] K.H. Kingdon
A method for the neutralization of electron space charge by positive ionization at very low gas pressures.
Phys. Rev., **21**(1923)408

[Kin96] T. Kinoshita
The fine structure constant.
Rep. Prog. Phys., **59**(1996)1459

[Kin06] T. Kinoshita and M. Nio
Improved α^4 term of the electron anomalous magnetic moment.
Phys. Rev. D, **73**(2006)013003

[Koh04] W. S. Koh and L. K. Ang
Simulation of high current field emission from vertically well-aligned metallic carbon nanotubes.
Int. J. Nanosc., **3**(2004)677

[Kre99] M. Kretzschmar
Trapped charged particles and fundamental physics.
AIP Conference Proceedings, **457**(1999)242

[Kru95] E. Krüger, W. Nistler and W. Weirauch
Fourth-order corrections in quantum electrodynamics and the magnetic moment of the electron.
Phys. Rev., **77**(1947)536

[Kuz01] T. Kuzumaki, Y. Takamura, H. Ichinose and Y. Horiike
Structural change at the carbon-nanotube tip by field emission.
App. Phys. Lett., **78**(2001)3699

[Lam47] W.E. Lamb and R.C. Retherford
Fine structure of the hydrogen atom by a microwave method.
Phys. Rev., **72**(1947)241

[Lan23] I. Langmuir
The effect of space-charge and residual gases on thermionic currents in high vacuum.
Phys. Rev., **21**(1923)419

[Lan91] L.D. Landau and E.M. Lifshitz
Quantum mechanics.
Pergamon (1991)165

[Lap96] S. Laporta and E. Remiddi
The analytical value of the electron $(g-2)$ at order α^3 in QED.
Phys. Lett. B, **379**(1996)283

[Lev88] M.A. Levine, R.E. Marrs, J.R. Henderson, D.A. Knapp and M.B. Schneider
Physica Scripta **T22**(1988)157

[Lev89] M.A. Levine, R.E. Marrs, J.N. Bardsley, P. Beiersdorfer, C.L. Bennett, M.H. Chen, T. Cowan, D. Dietrich, J.R. Henderson, D.A. Knapp, A. Osterheld, B.M. Penetrante, M.B. Schneider and J.H. Scofield
The use of an electron beam ion trap in the study of highly charged ions
Nucl. Instr. Meth. B, **43**(1989)431

[Lia06] X.H. Liang, S.Z. Deng, N.S. Xu, J. Chen, N.Y. Huang and J.C. She
On achieving better uniform carbon nanotube field emission by electrical

treatment and the underlying mechanism.
Appl. Phys. Lett., **88**(2006)111501

[Liu99] W. Liu, M.G. Boshier, S. Dhawan, O. van Dyck, P. Egan, X. Fei, M. Grosse Perdekamp, V.W. Hughes, M. Janousch, K. Jungmann, D. Kawall, F.G. Mariam, C. Pillai, R. Prigl, G. zu Putlitz, I. Reinhard, W. Schwarz, P.A. Thompson and K.A. Woodle
High precision measurements of the ground state hyperfine structure interval of muonium and of the muon magnetic moment.
Phys. Rev. Lett., **82**(1999)711

[Lot67] W. Lotz
An empirical formula for the electron-impact ionization cross-section.
Z. Phys., **206**(1967)205

[Lug96] J.W. Luginsland, Y.Y. Lau and R.M. Gilgenbach
Two-dimensional Child-Langmuir law.
Phys. Rev. Lett., **77**(1996)4668

[Maj04] F.G. Major, V.N. Gheorghe and G. Werth
Charged particle traps: The physics and techniques of charged particle field confinement.
Springer (2004)

[Mal80] J.H. Malmberg and C.F. Driscoll
Long-time containment of a pure electron plasma.
Phys. Rev. Lett., **44**(1980)654

[Mar82] F.G. Mariam, W. Beer, P.R. Bolton, P.O. Egan, C.J. Gardner, V.W. Hughes, D.C. Lu, U. Moser, H. Orth, G. zu Putlitz, P.A. Souder and J. Vetter
Higher precision measurement of the hfs interval of muonium and of the muon magnetic moment.
Phys. Rev. Lett., **49**(1982)993

[Mar94] R.E. Marrs, S.R. Elliott and D.A. Knapp
Production and trapping of hydrogenlike and bare uranium ions in an electron beam ion trap.
Phys. Rev. Lett., **72**(1994)4082

[Mar06] M. Marie-Jeanne, J. Alonso, K. Blaum, S. Djekic, M. Dworschak, U. Hager, A. Herlert, H.-J. Kluge, S. Nagy, R. Savreux, L. Schweikhard, S. Stahl and C. Yazidjian
Magnetic field stabilization for high-accuracy mass measurements on exotic nuclides.
Submitted to Int. J. Mass. Spectrom. (2006)

[Mau06] F. Maurer, A. Dangwal, D. Lysenkov, G. Müller, M.E. Toimil-Molares, C. Trautmann, J. Brötz and H. Fuess
Field emission of copper nanowires grown in polymer ion-track membranes.
Nucl. Instr. Meth. B, **245**(2006)337

[Moh05] P.J. Mohr and B.N. Taylor
CODATA recommended values of the fundamental physical constants: 2002.
Rev. Mod. Phys., **77**(2005)1

[Mül77] A. Müller and E. Salzborn
Scaling of cross sections for multiple electron transfer to highly charged ions colliding with atoms and molecules.
Phys. Lett., **62A**(1977)391

[Mur56] E.L. Murphy and R.H. Good
Thermionic emission, field emission, and the transition region.
Phys. Rev., **102**(1956)1464

[NIFS] NIFS database: Atomic and molecular numerical databases
AMDIS (Atomic and Molecular Data Interactive System).
http://dpc.nifs.ac.jp/amdata/amdis.html

[NIST] NIST database
Electron impact cross sections for ionization and excitation.
http://physics.nist.gov/PhysRefData/Ionization/atom_index.html

[Nyq28] H. Nyquist
Thermal agitation of electric charge in conductors.
Phys. Rev., **32**(1928)110

[Nor28] L.W. Nordheim
The effect of the image force on the emission and reflection of electrons by metals.
Proc. R. Soc. Lond., **A121**(1928)626

[Odo06] B. Odom, D. Hanneke, B. D'Urso and G. Gabrielse
New measurement of the electron magnetic moment using a one-electron quantum cyclotron.
Phys. Rev. Lett, **97**(2006)030801

[Ope89] A.V. Oppenheim and R.W. Schafer
Discrete time signal processing.
Prentice-Hall, Inc., New Jersey (1989)

[Pac05] K. Pachucki, A. Czarnecki, U.D. Jentschura and V.A. Yerokhin
Complete two-loop correction to the bound-electron *g-factor*.
Phys. Rev. A, **72**(2005)022108

[Pat06] S.K. Patra and G.M. Rao
Field emission current saturation of aligned carbon nanotubes - Effect of density and aspect ratio.
J. App. Phys., **100**(2006)024319

[Pau55] W. Paul and M. Raether
Z. Physik, **140**(1955)262

[Pen36] F.M. Penning
Glow discharge between coaxial cylinders at low pressure in an axial magnetic field.
Physica (Utrecht), **3**(1936)873

[Pen91] B.M. Penetrante, J.N. Bardsley, D. DeWitt, M. Clark and D. Schneider
Evolution of ion-charge-state distributions in an electron-beam ion trap.
Phys. Rev. A, **43**(1991)4861

[Pet57] A. Petermann
Fourth-order magnetic moment of the electron.
Helv. Phys. Acta, **30**(1957)407

[Pie54] J.R. Pierce
Theory and design of electron beams.
Macmillan & CO., London (1954)

[Pur02] S.T. Purcell, P. Vincent, C. Journet and V.T. Binh
Hot nanotubes: stable heating of individual multiwall carbon nanotubes to 2000 K induced by the field-emission current.
Phys. Rev. Lett., **88**(2002)105502

[Qui01] W. Quint, J. Dilling, S. Djekic, H. Häffner, N. Hermanspahn, H.-J. Kluge, G. Marx, R. Moore, D. Rodriguez, J. Schönfelder, G. Sikler, T. Valenzuela, J. Verdú, C. Weber and G. Werth
HITRAP: A Facility for Experiments with Trapped Highly Charged Ions.
Hyp. Int., **132**(2001)457

[Rea04] F.H. Read and N.J. Bowring
Field enhancement factors of random arrays of carbon nanotubes.
Nucl. Instr. Meth. A, **519**(2004)305

[Sak85] J.J. Sakurai
Modern quantum mechanics.
Addison-Wesley Publishing Company, Inc. (1985)

[Sch48] J. Schwinger
On quantum-electrodynamics and the magnetic moment of the electron.
Phys. Rev., **73**(1948)416

[Sch94] R. Schetgen
The ARRL handbook for radio amateurs.
The american radio relay league, Newington, USA (1994)

[Sed06] T.A. Sedrakyan, E.G. Mishchenko and M.E. Raikh
Penetration of external field into regular and random arrays of nanotubes: implications for field emission.
Phys. Rev. B, **73**(2006)245325

[Sha02a] V.M. Shabaev, D.A. Glazov, M.B. Shabaeva, V.A. Yerokhin, G. Plunien and G. Soff
g-factor of high-Z lithiumlike ions.
Phys. Rev. A, **65**(2002)062104

[Sha02b] V.M. Shabaev and V.A. Yerokhin
Recoil correction to the bound-electron *g-factor* in H-like atoms to all orders in αZ.
Phys. Rev. Lett., **88**(2002)091801

[Shk66] I.P. Shkarofsky, T.W. Johnston and M.P. Bachynski
The particle kinetics of plasmas.
Addison-Wesley, Reading, MA(1966)

[Sho38] W. Shockley
Currents to conductors induced by a moving point charge.
J. Appl. Phys., **9**(1938)635

[Smi30] P.T. Smith
The ionization of helium, neon, and argon by electron impact.
Phys. Rev., **36**(1930)1293

[Som58] C.M. Sommerfield
Ann. Phys. (N.Y.), **5**(1958)26

[Son04] J. Song, M. Sun, Q. Chen, J. Wang, G. Zhang and Z. Xue
Field emission from carbon nanotube arrays fabricated by pyrolysis of iron phthalocyanine.
J. Phys. D: Appl. Phys., **37**(2004)5

[Spi56] L. Spitzer
Physics of fully ionized gases.
Interscience, New York(1956)

[Sta98] S. Stahl
Aufbau eines Experimentes zur Bestimung elektronischer g-Faktoren einzelner wasserstoffähnlichen Ionen.
Dissertation, Universität Mainz (1998)

[Sta05] S. Stahl, J. Alonso, S. Djekic, F. Galve, W. Quint, T. Valenzuela, J. Verdú, M. Vogel and G. Werth
Phase-sensitive measurement of small frequency differences.
J. Phys. B: At. Mol. Opt. Phys., **38**(2005)297

[Ste79] J. Stefan
Über die Beziehung zwischen der Wärmestrahlung und der Temperatur.
Sitzungsberichte der mathematisch-naturwissenschaftlichen Classe der kaiserlichen Akademie der Wissenschaften, **79**(1879)391

[Str62] R. Stratton
Theory of field emission from semiconductors.
Phys. Rev., **125**(1962)67

[Tön96] M. Tönges
Aufbau einer Mikrowellenanlage zur Spektroskopie an wasserstoffähnlichen Ionen in einer Penningfalle.
Diplomarbeit Mainz (1996)

[Tur89] S. Turner
Superconductivity in particle accelerators.
CERN - Service d'information scientifique - RD/775-3500, Geneva (1989)

[Ude97] Th. Udem, A. Huber, B. Gross, J. Reichert, M. Prevedelli, M. Weitz, and T.W. Hänsch
Phase-coherent measurement of the hydrogen 1S-2S transition frequency with an optical frequency interval divider chain.
Phys. Rev. Lett., **79**(1997)2646

[Ulm06a] S. Ulmer
Entwicklung des experimentellen Aufbaus zur Messung des *g-Faktors* des Protons in einer Penning-Falle.
Diplomarbeit Mainz (2006)

[Ulm06b] S. Ulmer, J. Alonso, K. Blaum, F. Maurer, W. Quint, B. Schabinger and R. Steinborn
Field emission of nanowire arrays at temperatures ranging from 4 K to 300 K.
Publication in preparation

[Val04] T. Valenzuela
Mode coupling for precise measurements of the electronic *g-factor* of hydrogen-like ions in Penning traps.
Dissertation, Universität Mainz (2004)

[Ver01] J. Verdú
One experiment for the high precision measurement of the g_j*-factor* of the electron bound in hydrogenlike ions.
Diplomarbeit Mainz (2001)

[Ver03] J. Verdú
Ultrapräzise Messung des elektronischen g-Faktors in wasserstoffähnlichem Sauerstoff.
Dissertation, Universität Mainz (2003)

[Ver04a] J. Verdú, T. Beier, S. Djekic, H.-J. Kluge, W. Quint, S. Stahl, T. Valenzuela, M. Vogel and G. Werth
Electronic *g-factor* of hydrogenlike oxygen $^{16}O^{7+}$.
Phys. Rev. Lett., **92**(2004)093002

[Ver04b] J. Verdú, S. Djekic, S. Stahl, T. Valenzuela, M. Vogel, G. Werth, H.-J. Kluge and W. Quint
Determination of the *g-factor* of single hydrogen-like ions by mode coupling in a Penning trap.
Phys. Scr., **T112**(2004)68

[Ver05] J. Verdú, S. Kreim, J. Alonso, K. Blaum, S. Djekic, W. Quint, S. Stahl, S. Ulmer, M. Vogel, J. Walz and G. Werth
Penning trap measurement of the magnetic moment of the antiproton.
Proceedings of the LEAP 2005 Conference, Issue 1, **796**(2005)260

[Vog04] M. Vogel, J. Alonso, S. Djekic, H.-J. Kluge, W. Quint, S. Stahl, J. Verdú and G. Werth
Towards electronic *g-factor* measurements in medium-heavy hydrogen-like and lithium-like ions.
Nucl. Inst. Meth. B, **235**(2005)7

[Wei92] S. Weinberg
Dreams of a final theory. The search for the fundamental laws of nature.
Pantheon Books, New York(1992)

[Wer06] G. Werth, J. Alonso, T. Beier, K. Blaum, S. Djekic, H. Häffner, N. Hermanspahn, W. Quint, S. Stahl, J. Verdú, T. Valenzuela and M. Vogel
Highly charged ions, quantum-electrodynamics, and the electron mass.
Int. J. Mass Spectrom., **251**(2006)152

[Win75] D. Wineland and H.G. Dehmelt
Principles of the stored ion calorimeter.
J. Appl. Phys., **46**(1975)919

[Yan01] Z.-C. Yan
Calculations of magnetic moments for three-electron atomic systems.
Phys. Rev. Lett., **86**(2001)5683

[Yer02] V.A. Yerokhin, P. Indelicato and V.M. Shabaev
Self-energy correction to the bound-electron *g-factor* in H-like ions.
Phys. Rev. Lett., **89**(2002)143001

[Zee97] P. Zeeman
On the influence of magnetism on the nature of the light emitted by a substance.
Phil. Mag., **43**(1897)226

[Zum84] J.D. Zumbro, E.B Shera, Y. Tanaka, C.E. Bemis, Jr., R.A. Naumann, M.V. Hoehn, W. Reuter and R.M. Steffen
E_2 and E_4 deformations in ^{233,234,235,238}U.
Phys. Rev. Lett., **53**(1984)1888